2015

Modeling and simulations of strain-induced phase transformations in materials under compression and compression-torsion in traditional and rotational diamond anvil cells

Biao Feng
Iowa State University

Recommended Citation

Feng, Biao, "Modeling and simulations of strain-induced phase transformations in materials under compression and compression-torsion in traditional and rotational diamond anvil cells" (2015). *Graduate Theses and Dissertations*. 14304.
https://lib.dr.iastate.edu/etd/14304

Modeling and simulations of strain-induced phase transformations in materials under compression and compression-torsion in traditional and rotational diamond anvil cells

by

Biao Feng

A dissertation submitted to the graduate faculty

in partial fulfillment of the requirements for the degree of

DOCTOR OF PHILOSOPHY

Major: Engineering Mechanics

Program of Study Committee:
Valery I. Levitas, Major Professor
Ashraf Bastawros
Thomas Rudolphi
Wei Hong
Baskar Ganapathysubramanian

Iowa State University

Ames, Iowa

2015

DEDICATION

I would like to dedicate this dissertation to my Baba and Mama (Dad and Mom), my dear wife Jiajia, and my cute son Raymond for their love, support, patience, and sacrifice.

TABLE OF CONTENTS

ACKNOWLEDGEMENTS

I would like to thank my Ph. D supervisor Dr. Valery I. Levitas for his continuous intellectual and financial support to my research as I am a Ph. D student. Dr. Levitas sets a great example on research to every student, and his dedication on research always encourages me. I met a number of challenges and problems in the research, and he always welcomed me to discuss with him at any time. Due to his wide range of knowledge, he always gave me very important and helpful suggestions and ideas for my research. I would have been unable to reach this point in my career without his constant guidance.

I would like to thank Dr. Zarechnyy for his help on learning using software and writing subroutines. I want to also offer my appreciation to my committee members for their efforts: Dr. Ashraf Bastawros, Thomas Rudolphi, Wei Hong, and Baskar Ganapathysubramanian. In addition, I would also like to give many thanks to Dr. Thomas Rudolphi, Dr. Wei Hong, and Dr. Leroy Sturges for helping me to understand their classes when I was a TA.

Finally, thanks to my family for their encouragement and to my wife for her patience, respect and love.

CHAPTER 1. GENERAL INTRODUCTION

1.1 Experimental phenomena in DAC and RDAC

Mechanochemistry investigates the effects of nonhydrostatic stresses and plastic strains on various structural changes including phase transformations (PTs) and chemical reactions[1]. PTs under high pressure and plastic shear are widespread in nature (e.g., in geophysics), physical experiments, and modern technologies. For examples, deep earthquakes are related to the instability due to shear strain-induced PT; the synthesis of various chemical compounds by ball milling is caused by strain-induced PTs; and shear ignition of energetic materials with goal to assess safety issues is another example. A diamond anvil cell (DAC) is a powerful tool to generate high pressure and large shear and *in situ* study PTs to high pressure phases, using modern diagnostics, like x-ray, Raman, and optical techniques[2-6]. After compression of the materials in DAC[7-9] when there is no liquid medium surrounding the sample, highly heterogeneous distributions on pressure were revealed; small steps of pressures which almost keep a constant with the growth of loading were found in the two-phases region. It is known from numerous experiments that the addition of plastic shear, due to the rotation of an anvil, leads to findings that have both fundamental and applied importance. Below, most experimental phenomena which occur during the compression and larger shear of various materials in DAC and rotational DAC (RDAC) were enumerated (see more details in Refs. 1 and 10):

1. Rotation of one anvil significantly reduces the PT pressure for some materials. For example, for PT from B1 to B2 in KCl, the pressure at the diffuse interface between these phases decreases from 2.4-3.0 to 1.8 GPa due to rotation of one anvil[8]. Note that

even in DAC without the rotation of an anvil, plastic deformation also significantly reduces the PT pressure. For example, an irreversible PT from $\gamma - Al_2O_3$ to a new phase occurred under a quasi-hydrostatic condition over 50 GPa but under a non-hydrostatic pressure above 35 GPa[11].

2. Small pressure plateaus (which almost keep a constant value during loading) were found on the very heterogeneous pressure distribution[8, 12]. These steps of pressure are located in two-phases regions where PTs occur. It is assumed that the pressure value at these plateaus could be used as the pressure to characterize the PTs [8].

3. The difference Δp between the starting pressures of direct and reverse PTs is reduced by rotation of an anvil. For PT in Insb, from semiconductor to metal Δp is 1.0 GPa under shear and it is 1.75 GPa under hydrostatic conditions[13].

4. Direct PT pressure under plastic shear is lower than equilibrium pressure (e.g. from semiconductor to metal in InSb, InTe, Ge (from I to II) and Si (from I to II)[13]) .

5. Rotation of an anvil induces the generation of new phases which did not appear without rotation. As examples, the rhombohedral Phase of GeTe[14], Cu I-VIII phase[15], phase V of fullerene C_{60}[7, 12] were not obtained without shear but obtained with large shear.

6. For some materials, a reversible PT is substituted an irreversible one under shear deformation[16].

7. The volume fraction of the new phase is an increasing function of the rotation angle[17] and plastic strain, and the PT is strain-controlled rather time controlled.

8. Pressure increases in the transforming region in RDAC. Sometimes, at a given compressive force and with increasing rotation angle, the pressure grows in the

transforming zone in spite of reduction in volume during PT[7-9, 12, 15], which is so-called 'pressure self-multiplication effect'. However, it is also found that pressure decreases in the centre of sample from 34 to 24 Gpa on the appearance of a new Cu I-VIII phase in RDAC at fixed axis force[18].

9. Without a PT, the pressure distribution is practically independent of rotation, e.g. for Nacl[12].

1.2 Motivations

Within a liquid the sample is subjected to hydrostatic loading and undergoes pressure-induced phase transformations and it starts by nucleation at pre-existing defects (pressure and stress concentrators). In order to study the effect of plastic deformations on PTs, a rotational DAC was utilized[7, 19-22], in which large plastic shear due to rotation of one of the anvils is superposed on high pressure. Such PTs are classified as strain-induced ones and they occur by nucleation at defects that continuously appear during the plastic deformation[1]. In fact, PTs under compression without hydrostatic media in traditional DAC are also strain-induced rather than pressure-induced, because they occur during intense plastic flow of materials[1, 23]. As it was discussed in Ref. 1, 23, 24, the only difference between PTs under compression in DAC and compression and torsion in rotational DAC is the pressure-plastic strain history for each material point of the sample. Thus, the main focus is on the strain-controlled kinetic equation (8) in Chapter 2 for the concentration of the high pressure phase, c, with respect to undeformed state, which is independent of time and depends on four main parameters: (1) kinetic parameter k which scales the rate of PTs, (2) the minimum pressure p_{ε}^{d} below which direct strain-induced PT cannot occur, (3) the maximum pressure p_{ε}^{r} above which reverse strain-induced PT does not take place, and (4) the ratio of yield strengths of low (σ_{y1}) and high pressure (σ_{y2}) phases. We are unaware of any publications that determine parameters of the kinetic equation and fields of stress and strain tensors experimentally. Pressure distribution and concentration of high pressure phase distributions along the radius of a sample are available only. As a consequence, theoretical and finite element methods have been developed and applied for investigation of variation of stress tensor, accumulated plastic strain, and concentration fields in a sample during plastic flow and PTs and for analysis and interpretation of experimental results.

Numerical results, published in Refs. 23, and 24, describe a number of experimental observations, however they are incomplete because they are obtained for $p_\varepsilon^d > p_\varepsilon^r$ only. In this case, both direct and reverse PTs cannot occur for values of pressure p in the range $p_\varepsilon^r < p < p_\varepsilon^d$; above p_ε^d direct PT occurs only and below p_ε^r reverse PT takes place only, reaching complete transformation at very large plastic strain. However, the case $p_\varepsilon^d < p_\varepsilon^r$ is at least of the same importance, for which both direct and reverse PTs occur in the pressure range $p_\varepsilon^d < p < p_\varepsilon^r$. One of the *goals* of the dissertation is to study in detail coupled plastic flow and PTs in a sample in DAC for the case with $p_\varepsilon^d < p_\varepsilon^r$. Another *goal* is to study plastic flow and PTs after *unloading* and *reloading,* which was never done before. In many cases, high pressure phase is metastable after pressure release and can exist and be studied at ambient conditions. However, if there is no reverse PT under hydrostatic loading-unloading, this does not mean that reverse PT will not occur during the reduction of the load to zero after strain-induced PT. In Chapters 2 and 3, the effects of $p_\varepsilon^d < p_\varepsilon^r$, and processes of unloading and reloading are investigated in detail for DAC and RDAC.

Without PTs (and, in some cases, with PTs), pressure p distribution within a sample along the radius r is determined by a simplified equilibrium equation $\frac{dp}{dr} = \frac{2\tau_{zr}^c}{h}$, where τ_{zr}^c is the radial frictional shear stress at the contact surface with an anvil, and h is the current thickness of the sample. Without friction, pressure is constant along the radius and there is no way to increase it to high value, namely above material hardness. In contrast, if the maximum possible friction stress is equal to the yield strength in shear τ_y and there is a large ratio of the sample radius R to the thickness, then pressure grows linearly from the periphery to the center and can reach several megabars in magnitude. Thus, the entire field of high pressure physics and material science is based on the ability to create frictional resistance to the radial plastic flow in the thin sample during its compression. Therefore, taking a suitable friction model into account is another goal. In Chapters 4 and 5, combined plastic and Coulomb friction are proposed to study the effects of friction including Coulomb friction coefficient and differences between slippage and cohesion models are compared.

In most cases, the sample is placed inside of a deformable gasket made of a material with different strength. If achieving maximum possible pressure in a reasonably large volume is the goal, the gasket is made of the strongest possible materials, such as T301 stainless steel[25], rhenium[26], and even diamond powder[27]. If the goal is just to avoid an intense flow of powder sample at the initial stage of compression, a weak gasket could be made of polymer, paper, or cardboard. Consequently studying on the effects of gasket will help us to design experiments to obtain faster/slower PT rate. In Chapter 6, the effects of gasket in DAC are studied in detail.

The paper is organized as follows. In Chapter 1, several important experimental phenomena in DAC and RDAC are enumerated and the motivations of this dissertation are elaborated. In Chapter 2, PTs under compression, unloading and reloading in DAC are investigated. In Chapter 3, simulation of loading, unloading, and reloading in RDAC is discussed. In Chapters 4 and 5, effect of contact sliding in DAC and RDAC is studied. In Chapter 6, effect of gasket's strength and size on the strain-induced PTs in a sample is investigated. And Chapter 7 draws the general conclusion about this dissertation and future directions for my research are introduced.

References

[1] V. I. Levitas, Phys Rev B **70,** 184118 (2004).

[2] C. Nisr, G. Ribarik, T. Ungar, G. B. M. Vaughan, P. Cordier, and S. Merkel, J Geophys Res-Sol Ea **117**, B03201 (2012).

[3] A. R. Oganov, et al., Nature **457**, 863 (2009).

[4] T. S. Duffy, G. Y. Shen, D. L. Heinz, J. F. Shu, Y. Z. Ma, H. K. Mao, R. J. Hemley, and A. K. Singh, Phys Rev B **60**, 15063 (1999).

[5] A. Lazicki, P. Loubeyre, F. Occelli, R. J. Hemley, and M. Mezouar, Phys Rev B **85** , 054103 (2012).

[6] C. S. Zha, Z. X. Liu, and R. J. Hemley, Phys Rev Lett **108**, 146402 (2012).

[7] V. Blank, et al., Phys Lett A **188**, 281 (1994).

[8] V. D. Blank, Y. Y. Boguslavsky, M. I. Eremets, E. S. Itskevich, Y. S. Konyaev, A. M. Shirokov, and E. I. Estrin, Zh. Eksp. Teor. Fiz. **87**, 922 (1984).

[9] V. D. Blank and S. G. Buga, Instrum. Exp. Tech. **36**, 149 (1993).

[10] Y. Gogotsi, V. Domnich, High-pressure surface science and engineering, Institute of Physics Pub, Bristol; Philadelphia, 2004, p. 639 p

[10] M. M. Aleksandrova, V. D. Blank, and S. G. Buga, Fizika Tverdogo Tela **35**, 1308 (1993).

[11] C. E. Moffitt, B. Chen, D. M. Wieliczka, and M. B. Kruger, Solid State Commun **116**, 631 (2000).

[12] N. V. Novikov, S. B. Polotnyak, L. K. Shvedov, and V. I. Levitas, Superhard Mater. **39** (1999).

[13] M. M. Alexandrova, V. D. Blank, A. E. Golobokov, and Y. S. Konyaev, Sov. Phys. Solid State **30**, 577 (1988).

[14] N. R. Serebryanaya, V. D. Blank, and V. A. Ivdenko, Phys Lett A **197**, 63 (1995).

[15] S. S. Batsanov, N. R. Serebryanaya, V. D. Blank, and V. A. Ivdenko, Kristallografiya **40**, 650 (1995).

[16] V. D. Blank, G. A. Dubitsky, and S. A. Plotyanskaya, High Pressure Science and technology Proceeding, 325 (1995).

[17] M. M. Aleksandrova, V. D. Blank, A. E. Golobokov, Y. S. Konyaev, and E. I. Estrin, Fizika Tverdogo Tela **29**, 2573 (1987).

[18] S. S. Batsanov, N. R. Serebryanaya, V. D. Blank, and V. A. Ivdenko, Crystallography Rep **40** (1995).

[19] V. V. Aksenenkov, V. D. Blank, N. F. Borovikov, V. G. Danilov, and K. I. Kozorezov, Dokl. Akad Nauk **338**, 472 (1994).

[20] I. A. Barabanov, V. D. Blank, and Y. S. Konyaev, Instrum Exp Tech **30**, 445 (1987).

[21] C. Ji, V. I. Levitas, H. Zhu, J. Chaudhuri, A. Marathe, and Y. Ma, P Natl Acad Sci USA (2012) , doi/10.1073/pnas.1214976109.

[22] V. I. Levitas, Y. Z. Ma, E. Selvi, J. Z. Wu, and J. A. Patten, Phys Rev B **85**, 054114 (2012).

[23] V. I. Levitas and O. M. Zarechnyy, Phys Rev B **82**, 174123 (2010).

[24] V. I. Levitas and O. M. Zarechnyy, Phys Rev B **82**, 174124 (2010).

[25] J. Zhao, R. J. Angel, and N. L. Ross, J. Phys.-Condens. Mat. **23**, 175901 (2011).

[26] K. Shimizu, K. Suhara, M. Ikumo, M. I. Eremets, and K. Amaya, Nature **393**, 767 (1998).

[27] G. T. Zou, Y. Z. Ma, H. K. Mao, R. J. Hemley, and S. A. Gramsch, Rev. Sci. Instrum. **72**, 1298 (2001).

CHAPTER 2. STRAIN-INDUCED PHASE TRANSFORMATIONS UNDER COMPRESSION, UNLOADING, AND RELOADING IN A DIAMOND ANVIL CELL

Modified from a paper published in Journal of Applied Physics

Biao Feng[1], Oleg M. Zarechnyy[1], and Valery I. Levitas[2,*]
1) Department of Aerospace Engineering, Iowa State University, Ames, Iowa 50011, USA

2) Departments of Aerospace Engineering, Mechanical Engineering, and Material Science and Engineering, Iowa State University, Ames, Iowa 50011, USA

Abstract

Strain-induced phase transformations (PTs) in a sample under compression, unloading, and reloading in a diamond anvil cell (DAC) are investigated in detail, by applying finite element method. In contrast to previous studies, the kinetic equation includes the pressure range, in which both direct and reverse PTs occur simultaneously. Results are compared to the case when "no transformation" region in the pressure range exists instead, for various values of the kinetic parameters and ratios of the yield strengths of low and high pressure phases. Under unloading (which has never been studied before), surprising plastic flow and reverse PT are found, which were neglected in experiments and change interpretation of experimental results. They are caused both by heterogeneous stress redistribution and transformation-induced plasticity. After reloading, the reverse PT continues followed by intense direct PT. However, PT is less pronounced than after initial compression and geometry of transformed zone changes. In

---

[*] Corresponding author.
Email: vlevitas@iastate.edu

particular, a localized transformed band of a weaker high pressure phase does not reappear in comparison with the initial compression. A number of experimental phenomena are reproduced and interpreted.

2.1 Introduction

A diamond anvil cell is a powerful tool to generate high pressure and in situ study PTs to high pressure phases, using modern diagnostics, like x-ray, Raman, and optical techniques[1-5]. When hydrostatic media is used, PT is classified as pressure-induced one and it starts by nucleation at pre-existing defects (pressure and stress concentrators). In order to study the effect of plastic deformations on PTs, a rotational DAC was utilized[6-10], in which large plastic shear due to rotation of one of the anvils is superposed on high pressure. Such PTs are classified as strain-induced ones and they occur by nucleation at defects that continuously appear during the plastic deformation[11]. In fact, PTs under compression without hydrostatic media in traditional DAC are also strain-induced rather than pressure-induced, because they occur during intense plastic flow of materials[11,12]. As it was discussed in Refs. 11-13, the only difference between PTs under compression in DAC and compression and torsion in rotational DAC is the pressure-plastic strain history for each material point of the sample. It was found in Refs. 11, 14, and 15 that strain-induced PTs require completely different thermodynamic and kinetic treatment and experimental characterization than pressure-induced PTs. Thus, the main focus is on the strain-controlled kinetic equation (8) for the concentration of the high pressure phase, c, with respect to undeformed state, which is independent of time and depends on four main parameters: (1) kinetic parameter k which scales the rate of PTs, (2) the minimum pressure p_{ε}^{d} below which direct strain-induced PT cannot occur, (3) the maximum pressure p_ε^r above which reverse strain-induced PT does not take place, and (4) the ratio of yield strengths of low (σ_{y1}) and high pressure (σ_{y2}) phases. We are unaware of any publications that determine parameters of the kinetic equation and fields of stress and strain tensors experimentally. Pressure distribution[8, 16-20] and concentration of high pressure phase distributions[18, 19] along the radius of a sample are available only. As a consequence, theoretical and finite element methods have been developed and applied for investigation of variation of stress tensor, accumulated plastic strain, and concentration fields in a sample during plastic flow and PTs and for analysis and interpretation of experimental results[11-13, 21, 22]. Numerical results, published in Refs.12, 13, 21, and 22, describe a number of experimental observations, however they are incomplete because they are obtained for $p_\varepsilon^d > p_\varepsilon^r$ only. In this case, both direct and reverse PTs cannot occur for values of pressure p in the range $p_\varepsilon^r < p < p_\varepsilon^d$; above p_ε^d direct PT occurs only and below p_ε^r reverse PT takes place only, reaching complete transformation at very large plastic strain. However, the case $p_\varepsilon^d < p_\varepsilon^r$ is at least of the same importance, for which both direct and reverse PTs occur in the pressure range $p_\varepsilon^d < p < p_\varepsilon^r$. This leads to a stationary value of concentration $0<c<1$ at very large plastic strains, which was observed experimentally for various pressure-shear loading, e.g., under high pressure torsion[23-25] and ball milling[26-29]. Therefore, new PT features and phenomena may appear. One of the *goals* of the paper is to study in detail coupled plastic flow and PTs in a sample in DAC for the case with $p_\varepsilon^d < p_\varepsilon^r$ and various values of the kinetic parameter k and the ratio of the yield strengths, and to compare results with the case of $p_\varepsilon^d > p_\varepsilon^r$. Another *goal* is to study plastic flow and PTs after *unloading* and *reloading,* which was never done before.

In many cases, high pressure phase is metastable after pressure release and can exist and be studied at ambient conditions. However, if there is no reverse PT under hydrostatic loading-unloading, this does not mean that reverse PT will not occur during the reduction of the load to zero after strain-induced PT. In many cases (excluding in situ studies), concentration of phases is determined after unloading[23-29] but is related to the loading process with a salient assumption that it does not change during unloading because of the absence of plastic deformation. As we will show, in contrast, unloading is accompanied in many cases by plastic flow and reverse PT, which should be taken into account in experiments. Finally, reloading is studied to explore an additional pressure-plastic strain path and its relevance for experimental realization.

2.2 Problem formulation

Phase transformations coupled to plastic flow, in a sample of radius $\tilde{R}$ compressed by axial force P between two rigid diamonds under loading, unloading, and reloading are studied in this paper using the same physical and geometric models as in Refs. 12, 13,22. Geometry and boundary conditions are shown in Fig. 1.

To obtain generic results, we consider the simplest isotropic, perfectly plastic model, and the total system of equations are given as follows[12]:

Decomposition of deformation rate $\mathbf{d}$ into elastic (subscript *e*), transformational (*t*), and plastic (*p*) contributions:

$$\mathbf{d} = \overset{\nabla}{\boldsymbol{\varepsilon}}_e + \dot{\varepsilon}_t \mathbf{I} + \mathbf{d}_p \,. \qquad (1)$$

Elasticity rule (Hooke's law):

$$p = K\varepsilon_{e0}\,; \qquad \mathbf{s} = 2G\, dev \boldsymbol{\varepsilon}_e \,. \qquad (2)$$

Transformation volumetric strain:

$$\varepsilon_t = \bar{\varepsilon}_t c\,. \tag{3}$$

Von Mises yield condition:

$$\sigma_i = \left(\frac{3}{2}\mathbf{s}:\mathbf{s}\right)^{0.5} \le \sigma_y\left(c\right) = \left(1-c\right)\sigma_{y1} + c\sigma_{y2}\,. \tag{4}$$

Plastic flow rule in the plastic region:

$$\sigma_i = \sigma_y(c) \text{ and } \mathbf{s}\cdot\dot{\mathbf{s}} > 0 \qquad \rightarrow \qquad \mathbf{d}_p = \lambda\mathbf{s}\,; \quad \lambda = \frac{3}{2}\frac{\mathbf{s}:\mathbf{d}}{\sigma_y^2} - \frac{\dot{c}\left(\sigma_{y2}-\sigma_{y1}\right)}{\sigma_y G}\;; \tag{5}$$

in the elastic region:

$$\sigma_i < \sigma_y(c) \text{ or } \sigma_i = \sigma_y(c) \text{ and } \mathbf{s}\cdot\dot{\mathbf{s}} \le 0 \qquad \rightarrow \qquad \mathbf{d}_p = 0\,. \tag{6}$$

Momentum balance equation:

$$\nabla\cdot\mathbf{T} = 0. \tag{7}$$

Strain-controlled kinetics for phase transformations:

$$\frac{dc}{dq} = 10k\frac{(1-c)\bar{p}_d H\left(\bar{p}_d\right)\dfrac{\sigma_{y2}}{\sigma_{y1}} - c\bar{p}_r H\left(\bar{p}_r\right)}{c + \left(1-c\right)\sigma_{y2}/\sigma_{y1}}\;; \tag{8}$$

with $q = (2/3\mathbf{d}_p:\mathbf{d}_p)^{1/2}$, $\bar{p}_d = \dfrac{p-p_\varepsilon^d}{p_h^d - p_\varepsilon^d}$ and $\bar{p}_r = \dfrac{p-p_\varepsilon^r}{p_h^r - p_\varepsilon^r}$.

Here, $\mathbf{s}$ is the deviator of the true stress tensor $\mathbf{T}$, $\mathbf{s} = dev\mathbf{T}$; $\overset{\nabla}{\varepsilon}_e$ and $\overset{\nabla}{\mathbf{s}}$ is the Jaumann objective time derivative of the elastic strain and deviatoric stress; $\mathbf{I}$ is the second-rank unit tensor; K and G designate bulk and shear moduli, respectively; σ_i is the second invariant of the stress deviator; ε_{e0} and $\bar{\varepsilon}_t$ are the elastic and transformation volumetric strains for complete PT, respectively; H is the Heaviside step function; p_h^d and p_h^r are the pressures for direct and reverse PTs under hydrostatic loading, respectively, and q is the accumulated plastic strain (Odqvist parameter). Without PTs, the applicability of the perfectly plastic and isotropic model for monotonous loading is justified in Ref. 30 for various classes of materials (rocks, metals, pressed powders, etc.) starting with plastic strains $q>0.6\div1$ both for normal and high pressure. Additional confirmations for steel and NaCl were obtained with rotational DAC in Ref. 31. Note that the yield strength in the perfectly plastic state is independent of the deformation history[30]. Also, our goal is to perform simulation of *strain-induced* PTs rather than just plastic flow. Since there is no available experimental data on such transformations, there is no sense to combine more sophisticated models for plastic straining (e.g., model for a polycrystalline aggregate[32]) with the simplest model for PT.

Assumption of small elastic strains limits pressure to the value of 0.1 K, which is of the order of magnitude of 10 GPa. Under such a maximum pressure, change in geometry of the diamond anvils is negligible, which can be shown by solution of elastic problem for an anvil[33-35]. Thus, assumption that the anvils are rigid is justified.

It is not a problem to include deformation of anvils and strain hardening in the model, if it would be necessary. However, this paper is among very few first numerical studies of *strain-induced* PTs in DAC and as we wrote before, we want to obtain results that are generic for a wide class of materials. If we introduce some hardening parameters and/or specific geometry of an anvil and way of its fixation, we will lose the generic character of the results and gain the secondary effects only.

Finite element method and code ABAQUS[36] have been utilized for solution of axial symmetric problems. In the dimensionless form, all stress related parameters (excluding shear stress, see below) are divided by σ_{y1}; the dimensionless axial force F normalized by the product of total initial contact area of a sample and σ_{y1}. For precise comparison with the results for $p_\varepsilon^d > p_\varepsilon^r$ in Ref. 22, we assume dimensionless $p_\varepsilon^d = 6.375$ and $p_\varepsilon^r = 6.75$ (i.e., just switch values $p_\varepsilon^d = 6.75$ and $p_\varepsilon^r = 6.375$) and keep other material parameters, $p_h^d = 11.25$ and $p_h^r = 1.875$ exactly the same like in Ref. 22.

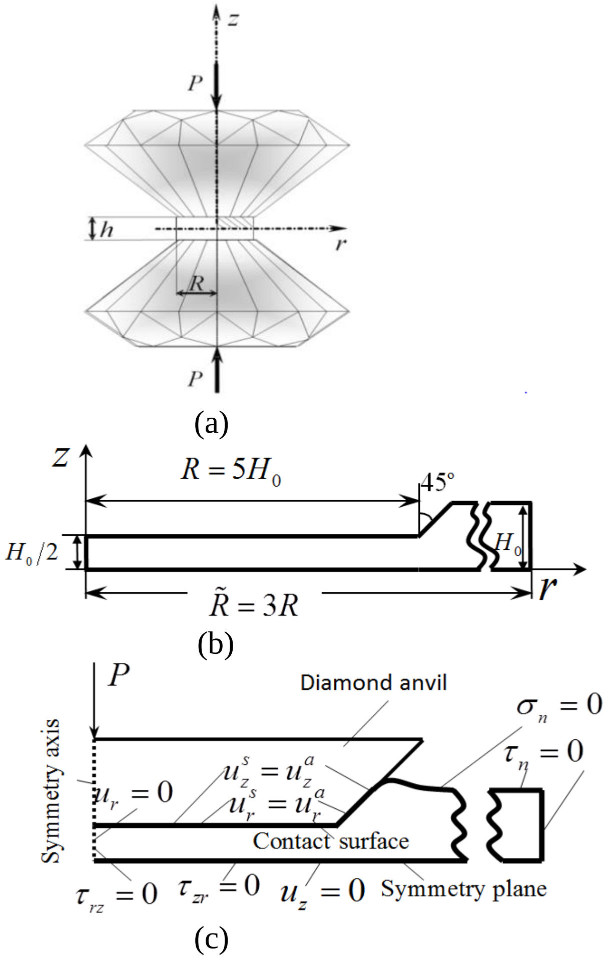

FIG. 1 (a) Diamond anvil cell scheme, (b) quarter of a sample in initial undeformed state, and (c) boundary conditions including no slipping on the contact surface between sample and diamond anvil.

2.3 Phase transformations under loading

In this section, our principal aim is to investigate effects of characteristic pressures for $p_\varepsilon^d < p_\varepsilon^r$ (in contrast to Ref. 22) on PTs, for various kinetic parameters k and ratios of yield strengths of high and low pressure phases. Previous simulations[12, 13, 21, 22] with $p_\varepsilon^d > p_\varepsilon^r$ did not allow the PTs to occur when pressure p lies between two characteristic pressures, $p_\varepsilon^r < p < p_\varepsilon^d$. In the current simulations, $p_\varepsilon^d < p_\varepsilon^r$ and therefore there is no such limitation, and both direct and reverse PTs can happen when $p_\varepsilon^d < p < p_\varepsilon^r$. Before high pressure phase appears, the largest pressure is located at the center of a sample, and pressure is gradually decreasing with increase of coordinates r or z. Once pressure reaches p_ε^d at the center of sample and since accumulated plastic strain increases in most region of $r \leq R$, high pressure phase firstly appears there, regardless of the value of k and the ratio of yield strengths. However, close to p_ε^d concentration of high pressure phase is still pretty low and is not shown in Fig. 2.

Concentration of a weaker ($\sigma_{y2} = 0.2\sigma_{y1}$) high pressure phase c is shown in Fig. 2 with $k = 5, 10, 30$ and under the rising dimensionless load F. One can note that: (1) with load F rising, PT shifts from the center to a localized plastic shear and PT bands and then propagates within these bands; (2) geometry of the transformed zone differs from the case with $p_\varepsilon^d > p_\varepsilon^r$ [12, 13, 21, 22], especially for k=5, when the multi-connected transformed region first appears due to strain localization and heterogeneous pressure distribution; and (3) in contrast Ref. 22, PTs for all k reach the contact surface at lower load, which is convenient for detecting PTs using surface-based (e.g., optical and Raman) methods in experiments; especially for k=30 PTs in Ref. 22 did not reach the surface at all. Because the threshold value p_ε^d for direct PT is accepted lower in this paper than that in Ref. 22, direct PT occurs at lower load in the region close to contact surface, where the pressure is usually lower than the one at the symmetry plane at the same coordinate r.

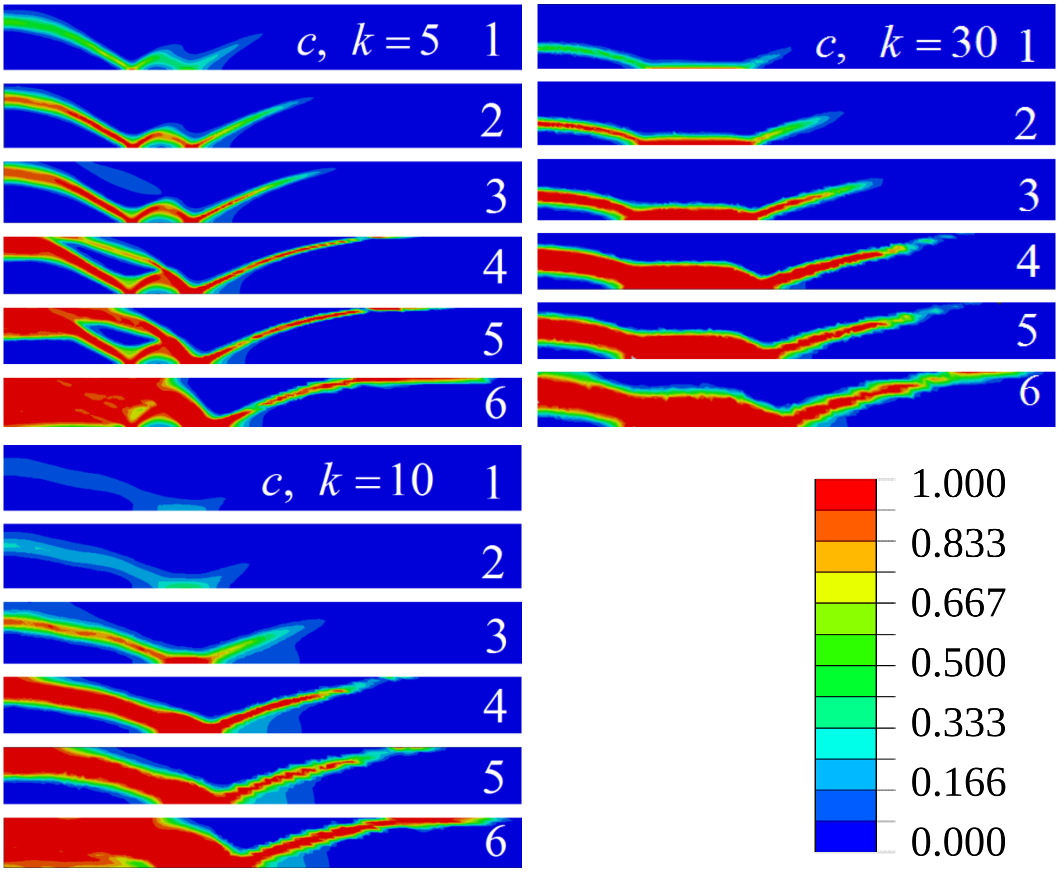

FIG 2 Concentration of high pressure phase c under loading for $k=5$, 10, and 30; $\sigma_{y2}=0.2\sigma_{y1}$ and $r/R\le 0.72$ in Fig.1 (b). The dimensionless axial force F is (1) 4.09, (2) 4.23, (3) 4.37, (4) 4.54, (5) 4.71, (6) 4.97.

Fig. 3 shows the distributions of pressure p and the volume fraction of a weaker high pressure phase c at the contact surface of the sample for k equal to 5 and 10. There are two separate regions where PT occurs, and two pressure plateaus appear there with pressures well above p_ε^d and p_ε^r. Between two PT regions, another plateau in pressure distribution exists with the magnitude between p_ε^d and p_ε^r. However, concentration c in this region is quite low and even equal to zero because of low accumulated plastic strain increment. Also, both direct and reverse PTs occur in this range and even the maximum (stationary) value of c is quite low for the weaker high pressure phase[14,37] . Pressure at the plateau close to the symmetry axis is almost constant under different loads at k=5; pressure at other two plateaus is almost independent of load at k=10. Consequently, the kinetic parameter k not only influences the rate of PT and configuration of PT regions (see Fig. 2) but also determines the positions of constant pressures. In contrast to the case with $p_\varepsilon^d > p_\varepsilon^r$ [22], where the pressure in the weakly or non-transformed region corresponded to p_ε^d, here it is between p_ε^d and p_ε^r. Thus, none of the plateaus correspond to p_ε^d and p_ε^r, and they are determined by mechanics of interaction of plastic flow and PT kinetics. In addition, Fig. 3 exhibits similar oscillatory features of experimental plots for ZnSe[17] and simulation results[22].

In the rest of this section, PTs to high pressure phase with $\sigma_{y2} \geq \sigma_{y1}$ are discussed. Small steps (plateaus) with almost constant pressure are found in experiments[8, 16, 17, 31] at the very heterogeneous pressure distribution plots. They correspond to the two-phase region, which, like in Ref. 22, is clearly reproduced for k=30 only rather than for k=1, 5, or 10. Therefore, for brevity, the concentrations of high pressure phase and pressures on the contact surface are discussed for $k = 30$ only.

Fig. 4 exhibits the same trends as in the experiments in Ref. 17: pressure monotonously grows from the periphery to center; there are two steps in pressure; the first one located in the center of the sample is much wider than the second one, which is located in the two-phase region. Comparing to the case for $\sigma_{y2} = 0.2\sigma_{y1}$ (Fig. 2), the PT localization and pressure oscillations are almost eliminated. Therefore one wider region instead of two isolated regions with high pressure phase appears on the contact surface of the sample.

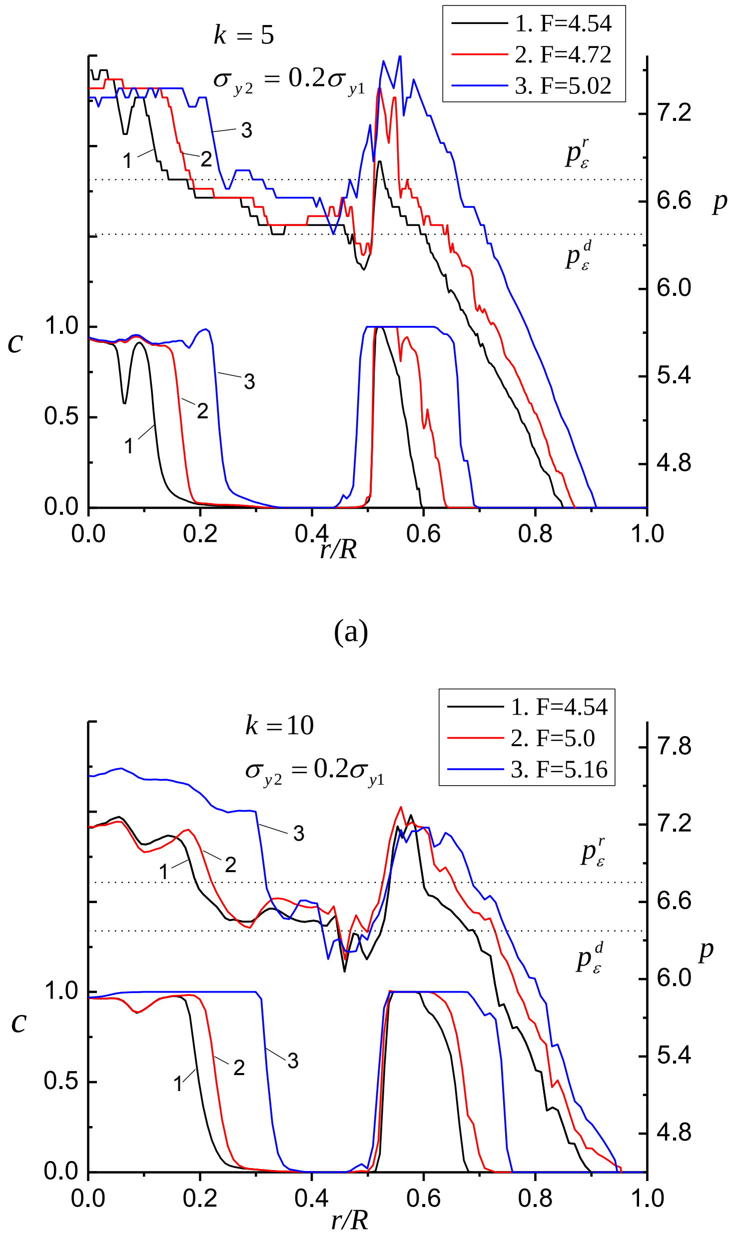

(a)

(b)

FIG. 3 Distributions of dimensionless pressure p and high pressure phase concentration c on contact surface under loading , for $k = 5$, 10 and $\sigma_{y2} = 0.2\sigma_{y1}$.

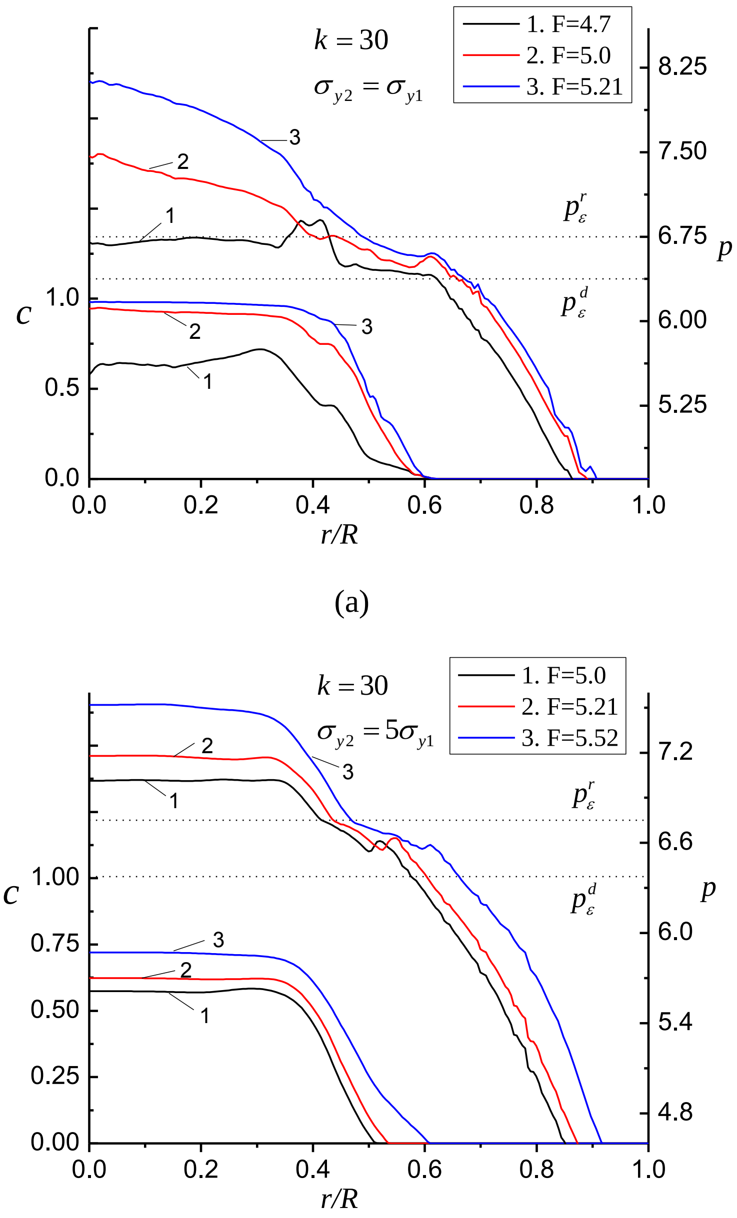

(a)

(b)

FIG. 4 Distributions of dimensionless pressure p and high pressure phase concentration c on contact surface under loading, for $k=30$ and $\sigma_{y2} \geq \sigma_{y1}$.

While in Ref. 22 pressure at the step in the two-phase region was independent of the load and just slightly above p_ε^d, here it varies between two characteristic pressures p_ε^d and p_ε^r, and increases with increasing load. Thus, it is more difficult to determine the value p_ε^d from experiment for $p_\varepsilon^d < p_\varepsilon^r$ than for $p_\varepsilon^d > p_\varepsilon^r$. Plateaus in the central region of the sample, while similar to those in experiments[16,31], are not related to p_ε^d and p_ε^r at all.

Fig. 5 shows the distribution of contact shear (friction) stress normalized by the yield strength in shear $\tau_{y1} = \sigma_{y1} / \sqrt{3}$ for $k = 30$ and $\sigma_{y2} \geq \sigma_{y1}$. We accept that the positive direction of shear stress points to the center and corresponds to the flow toward periphery. Due to compression, the material flows from the center to periphery. On the contrary, volumetric reduction due to PT at the center causes the material to flow from periphery to the center in the initial stage of PTs. With further compression, PT has almost completed in the center of the sample and mostly propagated into the two-phase region close to periphery, and then PT causes the material to flow toward this two-phase region instead of the sample's center. Both the direction and magnitude of shear stress on the contact surface result from the competition between these two flows. Because of the symmetry, shear stress is equal to zero at the axis of symmetry; at the periphery $0.7 < r/R < 1$, shear stress is equal to yield strength in shear τ_{y1}. Fig. 5(a) shows that: (1) at the initial stage of PTs at $F = 4.44$, shear stress close to the center is near to zero because both flows due to compression and volume reduction due to PT are small and compensate each other; (2) under further compression, because the flow due to PTs in the center surpasses the flow due to compression, the shear stress becomes negative but then changes sign, and increases until it reaches the yield shear strength; (3) At $F = 5.22$, the PT at the center is fully completed (therefore no further reduction in volume is possible) and flow to the periphery due to compression dominates, which causes shear stress to increase from zero to a maximum followed by a drop due to fast PT-induced reduction in volume in two-phase region. Similarly, one could interpret the plots in Fig. 5(b). Like pressure in Fig.4, the shear stress curve also becomes smoother due to the increase in strength of high pressure phase. Comparison with Ref. 22 demonstrates the similar trends in shear stress, but with some quantitative differences. In particular, the extrema in two-phase region are closer to periphery in our simulations because PTs propagates faster towards periphery due to lower p_ε^d.

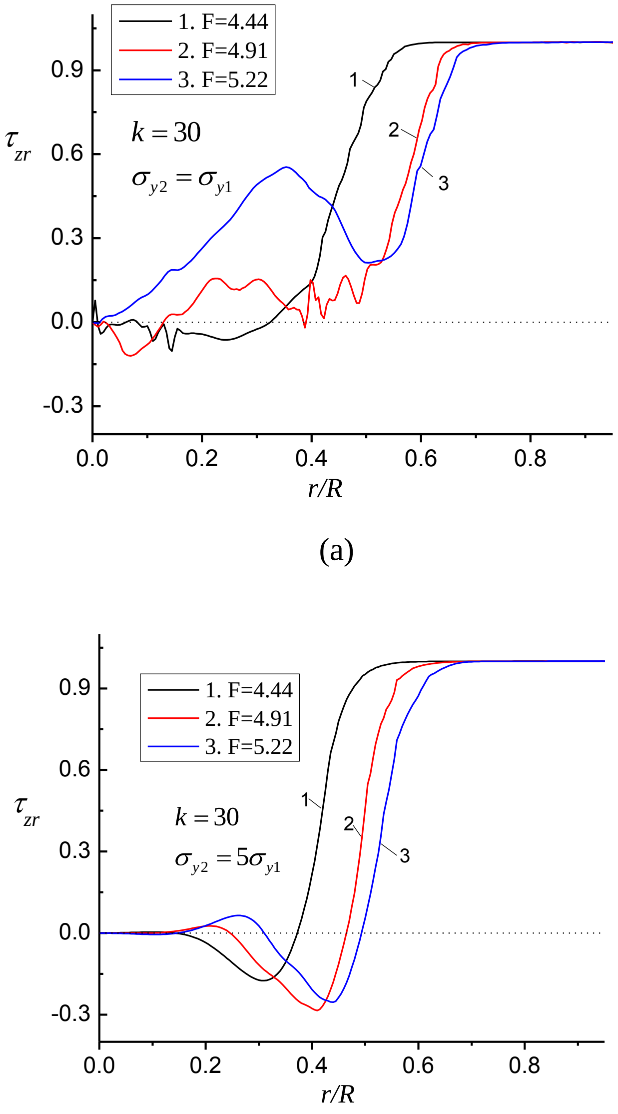

(a)

(b)

FIG. 5 Distributions of dimensionless pressure τ_{zr} normalized by yield strength in shear τ_{y1} on contact surface under loading, for $k=30$ and $\sigma_{y2} \ge \sigma_{y1}$.

2.4 Strain induced phase transformations during unloading

Change in concentration of high pressure phase during reduction of applied force down to zero was never studied numerically or in experiments. Characterization of PT processes under pressure based on the results of measurements after complete pressure release [23-29] is based on the strong assumption that there are no PTs during unloading. In this section, the unloading is studied and a surprising result is obtained: for a fast kinetics, k=30, and $\sigma_{y2} \leq \sigma_{y1}$, unloading is accompanied by plastic flow, which causes first a small increase in c above p_ε^d followed by much stronger reverse PT below p_ε^r. We will focus on k=30, because for k =10 and smaller, the change in concentration during unloading is small.

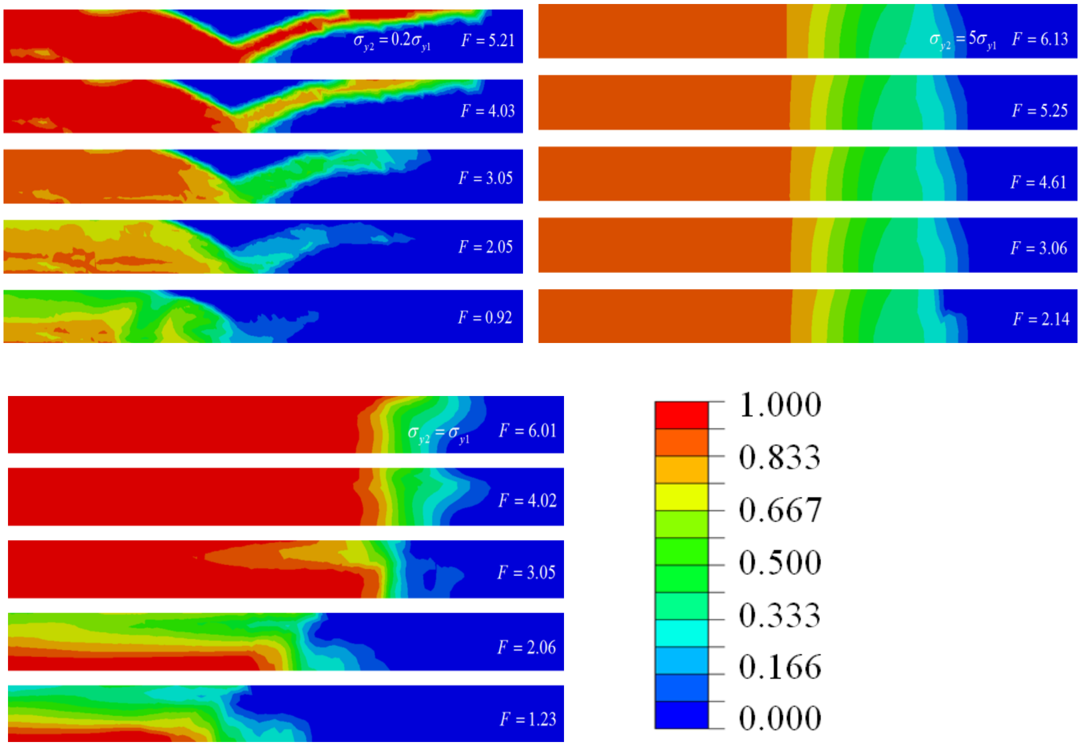

FIG. 6 Concentration of high pressure phase c under unloading for $k = 30$ and $r/R \leq 0.84$. Initial axial force F for unloading is 5.21 for $\sigma_{y2} = 0.2\sigma_{y1}$, 6.01 for $\sigma_{y2} = \sigma_{y1}$ and 6.13 for $\sigma_{y2} = 5\sigma_{y1}$, respectively.

Fig. 6 exhibits variation of concentration c during unloading for three ratios of the yield strengths. Fig. 7 shows distributions of pressure, concentration of the high pressure phase, and accumulated plastic strain along the symmetry plane. The symmetry plane is chosen for comparing with results of reloading, because PTs do not occur on the contact surface under reloading but occur at the symmetry plane (see section V). For $\sigma_{y2} = 5\sigma_{y1}$, PT is not visible under unloading, because the high pressure phase with large yield strength practically does not deform. For $\sigma_{y2} \leq \sigma_{y1}$, significant reduction in concentration, down to complete reverse PTs in some regions is clearly shown. In particular, for the case with $\sigma_{y2} = 0.2\sigma_{y1}$, the transformed band disappears completely. Unlike the evolution of the direct PT under loading, reverse PT on unloading progresses from contact surface to symmetry plane and from periphery to center, where pressure is below p_ε^r (see Fig. 7). After almost complete unloading, the high pressure phase mostly retains in the region close to the center and symmetry plane.

It is clear that the reverse PT occurs in the regions where pressure drops below p_ε^r and where plastic straining occurs. For the case $\sigma_{y2} = 0.2\sigma_{y1}$, plastic strain localizes in the weaker high pressure phase, which promotes the reverse PT as soon as p is getting below p_ε^r (Fig. 7a). Pressure significantly reduces in the peripheral low pressure phase region of the sample and much smaller reduction is in the central high pressure phase or two phase regions. Plastic strain increment reaches 0.1-0.13 and caused reduction in concentration Δc by up to 0.8. For $\sigma_{y2} = \sigma_{y1}$, the increment of accumulated plastic strain on the symmetry plane in the central region (r<0.2R) appears in the initial stage of unloading only when the pressure is above p_ε^r; at the later stage, there is no change in plastic strain, which results in almost negligible reverse PT (see Fig. 6 and Fig. 7b). In the region 0.3<r<0.7, plastic strain increment is in the range 0.1-0.25, which in combination with low pressure leads to very intense reverse PT, including complete reverse PT for r>0.47. We would like also to notice that at the very initial stage of unloading, in the region where $p > p_\varepsilon^d$, a small increase in concentration (i.e., direct PT) is observed. This is visible when distributions of c are compared (Fig. 6) in the central region at F=5.21 and F=4.03.

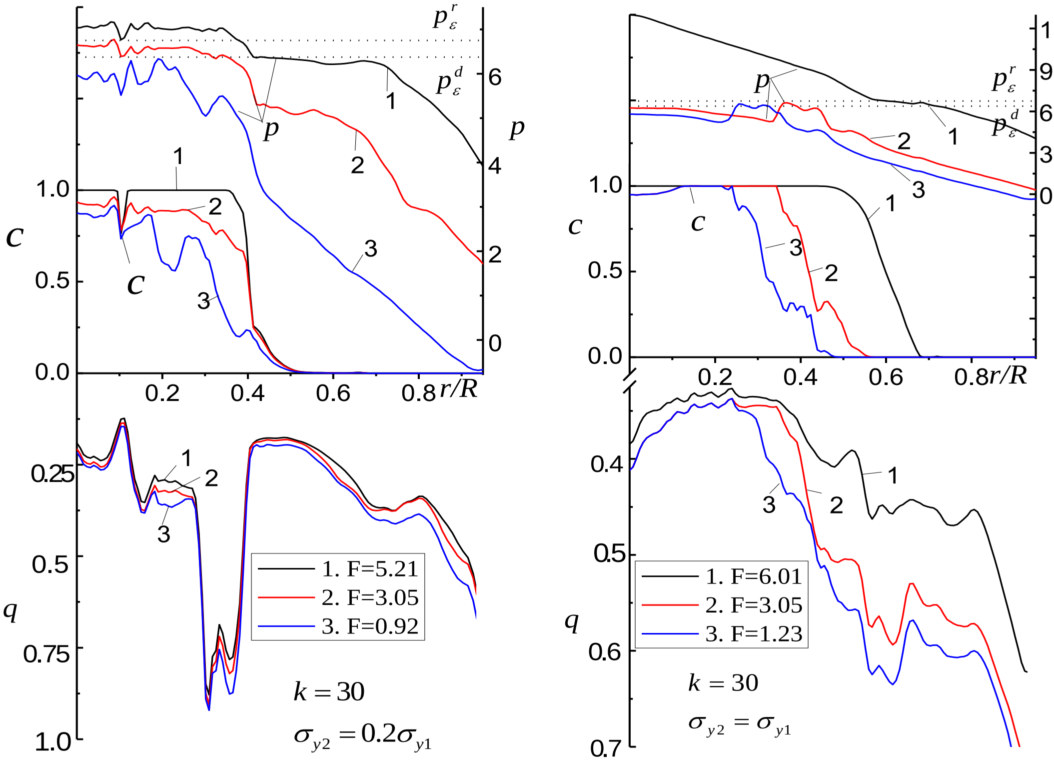

(a) (b)

FIG. 7 Distributions of accumulated plastic strain q, pressure p and high pressure phase concentration c on symmetry plane under unloading, for $k = 30$ and $\sigma_{y2} \leq \sigma_{y1}$.

Similar to the pressure distribution on the contact surface, pressure distribution curves on the symmetry plane show steps some of which are in the two-phase region. With the reduction of load, these steps move from the periphery towards the center along with moving two-phase region. Localization of PTs and strains determines the irregular distribution of shear stress in Fig. 8a. Before unloading, there are three drops in shear stress due to heterogeneous reduction in volume during PT and plastic flow. Under unloading, Fig. 8a shows that the rise in shear stress due to increase in volume during the reverse PT surpasses the reduction of shear stress due to unloading. Shear stress reaches the yield strength in shear in the major part of the contact surface. For the case $\sigma_{y2} = \sigma_{y1}$ in Fig. 8b, the initial stage of unloading, reverse PT mostly occurs in the two-phase region rather than at center (see Fig. 6). This causes shear stress increase in the two-phase region and decrease at the center due to reduction of loading. At further unloading, the reverse PT shifts to the center, which results the increase of shear stress in the center.

To summarize, for fast kinetics (*k*=30) and $\sigma_{y2} \leq \sigma_{y1}$, unloading causes plastic flow, which first induces a small increase in c above p_{ε}^{d} followed by quite intense reverse PT below p_{ε}^{r}.

There are two reasons for plastic flow under unloading. First, because of heterogeneous stress, strain, concentration, and, consequently, strength fields before unloading, reduction in the load leads to stress redistribution, during which stress intensity exceeds the yield strength in some regions. Then in the regions with $p < p_{\varepsilon}^{r}$ (or $p > p_{\varepsilon}^{d}$) the reverse (or direct) PT starts. Volume change due to PTs under nonhydrostatic conditions causes additional plastic straining called transformation-induced plasticity (TRIP)[11, 18, 19]. TRIP in turn leads to PTs thus serving as mechanochemical feedback.

Obtained results require reconsideration of the reported values of concentration in experiments[24-29], which are based on the measurements of concentration after unloading.

To avoid this problem for DAC, one can try to find loading, which will minimize reverse PT during unloading. Intuitively, utilization of a gasket with specially designed parameters that lead to quasi-homogenous pressure distribution during loading[19] should lead to minimization of plastic deformation and reverse PT during unloading. This case will be studied in the future.

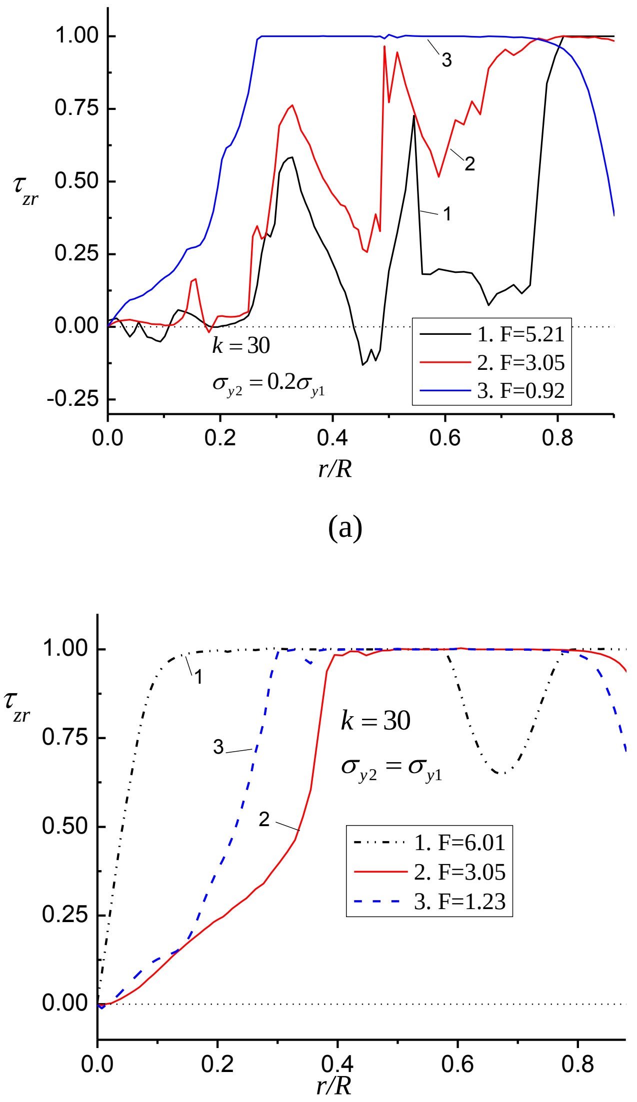

(a)

(b)

FIG. 8 Distribution of dimensionless shear stress τ_{zr} on contact surface under unloading, for $k = 30$ and $\sigma_{y2} \le \sigma_{y1}$.

2.5 Phase transformations under reloading

The aim of this section is to explore a new pressure-plastic strain path for strain-induced PTs by reloading sample after unloading to the same force. From Fig. 9, one can observe that with increase of load, first reverse PT propagates slowly, and direct PT does not occur until pressure is above p_ε^d. Further, in the pressure range $p_\varepsilon^r < p < p_\varepsilon^d$, direct PT starts to propagate along with reverse PT. When pressure reaches p_ε^r value, reverse PT cannot occur, and direct PT propagates through the sample with increased rate (Fig. 10, a, *F*=5.21; and b, *F*=6.01).

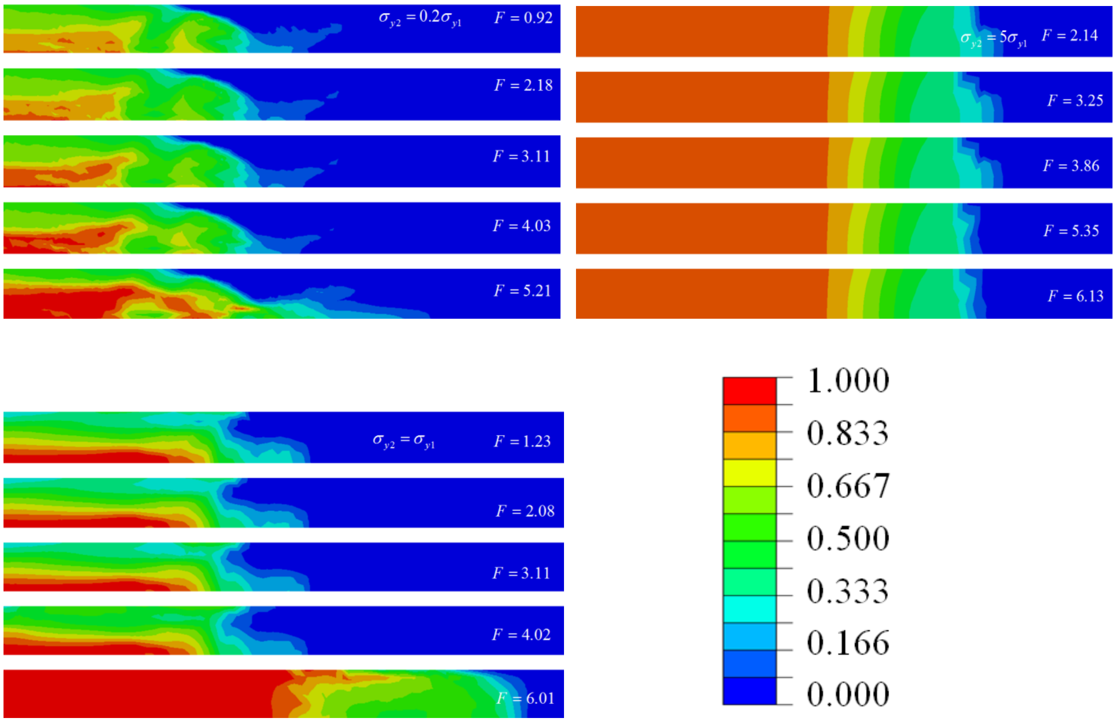

FIG. 9 Concentration of high pressure phase c under reloading for $k = 30$ and $r/R = 0.84$. Initial axial force for reloading F are respectively 0.92 for $\sigma_{y2} = 0.2\sigma_{y1}$, 1.23 for $\sigma_{y2} = \sigma_{y1}$ and 2.14 for $\sigma_{y2} = 5\sigma_{y1}$.

For a strong high pressure phase ($\sigma_{y2} = 5\sigma_{y1}$), PTs practically do not occur (similar to unloading), because the reloading occurs in the elastic regime due to high yield strength of the high pressure phase. For other cases, comparing the PTs before unloading in Fig. 6, direct PT is obviously less pronounced after unloading and reloading than during the first loading. In addition, reloading essentially changes the PT path and the PT region is more close to the center and plane of symmetry of a sample. For the case with $\sigma_{y2}=0.2\sigma_{y1}$, after unloading and reloading, the thin PT band in Fig. 6 does not reappear and PT is not complete in the central region of a sample. For the case with $\sigma_{y2}=\sigma_{y1}$, while radius of the transformed zone is slightly increased, region with complete PT is slightly reduced.

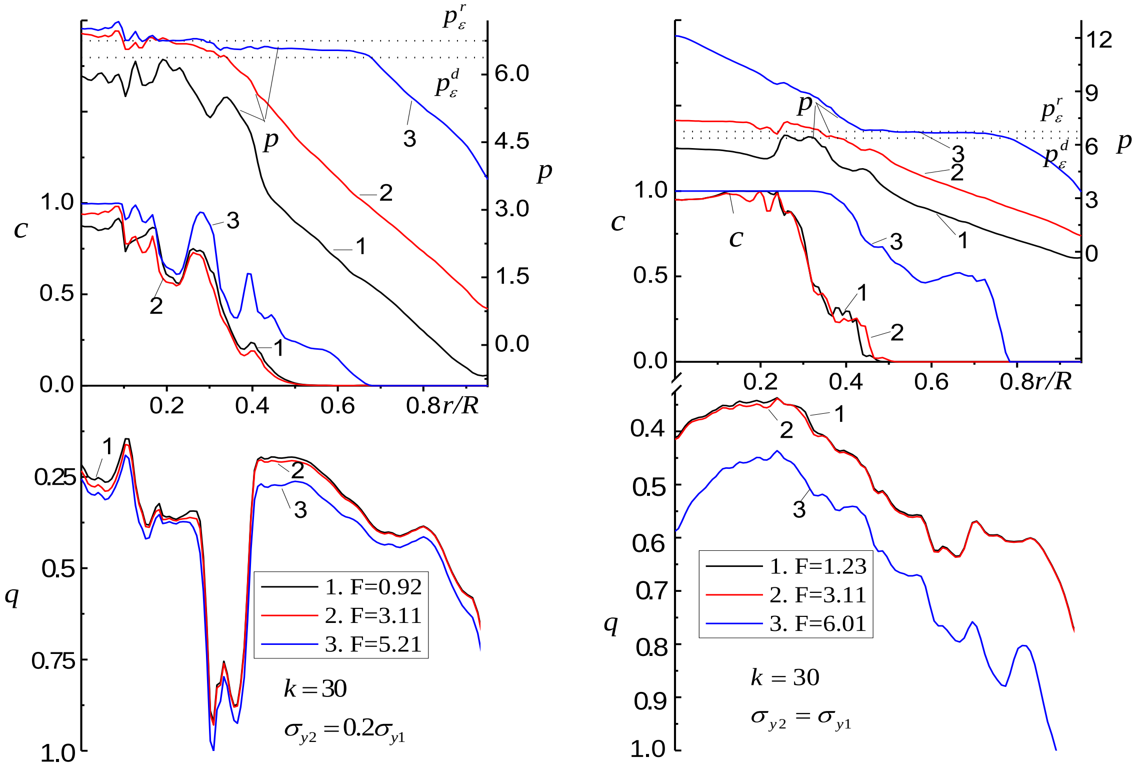

(a) (b)

FIG. 10 Distributions of accumulated plastic strain q, pressure p and high pressure phase concentration c on symmetry plane under reloading, for $k=30$ and $\sigma_{y2}\le\sigma_{y1}$.

Fig. 10 presents the distribution of accumulated plastic strain q, pressure p, and concentration of the high pressure phase c on the symmetry plane. At the initial stage of reloading, the strain is mostly elastic and an essential increase of plastic strain is only found at the higher force. Combination of low pressure and small increment in plastic strain, leads to practically unchanged concentration of the high pressure phase when dimensionless load F increases to 3.11. Further force growth results in pronounced growth in concentration of the high pressure phase, especially in two-phase region. Larger two phase region leads to a wider plateau region, where pressure is between p_{ε}^{r} and p_{ε}^{d}. One can note that at initial reloading, due to low pressure, reverse PT instead of direct PT occurs in some regions. However, once the pressure in most regions is above p_{ε}^{d}, direct PT takes over and quickly propagates due to a relatively large accumulation of plastic strain. We also notice that the concentration of the high pressure phase in Fig.10 b slightly increases at $r \approx 0.43$ when load F increases to 3.11, despite the fact that the pressure is below p_{ε}^{d}. This occurs due to the flow of the high pressure phase toward the periphery rather than due to direct PT. Such a convective increase in concentration was not observed under first loading here and in previous papers[13, 21, 22].

Fig. 11 shows the distribution of shear stress at contact surface under reloading. For the case with $\sigma_{y2} = 0.2\sigma_{y1}$, direct PT in the center of sample (Fig. 10a) results in the reduction of volume and flow of materials towards the center, which reduces the flow towards periphery due to recompression. Therefore, under reloading, shear stress in Fig. 11 (a) gradually declines. However, for the case with $\sigma_{y2} = \sigma_{y1}$, the rate of direct PT in the two-phase region significantly surpasses that at the center (Fig. 10b), which caused flow of the material towards the two-phase region rather than the center of sample. Therefore, shear stress increases closer to the center due to recompression, and shear stress reduces in the two-phase region due to PTs. Comparing to the shear stress before unloading in Fig. 8, shear stress in a wide region significantly reduces after reloading.

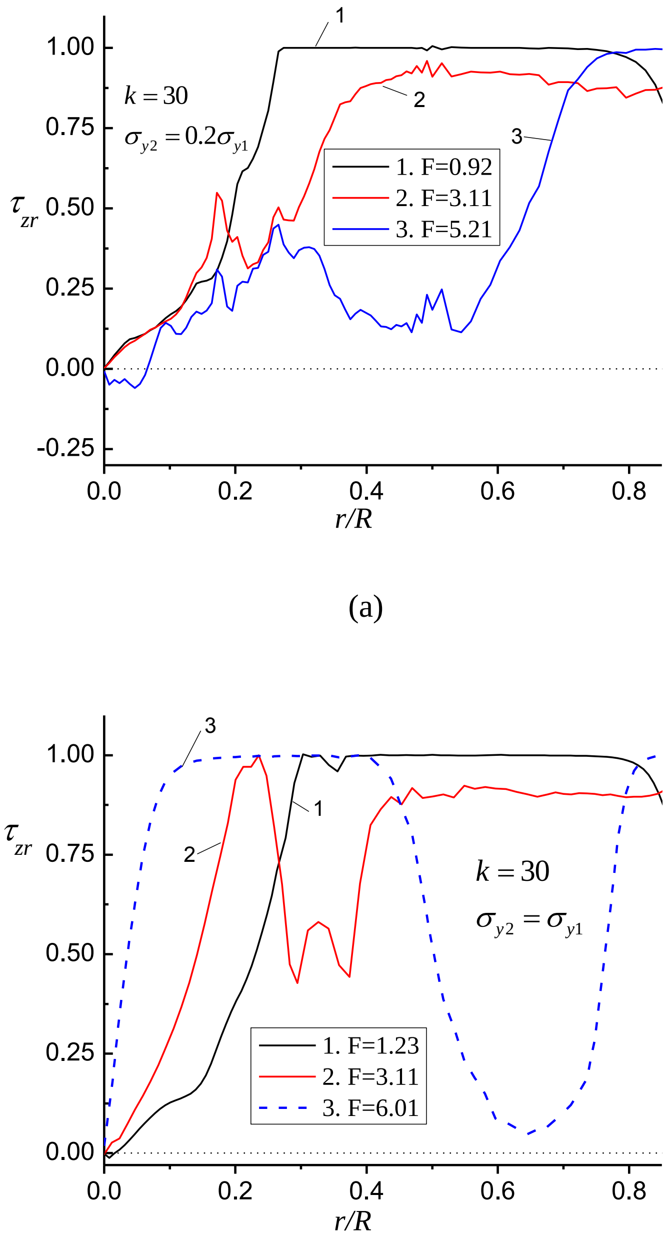

(a)

(b)

FIG.11 Distribution of dimensionless shear stress τ_{zr} on contact surface under reloading, for $k = 30$ and $\sigma_{y2} \le \sigma_{y1}$

2.6 Concluding remarks

In this paper, strain-induced PTs in a sample in the DAC under loading, unloading, and reloading to the same force are investigated. A finite element approach and software ABAQUS are utilized for solving a coupled system of equations for large plastic deformations and strain-induced PTs. In contrast to Ref. 22, where case $p_\varepsilon^d > p_\varepsilon^r$ was treated, here characteristic pressures satisfied the opposite inequality $p_\varepsilon^d < p_\varepsilon^r$ and values of p_ε^d and p_ε^r were exchanged. PTs were studied for different kinetic parameters k and ratios of the yield strengths of high and low pressure phases. In general, under loading slightly more pronounced PT occurs for $p_\varepsilon^d < p_\varepsilon^r$ because of slightly lower p_ε^d. Geometry of the transformed zone is quite different for the case with $\sigma_{y2} = 0.2\sigma_{y1}$ that in Ref. 22. PT reaches the contact surface under smaller load, which is convenient for probing PTs by surface-based methods (e.g., Raman and optical methods) in experiments. However, extraction of the constants p_ε^d and p_ε^r from experimental pressure distribution is more problematic than for the case with $p_\varepsilon^d > p_\varepsilon^r$. Note that at the very initial stage of unloading, in the region where $p > p_\varepsilon^d$, a small increase in concentration (i.e., direct PT) is observed. Obtained pressure fields reproduce qualitative features observed in some experiments.

Under unloading, surprising plastic flow and extensive reverse PT are found for $\sigma_{y2} \le \sigma_{y1}$, which were neglected in experiments. They are caused both by heterogeneous stress redistribution and TRIP. This PT requires reconsideration of quantitative values of phase concentrations in experiments on the unloaded sample, like in high pressure torsion[24,25] and ball milling[26-29]. The reverse PT may potentially be reduced or even avoided if a gasket with specially designed parameters will be used[19], which creates quasi-homogenous pressure distribution under loading. This assumption will be checked in future studies. After reloading, the reverse PT continues followed by intense direct PT. However, PT is less pronounced than after initial compression to the same force and geometry of transformed zone changes. In particular, the localized transformed band of a weaker high pressure phase does not reappear in comparison with the initial compression. Also, an increase in concentration at a pressure below p_{ε}^{d} is observed, which occurs due to convective flow of the high pressure phase toward the periphery rather than due to direct PT. In the future, similar work will be performed for a sample under compression and torsion in rotational DAC. Since in majority of experiments devoted to study of strain-induced PTs in traditional DAC or rotational DAC [6-8,16,17,31] and high pressure torsion experiments[23-25], there is no special gasket (i.e., the same material is used as the sample and gasket), we studied such a case here. However, to receive quasi-homogeneous pressure distribution, we recently introduced a gasket with specially determined parameters for strain-induced PTs as well[18, 19, 38]. We will study such a case numerically in the future.

Acknowledgments

The support of Army Research Office (Grant No. W911NF-12-1-0340) managed by Dr. David Stepp, Defense Advanced Research Projects Agency (Grant W31P4Q-13-1-0010) managed by Dr. Judah Goldwasser, and Iowa State University is gratefully acknowledged.

References

[1] C. Nisr, G. Ribarik, T. Ungar, G. B. M. Vaughan, P. Cordier, and S. Merkel, J. Geophys. Res.-Sol. Earth **117**, B03201 (2012).

[2] A. R. Oganov, J. H. Chen, C. Gatti, Y. Z. Ma, Y. M. Ma, C. W. Glass, Z. X. Liu, T. Yu, O.O. Kurakevych, and V. L. Solozhenko, Nature **457**, 863 (2009).

[3] T. S. Duffy, G. Y. Shen, D. L. Heinz, J. F. Shu, Y. Z. Ma, H. K. Mao, R. J. Hemley, and A. K. Singh, Phys. Rev. B **60**, 15063 (1999).

[4] A. Lazicki, P. Loubeyre, F. Occelli, R. J. Hemley, and M. Mezouar, Phys. Rev. B **85**, 054103 (2012).

[5] C. S. Zha, Z. X. Liu, and R. J. Hemley, Phys. Rev. Lett. **108**, 146402 (2012).

[6] V. V. Aksenenkov, V. D. Blank, N. F. Borovikov, V. G. Danilov, and K. I. Kozorezov, Dokl. Akad. Nauk **338**, 472 (1994).

[7] I. A. Barabanov, V. D. Blank, and Y. S. Konyaev, Instrum Exp Tech **30**, 445 (1987).

[8] V. Blank, et al., Phys. Lett. A **188**, 281 (1994).

[9] C. Ji, V. I. Levitas, H. Zhu, J. Chaudhuri, A. Marathe, and Y. Ma, Proc. Natl. Acad. Sci. USA (2012), doi/10.1073/pnas.1214976109.

[10] V. I. Levitas, Y. Z. Ma, E. Selvi, J. Z. Wu, and J. A. Patten, Phys. Rev. B **85**, 054114 (2012).

[11] V. I. Levitas, Phys. Rev. B **70**, 184118 (2004).

[12] V. I. Levitas and O. M. Zarechnyy, Phys. Rev. B **82**, 174123 (2010).

[13] V. I. Levitas and O. M. Zarechnyy, Phys. Rev. B **82**, 174124 (2010).

[14] V. I. Levitas, Europhys. Lett. **66**, 687 (2004).

[15] V. I. Levitas, Phys Lett A **327**, 180 (2004).

[16] V. D. Blank, Y. Y. Boguslavsky, M. I. Eremets, E. S. Itskevich, Y. S. Konyaev, A. M. Shirokov, and E. I. Estrin, Zh. Eksp. Teor. Fiz. **87**, 922 (1984).

[17] V. D. Blank and S. G. Buga, Instrum. Exp. Tech. **36**, 149 (1993).

[18] V. I. Levitas, Y. Z. Ma, and J. Hashemi, Appl. Phys. Lett. **86**, 071912 (2005).

[19] V. I. Levitas, Y. Z. Ma, J. Hashemi, M. Holtz, and N. Guven, J. Chem. Phys. **125**, 044507 (2006).

[20] H. K. Mao and P. M. Bell, Science **200**, 1145 (1978).

[21] V. I. Levitas and O. M. Zarechnyy, Europhys. Lett. **88**, 16004 (2009).

[22] O. M. Zarechnyy, V. I. Levitas, and Y. Z. Ma, J. Appl. Phys. **111**, 023518 (2012).

[23] M. T. Perez-Prado and A. P. Zhilyaev, Phys. Rev. Lett. **102**, 175504 (2009).

[24] K. Edalati, S. Toh, Y. Ikoma, and Z. Horita, Scripta Materialia **65**, 974 (2011).

[25] A. P. Zhilyaev, I. Sabirov, G. Gonzalez-Doncel, J. Molina-Aldareguia, B. Srinivasarao, and M. T. Perez-Prado, Mat. Sci. Eng. A **528**, 3496 (2011).

[26] F. Delogu, Scripta Mater. **67**, 340 (2012).

[27] F. Delogu, J. Mater. Sci. **47**, 4757 (2012).

[28] C. Suryanarayana, Rev. Adv. Mater .Sci. **18**, 203 (2008).

[29] L. Takacs, Prog. Mater. Sci. **47**, 355 (2002).

[30] V. I. Levitas, *Large Deformation of Materials with Complex Rheological Properties at Normal and High Pressure* (Nova Science, New York, 1996).

[31] N. V. Novikov, S. B. Polotnyak, L. K. Shvedov, and V. I. Levitas, J. of Superhard Mater. **3**, 39 (1999).

[32] W. Kanitpanyacharoen, S. Merkel, L. Miyagi, P. Kaercher, C. N. Tome, Y. Wang, and H. R. Wenk, Acta Mater. **60**, 430 (2012).

[33] N. V. Novikov, V. I. Levitas, S. B. Polotnyak, and M. M. Potemkin, Strength Mater. **26**, 309 (1994).

[34] N. V. Novikov, V. I. Levitas, S. B. Polotnyak, and M. M. Potyomkin, High Pressure Res. **8**, 507 (1991).

[35] N. V. Novikov, V. I. Levitas, and S. B. Polotnyak, J. of Superhard Mater. **9**, 1 (1987).

[36] Abaqus V6.11. Abaqus User Subroutines Reference Manual: HETVAL and USDFLD. Providence RI, USA: Abaqus INC (2011).

[37] V. I. Levitas and O. M. Zarechnyy, J. Phys. Chem. B **110**, 16035 (2006).

[38] Levitas, V. I., Hashemi, J., and Ma, Y. Europhysics Letters, **68**, 550 (2004).

CHAPTER 3. STRAIN-INDUCED PHASE TRANSFORMATIONS UNDER HIGH PRESSURE AND LARGE SHEAR IN A ROTATIONAL DIAMOND ANVIL CELL: SIMULATION OF LOADING, UNLOADING, AND RELOADING

Modified from a paper published in Computational Materials Science

Biao Feng[a], Valery I. Levitas[b,*], Oleg M. Zarechnyy[a]

[a] *Department of Aerospace Engineering, Iowa State University, Ames, Iowa 50011, USA*

[b] *Departments of Aerospace Engineering, Mechanical Engineering, and Material Science and Engineering, Iowa State University, Ames, Iowa 50011, USA*

Abstract

Coupled plastic flow and strain-induced phase transformations (PTs) under high pressure and large plastic shear in a micron scale sample under loading, unloading, and reloading in a rotational diamond anvil cell (RDAC) are studied in detail, utilizing finite element approach. A plastic strain-controlled, pressure-dependent kinetic equation, which describes strain-induced PTs, is used. The effects of four main material parameters in this equation on PTs and plastic flow in RDAC in three-dimensional formulation are systematically analyzed. Multiple experimental phenomena are reproduced and interpreted, including pressure self-multiplication/demultiplication effects, small 'steps' on pressure distribution in the two-phase region, simultaneous occurrences of direct and reverse PTs, oscillatory distribution of pressure for weaker high-pressure phase, and a thin layer of high-pressure phase on a contact surface. During unloading, unexpected

---

[*] Corresponding author. E-mail address: vlevitas@iastate.edu

intensive plastic flow and reverse PT are revealed, which change the interpretation of experimental results. The effect of unloading and reloading paths on PTs is examined. Two types of pressure variations are revealed, which are qualitatively consistent within experimental observations for ZnSe and KCl. Obtained results lead to ways of controlling PTs by varying compression-torsion paths and can be utilized for the search of new high pressure phases, ways to reduce pressure for the synthesis of high pressure phases, and to retain them at ambient pressure.

3.1 Introduction

Study of PTs under high pressure and large plastic shear is of interest for various fundamental and applied problems. They include: (a) search for new high pressure phases, especially superhard phases, in particular, those that can be kept at normal pressure and utilized in engineering applications; (b) processes in shear bands in geophysics (in particular, during initiation of earthquakes), during penetration of projectiles in materials, and shear ignition of energetic materials; (c) technological applications (cutting and polishing of Si, Ge, silicon and boron carbides, PTs during ball milling and high pressure torsion), see in [1] and references herein. In RDAC, large plastic shear deformation can be superposed on high pressures by rotating of one of the anvils with respect to another (Fig. 1(a)). Experiments in RDAC have resulted in a revealing of numerous exciting phenomena: 1) a remarkable reduction, by a factor of 2-5 [1-5] and even almost 10 [6] in PT pressure; 2) fast strain-controlled kinetics in which time is not significant and strain plays the role of a time-like parameter [1, 7]; 3) an appearance of new phases, especially, superhard phases, which would not appear without shear straining [4, 8-10]; 4) a reduction (up to zero) in pressure hysteresis [3]; and 5) the replacement of a reversible PT by an irreversible one [11, 12]. These findings are rationalized within three-scale theory (nano-, micro, and macroscales) [1], its further developments at the micro [7] and macroscales [13, 14], and within numerical simulations at the macroscales [13, 14].

It was suggested in [1] that the main process for strain-induced transformation is nucleation at the defects generated during plastic flow. While there are some analytical and numerical solutions for interaction of PTs and plasticity at the nanoscale [1, 15], they cannot be utilized in the current study. Indeed, the size of the sample is of the order of magnitude of 1 *millimeter* and there is no way to use nanoscale models and specific defects for such a large scale. That is why we developed in [1] a coarse grained microscale model (see Eq.(8)), which operates with parameters that can be in principle measured in RDAC experiment (phase concentration, pressure, stress tensor, and plastic strain). Information about the effect of defects, mechanisms, nanostructure, and nanoscale thermodynamics are encoded in the structure and parameters of this equation. That is why by solving coupled problems and varying material parameters, we can analyze, predict, and interpret experimental results for various classes of materials and transformations, see examples in [13, 14]. The current paper applies the same equations but for different experimental processes and material parameters. This is important because different combinations of material parameters encode different nanoscale mechanisms, defects, and nanostructures that lead to different experimental phenomena.

Thus, the strain-induced PTs can be characterized in terms of a pressure-dependent, strain-controlled kinetic Eq. (8), which includes four main parameters: 1) a kinetic parameter k which scales the PT rate, 2) the minimum pressure p_{ε}^{d} below which direct strain-induced PT does not take place, 3) the maximum pressure p_{ε}^{r} above which reverse strain-induced PT cannot occur, and 4) the ratio of yield strengths of high (σ_{y2}) and low (σ_{y1}) pressure phases. All of these material parameters should be determined experimentally, but it has not been done yet because of the complexity and heterogeneity on stress and strain fields and the distribution of the phases. Pressure distribution of high-pressure phase at the contact surface of sample and concentration distribution averaged over the sample thickness are experimentally available only [11]. As a consequence, theoretical and finite element approaches have become the significant and necessary means to investigate the stress and strain fields and distribution of concentration of the high pressure phase in the whole sample, and to analyze and interpret experimental phenomena. Since PT progress depends on pressure, plastic strain and stress tensors, one has to determine these fields in a sample. This is similar to the study of the fields of pressure and temperature for pressure-temperature induced PTs, particularly in the shock wave. All fields in a sample are very heterogeneous and one needs to understand how to extract information from the experiment, i.e., to know these fields in the sample. There is currently only one numerical study of the strain-induced PTs in RDAC [14]. Therefore, the first *objective* of this paper is to investigate the effects of the above four parameters in the kinetic equation (8) on PTs and plastic flow in RDAC, in particular, parameter *k* and the ratios of the yield strengths of phases. Recently we found [16] that the kinetic parameter *k* significantly affects the appearance of small 'steps' in pressure distribution under compression in ordinary DAC, which were found in experiments [3, 4, 8, 10], and also essentially changes the geometry of PT zones and rate of PTs. In addition, numerical results in [14] obtained for the case $p_{\varepsilon}^{d} > p_{\varepsilon}^{r}$ only, which means that no strain-induced

PTs can exist in the pressure range of $p_\varepsilon^r < p < p_\varepsilon^d$. Here, we will study the opposite case $p_\varepsilon^r > p_\varepsilon^d$, for which both direct and reverse PTs take place in the range $p_\varepsilon^r > p > p_\varepsilon^d$. For this case, a stationary value of concentration $0 < c < 1$ exists at very large plastic shears. The fact that such an incomplete PT was observed experimentally for various pressure-shear loadings, e.g., during ball milling [17-20] and high pressure torsion [21-24], confirms that this combination of parameters is realistic and should be studied. In particular, we will show that the utilization of condition $p_\varepsilon^d < p_\varepsilon^r$ leads to the reproduction of pressure self-demultiplication effect for CuI [25], which was not found in previous simulations. Also, previous studies failed to reproduce occurrence of a weaker high-pressure phase at the contact surface at the center of sample, but we obtained this in the current paper by the utilization of $p_\varepsilon^d < p_\varepsilon^r$. What is more, for a stronger high pressure phase, “steps” in pressure distributions could not be related directly to p_ε^r or p_ε^d for $p_\varepsilon^d < p_\varepsilon^r$, in contrast to results in [14].

In many cases, after complete unloading, high-pressure phase is metastable and can exist at ambient conditions. However, since distribution of all parameters in a sample treated in RDAC is very heterogeneous, reduction in axial force may lead to essential plastic deformations and strain-induced reverse PT, which has never been studied before for RDAC. In the most experimental studies (with exception for *in situ* experiments), concentration of high pressure phases is measured after complete unloading after ball milling [17-20] and high pressure torsion [21-24] but is related to the loading process. This includes a strong presumption that there is no plastic deformation and no change in the phase concentration during the unloading. On the contrary, as we will show, unloading is accompanied in many cases by intense plastic flow and clear reverse PT. Since one of the goals of study of materials in RDAC is to preserve metastable high pressure phase, these processes should be taken into account, or better yet, avoided in the designing and interpretation of the experiments. In addition, PTs are also influenced by unloading paths. Two different paths will be discussed in this paper.

Finally, reloading (which also was not studied previously for RDAC) is investigated to explore new pressure-plastic strain trajectories and PT progress for them. There were two interesting experimental phenomena: after slight release on the compressive force followed by torsion, pressure for weaker [8] (stronger [3]) high-pressure phase increases (decreases) at the center of sample on contact surface, and reduces (grows) in the periphery. Such a reloading path will be modeled in this paper.

3.2 Problem formulation

To obtain generic results and to be able to compare with our previous results for RDAC [14] and for traditional DAC [13], we consider the same simplest isotropic, perfectly plastic model from [14]. The applicability of the perfectly plastic and isotropic model with the yield strength, which is independent of the deformation history, for monotonous loading is justified in [26] for various classes of materials (metals, rocks, powders, etc.) starting with accumulated plastic strains $q>0.6\div 1$. This was done both for normal and high pressure and the case without PTs. Further confirmations for NaCl and stainless steel were found in experiments with RDAC in [4]. Since our objective is to simulate *strain-induced* PTs rather than just plastic flow and there is no available experimental data on such transformations, there is no reason to utilize more sophisticated models for plastic straining with the simplest model for PT. We assume also small elastic strains, which limits pressure to the value of 0.1 K (i.e., in the range of 10-20 GPa). One could avoid these assumptions, if it would be necessary. However, this paper is among very few first numerical studies of *strain-induced* PTs in RDAC and we would like to obtain results that are generic for a wide class of materials. With any sophistication, the generic character of the obtained results will be lost while we would gain the secondary effects only. Complete system of equations is enumerated below. Subscripts e, t, and p mean elastic, transformational, and plastic.

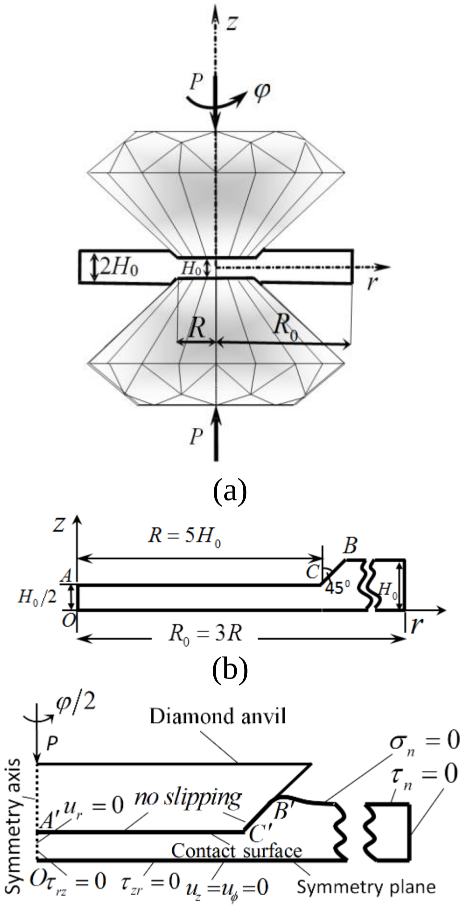

(a)

(b)

(c)

FIG. 1. (a) A RDAC schematics; φ is rotation angle of upper diamond anvil with respect to the lower one; (b) a quarter of sample in initial undeformed state in a cylindrical coordinate system $rz\phi$; and (c) boundary conditions in the deformed configuration, in particular, complete cohesion is assumed on the contact surface between sample and diamond anvil.

Decomposition of deformation rate $\mathbf{d}$ into elastic, transformational, and plastic parts:

$$\mathbf{d} = \overset{\nabla}{\varepsilon}_e + \dot{\varepsilon}_t \mathbf{I} + \mathbf{d}_p \, . \tag{1}$$

Hooke's law for pressure p and deviatoric part $\mathbf{s} = dev\mathbf{T}$ of the true stress tensor **T**:

$$p = -\frac{\sigma_{rr} + \sigma_{\phi\phi} + \sigma_{zz}}{3} = -K\varepsilon_{e0} ; \qquad \mathbf{s} = 2G\, dev\boldsymbol{\varepsilon}_e \, .$$

(2)

Transformation volumetric strain:

$$\varepsilon_t = \bar{\varepsilon}_t c \, . \tag{3}$$

Von Mises yield condition for two-phase mixture:

$$\sigma_i = \left(\frac{3}{2}\mathbf{s} : \mathbf{s}\right)^{0.5} \le \sigma_y\left(c\right) = \left(1-c\right)\sigma_{y1} + c\sigma_{y2} \, . \tag{4}$$

Plastic flow rule in the plastic region:

$$\sigma_i = \sigma_y(c) \qquad \rightarrow \qquad \mathbf{d}_p = \lambda \mathbf{s} ; \quad \lambda \ge 0 \quad ; \tag{5}$$

in the elastic region:

$$\sigma_i < \sigma_y(c) \qquad \rightarrow \qquad \mathbf{d}_p = 0 \, . \tag{6}$$

Momentum balance equation:

$$\nabla \cdot \mathbf{T} = 0. \tag{7}$$

Strain-controlled kinetics for phase transformations:

$$\frac{dc}{dq} = 10k \frac{(1-c)\bar{p}_d H\left(\bar{p}_d\right)\dfrac{\sigma_{y2}}{\sigma_{y1}} - c\bar{p}_r H\left(\bar{p}_r\right)}{c + (1-c)\sigma_{y2}/\sigma_{y1}} \quad . \tag{8}$$

Here q is the accumulated plastic strain, $\dot{q} = (2/3\mathbf{d}_p : \mathbf{d}_p)^{1/2}$; $\bar{p}_d = \frac{p - p_\varepsilon^d}{p_h^d - p_\varepsilon^d}$ and $\bar{p}_r = \frac{p - p_\varepsilon^r}{p_h^r - p_\varepsilon^r}$ are dimensionless characteristic pressures for direct and reverse PT; $\mathbf{I}$ is the second-rank unit tensor; ε_{e0} and $\bar{\varepsilon}_t$ are the elastic and transformation volumetric strains for complete PT, respectively; $\overset{\nabla}{\varepsilon}_e$ and $\overset{\nabla}{\mathbf{s}}$ is the objective Jaumann time derivative of the elastic strain and deviatoric stress; K and G are the bulk and shear moduli, respectively; σ_i is the stress intensity or effective stress; λ is a parameter which is determined iteratively in order to satisfy the yield condition (4); H is the Heaviside step function; and p_h^d and p_h^r are the pressures for direct and reverse PTs under hydrostatic loading, respectively.

Geometry and boundary conditions for the problems under study are presented in Fig. 1. Note that a typical radius if an anvil R is 200 – 500 microns and thickness of a sample under the load is 10 -50 microns; however, problem formulation and solution are independent of the absolute size of the system. While RDAC will be considered to have axial symmetry, loading under compression and torsion is three-dimensional. Thus, the problem should be classified as the generalized axisymmetric problem, and therefore cylindrical coordinate system $rz\phi$ is utilized. Change in the diamond anvils geometry is negligible under the maximum pressure mentioned above (see justification in [27-29]), and rigid anvils will be utilized. Two loading steps are included: first, the sample is subjected to rising axial compressive force P until the final value P_f, and then the one of the diamond anvils is gradually twisted from rotation angle $\varphi = 0$ to the final $\varphi = \varphi_f$ with respect to another. Due to symmetry with respect to $z = 0$ plane, a quarter of a sample (shown in Figs. 1 (b) and (c)) participates in simulations only. The twisting displacement $u_{\varphi} = 0$ at the symmetry plane is prescribed, and the half of the rotation angle $\varphi/2$ of an upper anvil is applied with respect to this plane. When pressure exceeds $\sim 2\sigma_{y1}$, asperities of the diamond penetrate into a deformed sample, which leads to a complete cohesion between rigid diamond and sample (similar to [14] and [30]).

During unloading, which has never been studied before for RDAC, two different paths will be studied: 1) the axial force P is gradually released to a small value at the fixed rotation angle φ_f; and 2) the torque about z direction applied to a diamond is first reduced down to zero at a constant axial force P_f followed by the release of axial force P. During reloading, there are also two paths: 1) after unloading according to the first path mentioned above, the axial force P grows from the small value to the final one at the fixed rotation angle φ_f, and then diamond anvil is subjected to further torsion with addition rotation angle φ_a at this final axial force; and 2) after slight release in the axial compressive force during unloading process, one of anvil is subjected to further torsion. Such a program was experimentally investigated for weaker high pressure phase for ZnSe in [8] and for stronger high pressure phase for KCl in [3], respectively.

The FEM software ABAQUS [32] is utilized for the solution of the above-formulated generalized axisymmetric problem. To consider the strain-controlled kinetic Eq. (8), ABAQUS subroutines USDFLD and HETVAL are implemented, in which transformation strain is modeled through the thermal strain, and concentration c is treated as temperature. In the dimensionless form, except for shear stresses (which are normalized by yield shear stress $\tau_{y1} = \sigma_{y1}/\sqrt{3}$), all stress-related parameters (e.g., pressure p) are normalized by σ_{y1}; the dimensionless force F is the axial force P normalized by the total initial contact area of sample. For precise comparison with the results for $p_\varepsilon^d > p_\varepsilon^r$ in [14], we assume dimensionless $p_\varepsilon^d = 6.375$ and $p_\varepsilon^r = 6.75$ in this paper (i.e., just switch values $p_\varepsilon^d = 6.75$ and $p_\varepsilon^r = 6.375$ used in [14]) and keep other material parameters exactly same as in [14]: $p_h^d = 11.25$, $p_h^r = 1.875$, Young modulus $E = 162.5$, Poison's ratio $\nu = 0.3$, and volumetric transformation strain $\bar{\varepsilon}_t = -0.1$.

3.3 Phase transformations under high pressure and large shear loading

We will discuss PTs under torsion at the constant axial compressive force $F = 4.44$, for weaker, equal-strength, and stronger high-pressure phases, respectively. Previous studies [14] focusing on the case with k=1 and $p_\varepsilon^d > p_\varepsilon^r$ successfully described a number of experimental phenomena but fail to explain some of them due to limited choice of material parameters. In this section, the primary goal is to investigate effects of some parameters in Eq. (8) on PTs and plastic flow, and explain those experimental phenomena, which could not be reproduced before. Specifically, by prescribing k=1, 5, and 10 respectively, the effects of kinetic parameter k will be investigated; by prescribing $\sigma_{y2}/\sigma_{y1} =$0.2, 1, and 5, the weaker, equal-strength, and stronger high-pressure phase will be considered; and by prescribing $p_\varepsilon^d < p_\varepsilon^r$ and in comparison with the case $p_\varepsilon^d > p_\varepsilon^r$ in [14], effects of characteristic pressure parameters will be taken into account. For all cases, during torsion, the material’s flow from the center to outside causes significant reduction in the thickness of sample, which accelerates the plastic deformation and thus provides an additional driving force for PTs.

Weaker high-pressure phase

Evolution of concentration of a weaker $\left(\sigma_{y2}=0.2\sigma_{y1}\right)$ high-pressure phase *c* with rising rotational angle φ is shown in Fig. 2, under the constant compressive axial force *F*=4.44 for kinetic parameter *k*=1, 5, and 10. Results for φ=0 correspond to the end of compression stage, which already leads to PT. As shown in Fig. 2(a), PTs start at the center of sample on the symmetry plane rather than at contact surface, because there pressure first exceeds p_{ε}^{d} above which direct PTs could occur. For *k*=5 and 10, while PT also initiates at the center, then the major PT progress shifts from the symmetry plane to contact surface (shown in Figs. 2 (b) and (c)), at $\varphi=0$. Both the softening of materials during PTs and the transformation-induced volumetric reduction cause localizations of strains and concentrations *c* in some regions, which induce the irregular distributions of all of the fields. At the initial stage of torsion, PT zones are mostly localized within the thin and long shear and PT bands, which are clamped by stronger low-pressure phase. Consequently, with the rising rotation angle φ, plastic flow mostly appears in the bands due to lower strength and PT propagates inside of them. From Fig. 2, one notes that with growth of the kinetic parameter *k*, the rate of PTs increases and the geometry of PT zones evidently changes. Under compression, total amount of high pressure phase is surprisingly larger for *k*=5 than for *k*=10, while for all stages of torsion it is the opposite. Fig. 2 also shows a fully transformed high-pressure phase appears on the contact surface in the center of sample and it could be detected by X-ray or surface-based (Raman or optical) method. In contrast, PTs in [14] with $p_{\varepsilon}^{d}>p_{\varepsilon}^{r}$ and *k*=1 almost does not appear there, even for a very large rotation angle because of very small plastic strains. This prevents observations of the high pressure phase by surface-based methods. Direct PT occurs at lower pressure than in [14], because the threshold value p_{ε}^{d} for direct PT is accepted lower in this paper than that in [14]. After PT starts, volumetric transformation strain generates significant internal stresses, which in combination with external nonhydrostatic stresses cause additional plastic straining called transformation-induced plasticity (TRIP) [1, 11, 33]. TRIP leads to further PTs thus providing an additional driving force for PTs and mechanochemical feedback.

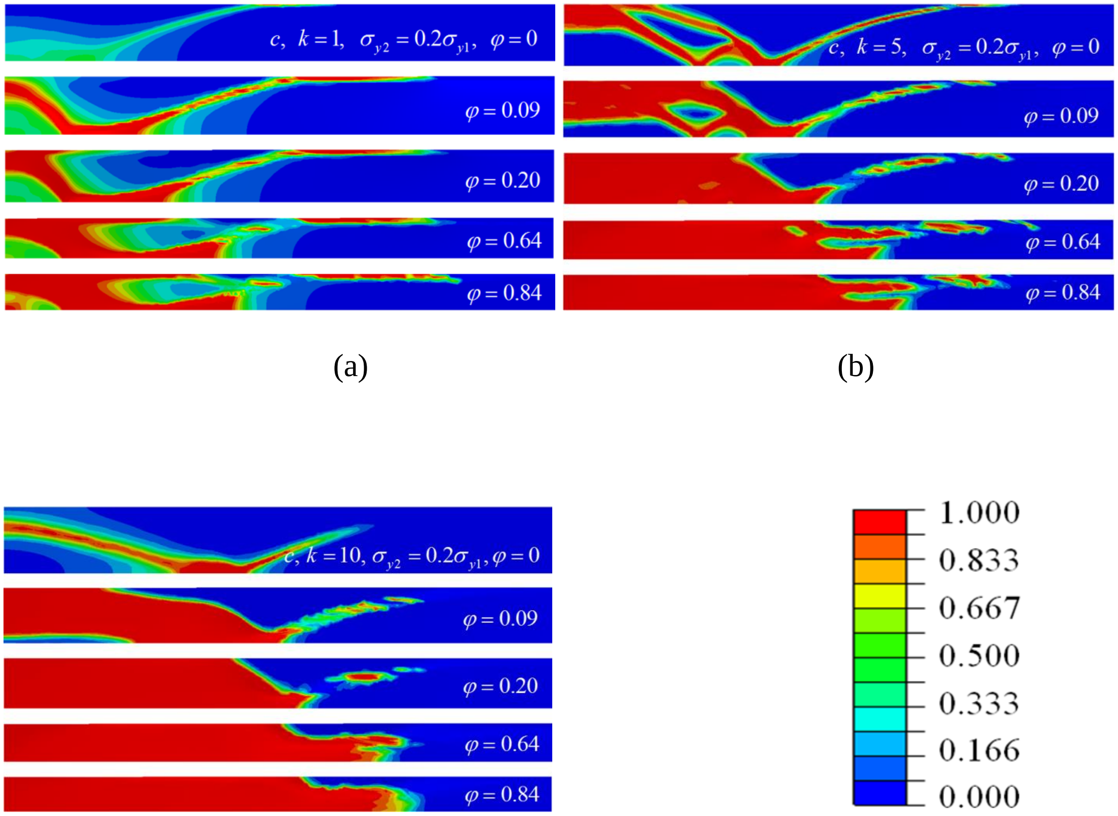

(a)

(b)

(c)

FIG. 2. Evolution of concentration of a weaker $(\sigma_{y2}=0.2\sigma_{y1})$ high-pressure phase *c* with increasing rotation angle φ under a constant compressive axial force *F*=4.44, for *k*=1, 5, and 10. Part of the sample with $r/R<0.72$ (Fig. 1 (b)) is shown.

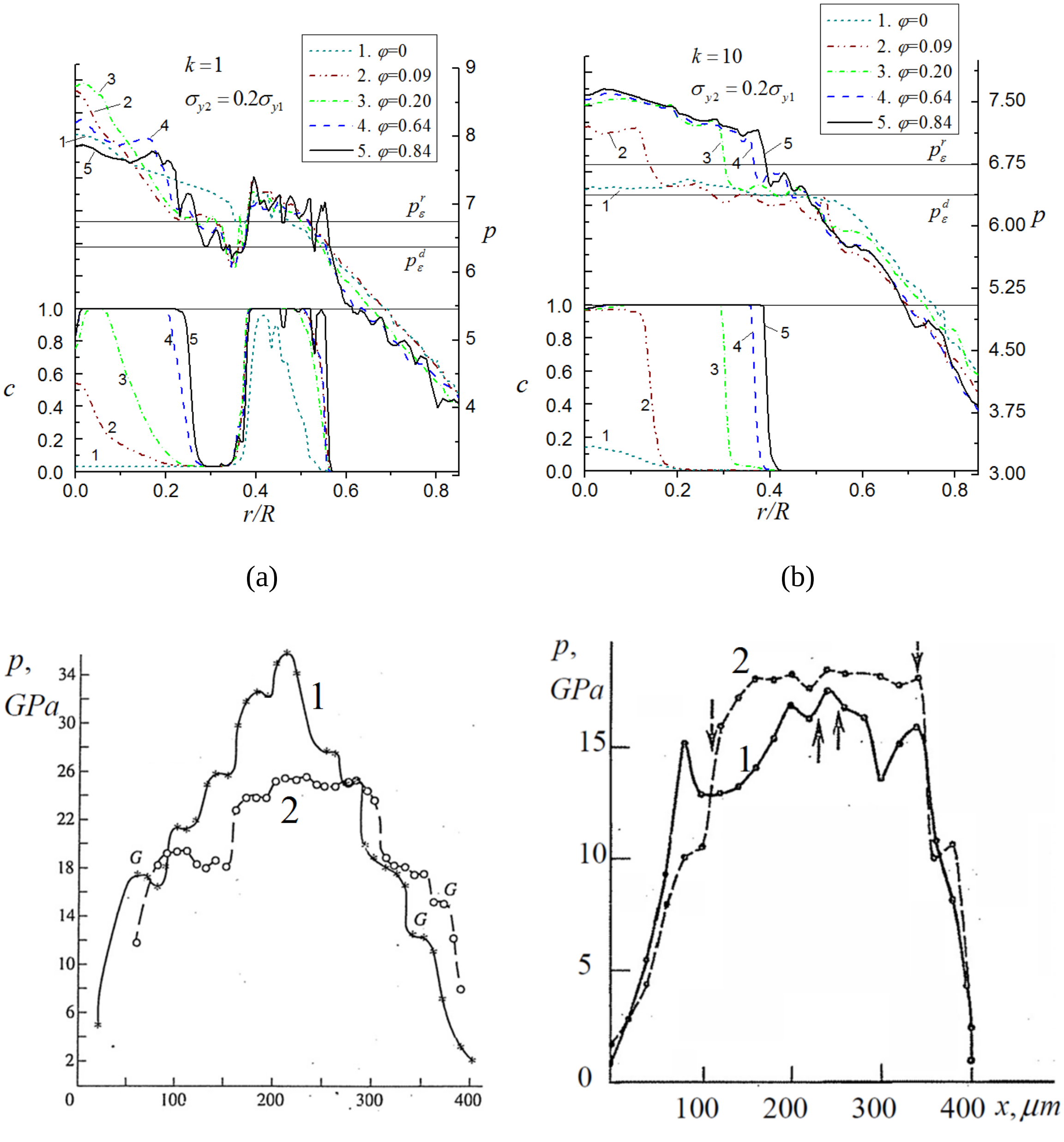

(a)

(b)

(c)

(d)

FIG. 3. Distributions of dimensionless pressure *p* and high-pressure phase concentration *c* at the contact surface during torsion under constant axial force *F* for $\sigma_{y2}=0.2\sigma_{y1}$ and *k*=1 (a) and 10 (b). Experimental pressure distributions on the contact surface of the sample for CuI (adopted form in [25]) (c) and ZnSe (adopted form in [8]) (d), respectively. Sold line 1 is for compression without torsion and dashed line 2 is after torsion under the fixed axial force. Arrows indicate visible interface between low- and high-pressure phases.

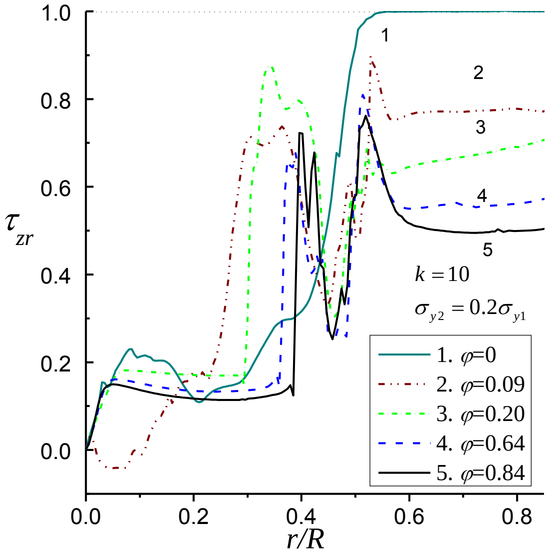

(a)

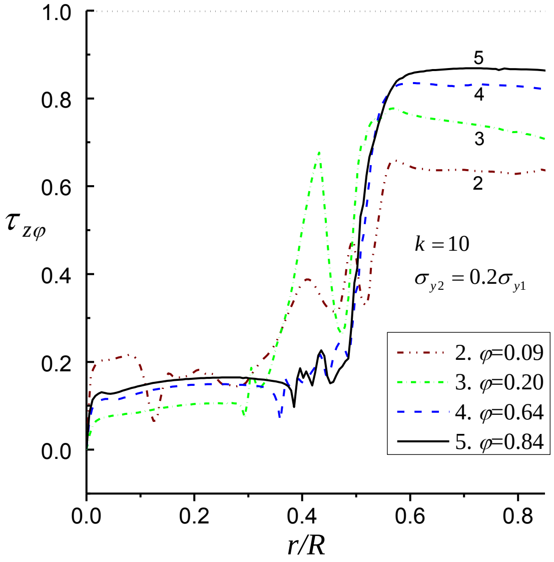

(b)

FIG. 4. Distributions of shear stresses (a) τ_{zr} and (b) $\tau_{z\varphi}$ at the contact surface during torsion under constant axial force *F* for *k*=10, $\sigma_{y2} = 0.2\sigma_{y1}$, and different rotation angles of an anvil.

It is worth to mention that the PT from semiconducting Si I to weaker metallic Si II under compression in diamond anvils [34] was found in a thin contact layer only but not in the bulk, which agrees with our results in Figs. 2 (a) and (b) for *k*=5 and 10, and $\varphi = 0$. This coincidence also confirms the possibility of strain-induced (rather than pressure-induced) PT under compression without torsion. From Fig. 2(c), high pressure phase gradually propagates from center to periphery which is also accompanied by disappearance of PT band during increase of the rotational angle from 0.09 to 0.64. Both direct and reverse PTs occur simultaneously but in different regions.

The oscillatory pressure distribution at the contact surface for weaker high pressure phase in Fig. 3 is not a numerical error because it is caused by multiple instabilities due to material softening and TRIP during PT. Such an irregular pressure field on the contact surface was experimentally observed for CuI [25] and ZnSe [8] (Figs. 3 (c) and (d)). For *k*=1, pressure at the center evidently increases at initial torsion $\varphi < 0.2$. However, pressure at the later stage of torsion greatly reduces at the center because of both appearance of a weaker phase on the contact surface and volumetric reduction during PT at the later stage. Such a pressure reduction was called as "pressure self-demultiplication" and was experimentally observed for CuI [25] (Fig. 3(c)). It was not found for the case $p_\varepsilon^d > p_\varepsilon^r$ in [14] due to absence of weaker phase on the contact surface in the center of a sample. For *k*=10, pressure in the center grows during the whole process of torsion, which corresponds to experiments in ZnSe [8] (Fig. 3(d)). This happens because PT in the center of sample are completed at the initial stage of torsion, and thus could not occur any more at the later stage (see Fig. 2(c)), which does not lead to further reductions of strength on contact surface and volume in the center. From Fig. 4, one notes that distribution of shear stresses τ_{zr} or $\tau_{z\varphi}$ is also oscillatory due to strain softening and TRIP during PT, and their magnitudes in the center $(r/R < 0.3)$ are much smaller than those at the periphery caused by reduction of material strength. At the periphery, where there is no PTs due to low pressure, shear stresses are almost homogeneously distributed and decrease in the radial shear stress τ_{zr} leads to increase in torsional $\tau_{z\varphi}$ to keep $\tau = \sqrt{\tau_{zr}^2 + \tau_{z\varphi}^2} = \tau_{y1}$.

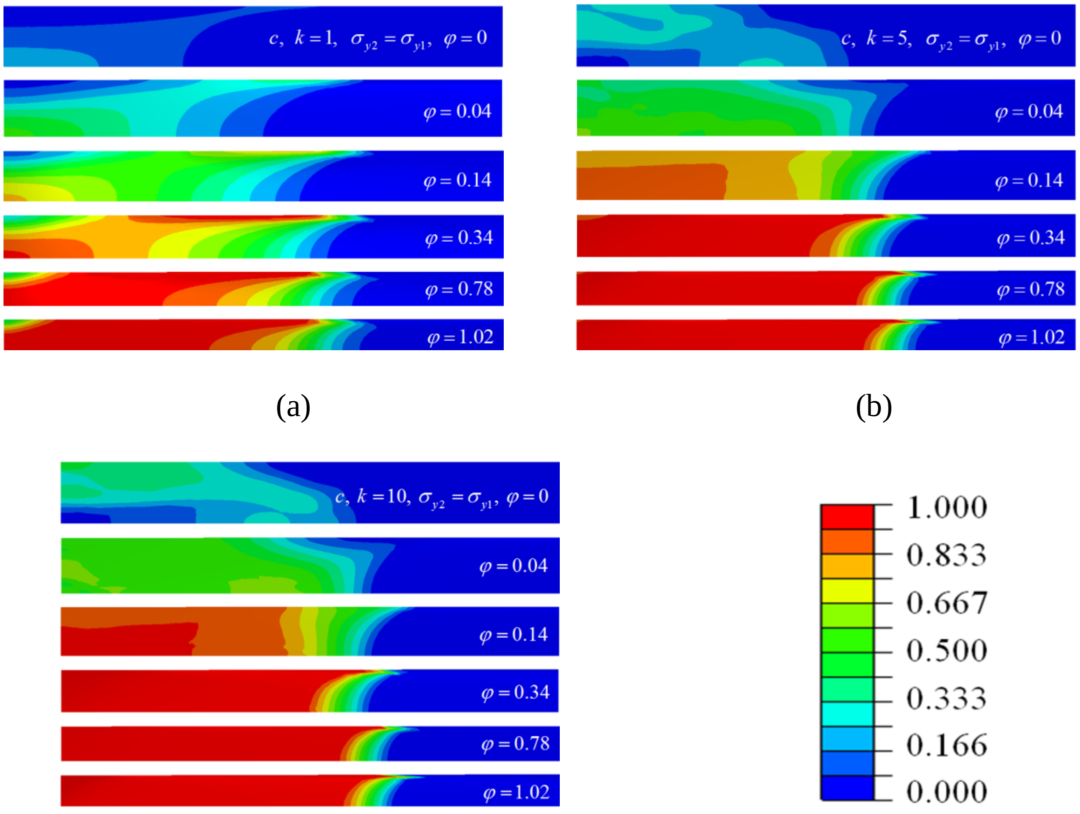

(a)

(b)

(c)

FIG. 5. Evolution of concentration of high-pressure phase c with increasing rotation angle φ under a constant compressive axial force F=4.44 for k=1, 5, and 10; $\sigma_{y2} = \sigma_{y1}$ and $r/R < 0.72$.

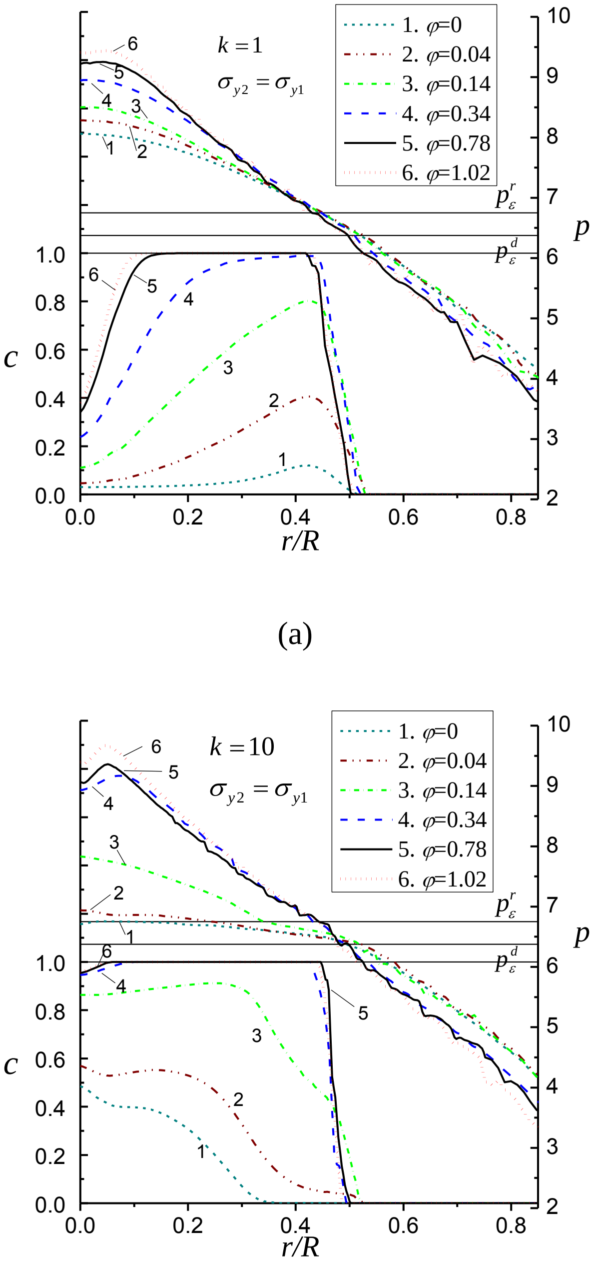

(a)

(b)

FIG. 6. Distributions of dimensionless pressure *p* and high-pressure phase concentration *c* at the contact surface during torsion under constant axial force *F* for *k*=1 and 10 and $\sigma_{y2} = \sigma_{y1}$.

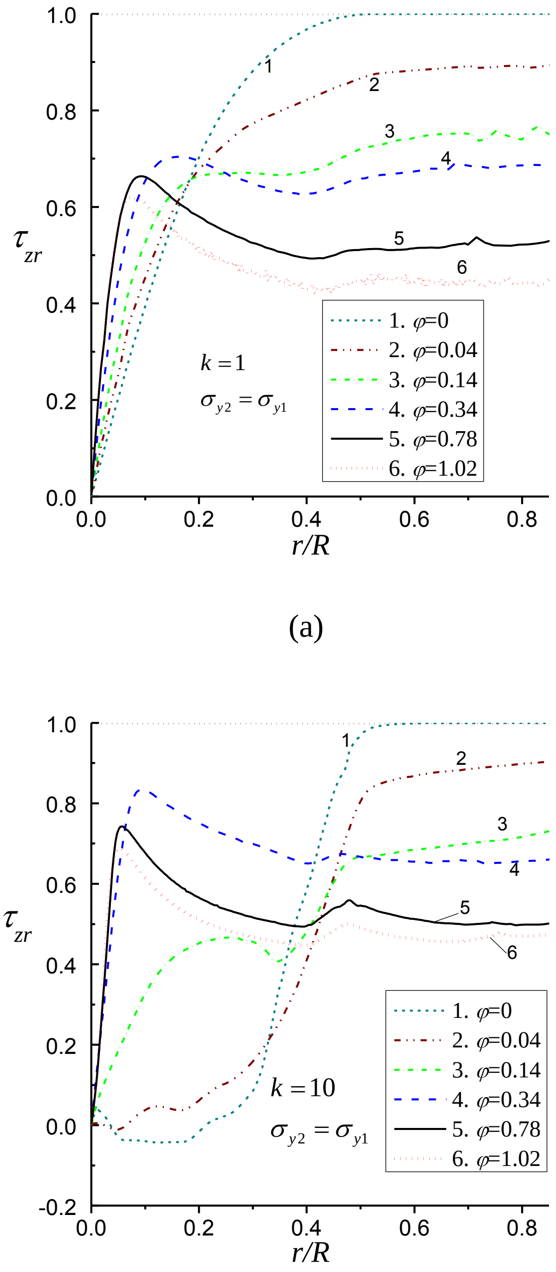

(a)

(b)

FIG. 7. Distributions of shear stresses τ_{zr} at the contact surface during torsion under constant axial force F for k=1 and 10 and $\sigma_{y2} = \sigma_{y1}$.

Equal-strengths phases

At the initial stage of torsion, with different kinetic parameters *k*, the geometry of PT zone is also quite different. For example, PT does not occur on the contact surface in the center of sample for *k*=1, but it occurs for *k*=5 and 10. At the later stage of torsion, the geometries of PT zones for *k*=5 and 10 are very similar because PT completes in the entire region with pressure above p_ε^r. In comparison with case with $\sigma_{y2} = 0.2\sigma_{y1}$, the localization of high-pressure phase concentration *c* obviously reduces and oscillatory distributions on pressure and shear stress almost disappear due to absence of material softening during PT. At the same time, geometry of PT zones, the distributions of pressure and shear stress are very similar to those for $p_\varepsilon^d > p_\varepsilon^r$ and *k*=1 in [14].

Fig. 6 shows the distributions of dimensionless pressure *p* and high-pressure phase concentration *c* at constant axial force *F*=4.44. One can note that during compression ($\varphi = 0$), the amount of high pressure phase in the center of sample for *k*=10 is much larger than the one for *k*=1, which leads to larger volumetric reduction and therefore lower pressure for *k*=10. In the PT zone, pressure grows in the center of sample with rising rotation angle, because a simplified equilibrium[1] $dp/dr = 2\tau_{zr}/h$ is applicable in this case and both τ_{zr} and $\tau_{z\varphi}$ (and, consequently, the resultant shear stress $\tau = \sqrt{\tau_{zr}^2 + \tau_{z\varphi}^2}$) at the center of sample gradually increases (similar to the case for stronger phase in Fig. 14), while the thickness *h* reduces. In addition, since shear stress $\tau = \tau_{y1}$ at the periphery, the radial shear stress τ_{zr} at the periphery reduces during torsion (from τ_{y1} for $\varphi = 0$) with rising torsional shear stress $\tau_{z\varphi}$. With growth of *k*, distribution of shear stresses in the center of sample becomes obviously different (Fig. 7), especially at the initial stages of torsion, because there PT occurs and rate of PT strongly depends on *k*. During compression ($\varphi = 0$), materials flows to the center for *k*=10 because of fast reduction in volume during direct PT, which compensates the flow to the periphery due to compression, and as a result, shear stress τ_{zr} is much smaller and change sign in the PT region for *k*=10, in contrast to the case with *k*=1 with flow from the center.

Stronger high-pressure phase

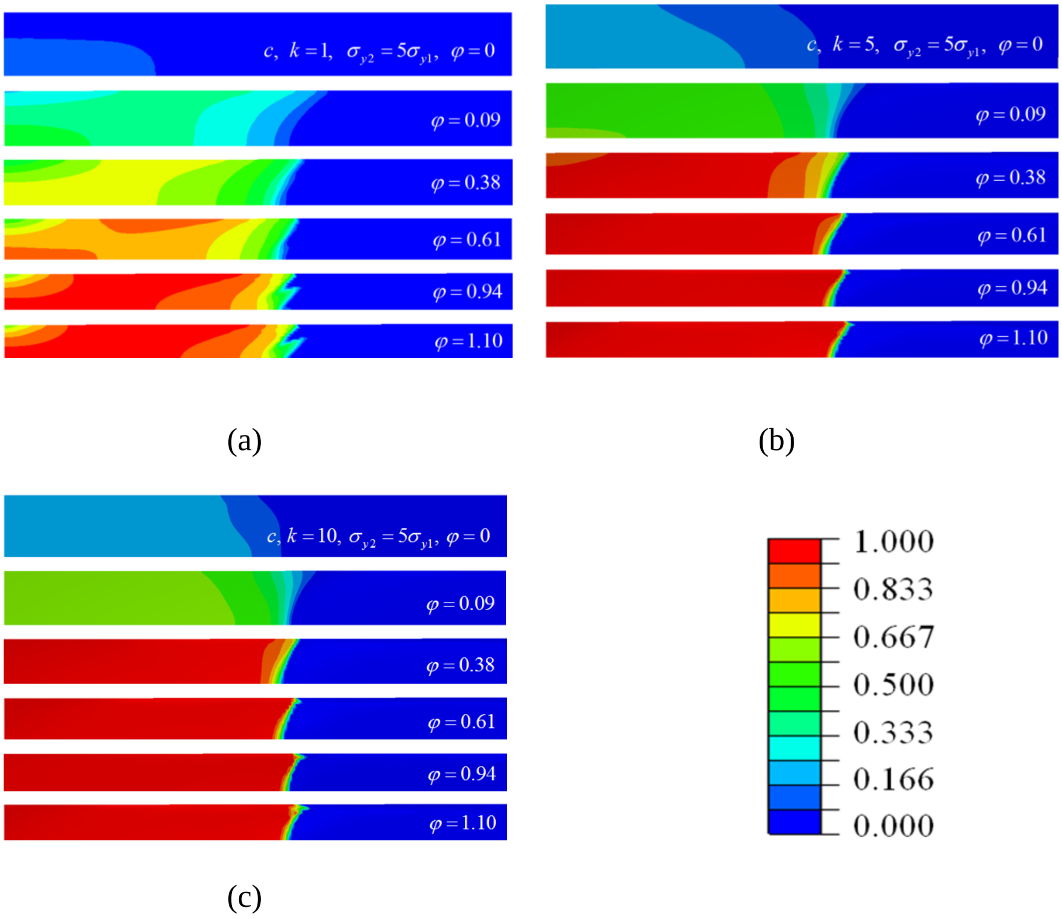

FIG. 8. Concentration of high-pressure phase *c* with increasing rotation angle φ under a constant compressive axial force *F*=4.44, for *k*=1, 5, and 10, and $\sigma_{y2} = 5\sigma_{y1}$.

Qualitatively, the character of evolution of distribution on concentration *c* of stronger high-pressure phase $\left(\sigma_{y2}=5\sigma_{y1}\right)$ with rising rotational angle in Fig. 8 is similar to the case with equal strengths of the phases $\left(\sigma_{y2}=\sigma_{y1}\right)$ and one could note that: 1) the rate of PTs for *k*=1 is lower than that for *k*=5 and 10, which causes that there is a large two-phases (0<*c*<1) region for *k*=1; 2) at the later stage of torsion, PT for *k*=5 and 10 completes in the region with pressure $p>p_{\varepsilon}^{r}$ and geometries of PT zones are quite similar; 3) after twisting diamond with 0.94 radians, further torsion does not practically change the concentration *c*; and 4) thickness of sample evidently reduces during torsion. In comparison with [14], the rate of PTs in the current paper is slightly slower, and geometry of the border zone between fully transformed and untransformed materials is obviously different because higher value of p_{ε}^{r} is accepted in this paper and both direct and reverse PTs could occur at $p_{\varepsilon}^{d}<p<p_{\varepsilon}^{r}$ in the current model. From Figs. 8 (b) and (c), there is very sharp interface between two phases, which leads to the jump in pressure and shear stresses due to a sudden change in material strength. Sharpening of the two-phase region (interface) with increasing rotation angle is observed in experiments for KCl [3].

Fig. 9 shows the distributions of dimensionless pressure *p* and concentration *c* of stronger high pressure phase on contact surface for *k*=1, 5, and 10. In the PT region, pressure increases significantly despite of the volume reduction due to PT, which is experimentally observed as pressure self-multiplication effect [3, 4, 11, 35]. The reduction of thickness of sample during

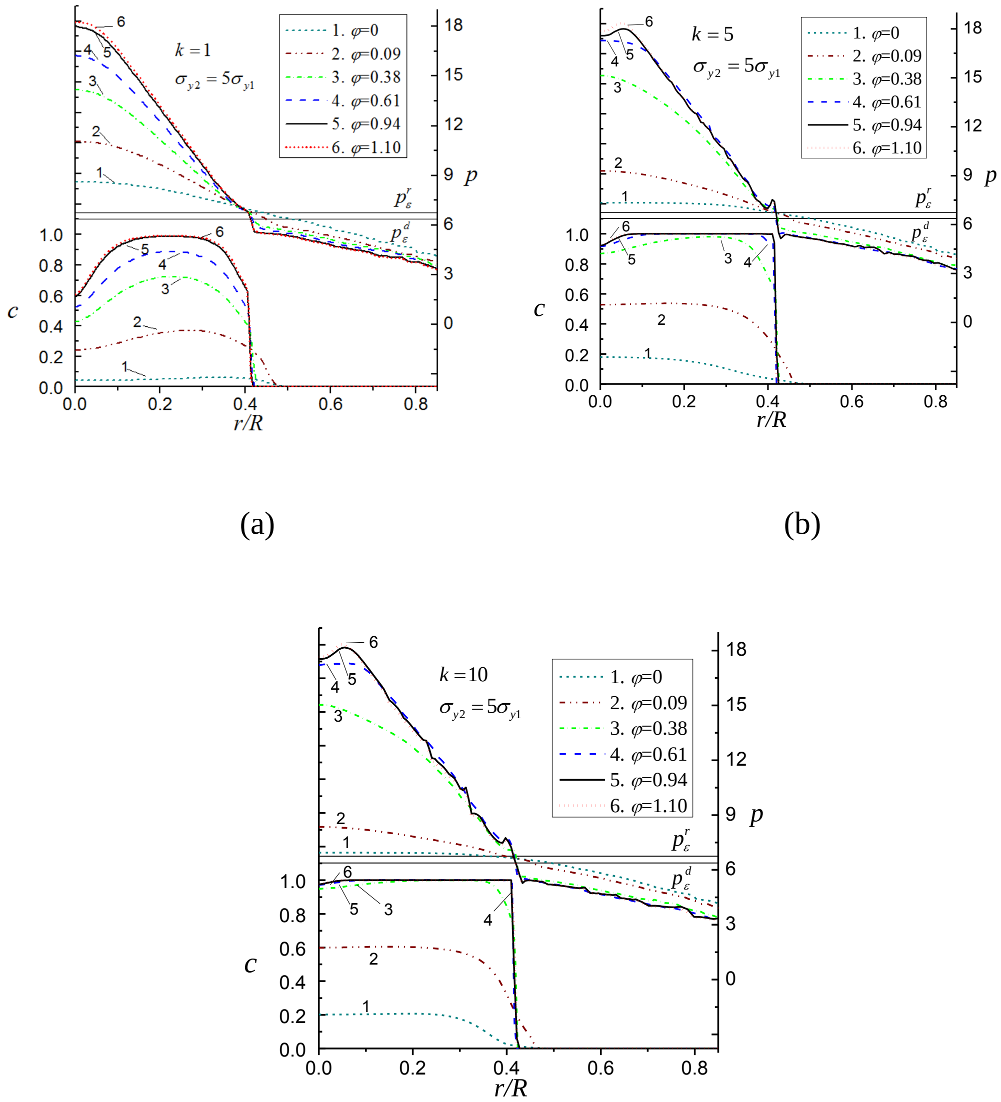

(a) (b)

(c)

FIG. 9. Distributions of dimensionless pressure *p* and high-pressure phase concentration *c* at the contact surface during torsion under constant axial force *F* for *k*=1, 5, and 10, and $\sigma_{y2} = 5\sigma_{y1}$.

torsion compensates the transformation-induced volume reduction, and higher yield strength for high pressure phase results in a growth of friction stress (see Fig. 10), and consequently leads to an increase in pressure. The growth of pressure in the center of sample during PT provides a positive driving force to accelerate direct PT kinetics, but leads to reduction of pressure in the periphery due to a fixed constant axial force. Then, in the region $0.42 < r/R < 0.48$, pressure drops from the value above p_ε^d to the one much below p_ε^d and leads to the reverse PTs, which is consistent with experimental observation for KCl [3]: both direct and reverse PTs could occur simultaneously but in different regions. At the initial stage of torsion, concentration of the high pressure phase increases significantly and therefore pressure grows quickly as well. For example, during increase in the rotation angle from 0 to 0.38 radians, pressure in the center for *k*=10 increases by more than 2 times. At the later stages of torsion, with rising rotation angle, PT does not proceed visibly, and pressure also has almost no change. For example, when φ increase from 0.94 to 1.10 radians, concentration of high pressure phase and pressure almost do not change for *k*=1, 5, and 10 in Fig. 9. This is consistent with experimental observation [4]: without PTs, pressure distribution on contact surface is independent on rotational angle. Small "steps" in pressure distribution, which are localized near the two-phases region, are found in our simulations, similar to those in experiments for KCl and fullerene C_{60} [3, 4, 35]. It is also found that pressure steps for *k*=1, both in this paper (Fig. 9(a)) and [14], are not as obvious as the steps in Figs. 9(b), and (c) for a larger *k*. Interface between PT and no-PT zones is much sharper for the case with *k*=5 and 10 than that for *k*=1. However, in contrast to the cases in [14] for $p_\varepsilon^d > p_\varepsilon^r$ with torsion and in [31] for $p_\varepsilon^d < p_\varepsilon^r$ without torsion, these steps are not close to characteristic pressures p_ε^d and p_ε^r, which *does not allow them to be determined experimentally* from the pressure distribution. Also, there is a region with large pressure gradient and change in pressure, which includes a quite sharp interface between low and high pressure phases.

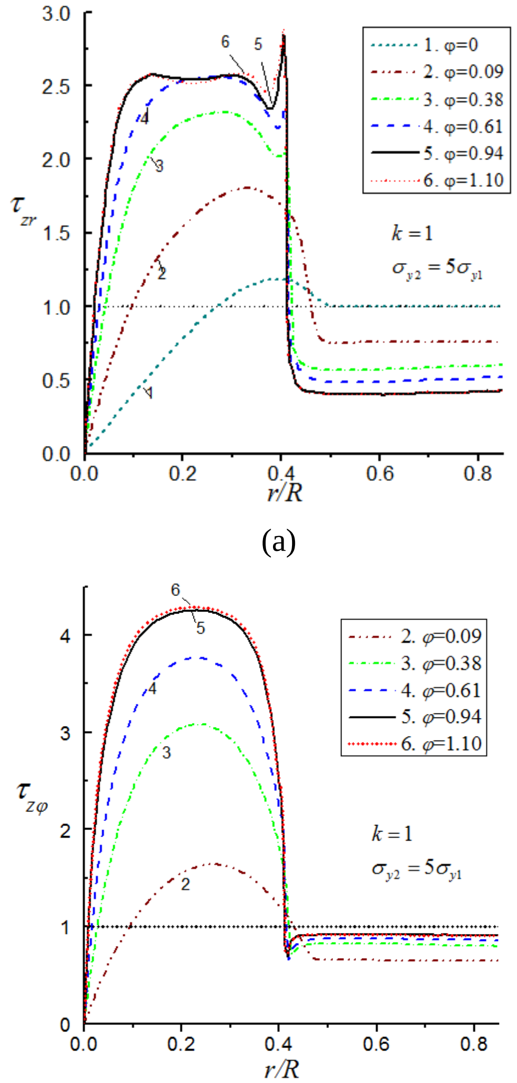

(a)

(b)

FIG. 10. Distributions of shear stresses (a) τ_{zr} and (b) $\tau_{z\varphi}$ at the contact surface under constant axial force *F* for *k*=1 and $\sigma_{y2}=5\sigma_{y1}$ for different rotation angles of an anvil.

As in previous cases, both radial shear stress τ_{zr} and torsional shear stress $\tau_{z\varphi}$ on the contact surface are almost homogenous in nontransformed regions. Also, the increase in $\tau_{z\varphi}$ is accompanied by a decrease in τ_{zr} to keep a constant resultant shear stress $\tau=\sqrt{\tau_{zr}^2+\tau_{z\varphi}^2}=\tau_{y1}$. In the transformed region, radial and torsional shear stresses grow because of the increase of material strength, and the increase in shear stress $\tau_{z\varphi}$ causes the growth of torque. Both radial and torsional shear stresses drop drastically at the sharp interface. In comparison with the case $p_{\varepsilon}^{d} > p_{\varepsilon}^{r}$ in [14], radial shear stress distribution at the interface of transformed and untransformed region in Fig. 10(a) looks slightly different, due to a different geometry of PT zone (see Fig. 8(a))

3.4 Phase transformations under unloading

Except for *in-situ* study, descriptions of PT process under pressure and shear are based on the results of measurements after complete unloading [17-23], and therefore they are based on a strong assumption that there is no PT during unloading. Evolution of concentration of high-pressure phase during the reduction of applied force and torque down to zero was never studied in experiments and simulations. In this section, the process of releasing axial force and torque will be investigated numerically, and the effects of the ratio of the yield strength of phases, kinetic parameter *k*, and different unloading paths on PTs will be elucidated. For all of cases in this section, unloading initiates from the last step of loading process in section III (See Figs. 2, 5, and 8); specifically, (a) for $\sigma_{y2} = 0.2\sigma_{y1}$, unloading initiates at rotational angle $\varphi = 0.84$; (b) for $\sigma_{y2} = \sigma_{y1}$, at $\varphi = 1.02$; and (c) for $\sigma_{y2} = 5\sigma_{y1}$, at $\varphi = 1.10$. Two unloading paths are considered: (a) axial force is reduced from *F*=4.44 to *F*=1.29 at a fixed rotation angle and (b) first torque is reduced to zero and then axial force is reduced from *F*=4.44 to *F*=1.29.

From Fig. 11, one can note that with the reduction in ratios σ_{y2}/σ_{y1}, reverse PT becomes obvious during the release of the axial load; unlike the evolution of direct PT during loading, reverse PT under unloading progresses from contact surface to symmetry plane and from periphery to center because reverse PT initiates where pressure is below

p_{ε}^{r} in the presence of plastic flow. In comparison to the process of unloading in ordinary DAC [31], results are quite different, because of reduction of torque in spite of constant rotational angle in RDAC.

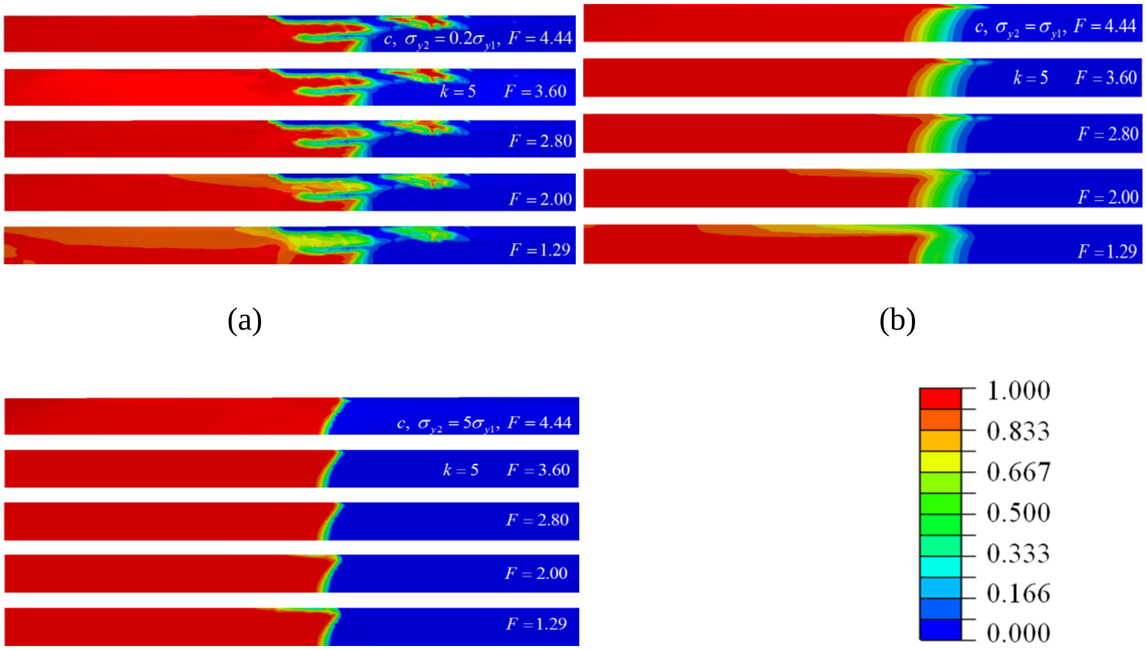

(a) (b)

(c)

FIG. 11. Concentration of high-pressure phase *c* with decreasing axial compressive force F under a constant rotation angle φ: (a) 0.84, (b) 1.02, (c), 1.10, for $\sigma_{y2}/\sigma_{y1}=0.2$, 1, and 5, and k=5.

From Fig. 12, the rate of pressure reduction is faster in the periphery ($r/R>0.6$) than that in the central region ($r/R<0.5$) of sample because reverse PT leads to increase in volume and therefore reduces the rate of reduction in pressure. For example, combining Figs. 11 and 12, pressure reduces much slower at the center ($r/R<0.5$) when axial force releases from 2.80 to 1.29 than at the initial stage of unloading the axial force, because PT mostly occurs at the later stage. During the unloading, evident plastic flow appears in the whole sample especially in the two-phase region. The rate of plastic flow is faster at the later stage of unloading than at the initial stage, which differs from the case for unloading after compression in the ordinary DAC [31]. Torque and shear stress $\tau_{z\varphi}$, which, however, significantly reduce during axial force release in RDAC under fixed rotation angle, play a significant role in plastic flow during unloading in RDAC. In [31] for DAC, plastic flow at the later stage of unloading become not so obvious as at initial stage, and in some cases there is a quite large region at center of a sample without change in plastic strain at all.

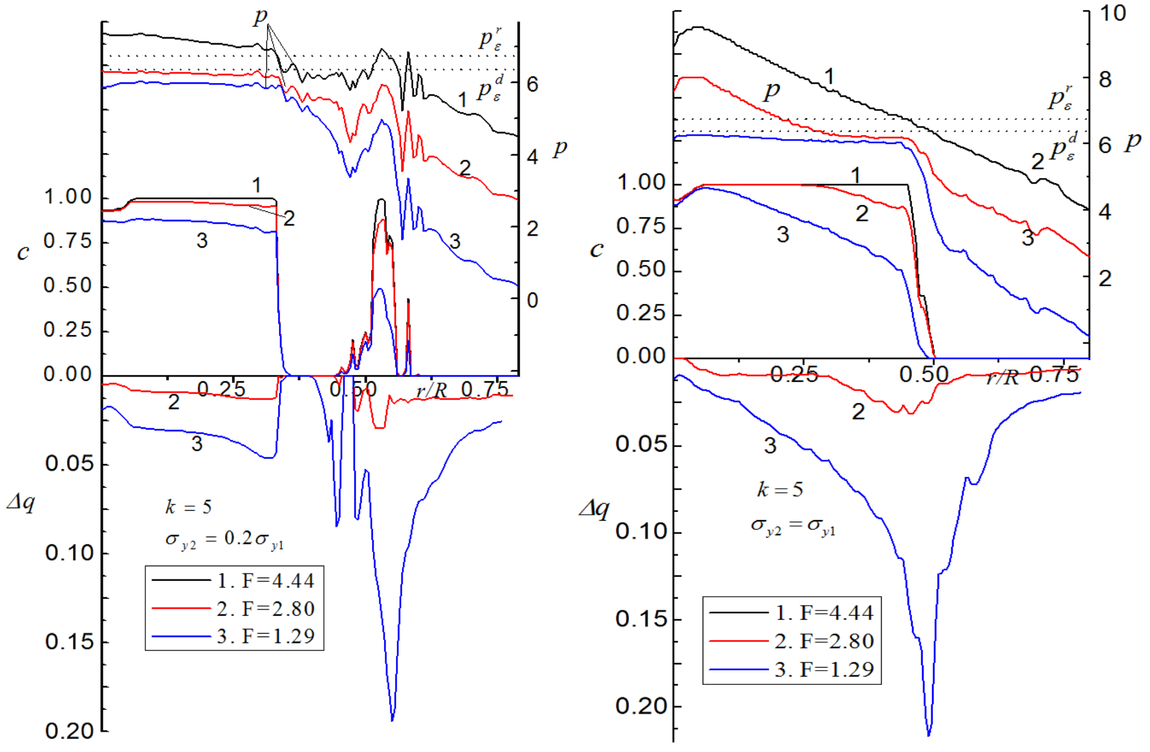

(a) (b)

FIG. 12. Distributions of pressure *p*, high-pressure phase concentration *c*, and the increment in accumulated plastic strain Δq after starting unloading, under unloading at a fixed rotation angle, for $\sigma_{y2}/\sigma_{y1} = 0.2$ and 1, and *k*=5.

Fig. 13 shows distribution of the concentration of lower-strength high-pressure phase *c* with different kinetic parameters *k* under release of the axial force at a fixed rotational angle. With the growth of *k*, the rate of the reverse PT increases. Change in concentration for *k*=1 is not very obvious, but it is for *k*=10. One can find that in addition to growth in *k* itself, another important reason for rising rate of reverse PT is the growing rate of change in plastic flow: by combination of Figs. 12(a) and 14, change in accumulated plastic strain is much larger for *k*=5 than that for *k*=1, which provides a stronger driving force for reverse PT. Also, TRIP strongly affects the PTs due to both transformation strain and mismatch of strengths. In addition, reverse PT reduces the rate of reduction in pressure under unloading by an increase in volume, but unlike the case in Fig. 12(a), pressure curves in Fig. 14 are almost parallel in the whole sample during unloading due to relatively low reverse PT increment.

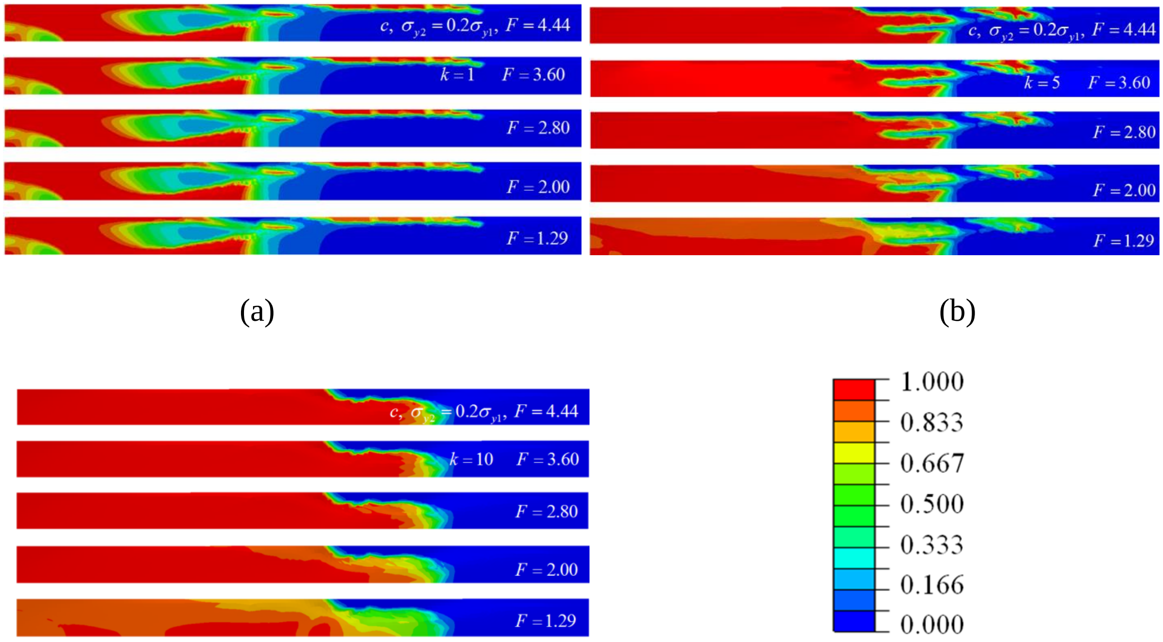

(a)

(b)

(c)

FIG.13. Concentration of high-pressure phase *c* with decreasing axial compressive force F under a constant rotation angle 0.84, for $\sigma_{y2}=0.2\sigma_{y1}$, and *k*=1, 5 and 10.

Different compared to the previous unloading path, the process of unloading in Fig. 15 consists of two steps: first, torque is released to zero at a fixed axial force *F*=4.44, and after that the axial force *F* is released. When comparing two types of unloading paths in Figs. 13(c) and 15, we find that the rate of reverse PT in Fig. 15 is slower. During the release of the moment, reverse PT almost does not occur due to high pressure in the high pressure phase and then changes of accumulated plastic strain become smaller during releasing axial force than the case in Fig. 12(c). These results can be useful in designing unloading program and may help, for example, to preserve ε phase of iron after large plastic shear (see [36]).

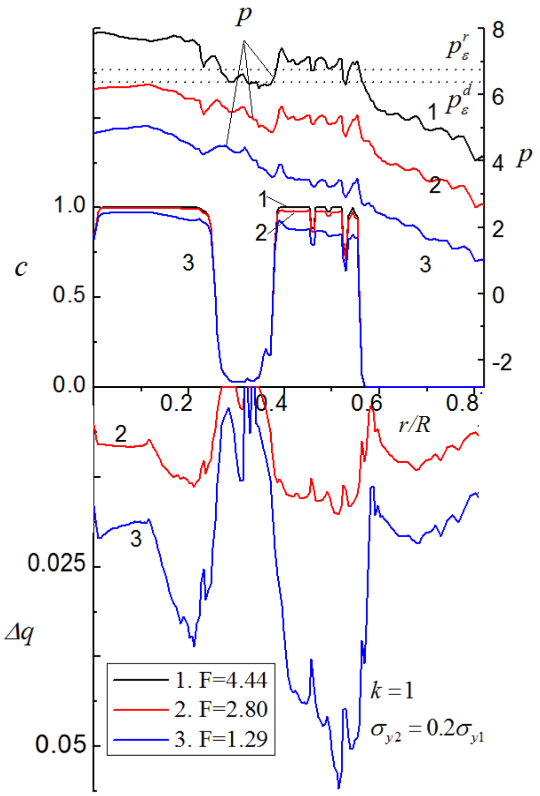

FIG. 14. Distributions of pressure *p*, high-pressure phase concentration *c*, and the increment in accumulated plastic strain Δq after starting unloading, under unloading at a fixed rotation angle, for $\sigma_{y2}=0.2\sigma_{y1}$ and *k*=1.

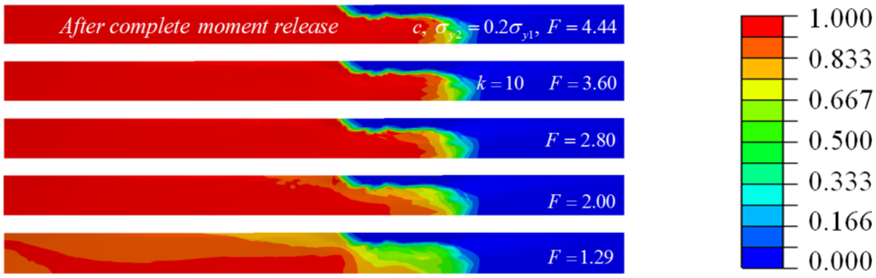

FIG. 15. Concentration of high-pressure phase *c* under unloading. The first bar is the concentration of high pressure phase after complete moment release at a fixed axial force *F*=4.44, and from the second bar to the fifth bar, the axial force *F* reduces from 4.44 to 1.29.

3.5 Phase transformations under reloading

In this section, we will discuss the reloading process to explore new pressure-plastic strain paths for strain-induced PTs in RDAC, and to interpret experimental phenomena. Two kinds of reloading paths were carried out. First, after unloading to a low load *F*=1.29 at the last step in Fig. 11(a), the diamond anvil cell is subjected to rising axial force to the final value at a fixed angle and then is further twisted by an additional angle $\Delta\varphi_a$ at the fixed final axial force. Second, after the final loading in section III (Figs. 2(b), 5(b), and 8(b)), the axial force is slightly released at a fixed rotational angle. After that, the diamond anvil is subjected to further torsion without changes in the axial force. In comparison with Fig. 16(a), after re-increasing axial force to 4.44, without additional twisting ($\Delta\varphi_a = 0$) in Fig. 16(b), PT zone still does not return to the case before loading. Therefore reverse PT is not completely recoverable during this process; but once a small rotational angle $\Delta\varphi_a$ is applied, geometry of PTs is very similar to the case with loading in Fig. 16(a) only. In addition, further increasing in rotation angle does not essentially boost direct PT because PT has almost completed in the regions where pressure is larger than p_ε^d. A possible way to stimulate direct PT is to raise the axial force

F which could increase the area where pressure is above p_{ε}^{d}, and Fig. 16(c) shows that after increasing the axial force F to 4.91, extra torsion makes high-pressure phase to propagate to the periphery.

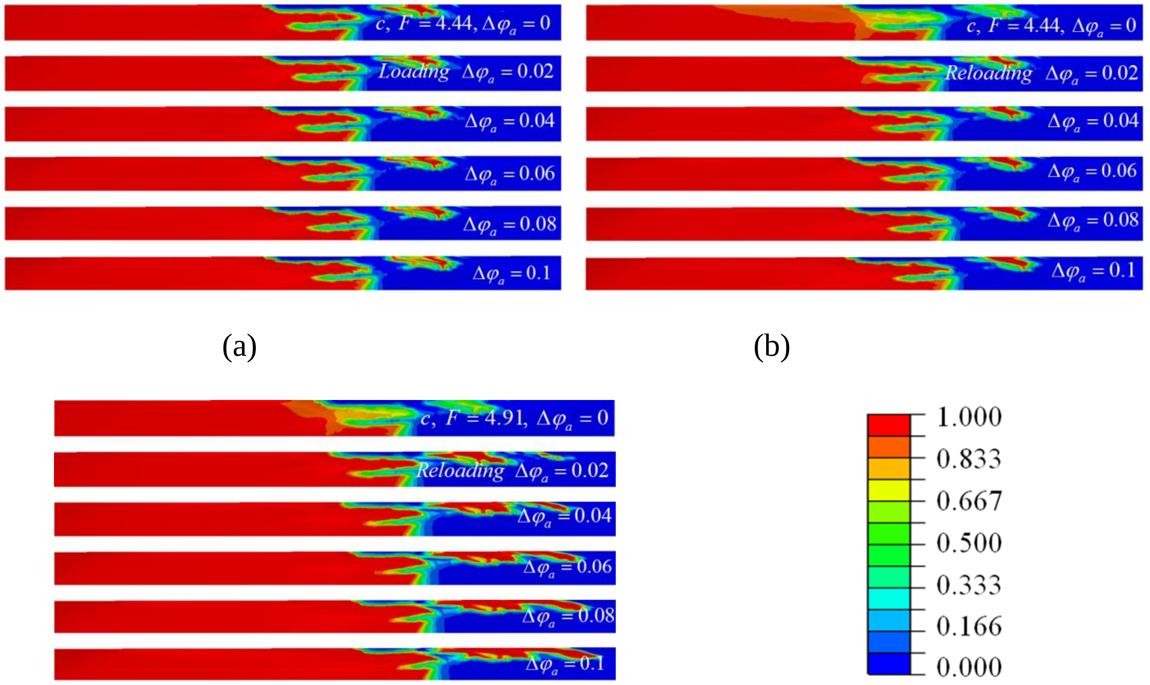

(a) (b)

(c)

FIG. 16. Concentration of high-pressure phase c for $\sigma_{y2} = 0.2\sigma_{y1}$, and k= 5. (a) The first bar is the same as in the last step in Fig. 2(b) (i.e., after rotation of an anvil by $\varphi = 0.84$ at F=4.44) and then diamond anvil is subjected to an additional torsion $\Delta\varphi_a$ at constant force F=4.44; (b) the first bar is after an increase in axial force F to 4.44 from last step of Fig. 13(b) (i.e., after unloading down to F=1.28 at the fixed φ =0.84), and then further torsion $\Delta\varphi_a$ is applied at the fixed F=4.44; (c) the first bar is after an increase in axial force F to 4.91 from last step of Fig. 13(b), and then an additional torsion is applied at the fixed F=4.91.

After loading process described in the last step in Section III (i.e., torsion at the fixed axial force), the axial force F is slightly released from 4.44 to 3.68 at fixed φ and then diamond anvil is twisted with additional angle $\Delta\varphi_a$ (Fig. 17). One can note that with growth of $\Delta\varphi_a$, obvious reverse PT occurs for $\sigma_{y2}/\sigma_{y1} = 0.2$, 1 and 5; with growth of the yield strength of high pressure phase, the rate of reverse PT reduces. For weaker high pressure phase in Fig. 18(a), the pressure at the contact surface after extra torsion increases in the center of sample $(r/R < 0.3)$ where a small amount of reverse PT occurs and leads to slight increase in the volume, and pressure reduces at the periphery $(r/R \approx 0.5)$, both are qualitatively consistent with the experimental results for ZnSe [8] (see Fig. 18(c)). However, for stronger high pressure phase in Fig. 18(b), the pressure goes down in the center $(r/R < 0.4)$; in most region of phase pressure is still very high and above p_ε^r, which limits the occurrence of reverse PT, and obvious reverse PT only take place in the very small two-phases region. Due to a fixed axial force during extra torsion, decrease of pressure is found on the inclined surface *C'B'* in Fig. 1(c). Reduction in pressure for a similar process for stronger high pressure phase corresponds to the experimental observation for KCl in [3].

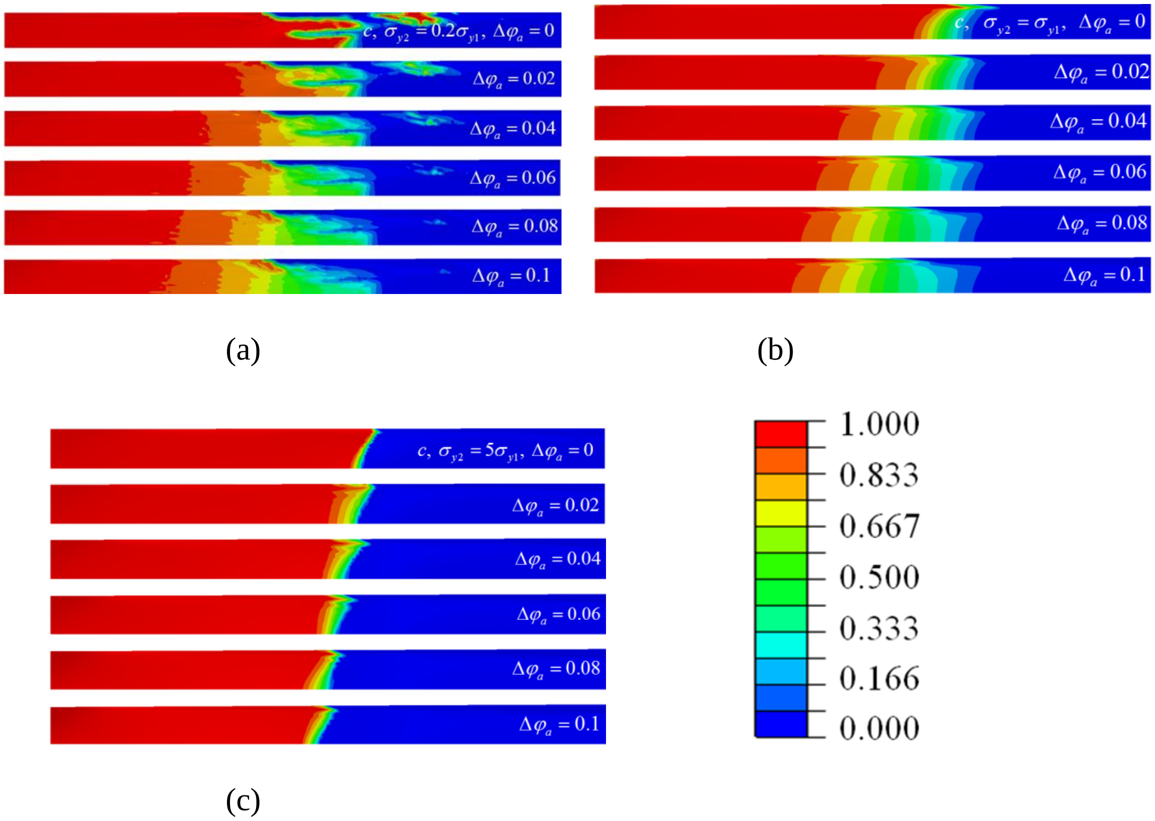

(a) (b)

(c)

FIG. 17. Concentration of high-pressure phase *c*, for $\sigma_{y2}/\sigma_{y1}=$0.2, 1, 5 and *k*= 5. Following by the last step in Fig. 2(b), Fig. 5(b) and Fig. 8(b), respectively, the first bars for (a), (b) and (c) are for the case when the axial force *F* is released to 3.68 at the fixed rotation angle, and the next bars correspond to additional torsion of a diamond anvil at the constant axial force *F*=3.68.

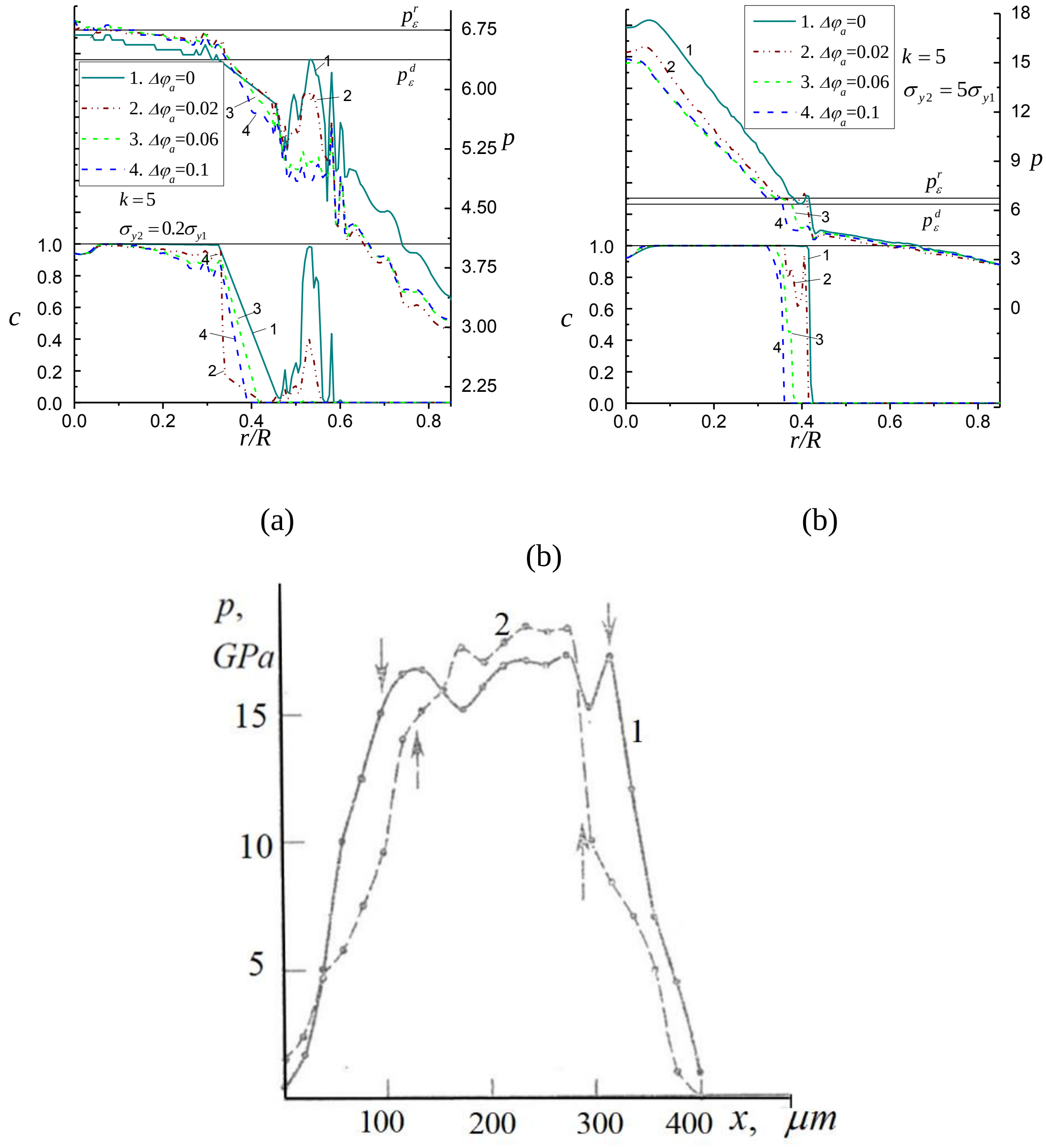

(a) (b)

(b)

(c)

FIG. 18. Distributions of dimensionless pressure p and high-pressure phase concentration c at the contact surface for weaker (a) and stronger (b) high pressure phases, corresponding to reloading process in Figs.17 (a) and (c), respectively. Solid line 1 is for the case after unloading axial force F down to 3.86, without additional rotation, and other lines correspond to increasing additional rotation angle $\Delta\varphi_a$. (c) Experimental distributions of pressure p at the contact surface of the sample for ZnSe [8]. Solid line 1 corresponds to a slight reduction of the axial force and dashed line 2 to further torsion under a constant axial force.

3.6 Concluding remarks

Coupled plastic flow and strain-induced PTs under high pressure and large plastic shear in a sample under various types of loading, unloading, and reloading in a RDAC are studied in detail. FEM and software ABAQUS have been used. The effect of four main parameters in the pressure-dependent, strain-controlled kinetic Eq.(8) is elucidated, which includes: 1) a parameter k which scales the PT rate, 2) the minimum pressure p_{ε}^{d} below which direct strain-induced PT is impossible, 3) the maximum pressure p_{ε}^{r} above which reverse strain-induced PT cannot occur, and 4) the ratio σ_{y2}/σ_{y1} of yield strengths of high and low pressure phases. Multiple nontrivial experimental phenomena are reproduced and interpreted, including pressure self-multiplication and demultiplication effects, small 'steps' on pressure distribution on the contact surface in the two-phase region, simultaneous occurrences of direct and reverse PTs, oscillatory distribution of pressure for weaker high-pressure phase, localization of a weaker high-pressure phase at a contact surface, as well as some types of behaviors under complex loading/unloading/reloading processes. During unloading, unexpected essential plastic flow and reverse PT are revealed, which change interpretation of the experimental results. Obtained results allow better understanding of the experimental phenomena occurring in RDAC, possibility of extracting experimental information from the heterogeneous fields in a sample, and ways of controlling PTs by controlling pressure-plastic strain paths. They also can be utilized for the search of new high pressure phases, ways to reduce pressure for synthesis of high pressure phases and to retain them at ambient pressure. Future work will be directed toward taking into account of contact sliding between sample and diamond, consideration of a sample-gasket system, and combining results of simulations and experiments to determine all parameters and functions for PT and plastic flow in specific materials. Similar numerical approach can be applied to study strain-induced PTs during ball milling [17-20], high pressure torsion [21-23], and other processes. Current FEM approaches to high pressure torsion [37-42], and twist [43] or spiral [44, 45] extrusion consider plastic flow only, while these processing methods are used also [21-23] or can be used for strain-induced PTs.

Acknowledgments

The support of Army Research Office (W911NF-12-1-0340) managed by Dr. David Stepp, Defense Advanced Research Projects Agency (W31P4Q-13-1-0010) managed by Dr. Judah Goldwasser, and Iowa State University is gratefully acknowledged.

References

[1] V.I. Levitas, Phys. Rev. B 70 (2004) 184118.

[2] M.M. Alexandrova, V. D. Blank, S.G. Buga, Solid State Phys. 35 (1993) 1308-1317.

[3] V.D. Blank, Y.Y. Boguslavsky, M.I. Eremets, E.S. Itskevich, Y.S. Konyaev, A.M. Shirokov, E.I. Estrin, Zh. Eksp. Teor. Fiz. 87 (1984) 922-926.

[4] N.V. Novikov, S.B. Polotnyak, L.K. Shvedov, V. I. Levitas, J. of Superhard Mater. 3 (1999) 39-51.

[5] M. Aleksandrova, V.D. Blank, A.E. Golobokov, Yu.S. Konyaev, E.I. Estrin, Solid State Phys. 29 (1987) 2573-2578.

[6] C. Ji, V.I. Levitas, H. Zhu, J. Chaudhuri, A. Marathe, Y.Z. Ma, P. Natl. Acad. Sci. USA 109 (2012) 19108-19112.

[7] V.I. Levitas, O.M. Zarechnyy, J. Phys. Chem. B 110 (2006) 16035-16046.

[8] V.D. Blank, S.G. Buga, Instrum. Exp. Tech. 36 (1993) 149-157.

[9] V.I. Levitas, Y.Z. Ma, E. Selvi, J.Z. Wu, J.A. Patten Phys. Rev. B 85 (2012) 054114.

[10] V. Blank, M. Popov, S. Buga, V. Davydov, V.N. Denisov, A.N. Ivlev, B.N. Mavrin, V. Agafonov, R. Ceolin, H. Szwarc, A. Rassat, Phys. Lett. A 188 (1994) 281-286.

[11] V.I. Levitas, Y.Z. Ma, J. Hashemi, M. Holtz, N. Guven, J. Chem. Phys. 125 (2006) 044507

[12] V.D. Blank, G.A. Dubitsky, High pressure science and technology. In: Proc Joint XV AIRAPT and XXXIII EHPRG International Conf (Warsaw), (ed Trzeciakowski WA.) London: World Scientific Publishing, 1995 pp 325-7.

[13] V.I. Levitas, O.M. Zarechnyy, Phys. Rev. B 82 (2010) 174123.

[14] V.I. Levitas, O.M. Zarechnyy, Phys. Rev. B 82 (2010) 174124.

[15] V.I. Levitas, M. Javanbakht, Phys. Rev. B 86 (2012) 140101(R).

[16] O.M. Zarechnyy, V.I. Levitas, Y.Z. Ma, J. Appl. Phys. 111 (2012) 023518.

[17] F. Delogu, Scripta Mater. 67 (2012) 340-343.

[18] F. Delogu, J. Mater. Sci. 47 (2012) 4757-4762.

[19] C. Suryanarayana, Rev. Adv. Mater. Sci. 18 (2008) 203-211.

[20] L. Takacs, Prog. Mater. Sci. 47 (2002) 355-414.

[21] M. T. Perez-Prado, A.P. Zhilyaev, Phys. Rev. Lett.102 (2009) 175504.

[22] B. Srinivasarao, A. P. Zhilyaev, M.T. Perez-Prado, Scripta Mater. 65 (2011) 241-244.

[23] A.P. Zhilyaev, I. Sabirov, G. Gonzalez-Doncel, J. Molina-Aldareguia, B. Srinivasarao, M.T. Perez-Prado, Mat. Sci. Eng. a-Struct. 528 (2011) 3496-3505.

[24] V.D. Blank, Z.H. Malyushitska, B.A. Kulnitskiy, High. Press. Phys. Eng. 3 (1993) 28.

[25] S.S. Batsanov, N.R. Serebryanaya, V.D. Blank, V.A. Ivdenko, Kristallografiya 40 (1995) 650-655.

[26] V.I. Levitas, Large deformation of materials with complex rheological properties at normal and high Pressure, Nova Science Publishers, Commack, N.Y. 1996. p. 374 p.

[27] N.V. Novikov, V.I. Levitas, S.B. Polotnyak, J. of Superhard Mater. 9 (1987) 1-9.

[28] N.V. Novikov, V.I. Levitas, S.B. Polotnyak, M.M. Potyomkin, Strength Mater. 26 (1994) 294-302.

[29] N.V. Novikov, V.I. Levitas, S.B. Polotnyak, M.M. Potyomkin, High Pressure Res. 8 (1991) 507-509.

[30] V.I. Levitas, O.M. Zarechnyy, High Pressure Res. 30 (2010) 653-669.

[31] B. Feng, O.M. Zarechnyy, V.I. Levitas, J. Appl. Phys. 113 (2013) 173514.

[32] Abaqus V6.11 Abaqus User Subroutines Reference Manual: HETVAL and USDFLD Providence RI, USA: ABAQUS INC 2011.

[33] V.I. Levitas, Y.Z. Ma, J. Hashemi, Appl. Phys. Lett. 86 (2005) 071912.

[34] Y. Gogotsi, V. Domnich, High-pressure surface science and engineering, Institute of Physics Pub, Bristol; Philadelphia, 2004, p. 639 p

[35] V.D. Blank, S.G. Buga, M.Y. Popov, V. A. Davydov, V. Agafonov, New J. Chem. 19 (1995) 149.

[36] Y.Z. Ma, E. Selvi, V.I. Levitas, J. Hashemi, J. Phys.: Con. Matt. 18 (2006) 1075.

[37] R. B. Figueiredo, P. R. Cetlin, T. G. Langdon, Mat. Sci. Eng. a-Struct. 528 (2011) 8198-8204.

[38] R. B. Figueiredo, P. H. R. Pereira, M. T. P. Aguilar, P. R. Cetlin, T. G. Langdon, Acta Mater. 60 (2012) 3190-3198.

[39] H. S. Kim, J. Materi. Process. Tech. 113 (2001) 617-621.

[40] S. C. Yoon, Z. Horita, H. S. Kim, J. Materi. Process. Tech. 201 (2008) 32-36.

[41] H. S. Kim, S. I. Hong, Y. S. Lee, A. A. Dubravina, I. V. Alexandrov, J. Materi. Process. Tech. 142 (2003) 334-337.

[42] D.J. Lee, E.Y. Yoon, S.H. Lee, S.Y. Kang, H. S. Kim, Rev. Adv. Mater. Sci. 31 (2012) 25-30.

[43] M.I. Latypov, I.V. Alexandrov, Y.E. Beygelzimer, S. Lee, H.S. Kim, Comp. Mater. Sci. 60 (2012) 194-200.

[44] A. Farhoumand, S. Khoddam, P.D. Hodgson, Model. Simul. Mater. Sci. Eng. 20 (2012) 085005.

[45] A. Farhoumand, P.D. Hodgson, S. Khoddam, J. Mater. Sci. 48 (2013) 2454-2461.

CHAPTER 4. PLASTIC FLOWS AND PHASE TRANSFORMATIONS IN MATERIALS UNDER COMPRESSION IN DIAMOND ANVIL CELL: EFFECT OF CONTACT SLIDING

Modified from a paper published in Journal of Applied Physics

Biao Feng[1] Valery I. Levitas[2,*] Oleg M. Zarechnyy[1]
1) Department of Aerospace Engineering, Iowa State University, Ames, Iowa 50011, USA

2) Departments of Aerospace Engineering, Mechanical Engineering, and Material Science and Engineering, Iowa State University, Ames, Iowa 50011, USA

Abstract

Modeling of coupled plastic flows and strain-induced phase transformations (PTs) under high pressure in a diamond anvil cell (DAC) is performed with the focus on the effect of the contact sliding between sample and anvils. Finite element software ABAQUS is utilized and a combination of Coulomb friction and plastic friction is considered. Results are obtained for PTs to weaker, equal-strength, and stronger high pressure phases, using different scaling parameters in a strain-controlled kinetic equation, and with various friction coefficients. Compared to the model with cohesion, artificial shear banding near the constant surface is eliminated. Sliding and the reduction in friction coefficient intensify radial plastic flow in the entire sample (excluding a narrow region near the contact surface) and a reduction in thickness. A reduction in the friction coefficient to 0.1 intensifies sliding and increases pressure in the central region. Increases in both plastic strain and pressure lead to intensification of strain-induced PT. The effect

---

[*] Corresponding author.
Email: vlevitas@iastate.edu

of self-locking of sliding is revealed. Multiple experimental phenomena are reproduced and interpreted. Thus, plastic flow and PT can be controlled by controlling friction.

4.1 Introduction

The majority of studies of material behavior and PTs under high static pressure are performed in a DAC. A DAC allows an *in-situ* study of PTs under high pressure using advanced diagnostics such as optical, Raman, and X-ray techniques[1-4]. Pressure-induced PTs are usually studied within a hydrostatic media. In contrast, strain-induced PTs under high pressure are studied without hydrostatic media, by superposing large plastic shear deformations in a rotational DAC[5-12]. They may occur under much lower pressure and sometimes lead to new phases that could not be obtained under hydrostatic conditions. While pressure-induced PTs start by nucleation at pre-existing defects (pressure and stress concentrators), strain-induced PTs occur by nucleation at new defects that are continuously generated during the plastic flow[13]. Quite often, especially at very high pressures, PTs under compression in a traditional DAC are studied without hydrostatic media in the process of large plastic deformations due to a reduction of the sample thickness. As stated in Ref. 10, such PTs should also be considered as strain-induced rather than pressure-induced PTs. This is not just a terminological difference, as strain-induced PTs occur by a different mechanism and require completely different thermodynamic and kinetic descriptions, as well as an interpretation of experimental phenomena. A multiscale theory[10] for high-pressure mechanochemistry was proposed, in which strain-induced PTs could be characterized by a strain-controlled (rather than time-controlled), pressure-dependent kinetic equation (see Eq. (8)). The only difference between PTs under compression and shear in a rotational DAC and compression in a traditional DAC is the pressure-plastic strain trajectory for each material point of the sample[10, 14-16]. Due to highly heterogeneous fields of stresses and strains and complex distributions on phases, the pressure and concentration of high pressure phases along the radius of the sample on a contact surface are experimentally available only[11]. As a result, theoretical and finite-element methods have been developed and applied for investigation of the evolution of stresses, strains, and concentration of phases in the entire sample during plastic flow and PTs with the growth of external force[10, 14, 15, 17, 18]. It is a coupled problem of mechanics and PT with a large deformation, which thus leads to high complexity in simulations using FEM software.

It is necessary to note that without PTs (and, in some cases, with PTs; see Refs. 10, 15), pressure p distribution within a sample along the radius r is determined by a simplified equilibrium equation $\frac{dp}{dr}=\frac{2\tau_{zr}^{c}}{h}$, where τ_{zr}^{c} is the radial frictional shear stress at the contact surface with an anvil, and h is the current thickness of the sample. Without friction, pressure is constant along the radius and there is no way to increase it to high value, namely above material hardness. In contrast, if the maximum possible friction stress is equal to the yield strength in shear τ_y and there is a large ratio of the sample radius R to the thickness, then pressure grows linearly from the periphery to the center and can reach several megabars in magnitude. Thus, *the entire field of high pressure physics and material science is based on the ability to create frictional resistance to the radial plastic flow in the thin sample* during its compression.

At the same time, though the first numerical results[15-19] were successful in interpreting multiple experimental phenomena, the simplest model was considered based on a strong assumption: there is no slipping on the contact surface between the sample and the diamond anvil. As a result, a real large-sliding contact problem was degraded into a problem under zero displacements along the boundary. Further, such a complete cohesion assumption on the contact surface leads to two major drawbacks. First, because material flows to the periphery during large compression but the tangent displacement at the contact surface is specified as zero, there is an unrealistic shear band at the periphery ($r/R > 0.6$ in Fig. 1(a)) within one finite element layer, i.e., it is mesh-dependent. Second, a very large plastic strain appears at the conical surface (see surface *AB* in Fig. 1(d)), which is unrealistic because the pressure and shear friction stress are very low, especially in the neighborhood of the point *B*.

To resolve the problems mentioned above, a large-sliding contact model based on a combination of classical isotropic Coulomb friction and plastic friction is utilized within ABAQUS code[20]. Thus, in addition to physical nonlinearities due to plasticity and PTs, and geometric nonlinearities due to large strains and rotations, contact nonlinearities are included, making the problem very sophisticated. The results obtained in this paper are compared with those for a no-slipping model, and the effects of the coefficient of friction on PTs and plastic flow are elucidated.

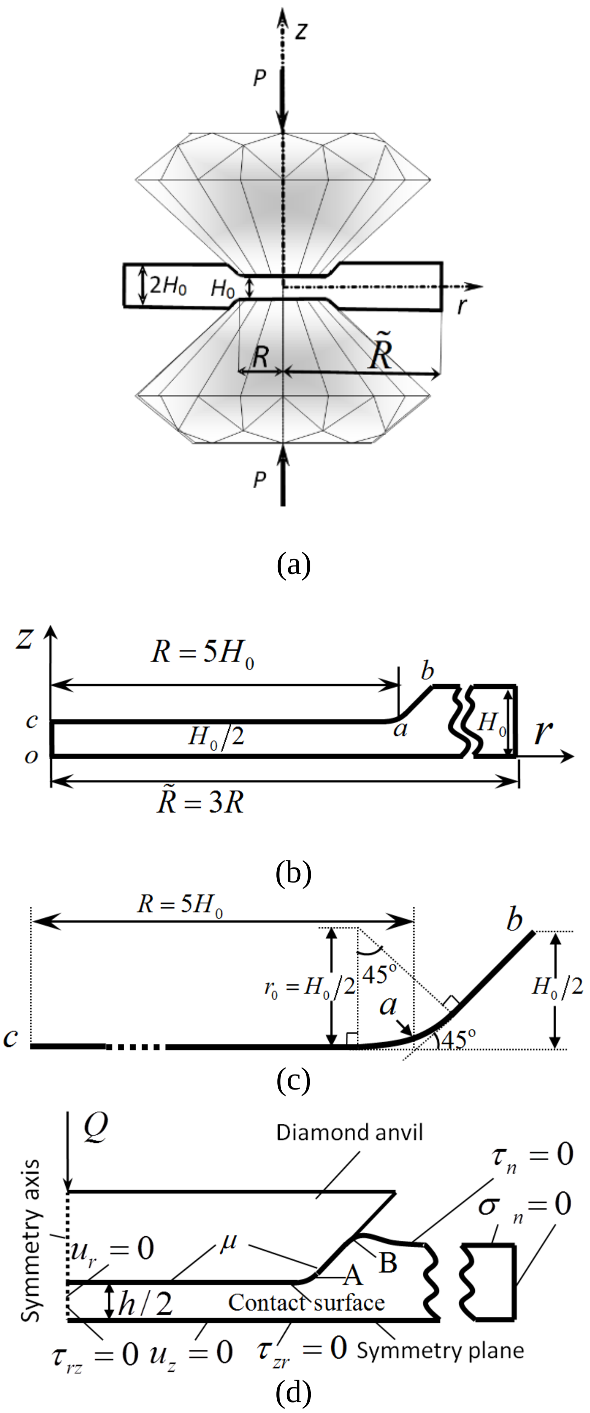

FIG. 1. (a) Diamond anvil cell scheme, (b) a quarter of a sample in the initial undeformed state, (c) geometries of contact surface in the undeformed state, and (d) boundary conditions.

4.2 Problem formulation

Geometry and boundary conditions. A large-sliding contact problem coupled with strain-induced PTs and plastic flow, in a sample of radius $\tilde{R}$ between two rigid diamond anvils under a rising axial compressive force *P*, is investigated in this paper by using the finite element software ABAQUS. A similar geometric model and the same physical equations for PTs as in Refs.15, 18 were utilized. Due to symmetries of geometry and load, a quarter of a sample is considered in the cylindrical coordinate system $rz\theta$ (see the undeformed configuration in Fig. 1(b) and the deformed one in Fig. 1(d)). The boundary conditions for the DAC are shown in Fig. 1(d). The contact algorithm in ABAQUS requires the master surface of a contact interaction (herein referring to the surface of the diamond anvil) to be smooth and therefore a small fillet radius $r_0 = H_0/2$ is utilized to smooth the sharp corners of the diamond and the sample (See Fig. 1(c)).

Material model. To obtain generic solutions, the simplest isotropic, perfectly plastic model for the sample found in Refs. 15, 18 is assumed. The applicability of the perfectly plastic and isotropic model with the yield strength independent of the deformation history for monotonous loading is justified in Ref. 21 for various classes of materials (rocks, metals, powders, etc.) starting with accumulated plastic strains q>0.6÷1. Compressive normal strains, stresses, and pressure will be considered positive. A complete system of equations for the coupled plastic flow and the strain-induced PT is enumerated below.

The deformation rate $\mathbf{d}$ is decomposed into elastic, plastic, and transformational parts:

$$\mathbf{d} = \overset{\nabla}{\boldsymbol{\varepsilon}}_e + \dot{\varepsilon}_t \mathbf{I} + \mathbf{d}_p \, . \qquad (1)$$

Transformation volumetric strain:

$$\varepsilon_t = \bar{\varepsilon}_t c\,. \tag{2}$$

Hooke's law for pressure p and deviatoric stress part $\mathbf{s} = dev\mathbf{T}$ of the true stress tensor $\mathbf{T}$ yields:

$$p = K\varepsilon_{e0}\,; \qquad \mathbf{s} = 2G\, dev\boldsymbol{\varepsilon}_e\,. \tag{3}$$

Von Mises yield condition for two-phase mixture:

$$\sigma_i = \left(\frac{3}{2}\mathbf{s}:\mathbf{s}\right)^{0.5} \le \sigma_y(c) = (1-c)\sigma_{y1} + c\sigma_{y2}\,. \tag{4}$$

Plastic flow rule in the elastic region:

$$\sigma_i < \sigma_y(c) \qquad \rightarrow \qquad \mathbf{d}_p = 0\,. \tag{5}$$

in the plastic region:

$$\sigma_i = \sigma_y(c) \qquad \rightarrow \qquad \mathbf{d}_p = \lambda\mathbf{s}\,; \qquad \lambda \ge 0\ . \tag{6}$$

Equilibrium equation:

$$\nabla \cdot \mathbf{T} = 0. \tag{7}$$

Strain-controlled kinetics for plastic strain-induced PT[10]:

$$\frac{dc}{dq} = 10k\,\frac{(1-c)\bar{p}_d H(\bar{p}_d)\dfrac{\sigma_{y2}}{\sigma_{y1}} - c\bar{p}_r H(\bar{p}_r)}{c + (1-c)\sigma_{y2}/\sigma_{y1}}\ . \tag{8}$$

Here elastic, transformational, and plastic components are distinguished by subscripts e, t, and p respectively; $\bar{p}_d = \dfrac{p - p_\varepsilon^d}{p_h^d - p_\varepsilon^d}$ and $\bar{p}_r = \dfrac{p - p_\varepsilon^r}{p_h^r - p_\varepsilon^r}$ are dimensionless characteristic pressures for direct and reverse PT; p_h^d and p_h^r are the pressures for direct and reverse PTs under hydrostatic loading, respectively; p_ε^d is the minimum pressure below which direct strain-induced PT to high pressure phase does not take place; p_ε^r is the maximum pressure above which reverse strain-induced PT to low pressure phase cannot occur; q is the accumulated plastic strain defined from $\dot{q} = (2/3\mathbf{d}_p : \mathbf{d}_p)^{1/2}$; $\mathbf{I}$ is the second-rank unit tensor; $\overset{\nabla}{\varepsilon}_e$ and $\overset{\nabla}{\mathbf{s}}$ is the objective Jaumann time derivative of the elastic strain and deviatoric stress; ε_{e0} and $\bar{\varepsilon}_t$ are the elastic and transformation volumetric strains for complete PT, respectively; H is the Heaviside step function; G and K are the shear and bulk moduli, respectively; σ_i is the stress intensity or effective stress; λ is a parameter that is determined by iterative satisfaction of the yield condition; k is the kinetic parameter which scales the rate of PTs.

Eq. (8) is derived in Ref. 10 as a coarse grained microscale model based on barrierless nucleation on defects (e.g., dislocation pile ups) generated during plastic flow. Since stress concentration near the tip of the defect sharply reduces away from the defect, the nucleus reaches thermodynamic equilibrium and does not grow further. That is why (and because of barrierless nucleation) time is not a parameter and accumulated plastic strain q is a time-like parameter. In a two-phase mixture plastic strain is localized in the phase with the smaller yield strength; this is the reason for appearance of the ratio of the yield strengths of phases in Eq. (8).

Friction model. The standard Coulomb friction suggests that no relative motion on a contact surface occurs if the friction stress τ is less than the critical friction stress $\tau_{crit} = \mu\sigma_n$, where σ_n is the normal to the contact surface stress, μ is the coefficient of friction that can be defined as a function of the contact normal stress, σ_n; the slip rate $\dot{u}_c$; the surface temperature and other field variables at the contact point. In this paper, the simplest case $\mu =$ constant is considered. While for elastic materials standard Coulomb friction is suitable, for elastoplastic materials the friction shear stress τ cannot exceed the yield strength in shear $\tau_y = \sigma_y / \sqrt{3}$ (von Mises yield condition (4) has been utilized). Thus, relative slip on a contact surface also occurs even though $\tau_{crit} < \mu\sigma_n$ and the critical friction stress is redefined as $\tau_{crit} = \min(\mu\sigma_n, \tau_y)$. During PTs, yield strength τ_y is not constant but depends on concentrations and yield strengths of phases. This is implied in Eq. (4) for the two-phase mixture $\tau_y = (1-c)\tau_{y1} + c\tau_{y2}$, where τ_{y1} and τ_{y2} are the yield shear strength of the low- and high-pressure phases, respectively.

In the classic version of the Coulomb friction there is no relative motion if friction stress $\tau < \tau_{crit}$. However, during actual simulations, a jump between a slip and cohesion conditions may induce a serious convergence problem in ABAQUS, especially for the large-sliding contact problem. Consequently, to regularize the problem, the cohesion condition is replaced by an elastic reversible tangential small slip u_e. Both elastic slip and elastic deformation are reversible during the loading and unloading process. While we use elastic slip as a mathematical regularization method, it can be physically interpreted as elastic deformation of a thin contact layer (asperities); then sliding corresponds to plastic flow in the contact layer or cutting asperities. For an accurate solution, the elastic slip should be constrained in the small range, for example, the specified maximum elastic relative slip u_{crit} equals 0.5% of the average element length for fine-meshing models.

One can relate the elastic slip to the frictional shear stress by the simplest linear relation $\tau = k_s u_e$, where k_s is the contact stiffness. We will define the contact stiffness from the condition that sliding starts at the prescribed critical values u_{crit}. Then one has $\tau_{crit} = k_s u_{crit}$ and $k_s = \tau_{crit} / u_{crit}$; consequently, k_s varies with the normal stress σ_n or the yield shear strength τ_y. Thus, the following complete system of equations will be used. It is in some extent similar to that for elastoplasticity theory.

Decomposition of total contact relative displacement into elastic and sliding parts:

$$u_c = u_e + u_s . \tag{9}$$

Yield strength in shear:

$$\tau_y(c) = \left(1-c\right)\tau_{y1} + c\tau_{y2} . \tag{10}$$

Critical friction stress

$$\tau_{crit} = \min(\mu\sigma_n ,\ \tau_y(c)) . \tag{11}$$

Rule for elastic contact displacement:

$$\begin{cases} \tau = \left[\left(1-c\right)\tau_{y1} + c\tau_{y2}\right]\dfrac{u_e}{u_{crit}} & if \quad \mu\sigma_n > \tau_y(c) \\ \tau = \mu\sigma_n \dfrac{u_e}{u_{crit}} & if \quad \mu\sigma_n \le \tau_y(c) \end{cases} \tag{12}$$

Sliding rule below critical friction stress:

$$|\,\tau\,| < \tau_{crit} \quad \to \quad \dot{u}_s = 0 . \tag{13}$$

Sliding rule at critical friction stress:

$$\begin{cases} \tau = \pm\left[\left(1-c\right)\tau_{y1} + c\tau_{y2}\right] & if \quad \mu\sigma_n > \tau_y \\ \tau = \pm\ \mu\sigma_n & if \quad \mu\sigma_n \le \tau_y \end{cases} \to \qquad Sign(\dot{u}_s) = Sign(\tau) \tag{14}$$

In Eq. (14), the signs of $\dot{u}_s$ and contact shear stress τ are the same, while the magnitude $\dot{u}_s$ is determined from the satisfaction of the sliding condition $|\,\tau\,| = \tau_{crit}$. Note that the numerical algorithm includes a possibility of elastic contact unloading even if Eq.

(14) is satisfied at the beginning of the loading step. Thus, if signs of $\dot{u}_c = \dot{u}_e + \dot{u}_s$ and τ are opposite for some incremental step, even though $\tau = \pm\left[\left(1-c\right)\tau_{y1} + c\tau_{y2}\right]$ at the beginning of this increment step, the governing equations (12) and (13) rather than Eq. (14) should be used in this step.

Numerical procedure. To consider the coupled mechanics and PT problem, the ABAQUS user subroutines^{20} USDFLD and HETVAL are implemented, in which transformation strain is modeled by the thermal strain and concentration *c* is treated as temperature.

For a contact problem, once $\tau_{y1} \neq \tau_{y2}$, the user subroutine FRIC in ABAQUS was implemented to define the critical friction stress. For constant shear yield strength$\left(\tau_{y1} = \tau_{y2}\right)$, one can also use standard procedure without subroutine FRIC, which was utilized to confirm the consistency of programming FRIC and standard procedure.

In the dimensionless form, except for friction stresses τ which are normalized by the yield strength in shear τ_{y1}, all stress-related parameters (e.g., pressure *p*) are normalized by σ_{y1}; the dimensionless force F is the axial force *P* normalized by the product of σ_{y1} and the undeformed contact area (which is equal to the area of the surface of revolution produced by complete revolution of the curve bac in Fig. 1(b) about the *z*-axis). To compare to the case with cohesion, material parameters are chosen to be the same as in the Ref. 18: $p_\varepsilon^d = 6.75$, $p_\varepsilon^r = 6.375$, $p_h^d = 11.25$, $p_h^r = 1.875$, Young modulus $E = 162.5$, Poisson's ratio $v = 0.3$, and volumetric transformation strain for direct PT $\bar{\varepsilon}_t = -0.1$. Since $p_\varepsilon^d > p_\varepsilon^r$, strain-induced PTs are impossible in the pressure range $p_\varepsilon^r < p < p_\varepsilon^d$ (see Ref. 10).

4.3 Study of coupled plastic flow and phase transformations

We will discuss strain-induced PTs at rising axial compressive force *F* for weaker, equal-strength, and stronger high-pressure phases in the large-sliding contact model respectively. In this section friction coefficient $\mu = 0.3$ is assumed for all problems. Current results will be also compared with those for no-slipping models in Ref. 18, and effects of the friction coefficient on PTs and plastic flow will be discussed in the next section.

Weaker high-pressure phase

With the increase of an axial compressive force *F*, when the minimum pressure p_{ε}^{d} for direct PTs is exceeded the high-pressure phase first appears and grows in the center of the sample $\left(r = z = 0\right)$ (see Fig. 2(a) and (b)). In Fig. 2(c) the high-pressure phase also nucleates at the center but then shifts towards the contact surface. Compared to the results of the case with cohesion in Ref. 18 there are three salient differences in our current results. First, the rate of PT with respect to change of load is higher. Without fixing displacements at the contact surface along the radial direction, there is a faster thickness reduction which causes a larger accumulation of plastic strain and increment of concentration of the high pressure phase. Second, the geometry of PT zones significantly differs from that in Ref. 18. For example, there is a high pressure phase at the center of the sample for *k*=5 and 10 and there is no PT at the center at the initial stages of loading for *k*=30, opposite to the results in Ref. 18. Third, localization of plastic strain and PT due to strain softening appears in a thin band for both cases. Without sliding[18], material flow towards the periphery in the sample, on the other hand a lack of radial motion at the contact surface will create a shear band located near the contact surface. This leads to a very large plastic strain on the contact surface and the promotion of PT. In the current model with contact sliding, plastic strain near the contact surface as well as the concentration of high pressure phase are reduced.

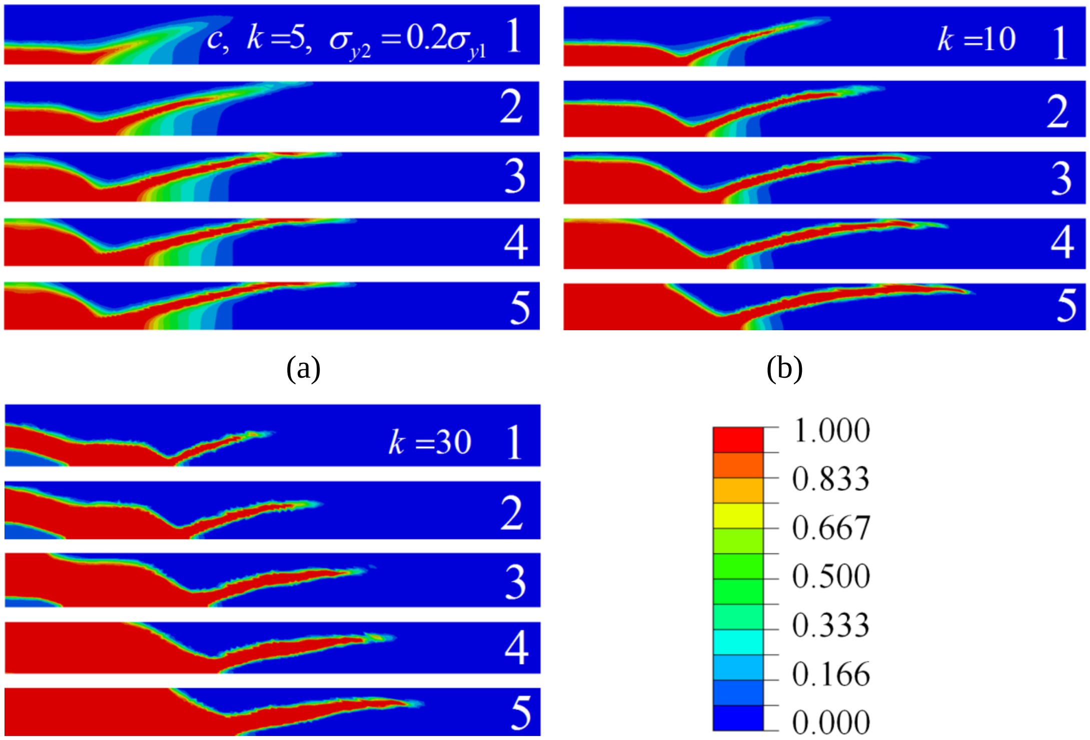

(a)

(b)

(c)

FIG. 2. Concentration of high pressure phase c under compression for (a) k=5, (b) k=10, and (c) k=30; $\sigma_{y2}=0.2\sigma_{y1}$ and $r/R \leq 0.72$ in Fig.1 (b). The dimensionless axial force F is (1) 4.0, (2) 4.2, (3) 4.4, (4) 4.5, (5) 4.66.

It is worth mentioning that PT from semiconducting Si I to weaker metallic Si II under compression in a DAC was observed experimentally[13] in a thin contact layer only but not in the bulk. Our results in Fig. 2(a) and (b) slightly away from the center also demonstrate PT predominantly near the contact surface only. This coincidence also confirms that the possibility of strain-induced (rather than pressure- or stress-induced) PT under high pressure. Indeed, stress intensity is constant in the entire sample. Pressure varies slightly along the thickness, but PT occurs where plastic strain is concentrated.

Such a PT in a thin surface layer could be observed using Raman method, while X-ray diffraction patterns, which are averaged over the sample thickness, may not detect it. Distributions of accumulated plastic strain q, pressure p and high-pressure phase concentration c on a contact surface are shown in Fig. 3. Oscillations in pressure and plastic strain are observed, being caused by material instabilities due to softening during PTs. However, they are much less pronounced than in the case with cohesion in Ref. 18 and oscillations in concentration are absent here completely. This is due to suppressed shear and the PT banding at the contact surface because of relative sliding of the material with respect to an anvil. Consistent to experimental results for ZnSe in Ref. 22, pressure for k=5 in Fig 3(a) first linearly increases from the periphery to the center followed by a drop, and then continues to increase until it reaches the center of a sample. One could note that pressure drops at one of the two-phase boundaries to the value which corresponds to the minimum pressure p_ε^d for direct strain-induced PTs. This could be utilized for experimental evaluation for the value of p_ε^d. However, at two other phase boundaries pressure is above p_ε^d. It should be mentioned that for k=5, although pressure is larger than p_ε^d in the region $0.12 < r/R < 0.32$, PTs do not occur because of very low plastic strain. In addition, when the tip of the PT band, clamped by stronger low-pressure phases, reaches the contact surface then strain localization will exist there and is shown on Fig. 3 (a). For k =30, pressure also linearly grows initially from the periphery to the center. For F=4.2, pressure curve has a plateau at the center with some oscillations in the range $p_\varepsilon^r < p < p_\varepsilon^d$, which is caused by low friction stress in this region. With increasing load, pressure and concentration c grow in the central region. Such a stress distribution was observed for PT in CuI in Ref. 5.

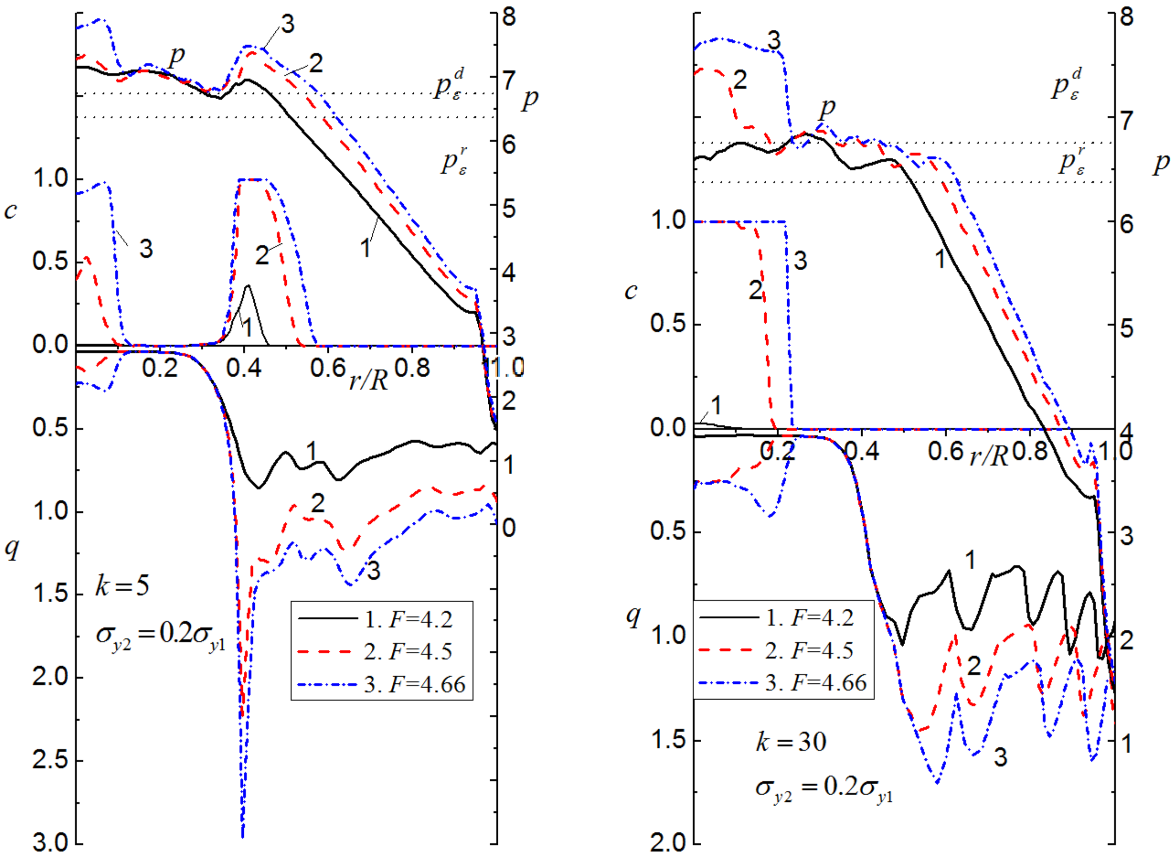

(a)

(b)

FIG. 3. Distributions of accumulated plastic strain q, pressure p, and high-pressure phase concentration c on the contact surface, for (a) k=5 and (b) k=30 and $\sigma_{y2}=0.2\sigma_{y1}$. The dimensionless axial force F is (1) 4.2, (2) 4.5, (3) 4.66.

Due to symmetry about the z-axis friction shear stress τ equals zero at the center. Due to compression, material flows from the center towards the periphery, and friction shear stress reaches its maximum value τ_{y1} at the periphery. From Fig. 4, there is a large oscillation in friction shear stress, especially for k=5 where a softer high-pressure phase arrives at the contact surface and is clamped by a harder low-pressure phase. Drops in friction shear stresses were found in the two-phase region, which are caused by the volume reduction during PTs. Under an increase in loading conditions, these drops move towards the periphery due to the propagation of the PTs to the periphery.

It is necessary to mention that the rate of decreasing of pressure in Fig. 3 suddenly changes at $r/R \approx 0.96$, which is caused by change of geometry from plane to curved surface (See Fig. 1(c)). The fast decrease of pressure in the region $r/R \approx 1$ leads to $up < \tau_{y1}$ and further to a sudden drop of friction stress in Fig. 4. Due to changes of geometry at $r/R \approx 0.96$, this induced features of pressure and friction stress is applicative for equal-strength and stronger high pressures, which will be shown in plots of pressure and friction stress in the following sections.

Fig. 5 exhibits the dimensionless accumulated relative slipping displacement of the sample with respect to the diamond on the contact surface. Large sliding is mostly localized in the periphery $r/R > 0.42$, where friction stress reached the yield strength (see Fig. 4 at *F*=4.0). It is clear from Fig. 5(b) that during an increase in load *F* from 4.2 to 4.66, there is no further slip in the region $0.42 < r/R < 0.52$, because friction stress reduces to a value lower than critical friction stress. However, there is still a slip in the region $0.4 < r/R < 0.5$ for k=5 despite the small shear stress (see in Fig. 4(a)) because the weaker high pressure phase reaches the contact surface (see Fig. 3(a)) and therefore critical friction stress also becomes small.

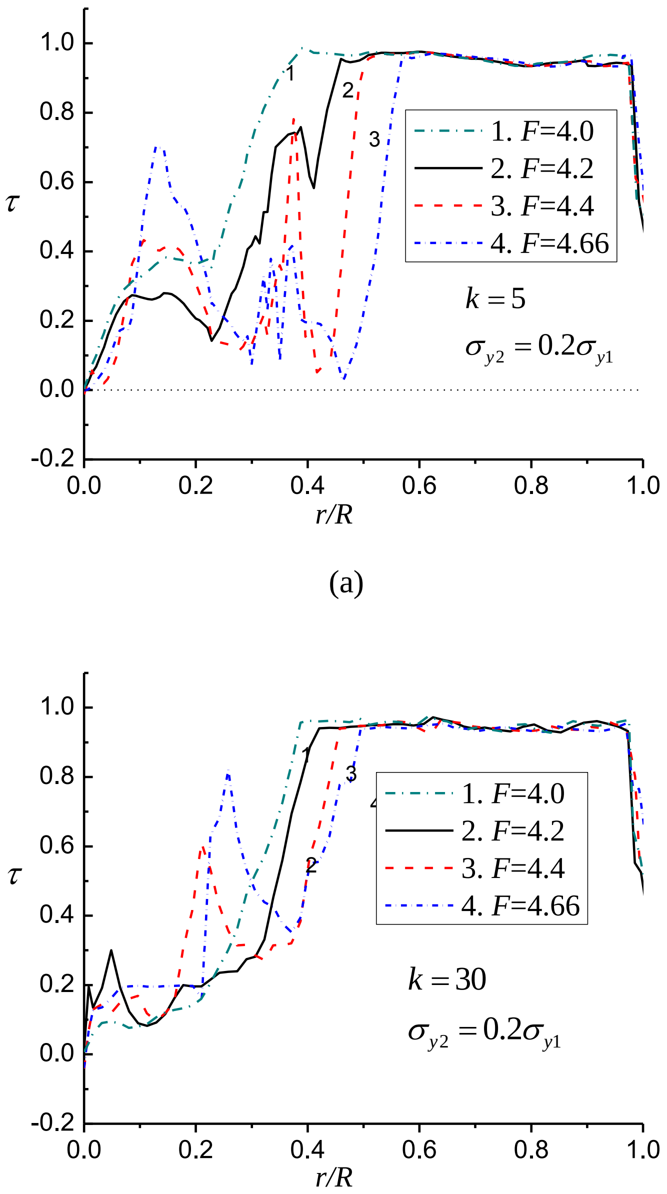

(a)

(b)

FIG. 4. Distribution of dimensionless friction shear stress τ normalized by τ_y on the contact surface, for (a) *k*=5 and (b) *k*=30, and $\sigma_{y2} = 0.2\sigma_{y1}$. The dimensionless axial force F is (1) 4.0, (2) 4.2, (3) 4.4 (4) 4.66.

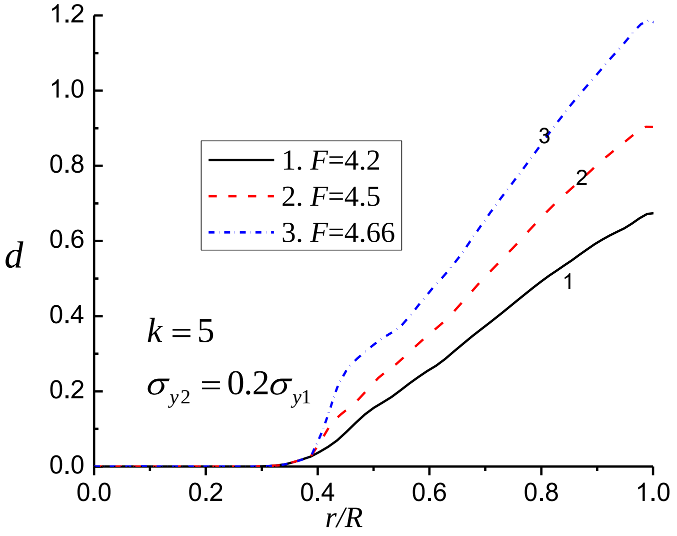

(a)

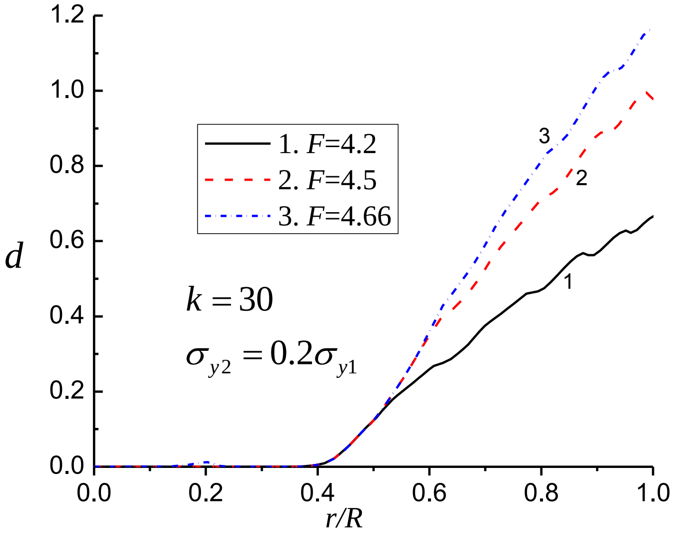

(b)

FIG. 5. Distribution of dimensionless accumulated relative slipping displacement $d = 2u_c / H_0$ on contact surface normalized by half of thickness of a sample, $H_0/2$, for (a) *k*=5 and (b) *k*=30, and $\sigma_{y2} = 0.2\sigma_{y1}$. The dimensionless axial force F is (1) 4.2, (2) 4.5, (3) 4.66.

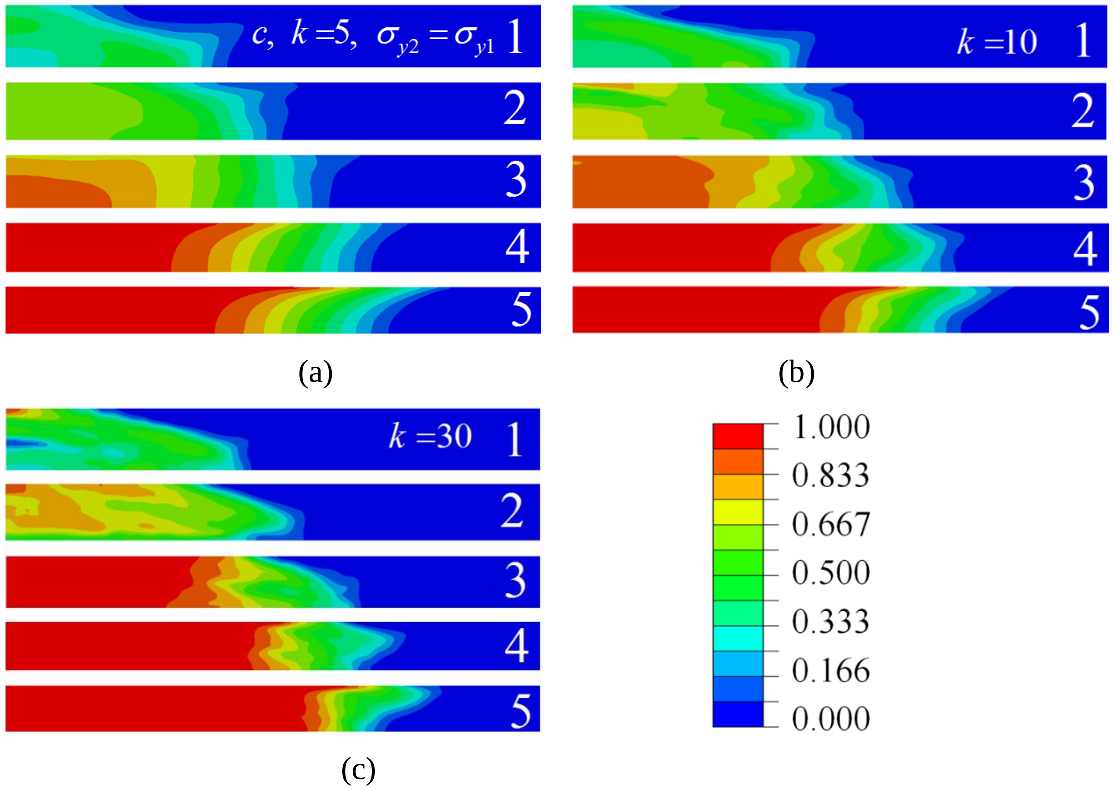

(a) (b)

(c)

FIG. 6. Concentration of high-pressure phase c under compression for (a) k=5, (b) k=10, and (c) k=30, and $\sigma_{y2}=\sigma_{y1}$. The dimensionless axial force F is (1) 4.0, (2) 4. 3, (3) 4.6, (4) 4.9, (5) 5.13

Equal strength of phases

In contrast to the case for weaker product phase $\left(\sigma_{y2}=0.2\sigma_{y1}\right)$, the obvious localizations of strain and PTs disappear for an equal strength of phases $\left(\sigma_{y2}=\sigma_{y1}\right)$ because of the absence of material softening during PTs. Fig. 6 shows that the thickness of a sample significantly decreases during rising axial force. There is a wider two-phase region compared to the weaker high-pressure phase, and with the growth of kinetic parameter k, the rate of PTs increases at the initial stages of compression. For a large force, the effect of k is less pronounced because the entire central part of the sample is completely transformed. Fig. 7 exhibits the distributions of pressure p and high-pressure phase concentration c on the contact surface under rising axial force. When PT starts in the center of a sample, pressure in the central region is almost constant because of low friction. At the initial stage of compression, PT occurs in the center of the sample and leads to a reduction in volume which counteracts the increase of pressure due to rising loading. Therefore, pressure increases slowly in the central region. In particular, for F=4.3 in Fig. 7, pressure in the center slightly reduces with the growth of the kinetic parameter k, because PT increases in the center with rising k. However, at the later stage of compression PT almost completes in the center. There is no volumetric reduction due to PT and pressure increases quickly during a rise in axial force F due to increased radial flow and shear frictional stresses (see Fig. 8). Small steps (plateaus) with almost constant pressure value were observed in experiments[6-8, 22] for KCl and fullerene at the very heterogeneous pressure distribution. With the growth of the kinetic parameter k, these small pressure steps in the two-phase region gradually become obvious. They are located in the two-phase region and are clearly visible for k=30. With the rising axial force F and a continuous movement of the position of this “step” towards the periphery, the pressure value at the step almost does not change and is around the minimum pressure for direct PT p_{ε}^{d} (Fig 7(c)). This result could be used for the evaluation of the value p_{ε}^{d} in experiments. Since such steps are not evident for smaller values of k, one can conclude that k is at least greater than 10 for KCl and fullerene.

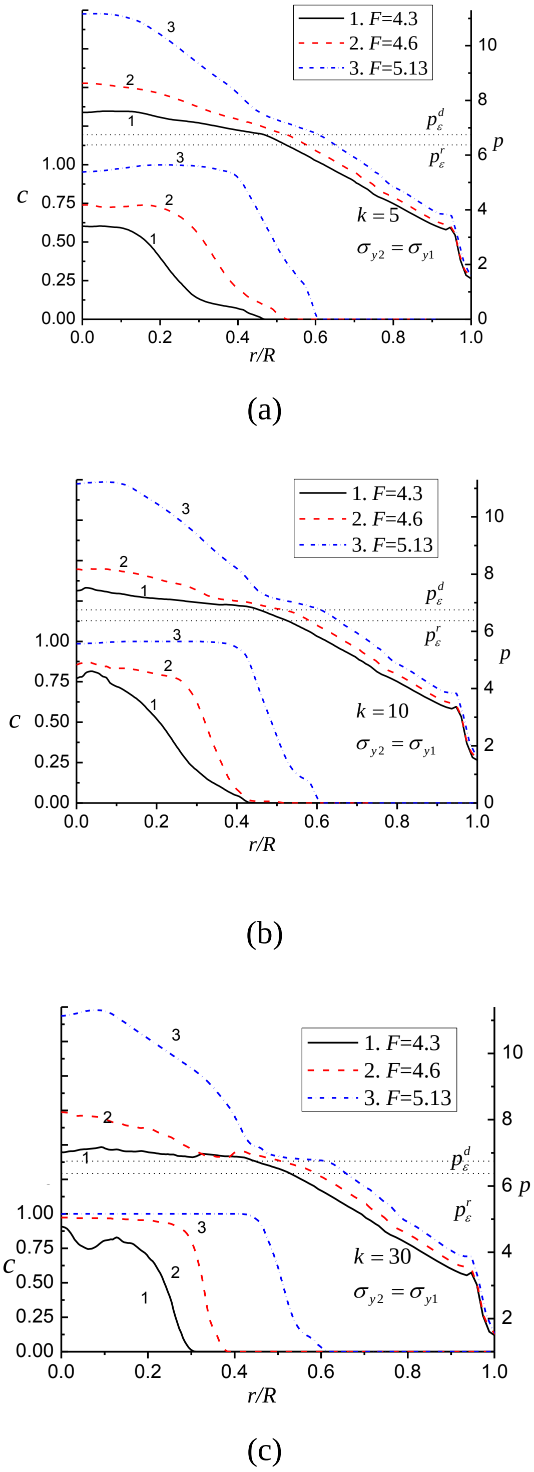

FIG. 7. Distributions of dimensionless pressure p and high-pressure phase concentration c on a contact surface, for (a) k=5, (b) k=10, and (c) k=30, and $\sigma_{y2} = \sigma_{y1}$. The dimensionless axial force F is (1) 4.3, (2) 4.6, (3) 5.13.

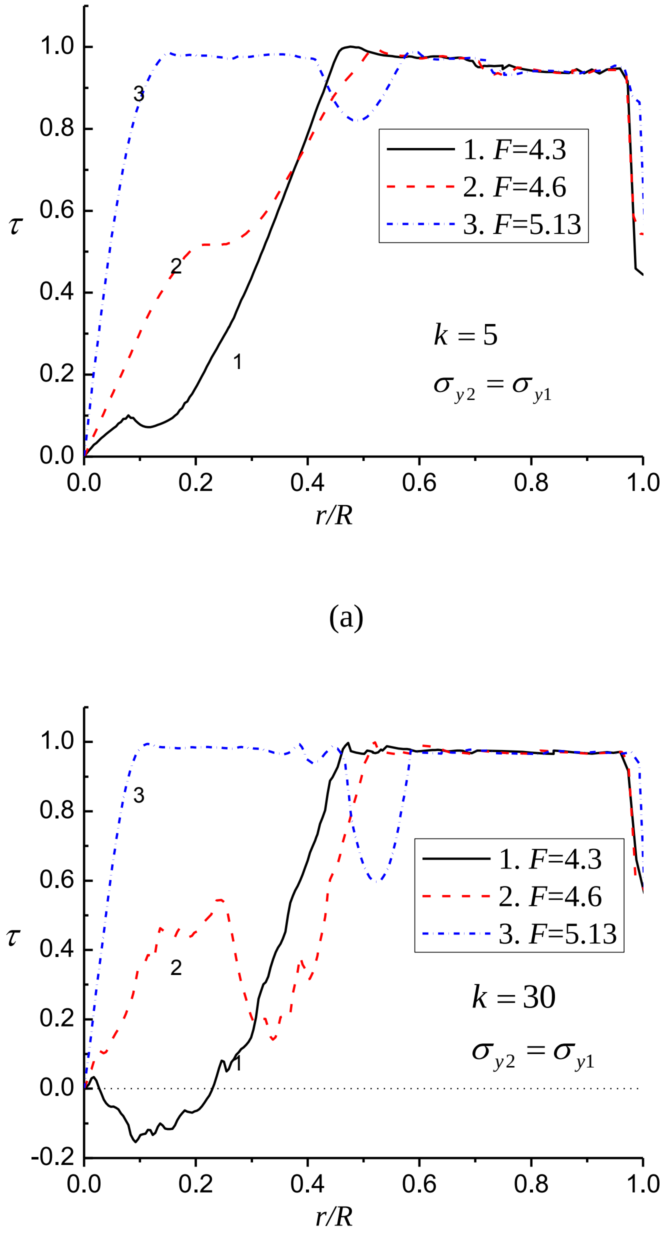

(a)

(b)

FIG. 8. Distribution of dimensionless friction shear stress τ normalized by τ_y on contact surface, for (a) *k*=5 and (b) *k*=30, and $\sigma_{y2}=\sigma_{y1}$. The dimensionless axial force F is (1) 4.3, (2) 4.6, (3) 5.13.

Fig. 8 shows the distribution of friction shear stresses at the contact surface. During compression material flows from the center to the periphery, and friction stress is zero at the axis of symmetry and reaches its maximum value, equal to the yield strength in shear τ_y, at the periphery. There is a drop in friction stresses located in the two-phase region where PT occurs, which is related to the volume reduction during the PT and less intense radial flow. In particular, PT at *F*=4.3 is much faster for *k*=30 than for *k*=5 (see Fig. 6). Therefore the drop in shear stress for *k*=30 is much larger and the value changes the sign in the PT region. Fig. 9 exhibits the dimensionless accumulated relative slipping displacement $d = 2u_c / H_0$ on the contact surface normalized by half of the sample thickness, $H_0/2$. Slipping mostly occurs at the periphery $r/R > 0.42$ and with growth of radial coordinate *r*, the sliding displacement becomes larger. It should be mentioned that in the region $0.42 < r/R < 0.52$ slipping distance does not change during rising axial force because friction stress τ reduces and becomes smaller than critical friction stress τ_{crit} due to PTs (see in Fig. 8). Even though shear stress τ attains the τ_{crit} in the region $0.1 < r/R < 0.37$ at *F*=5.13, slipping either does not occur for *k*= 5 or is very small for *k*=30 as there is no slipping on both the left and right sides of this region and the material becomes locked. In addition, slipping displacement *d* does not change obviously with the growth of *k*. This is because the PT does not essentially affect processes at the periphery and mostly occurs in the region where the sliding is locked.

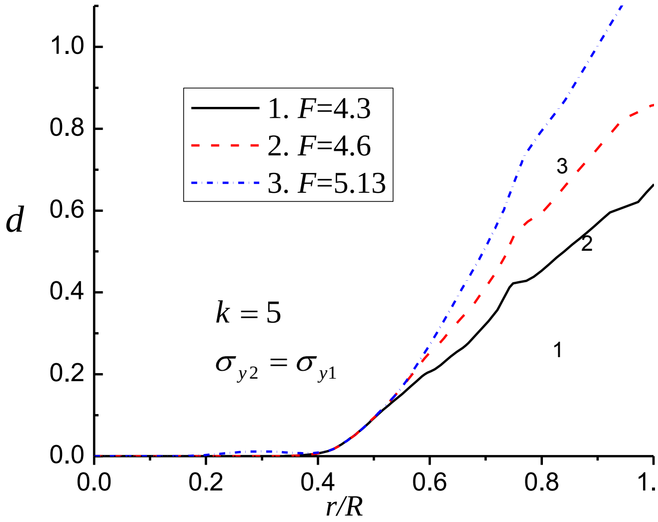

(a)

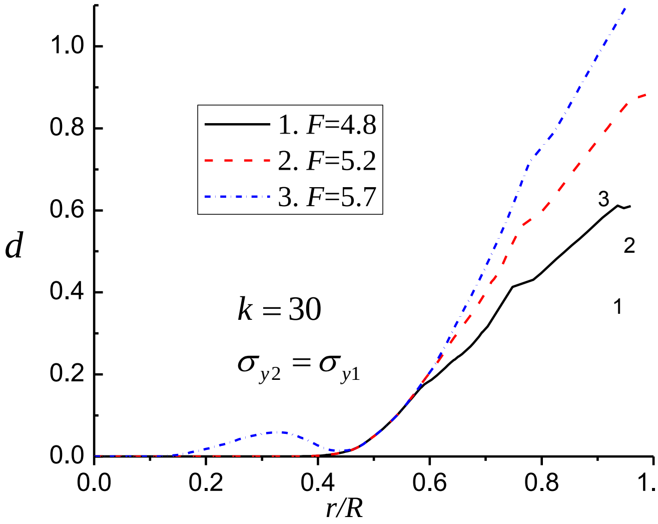

(b)

FIG. 9. Distribution of dimensionless accumulated relative slipping displacement $d = 2u_c / H_0$ on the contact surface, for (a) k=5 and (b) k=30, and $\sigma_{y2} = \sigma_{y1}$. The dimensionless axial force F is (1) 4.3, (2) 4.6, (3) 5.13.

Stronger high-pressure phase

For the case of $\sigma_{y2} = 5\sigma_{y1}$, the evolution of pressure and concentration is qualitatively similar to those for which $\sigma_{y2} = \sigma_{y1}$. Fig. 10 shows that with the growth of the kinetic parameter k the rate of the PT increases. Comparing Figs. 2, 6, and 10, one can see that with the growth of the yield strength the width of the two-phase region increases and the rate of PT reduces under the same loading. This occurs because the appearance of a material with higher strength leads to a reduction of plastic strains and slower transformation kinetics.

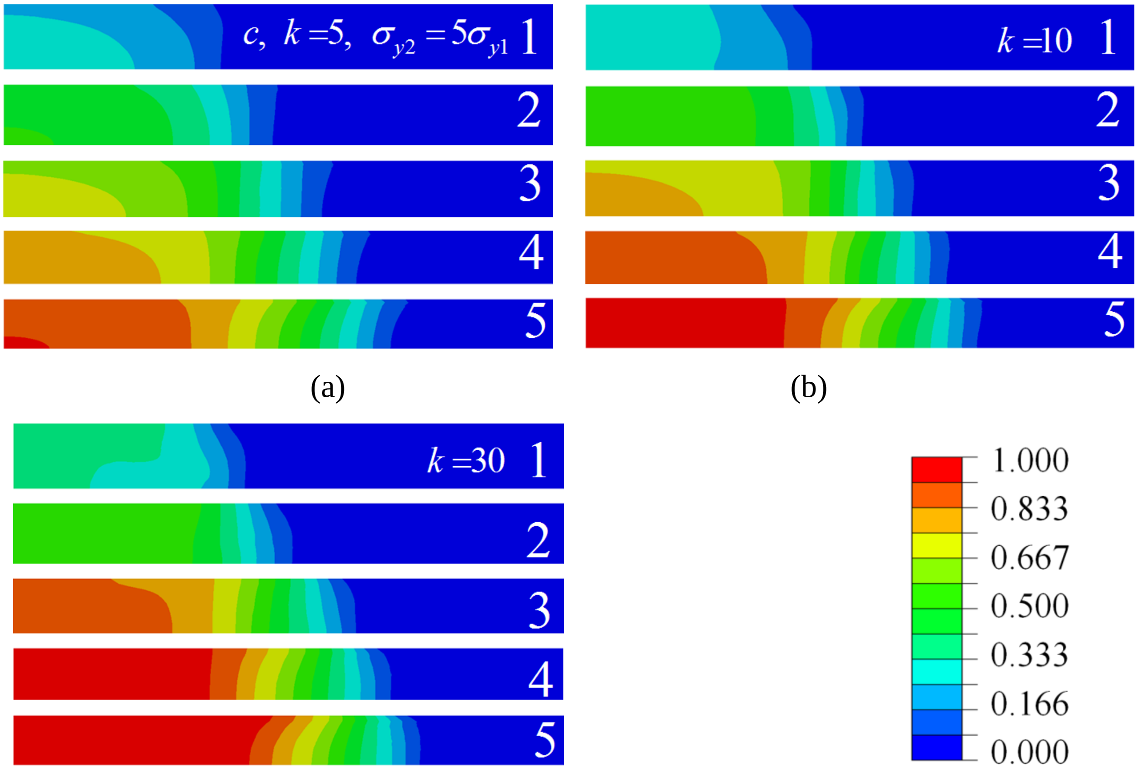

(a)

(b)

(c)

FIG. 10. Concentration of high-pressure phase c under compression for (a) k=5, (b) k=10, and (c) k=30, and $\sigma_{y2} = 5\sigma_{y1}$. The dimensionless axial force F is (1) 4.0, (2) 4.4, (3) 4.8, (4) 5.2, (5) 5.7.

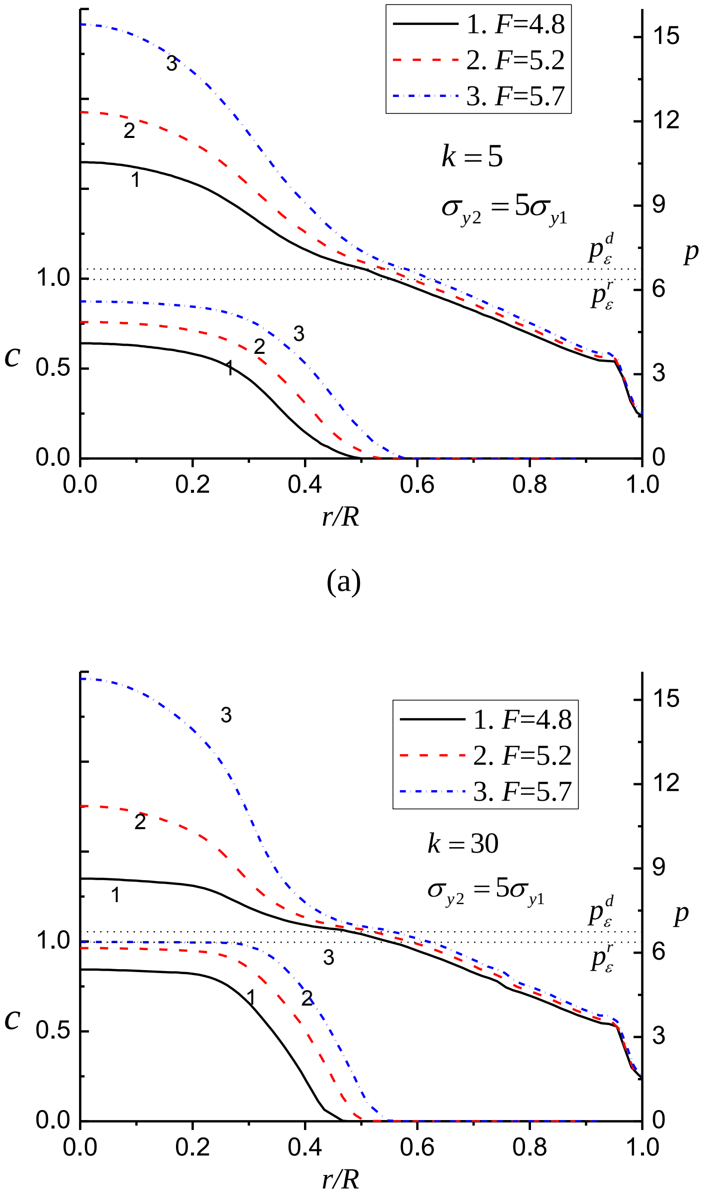

(a)

(b)

FIG. 11. Distributions of dimensionless pressure p and high-pressure phase concentration c on contact surface, for (a) k=5 and (b) k=30, and $\sigma_{y2}=5\sigma_{y1}$. The dimensionless axial force F is (1) 4.8, (2) 5.2, (3) 5.7.

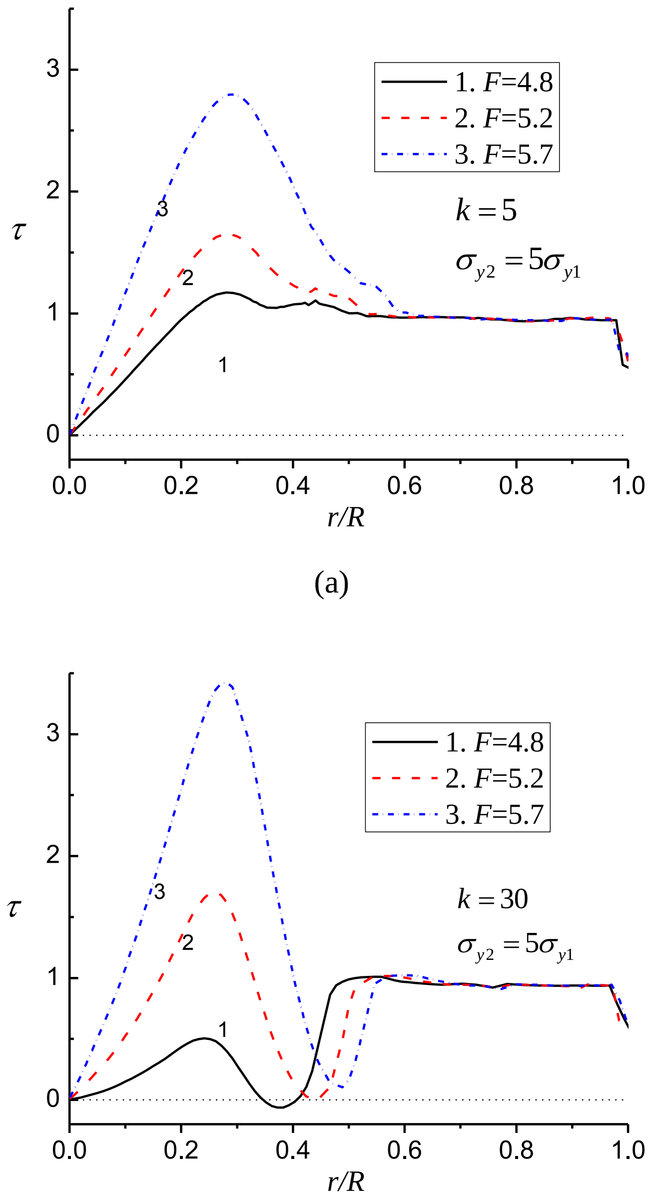

(a)

(b)

FIG. 12. Distribution of dimensionless friction shear stress τ normalized by τ_y on contact surface, for (a) *k*=5 and (b) *k*=30, and $\sigma_{y2}=5\sigma_{y1}$. The dimensionless axial force F is (1) 4.8, (2) 5.2, (3) 5.7.

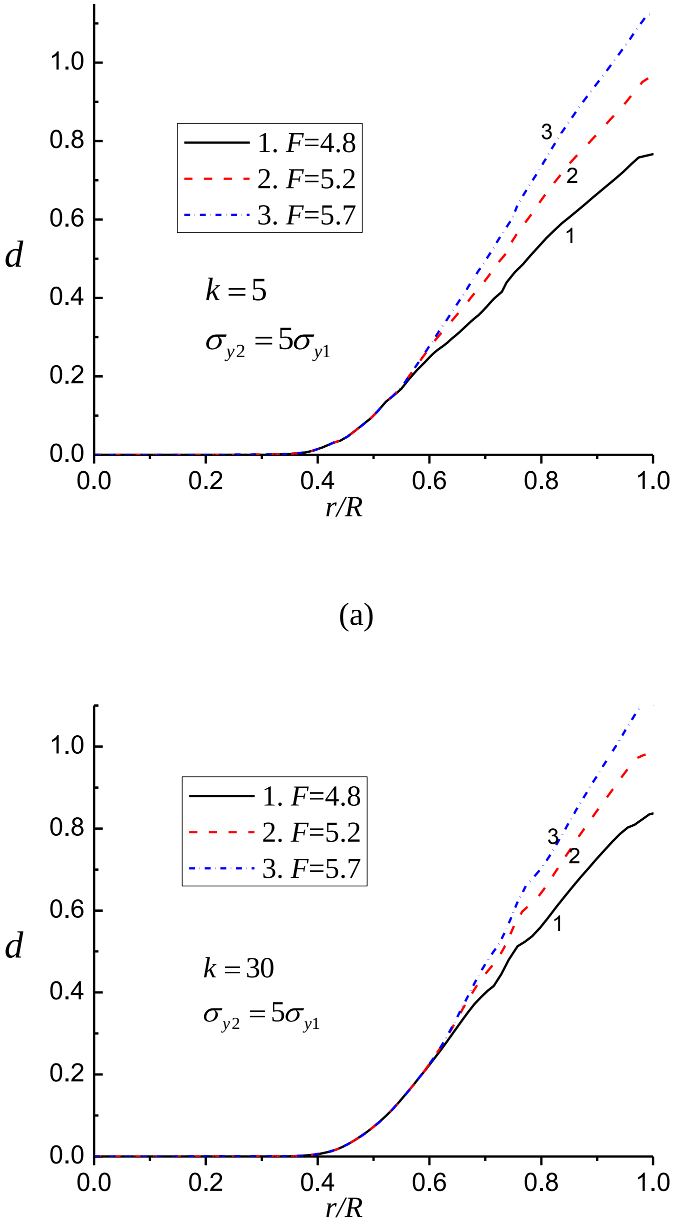

(a)

(b)

FIG. 13. Distribution of dimensionless accumulated relative slipping displacement $d=2u_c/H_0$ on contact surface for (a) *k*=5 and (b) *k*=30, and $\sigma_{y2}=5\sigma_{y1}$. The dimensionless axial force F is (1) 4.8, (2) 5.2, (3) 5.7.

Fig. 11 shows distributions of the concentration of high-pressure phase and pressure at the contact surface under rising axial loading. In comparison with the results for a no-slipping model in Ref. 18, the concentration of the high-pressure phase is larger in the current slipping model for all values of k for the same applied force. There are several reasons for such an acceleration. First, radial material plastic flows in a sample become faster due to permissible sliding at the contact surface, which accelerates the strain-induced PT. Second, the pressure distribution here is significantly higher at the center (where PT occurs) and a little bit lower at the periphery than in Ref. 18, which also promotes PT. The reason of the increased pressure in the central region is in the increased shear friction stress. A simplified equilibrium equation $\frac{dp}{dr} = \frac{2\tau_{zr}^{c}}{h}$ is applicable here (see Refs.10, 15), in which radial shear stress τ_{zr}^{c} on contact surface is equal to friction stress τ at $r/R < 0.96$. The rate of increase in friction stress with increasing force (see Fig. 12) in the region $r < 0.35$ is much faster here than that in Ref. 18, because the material's radial flow is less restricted. In addition, a faster increase in high-pressure phase concentration leads to a higher shear strength and stress, and a higher pressure, i.e., there is a positive feedback. Note that the friction shear stress at the periphery attains the shear strength of the low-pressure phase. The obvious growth of pressure in the central region leads to a slight decrease of pressure in the periphery to keep the same axial force. Surprisingly, steps in the pressure distribution in the two-phase region are less pronounced here than in Ref. 18, and there are no pressure drops here. Friction stress drops for k=30 in the two-phase region due to volume reduction during PT. For the lowest force friction stress and consequently the velocity of the relative sliding change sign, i.e., there is material flow to the center, as in some experiments. However, flow to the center is less pronounced than that for the cohesive boundary conditions.

Fig. 13 exhibits distribution of the dimensionless slipping displacement *d* on the contact surface which is very similar to that for $\sigma_{y2} = \sigma_{y1}$. With the growth of slipping displacement, *d* mostly occurs in the periphery and it does not change significantly with the growth of *k* which is similar to the case for $\sigma_{y2} = \sigma_{y1}$. There are two reasons for this sliding-locked region: (a) reduction of volume due to PT which affects the shear stress (similar to the case $\sigma_{y2} = \sigma_{y1}$), and (b) an increase in strength during PT and further increases in the critical friction stress τ_{crit}.

4.4 Effects of friction coefficient on plastic flow and phase transformations

In this section slipping and no-slipping models will be further compared for $\sigma_{y2} = \sigma_{y1}$ and the effect of friction coefficient on PTs and plastic flow will be examined. Fig. 14 shows the evolution of high-pressure phase concentration for models with slipping (coefficient of friction $\mu = 0$, 0.1 and 0.5) and without slipping. Combining Fig. 14 and Fig. 6(c) for $\mu = 0.3$, one can see that for the same applied force the PT progress reduces, and the width of the two-phase region increases with the increase in friction coefficient from 0.1 to 0.5. We should mention that the common magnitudes of the friction coefficient $\left(\mu = 0.1, 0.3, \text{and}\, 0.5 \right)$ were mostly considered. For a very small friction coefficient, e.g.,$\mu = 0.01$, or even without friction ($\mu = 0$), PT does not start down to quite small sample thicknesses, at which pressure attains the minimum pressure for direct PT p_{ε}^{d} (please check this sentence, we could find in Fig.18 that increase F, and maximum pressure reduces due to increases of contact surface area). For example, for $\mu = 0$ and the axial force F=4.0 in Fig. 14 (d) the thickness decreases to about 1/3 of its original size, yet maximum pressure is around 5 which is less than p_{ε}^{d}=6.75 (See Fig. 18).

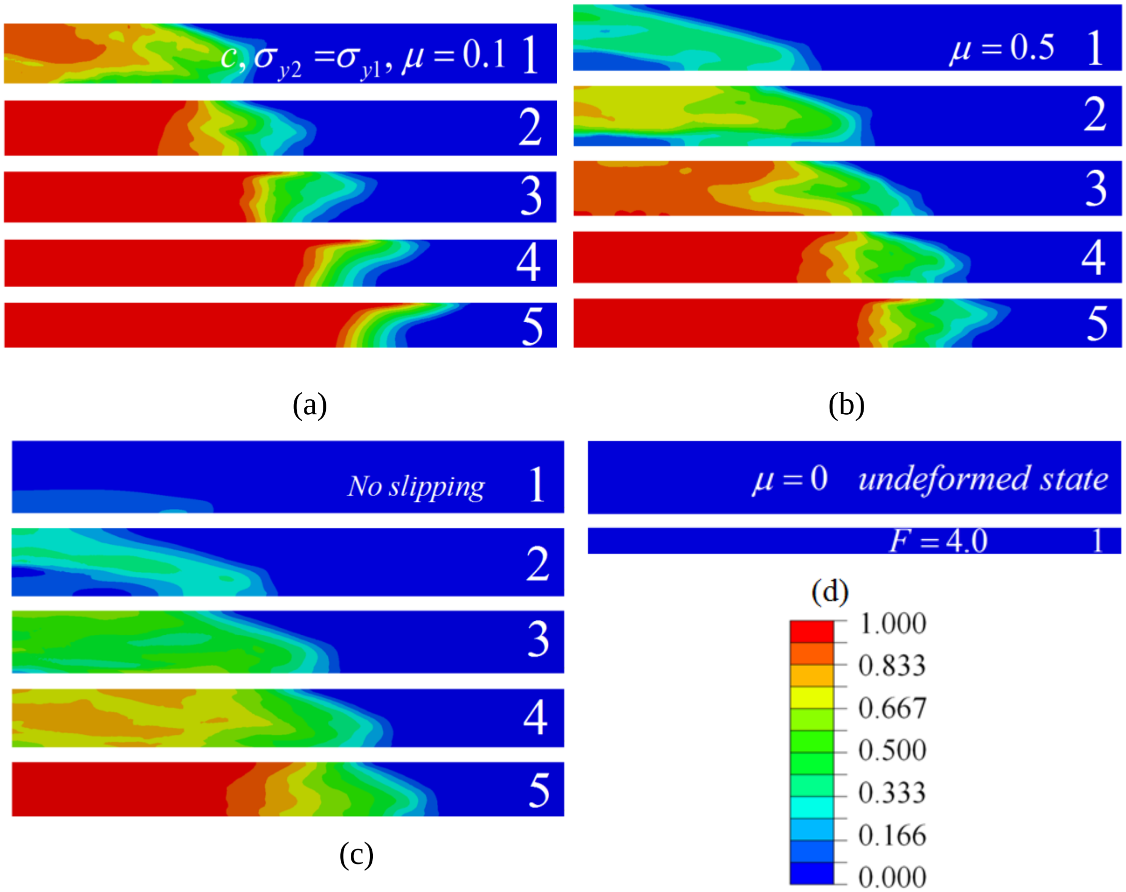

FIG. 14. Distribution of high-pressure phase concentration c, for $k = 30$, $\sigma_{y2} = \sigma_{y1}$, coefficient of friction (a) $\mu = 0.1$, (b) $\mu = 0.5$ and (d) $\mu = 0$, and (c) no slipping model. The dimensionless axial force F is (1) 4.0, (2) 4.3, (3) 4.6, (4) 4.9, (5) 5.13

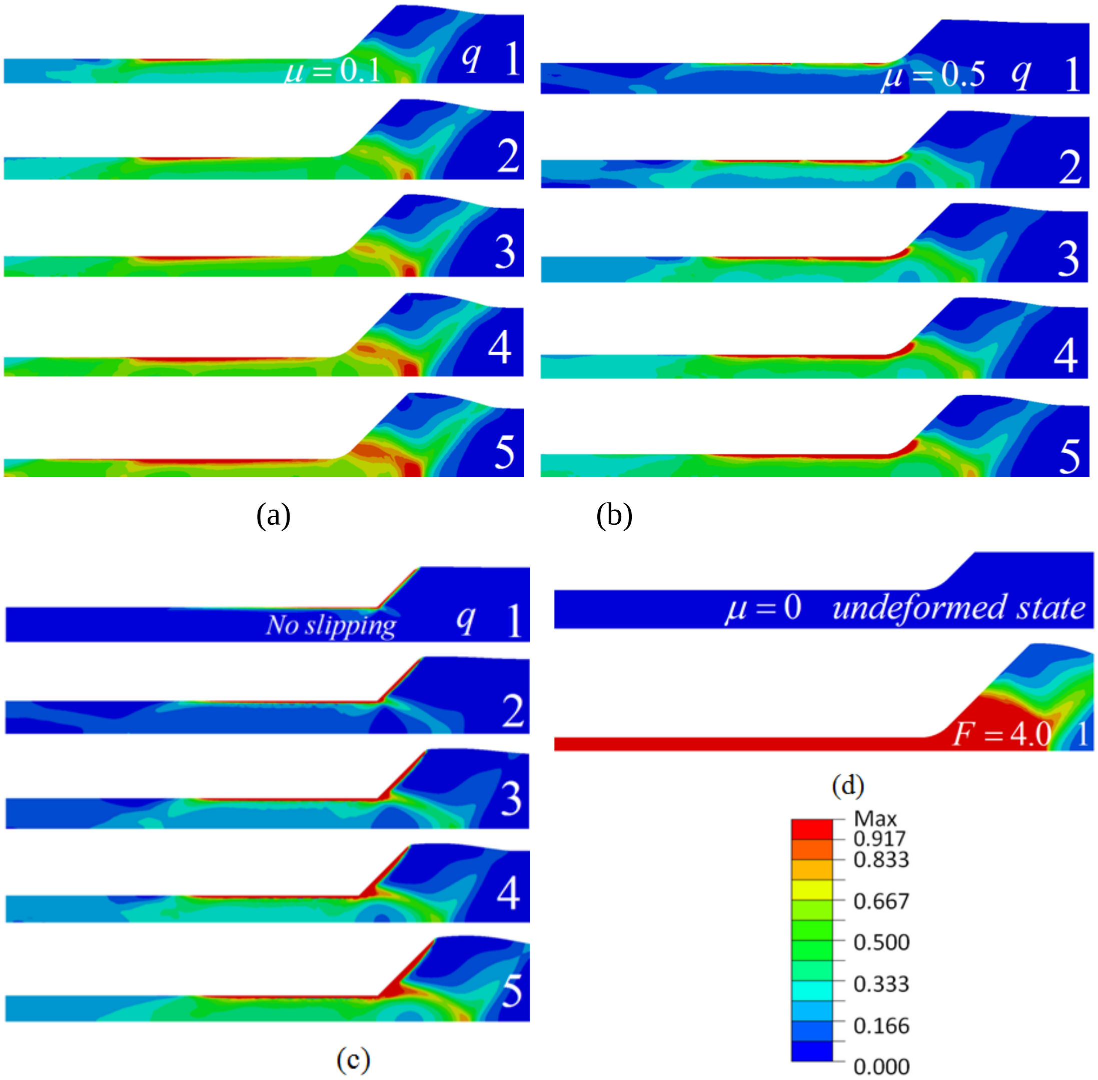

FIG. 15. Distribution of accumulated plastic strain q, for $k=30$, $\sigma_{y2}=\sigma_{y1}$, coefficient of friction (a) $\mu=0.1$, (b) $\mu=0.5$ and (d) $\mu=0$, and (c) no slipping model. The dimensionless axial force F is (1) 4.0, (2) 4.3, (3) 4.6, (4) 4.9, (5) 5.13.

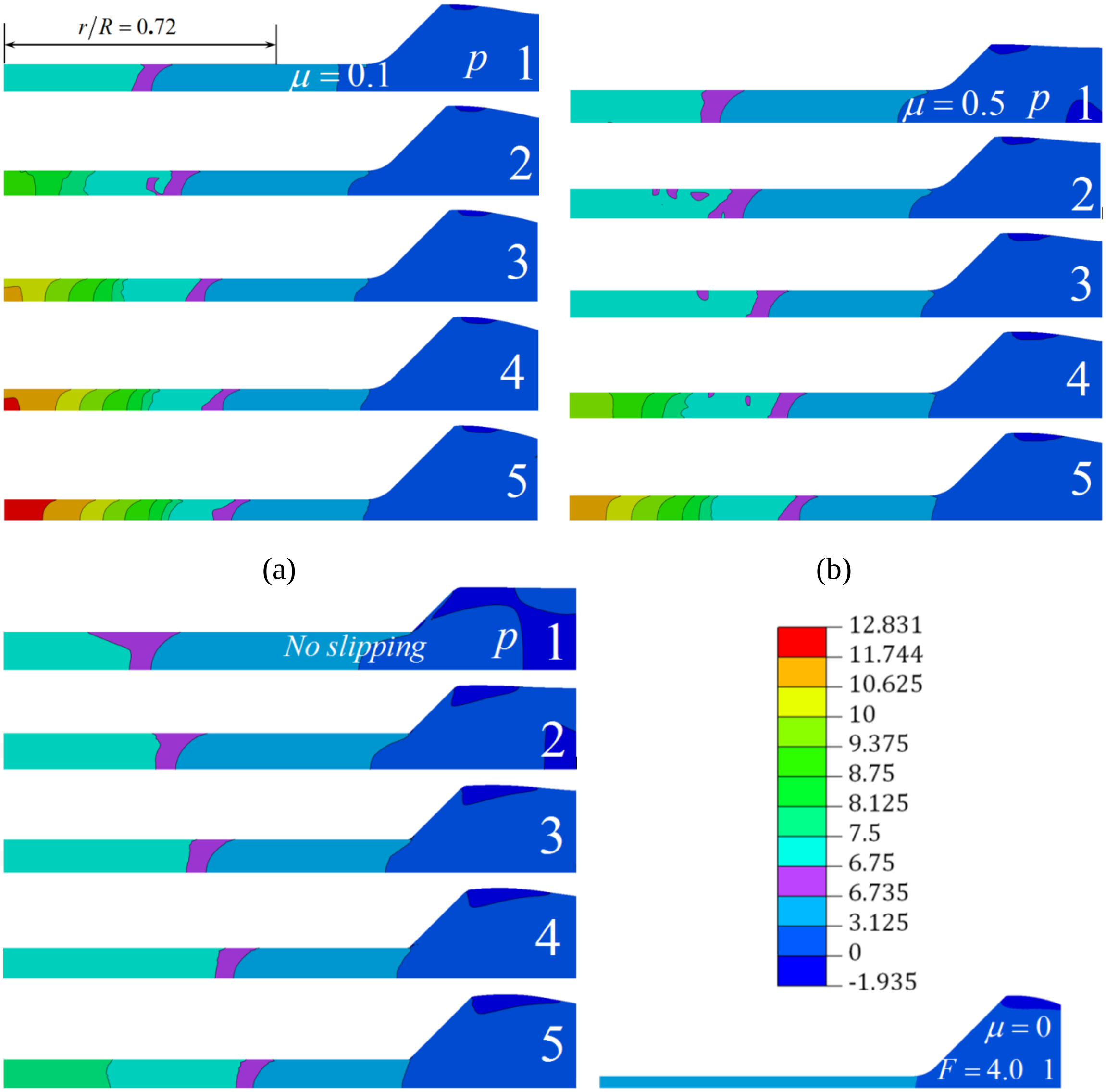

(a) (b)

(c) (d)

FIG. 16. Distribution of pressure, for $k = 30$, $\sigma_{y2} = \sigma_{y1}$, coefficient of friction (a) $\mu = 0.1$, (b) $\mu = 0.5$ and (d) $\mu = 0$, and (c) no slipping model. The dimensionless axial force F is (1) 4.0, (2) 4.3, (3) 4.6, (4) 4.9, (5) 5.13. Pressure range $p_{\varepsilon}^{r} < p < p_{\varepsilon}^{d}$ in which strain-induced PTs are impossible is shown in magenta.

Fig. 15 exhibits the evolution of accumulated plastic strain q with rising dimensionless axial force F for cases with the contact sliding (with $\mu = 0$, 0.1 and 0.5) and cohesion. With the reduction of friction coefficient μ from 0.1 to 0.5, the plastic strain in PT zones increases which is one of the reasons of promotion of strain-induced

PTs in Fig. 13. Another reason for higher concentration of a high pressure phase is related to the increase of pressure in the PT zone for a smaller friction coefficient, which is shown in Fig. 16. This happens due to a faster flow of material from the center to the periphery which leads to a larger shear stress. For $\mu = 0$, although plastic strian is much larger than other cases in Fig. 15 due to fast reduction of sample, it doesn't intensify PT knetics because pressure is more uniform in sample and lower than minimum pressure for direction PTs p_{ε}^{d} (See Fig. 16).

The obvious drawback for the cohesion model in Fig. 15(c) is related to the formation of a shear band on the contact surface (for $r > 0.6$, including inclined surface) within a single finite element, i.e., its thickness is mesh-dependent. When sliding is included localization of plastic strain at the contact surface is less pronounced and is mesh-independent. This is due to a smoother decrease of plastic strain from the contact surface to the symmetry plane (see Fig. 15(a)) in contrast to a sudden drop between the first two layers of elements near the contact surface in the adhesion model. In addition, because of relatively low pressure at the inclined surface AB in Fig. 1(d), cohesion and corresponding strain localization are unrealistic. When sliding is allowed, this drawback is eliminated.

The force-sample thickness plots are presented in Fig. 17 for different contact conditions. The reduction in friction coefficient μ intensifies the material radial flow and promotes a reduction in the sample thickness. This leads to an increase in accumulated plastic strain and acceleration in transformation kinetics. Fig. 18 shows the maximum pressure $p_{\mathbf{max}}$ in the sample versus sample thickness h/H_0 and applied force

F. Throughout this paper (except for $\mu = 0$), all comparisons have been made while using the same force because it is what is prescribed in experiments. However, thickness of the sample under the load is also of practical importance because it determines the total volume or mass of the high pressure phase. This may be important if such a process is utilized for production of a high pressure phase or for a very high pressure when the quality of the X-ray patterns is limited by the sample thickness. Plots of $p_{\mathbf{max}}$ versus *F* for $\mu = 0$ in Fig. 18(b) shows that when *F*>3.9, with increase of applied load *F*, maximum pressure $p_{\mathbf{max}}$ surprisingly reduces, which is caused by increase of contact surface due to fast reduction of thickness (See Fig. 17). Therefore, only increase of load *F* may not produce the pressure larger than p_ε^d. Results for $p_{\mathbf{max}}$ versus *F* for $\mu \neq 0$ are not surprising and have already been discussed in the paper. At the same time, results for $p_{\mathbf{max}}$ versus h/H_0 with $\mu \geq 0.1$ offer new perspective. The main point of interest is that for $h/H_0 > 0.72$ the relation between $p_{\mathbf{max}}$ and thickness is practically independent of contact conditions. At an initial loading process $p_{\mathbf{max}} < p_\varepsilon^d$, $p_{\mathbf{max}}$ increases linearly and fast with the reduction of thickness with the same slope for all of four cases. When $p_{\mathbf{max}}$ just exceeds the minimum pressure for direct PT p_ε^d, $p_{\mathbf{max}}$ is almost constant in some range of thickness reduction, because volume reduces during PT. Then $p_{\mathbf{max}}$ increases again due to rising axial force. For $0.65 < h/H_0 < 0.72$, maximum pressure is independent of thickness for $\mu \geq 0.3$ but reduces for smaller μ.

Fig. 19 exhibits the concentration at the typical sample point $\left(r/R = 0.3, z = 0\right)$ versus thickness of the sample and the applied force for various friction conditions.

Again, dependence on friction conditions for the same applied force is the same as was discussed above: in general, reduction in friction promotes PT. Comparison for the same thickness is less trivial. At the initial stage of loading the thickness reduces but PT does not occur due to low pressure; after pressure exceeds p_{ε}^{d}, concentration increases very fast with reduction of thickness. During an increase of concentration from 0 to 1, there are two plateaus where thickness reduces without (or with small) changes in concentration. This happens because at this local point plastic strain does not change. While for $\mu = 0.1$ concentration is the lowest for the same thickness, for larger friction coefficients the dependence of concentration on friction is non-monotonous. Note that Fig. 19 determines concentration in the spatial rather than in material point and that the effect of convection increases with reduction of friction. Heterogeneity in pressure and plastic strains and convection explain crossing of some curves in Fig. 19 for different friction conditions. Obtained results allow one to control strain-induced PTs by changing friction condition for the chosen goal.

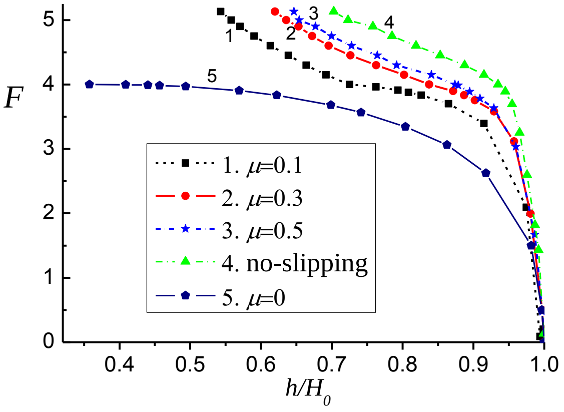

FIG. 17. The normalized axial force F versus the dimensionless current thickness of sample h/H_0 in deformed state for $k = 30$, $\sigma_{y2} = \sigma_{y1}$, $\mu = 0$, 0.1, 0.3 and 0.5, and cohesion condition.

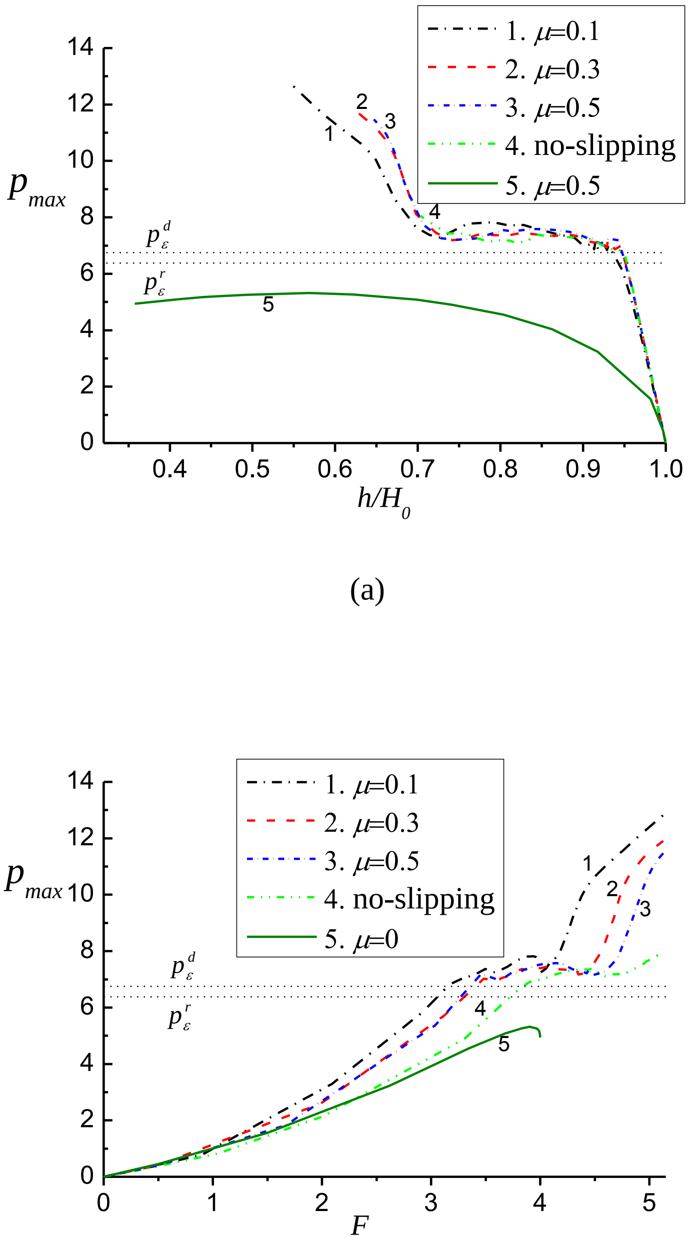

(a)

(b)

FIG. 18. The normalized maximum pressure $p_{\mathbf{max}}$ in the sample versus the dimensionless thickness of sample h/H_0 (a) and force F (b), for $k = 30$, $\sigma_{y2} = \sigma_{y1}$, $\mu = 0$, 0.1, 0.3 and 0.5, and cohesion condition. At the left end of plots in (a), the axial force in this point is F=5.13 for all of cases.

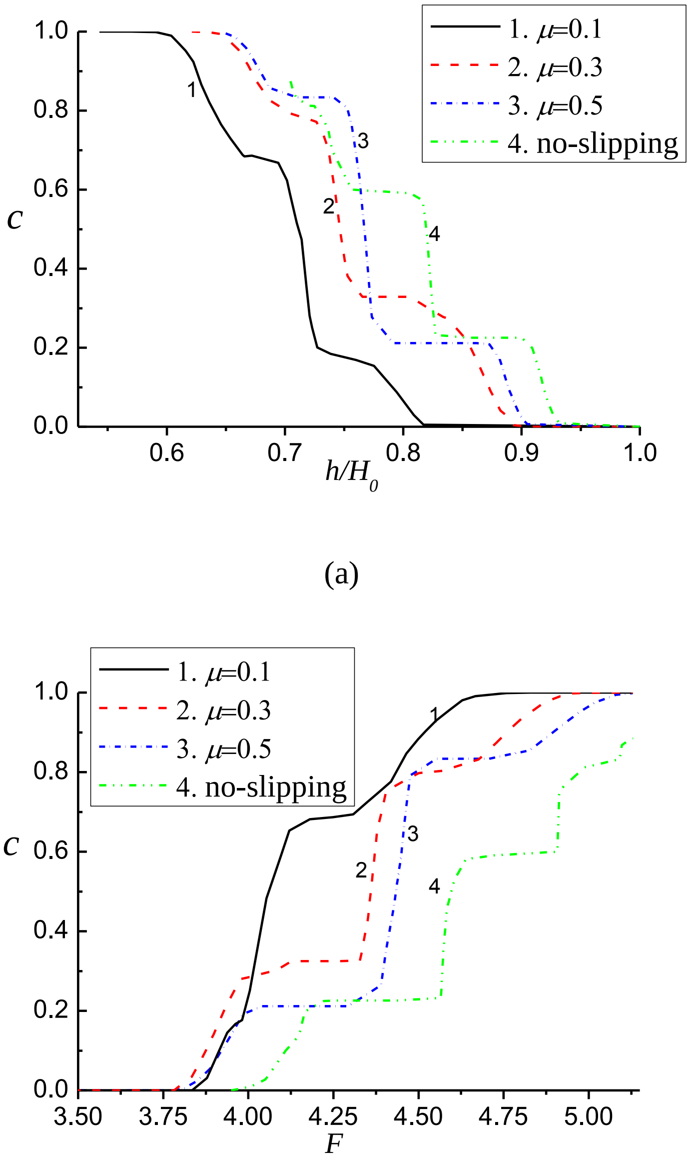

(a)

(b)

FIG. 19. The concentration at the point $(r = 0.3, z = 0)$ versus the dimensionless thickness of sample h/H_0 (a) and force F (b), for $k = 30$, $\sigma_{y2} = \sigma_{y1}$, $\mu = 0.1$, 0.3 and 0.5, and no slipping condition. At the left end of plots in (a), the axial force in this point is F=5.13 for all of cases.

4.5 Concluding remarks

In this paper, the effect of contact sliding and the friction coefficient at the anvil-sample contact surface on the pressure generation, plastic flow and strain-induced PT during compression in a DAC is studied using FEM and the software ABAQUS. Results are obtained for weaker, equal-strength, and stronger high pressure phases and for three values of the kinetic coefficient *k*. For all cases the general trends are as follows. Allowing for sliding and a reduction in the friction coefficient intensify radial plastic flow in the entire sample (excluding the narrow region near the contact surface) and a reduction in thickness for the same applied force. Sliding eliminates mesh-dependence of the localized shear band near the contact surface and eliminates the shear band near the inclined surface of the anvil. For the initial geometry of a sample considered here, a reduction in the friction coefficient down to 0.1 intensifies sliding and pressure increases in the central region for the same axial force. Both increases in plastic strain and pressure lead to a promotion of strain-induced PT. However, for much smaller friction coefficients (e.g., $\mu \leq 0.01$), pressure reaches the critical value required for PT at very large compression only.(same problem with Page 32) The interesting effect of self-locking of sliding is revealed for the equal strength and stronger high pressure phases. In this case, the sliding condition is met in a region yet sliding will not occur because this region is surrounded from both sides by regions where the sliding condition is not fulfilled. There are two reasons for this sliding-locked region: (a) a reduction of volume due to PT which reduces the shear stress in surrounding regions, and (b) an increase in strength during PT and further increase in the critical friction stress τ_{crit} for the case with $\sigma_{y2} = 5\sigma_{y1}$. The results obtained in this paper reproduce and interpret a number of experimental phenomena. Two main practical conclusions follow from our results. (a) Since the friction coefficient is unknown, it increases the complexity of the determination of material parameters in kinetic Eq.(8) from the experiment. (b) One can control plastic flow and PT by controlling friction, especially at the center of a sample and on the conical surface. The effect of friction is expected to be more pronounced for strain-induced PTs under compression and shear in rotational DACs[5-8, 10-12, 22].

References

[1] A. Lazicki, P. Loubeyre, F. Occelli, R. J. Hemley, and M. Mezouar, Phys. Rev. B **85**, 054103 (2012).

[2] C. Nisr, G. Ribarik, T. Ungar, G. B. M. Vaughan, P. Cordier, and S. Merkel, J. Geophys. Res.-Sol. Earth **117**, B03201 (2012).

[3] A. R. Oganov, J. H. Chen, C. Gatti, Y. Z. Ma, Y. M. Ma, C. W. Glass, Z. X. Liu, T. Yu, O.O. Kurakevych, and V. L. Solozhenko, Nature **457**, 863 (2009).

[4] C. S. Zha, Z. X. Liu, and R. J. Hemley, Phys. Rev. Lett. **108**, 146402 (2012).

[5] S. S. Batsanov, N. R. Serebryanaya, V. D. Blank, and V. A. Ivdenko, Crystallography Rep. **40**, 598 (1995).

[6] V. Blank, et al., Phys. Lett. A **188**, 281 (1994).

[7] V. D. Blank, Y. Y. Boguslavsky, M. I. Eremets, E. S. Itskevich, Y. S. Konyaev, A. M. Shirokov, and E. I. Estrin, Zh. Eksp. Teor. Fiz. **87**, 922 (1984).

[8] V. D. Blank and S. G. Buga, Instrum. Exp. Tech. **36**, 149 (1993).

[9] C. Ji, V. I. Levitas, H. Zhu, J. Chaudhuri, A. Marathe, and Y. Ma, P. Natl. Acad. Sci. USA **109**, 19108 (2012).

[10] V. I. Levitas, Phys. Rev. B **70**, 184118 (2004).

[11] V. I. Levitas, Y. Z. Ma, J. Hashemi, M. Holtz, and N. Guven, J. Chem. Phys. **125**, 044507 (2006).

[12] V. I. Levitas, Y. Z. Ma, E. Selvi, J. Z. Wu, and J. A. Patten, Phys. Rev. B **85**, 054114 (2012).

[13] Y. Gogotsi and V. Domnich, *High-pressure surface science and engineering.* (Institute of Physics Pub, Bristol; Philadelphia) (2004).

[14] V. I. Levitas, Europhys. Lett. **66**, 687 (2004).

[15] V. I. Levitas and O. M. Zarechnyy, Phys. Rev. B **82**, 174123 (2010).

[16] V. I. Levitas and O. M. Zarechnyy, Phys. Rev. B **82**, 174124 (2010).

[17] B. Feng, O. M. Zarechnyy, and V. I. Levitas, J. Appl. Phys. **113**, 173514 (2013).

[18] O. M. Zarechnyy, V. I. Levitas, and Y. Z. Ma, J. Appl. Phys. **111**, 023518 (2012).

[19] V. I. Levitas and O. M. Zarechnyy, Europhys. Lett. **88**, 16004 (2009).

[20] Abaqus V6.11. *User Subroutines Manual.* Providence RI, USA: Abaqus INC (2011).

[21] V. I. Levitas, *Large Deformation of Materials with Complex Rheological Properties at Normal and High Pressure* (Nova Science, New York, 1996).

[22] N. V. Novikov, S. B. Polotnyak, L. K. Shvedov, and V. I. Levitas, J. of Superhard Mater. **3**, 39 (1999).

CHAPTER 5. COUPLED PHASE TRANSFORMATIONS AND PLASTIC FLOWS UNDER TORSION AT HIGH PRESSURE IN ROTATIONAL DIAMOND ANVIL CELL: EFFECT OF CONTACT SLIDING

Modified by a paper published in Journal of Applied Physics

Biao Feng[1] Valery I. Levitas[2,*]

1) Department of Aerospace Engineering, Iowa State University, Ames, Iowa 50011, USA

2) Departments of Aerospace Engineering, Mechanical Engineering, and Material Science and Engineering, Iowa State University, Ames, Iowa 50011, USA

Abstract

A three-dimensional large-sliding contact model coupled with strain-induced phase transformations (PTs) and plastic flow in a disk-like sample under torsion at high pressure in rotational diamond anvil cell (RDAC) is formulated and studied. Coulomb and plastic friction are combined and take into account variable parameters due to PT. Results are obtained for weaker, equal-strength, and stronger high pressure phases, and for three values of the kinetic coefficient in a strain-controlled kinetic equation and friction coefficient. All drawbacks typical of problem with cohesion are overcome, including eliminating mesh-dependent shear band and artificial plastic zones. Contact sliding intensifies radial plastic flow, which leads to larger reduction in sample thickness. Larger plastic strain and increased pressure in the central region lead to intensification of PT. However, the effect of the reduction in the friction coefficient on PT kinetics is nonmonotonous. Sliding increases away from the center and with growing rotation, and is weakly dependent on the kinetic coefficient. Also, cyclic back and forth torsion is studied

---

[*] Corresponding author.
Email: vlevitas@iastate.edu

and compared to unidirectional torsion. Multiple experimental phenomena, e.g., pressure self-multiplication effect, steps (plateaus) at pressure distribution, flow to the center of a sample, and oscillatory pressure distribution for weaker high-pressure phase, are reproduced and interpreted. Reverse PT in high pressure phase that flowed to the low pressure region is revealed. Possible misinterpretation of experimental PT pressure is found. Obtained results represent essential progress toward understanding of strain-induced PTs under compression and shear in RDAC and may be used for designing experiments for synthesis of new high pressure phases and reduction in PT pressure for known phases, as well as for determination of PT kinetics from experiments.

5.1 Introduction

Diamond anvil cells are routinely utilized for research on material behavior and PTs under high hydrostatic or quasi-hydrostatic pressure. Recently, experiments in RDAC under high pressure and large plastic shear attracted researchers' interests due to a number of exciting phenomena: (a) a significant reduction in PT pressure in comparison with hydrostatic conditions, by a factor of 2-5[1-5] and even almost 10 in Ref. 6; (b) an appearance of new phases, which would not be obtained without shear straining[4, 7-9]; (c) fast strain-controlled kinetics in which strain instead of time plays a role of a time-like parameter[3, 10]; (d) the substitution of a reversible PT[9, 11] for an irreversible one, and (e) a reduction (up to zero) in pressure hysteresis[2]. Study on PTs under high pressure and large shear is of fundamental and applied significance in multiple problems, for example, 1) search for new high-pressure phases, in particular, for those that could be retained at ambient pressure and be utilized in engineering applications; 2) finding ways to reduce the PT pressure to level that makes the technology economically reasonable; 3) understanding processes in shear bands in geophysics (especially, during initiation of earthquakes), penetration of projectiles in materials, and shear ignition of energetic materials; and 4) technological applications (cutting and polishing of Ge, Si, silicon and boron carbides, PTs during ball milling and high pressure torsion), see in Ref. 3 and references herein.

When hydrostatic media is used, PT is classified as pressure-induced one which starts by nucleation at preexisting defects, which produce pressure/stress concentration. Without hydrostatic media and with or without rotation of an anvil, PTs are considered as strain-induced under high pressure. They occur by nucleation at new defects (e.g., dislocation pile ups and tilt boundaries) which are continuously generated during plastic deformation[3]. Since strain-induced defects produce much larger stress concentration than the pre-existing ones, external pressure can be significantly reduced. Strain-induced PTs in RDAC are described by three-scale theory (at the nano-, micro, and macroscales)[3], its further developments at the micro[10] and macroscales[12, 13], and within numerical simulations at the macroscale[12, 13]. While there are some analytical and numerical solutions for interaction of PTs and plasticity at the nanoscale[3, 14], they cannot be directly utilized in the current study on PTs in RDAC, due to the size of the sample of the order of magnitude of 1 *millimeter*. At the microscale[3, 10], the strain-induced PTs can be characterized in terms of a pressure-dependent, strain-controlled kinetic Eq. (8), which includes four main parameters: a) the ratio of yield strengths of high (σ_{y2}) and low (σ_{y1}) pressure phases; b) the minimum pressure p_ε^d below which direct strain-induced PT does not take place; c) the maximum pressure p_ε^r above which reverse strain-induced PT cannot occur, and d) a kinetic parameter k which scales the PT rate. Due to highly heterogeneous distributions of stresses, strains, and concentration of phases, these parameters have not been experimentally determined yet, and pressure distribution on the contact surface of sample and concentration of high-pressure phase distribution averaged over the sample thickness are experimentally available only[9]. That is why finite-element method (FEM) simulations have been developed to study the evolution of all fields, including concentration of high pressure phases, and effects of material parameters on them, as well as to interpret experimental phenomena[12, 13, 15, 16]. It is a nonlinear problem of coupled PTs and mechanics with large plastic deformations and displacements, which leads to nontrivial simulation challenges using FEM, including convergence.

First, we would like to stress importance of friction between anvil and sample for high pressure physics. For radial plastic flow of a sample of the current thickness h in traditional diamond anvil cell, pressure p gradient along the radius r is described by a simplified equilibrium equation $\frac{dp}{dr}=\frac{2\tau_{zr}^{c}}{h}$ (see in Ref. 3), where τ_{zr}^{c} is the radial frictional shear stress at the contact surface between sample and anvil. Without friction (τ_{zr}^{c}=0), pressure does not vary along the radius; it is impossible to increase it to high value; and it cannot exceed the yield strength for a cylindrical sample or material hardness for indentation. However, friction usually reaches the maximum possible shear stress equal to the yield strength in shear τ_y at the major part of the sample surface. Then, for large ratio R/h, where R is the sample radius, the pressure increases linearly from the periphery toward the center and can reach hundreds of GPa. Thus, the ability to create frictional resistance to the radial plastic flow in the thin sample during its compression is the main principle for producing high pressure and its application to physics, material science, and chemistry.

The main effect of rotation of an anvil in RDAC was also first explained in terms of friction stresses[3, 17, 18]. The magnitude of the friction stress vector $\boldsymbol{\tau}$, $\tau=|\boldsymbol{\tau}|$ is equal to the yield strength in shear τ_y (like in traditional DAC) but direction of $\boldsymbol{\tau}$ is opposite to the velocity of relative sliding of a sample material with respect to anvil, i.e., it is inclined to the radial direction. That means that the radial component τ_{zr}^{c} of the friction stress vector $\boldsymbol{\tau}$ is getting smaller during rotation of an anvil, reducing resistance to the radial plastic flow. It follows from the equilibrium equation that rotation of an anvil under constant axial force decreases sample thickness, producing additional plastic flow and compensating volume decrease due to PT. Thus, friction is one of the main players in the effect of plastic shear on PTs.

While first numerical results for modeling strain induced PTs in DAC[12, 16, 19] and in RDAC[13] have been very successful in interpreting multiple experimental phenomena, they involve a strong assumption: there is full cohesion on the contact surface between sample and diamond anvils. In this case, radial displacements at the contact surface are zero and circumferential displacements of material are equal to circumferential displacements of an anvil. Such a model possesses three main drawbacks: (a) there is an unrealistic shear band near the contact surface which substitutes contact sliding; it leads to overestimated plastic strain, which artificially promotes strain-induced PT, and thickness of the shear band is mesh-dependent; (b) artificial large plastic deformation occurs in some region at the periphery where pressure is small and large sliding is expected, and (c) artificially increased resistance to the radial plastic flow suppresses it as well as reduction in thickness leading to redistribution of plastic deformation and concentration of high pressure phase.

In the current paper, a large-slip contact model coupled with large plastic flow and strain-induced PTs is developed and studied using FEM approach and code ABAQUS. This work can be considered as generalization of the previous works[13] for simulation of the processes in RDAC when contact sliding is taken into account or generalization of the previous work [15] on modeling of the processes in DAC with contact sliding and friction, for much more complex three dimensional (3D) case of compression and shear in RDAC. Combination of classical isotropic Coulomb friction model with plastic friction model is extended to consider phase concentration-dependent friction stress and to include small elastic slipping. Significant effects of the contact sliding on the kinetics of plastic flow and strain-induced PT are revealed and quantified.

5.2 Problem formulation

Geometry and boundary conditions

A RDAC is considered to have axisymmetric geometry but subjected to 3D compression and torsion loading, which differs from standard axisymmetric models in a DAC in Refs, 12, 15, 16 and should be classified as the generalized axisymmetric one. Geometry of RDAC and disc-like sample, loading and boundary conditions are shown in Fig. 1 along with a cylindrical coordinate system $rz\phi$. First, an axial compressive force P is applied on the two diamond anvils to produce high pressure, and then one of diamond is gradually twisted at a fixed compressive force P. If relative rotation angle between two anvils is φ, the half of the rotation angle $\varphi/2$ is applied on one anvil with respect to the symmetry plane ($z=0$). Due to symmetry, a quarter of sample is considered with the following boundary conditions:

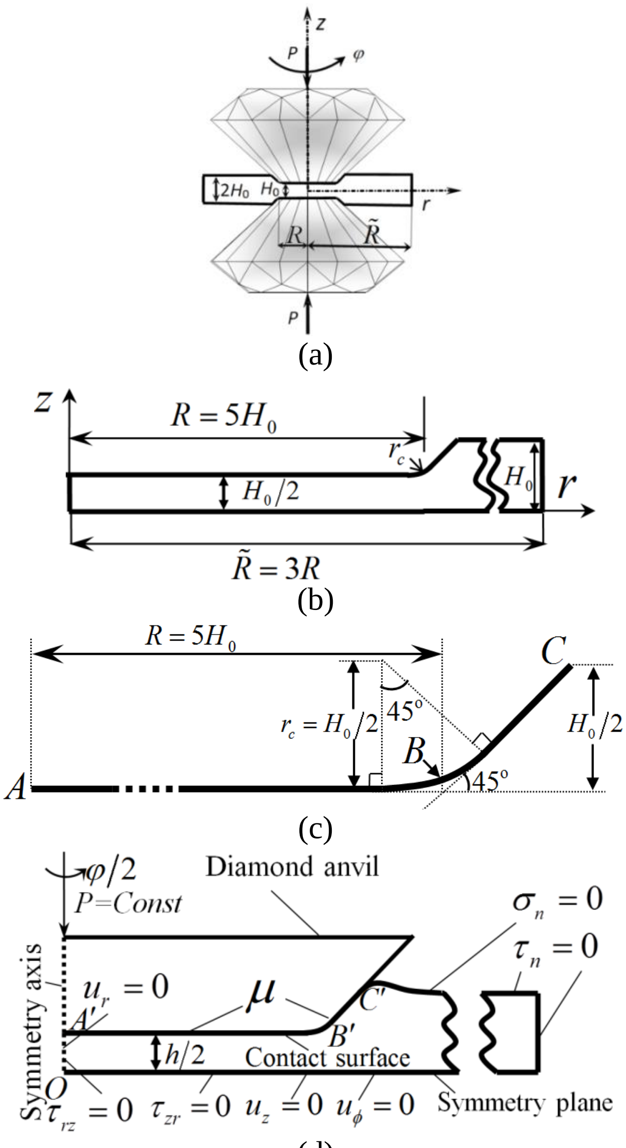

FIG. 1. (a) RDAC geometry and loading; (b) a quarter of sample in initial undeformed state; (c) geometry of a contact surface in the undeformed state, and (d) boundary conditions in the deformed state.

(1) At the axis $r = 0$, radial displacement u_r and shear stress τ_{rz} are zero.

(2) At the contact surface $A'B'C'$ between rigid diamond and deformed material, the contact sliding conditions are applied, which will be described in Sec. II. C.

(3) At the symmetry plane $z = 0$, the radial shear stress $\tau_{rz} = 0$, circumferential displacement $u_\phi = 0$, and the axial displacement $u_z = 0$.

(4) Surfaces which are not in contact with diamond are stress-free.

A large slip and plastic deformation problems coupled with strain-induced PTs in a sample between two rigid diamond anvils under high pressure and large shear is investigated using FEM software ABAQUS. The contact algorithm in ABAQUS requires the master surface in a contact interaction (herein referring to the surface of diamond anvil) to be smooth, and thus a small fillet radius $r_c = H_0/2$ is utilized to substitute the sharp corners of contact surface (Fig. 1(c)), where H_0 is the initial thickness of the sample. While our treatment is size-independent, typical radius *R* of an anvil is 100-250 microns.

Material model

To obtain generic results, plasticity of a sample material is described by the simplest isotropic perfectly plastic model and diamond anvils are rigid, which was utilized in our previous studies[12, 13, 15, 16, 19]. The applicability of the perfectly plastic and isotropic model with the yield strength independent of the deformation history is justified in Ref. 20 under monotonous loading for various classes of materials (metals, rocks, powders, etc.) starting with accumulated plastic strains $q > 0.6 \div 1$. The deformation of a sample is described by function $\boldsymbol{r} = \boldsymbol{r}(\boldsymbol{r}_0, t)$, where $\boldsymbol{r}_0$ and $\boldsymbol{r}$ are position vectors of the particle in the undeformed and deformed states, respectively, and *t* is time. The deformation gradient, $\boldsymbol{F} = \partial \boldsymbol{r}/\partial \boldsymbol{r}_0 = \boldsymbol{V}_{\mathrm{e}} \cdot \boldsymbol{F}_{\mathrm{t}} \cdot \boldsymbol{F}_{\mathrm{p}}$ is multiplicatively decomposed into symmetric elastic stretch tensor $\boldsymbol{V}_e$, transformational $\boldsymbol{F}_t$, and plastic $\boldsymbol{F}_p$ parts [21]. Under the assumptions of small elastic and transformational strains but large plastic strains and material rotations, the following total system of equations is utilized in simulation:

Decomposition of the deformation rate $\boldsymbol{d} = \left(\dot{\boldsymbol{F}} \cdot \boldsymbol{F}^{-1}\right)_{\boldsymbol{s}}$ into elastic, transformational, and plastic parts:

$$\boldsymbol{d} = \overset{\nabla}{\boldsymbol{\varepsilon}}_e + \dot{\varepsilon}_t \boldsymbol{I} + \boldsymbol{d}_p \,. \tag{1}$$

Transformation volumetric strain:

$$\varepsilon_t = \bar{\varepsilon}_t c \,. \tag{2}$$

Hooke's law for volumetric and deviatoric parts

$$p = -\frac{\sigma_{rr} + \sigma_{\phi\phi} + \sigma_{zz}}{3} = -K\varepsilon_{e0} \,; \qquad \boldsymbol{s} = 2G\, dev\boldsymbol{\varepsilon}_e \,. \tag{3}$$

Von Mises yield condition for two-phase mixture:

$$\sigma_i = \left(\frac{3}{2}\boldsymbol{s} : \boldsymbol{s}\right)^{0.5} \le \sigma_y\left(c\right) = \left(1 - c\right)\sigma_{y1} + c\sigma_{y2} \,. \tag{4}$$

Plastic flow rule in the elastic region:

$$\sigma_i < \sigma_y(c) \text{ or } \sigma_i = \sigma_y(c) \qquad \rightarrow \qquad \boldsymbol{d}_p = 0 \,. \tag{5}$$

in the plastic region:

$$\sigma_i = \sigma_y(c) \qquad \rightarrow \qquad \boldsymbol{d}_p = \lambda \boldsymbol{s} \,; \quad \lambda \ge 0 \,. \tag{6}$$

Momentum balance equation:

$$\nabla \cdot \boldsymbol{T} = 0 \,. \tag{7}$$

Our micro-scale theories[3,10] suggest that strain-induced PTs can be characterized in terms of pressure-dependent, strain-controlled kinetic equation:

$$\frac{dc}{dq} = 10k \frac{(1-c)\bar{p}_d H(\bar{p}_d)\dfrac{\sigma_{y2}}{\sigma_{y1}} - c\bar{p}_r H(\bar{p}_r)}{c + (1-c)\sigma_{y2}/\sigma_{y1}} \,. \tag{8}$$

where p is the pressure, $\bar{p}_d = \frac{p - p_\varepsilon^d}{p_h^d - p_\varepsilon^d}$ and $\bar{p}_r = \frac{p - p_\varepsilon^r}{p_h^r - p_\varepsilon^r}$; p_h^d and p_h^r are the pressures for direct and reverse PTs under hydrostatic condition, respectively; $\boldsymbol{s}$ is the deviator of the true stress tensor $\boldsymbol{T}$, $s = dev\boldsymbol{T}$; $\boldsymbol{\sigma}_i$ is the stress intensity; c is the concentration of the high pressure phase; $\overset{\nabla}{\boldsymbol{\varepsilon}}_e$ and $\overset{\nabla}{\boldsymbol{s}}$ is the Jaumann objective time derivative of the elastic strain and deviatoric stress; subscript s means symmetrization of a tensor; $\boldsymbol{I}$ is the unit tensor; ε_{e0} is elastic volumetric strain; H is the Heaviside step function; and K and G are the bulk and shear moduli.

Friction model

The traditional Coulomb friction assumes that the relative slip on a contact surface starts when magnitude of the friction stress vector $\boldsymbol{\tau}$, $\tau = |\boldsymbol{\tau}|$, reaches the critical friction stress $\tau_{crit} = \mu\sigma_n$, where σ_n is the normal contact stress and μ is the sliding friction coefficient. For elastoplastic materials, however, the magnitude of the friction stress cannot (could not) be larger than the yield strength in shear $\tau_y = \sigma_y / \sqrt{3}$, where the yield condition (4) has been utilized. Consequently, it is reasonable to redefine critical friction stress $\tau_{crit} = \min(\mu\sigma_n, \tau_y)$ and relative slip on a contact surface occurs when the magnitude of the friction stress τ reaches this critical value. During PTs, yield strength in shear τ_y varies based on the variation of concentrations and yield strengths of phases. For the case of two-phases mixture, Eq. (4) implies $\tau_y = (1-c)\tau_{y1} + c\tau_{y2}$, with τ_{y1} and τ_{y2} for the yield strength in shear of the low- and high-pressure phases, respectively. Three dimensional friction stress $\boldsymbol{\tau}$ along the contact surface in the generalized axisymmetric model can be decomposed into two orthogonal components τ_r^c and τ_ϕ^c along the contact surface: τ_ϕ^c is along the circumferential twist direction and τ_r^c is along the radial direction. Further, $\tau_r^c = \tau_{rz}$ and $\tau_\phi^c = \tau_{\phi z}$ for the horizontal contact region $(r/R < 0.96)$ in the Fig. 1.

Note that in FEM simulations a sharp change between slip and cohesion conditions may cause convergence problem, especially for the large sliding. To improve the efficiency of numerical procedure, penalty method is utilized, in which the complete cohesion condition is replaced by a small elastic (reversible) slip vector $\boldsymbol{u}^{\boldsymbol{e}}$, similar to the elastic strain for elastoplastic material. Elastic slip can be visualized as elastic deformation of a thin contact layer (asperities), while sliding corresponds to plastic flow in the contact layer or cutting asperities. For robustness and accuracy of the penalty method, the magnitude of the elastic slip should be small, e.g., smaller than 0.5% of average element length for fine-mesh discretization (which in our case is the same for every contact element).

It is assumed that the elastic slip vector is related to the friction stress vector by $\boldsymbol{\tau} = k_s \boldsymbol{u}^e$, where k_s is the (current) contact stiffness. Then we have for magnitudes $\tau = k_s u^e$. The contact stiffness is defined by the condition that sliding starts at the given critical elastic slip magnitude u_{crit}, i.e., $k_s = \tau_{crit}/u_{crit}$. Due to τ_{crit}, k_s linearly varies with the normal stress σ_n or yield strength in shear τ_y. The complete system of equations for contact friction is presented below.

Decomposition of total contact displacement into elastic and irreversible sliding parts:

$$\boldsymbol{u}^c = \boldsymbol{u}^e + \boldsymbol{u}^s . \tag{9}$$

Critical shear stress

$$\tau_{crit} = \min(\mu\sigma_n,\ \tau_y(c)) . \tag{10}$$

Yield strength in shear:

$$\tau_y(c) = \left(1-c\right)\tau_{y1} + c\tau_{y2} . \tag{11}$$

Equations for the vector of the elastic slip displacement:

$$\begin{cases} \boldsymbol{u}^e = \dfrac{u_{crit}}{\mu\sigma_n}\boldsymbol{\tau} & if \quad \mu\sigma_n < \tau_y . \\ \boldsymbol{u}^e = \dfrac{u_{crit}}{\left[\left(1-c\right)\tau_{y1} + c\tau_{y2}\right]}\boldsymbol{\tau} & if \quad \mu\sigma_n \ge \tau_y . \end{cases} \tag{12}$$

Sliding rule below critical shear stress:

$$\tau = |\boldsymbol{\tau}| = \sqrt{\left(\tau_r^c\right)^2 + \left(\tau_\phi^c\right)^2} < \tau_{crit} \quad \rightarrow \quad \left|\dot{\boldsymbol{u}}^s\right| = 0 . \tag{13}$$

Sliding rule at critical shear stress ($\tau = \tau_{crit}$):

$$\begin{cases} \dot{\boldsymbol{u}}_s = \dfrac{|\dot{\boldsymbol{u}}_s|}{\mu\sigma_n}\boldsymbol{\tau} & if \quad \mu\sigma_n \le \tau_y . \\ \dot{\boldsymbol{u}}_s = \dfrac{|\dot{\boldsymbol{u}}_s|}{\left[\left(1-c\right)\tau_{y1} + c\tau_{y2}\right]}\boldsymbol{\tau} & if \quad \mu\sigma_n > \tau_y . \end{cases} \tag{14}$$

The main difference between current formulation and formulation in Ref. 15 for compression in traditional diamond anvils is that contact shear stresses and displacements are two dimensional vectors rather than scalars.

Numerical procedure

To treat this coupled PT and intense plastic flow problem, ABAQUS user subroutines[22] USDFLD and HETVAL have been implemented, in which transformation strain is treated as the thermal strain, and concentration c as temperature. For $\tau_{y1} \neq \tau_{y2}$, user subroutine FRIC in ABAQUS should be implemented to define contact behavior. For $\tau_{y1} = \tau_{y2}$, one can also use standard procedure without subroutine FRIC, which could be utilized to confirm the consistency of standard procedure and programming in FRIC.

In the dimensionless form, shear stresses are normalized by the yield shear strength $\tau_{y1} = \sigma_{y1} / \sqrt{3}$; all other stress-related parameters (e.g., pressure p and minimum pressure for direct PT p_{ε}^{d}) are normalized by σ_{y1}; the dimensionless force F is the axial force P normalized by σ_{y1} and the initial contact area, which is equal to the area produced by complete revolution of the curve ABC in Fig. 1(b) about the *z*-axis. The following material parameters have been used: $p_{h}^{r} = 1.875$, $p_{h}^{d} = 11.25$ $p_{\varepsilon}^{d} = 6.75$, $p_{\varepsilon}^{r} = 6.375$; Poison's ratio $\nu = 0.3$; Young modulus $E = 162.5$; and volumetric transformation strain for direct PT $\bar{\varepsilon}_{t} = -0.1$. They are the same as for the problem with cohesion[13], in order to facilitate the study of the effect of sliding. Friction coefficient μ is the same for both phases. Due to $p_{\varepsilon}^{d} > p_{\varepsilon}^{r}$, strain-induced PT could not take place in the pressure range $p_{\varepsilon}^{r} < p < p_{\varepsilon}^{d}$; PT to the high pressure phase occurs for $p > p_{\varepsilon}^{d}$ and PT to the low pressure phase takes place for $p < p_{\varepsilon}^{r}$.

5.3 Coupled plastic flow and phase transformations under high pressure and large shear loading

Strain-induced PTs and plastic flow under high pressure and large shear with a large-slip contact model are investigated in detail, for weaker, equal, and stronger high-

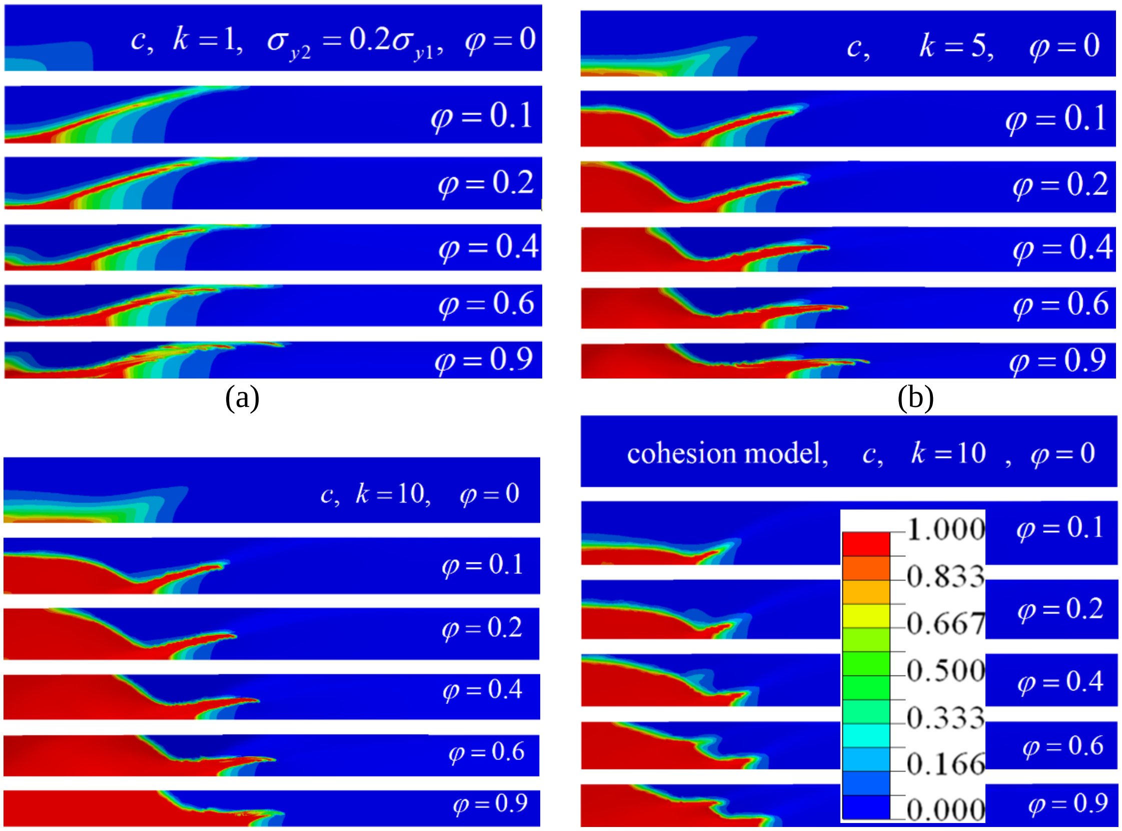

(a) (b)

(c) (d)

FIG. 2. Distribution of concentration c of a weaker $\left(\sigma_{y2}=0.2\sigma_{y1}\right)$ high-pressure phase with rising rotation angle φ under a constant compressive axial force F=3.75, for $r/R\le 0.72$ in Fig.1 (b). (a) k=1, (b) k=5, and (c) k=10 , all for the contact models with sliding and friction coefficient $\mu=0.3$; (d) k=10 cohesion model. Rotation angle is (1) 0, (2) 0.1, (3) 0.2, (4) 0.4, (5) 0.6, and (6) 0.9.

pressure phases, respectively. In this section, the primary goals are as follows: first, effects of some parameters in Eq. (8) on PTs and plastic flow will be studied. Specifically, by prescribing k= 1, 5, and 10, the effects of kinetic parameter k will be considered, and by prescribing σ_{y2}/σ_{y1} =0.2, 1, and 5, the weaker, equal-strength, and stronger high-pressure phases will be studied. Second, multiple experimental phenomena will be reproduced, which include oscillatory pressure distribution for weaker high-pressure phase, pressure self-multiplication effect, flow to the center of a sample, and small 'steps' on pressure distribution. Third, the main differences between current contact model with slip and the previous model with cohesion will be found. Friction coefficient $\mu = 0.3$ is accepted through this section; effect of variation of the friction coefficient on PT and plastic flow will be discussed in the Sec. IV.

Weaker high-pressure phase

We will discuss PTs and plastic flow in the sample for weaker high-pressure phase $\left(\sigma_{y2} = 0.2\sigma_{y1}\right)$ under the rising rotation angle at fixed compressive force *F*=3.75. During PT, the strength reduces which causes material instability and localization of strains and high-pressure phase distributions. Because of material instability, this case is qualitatively different from other two cases with equal and stronger high-pressure phases.

Fig. 2 exhibits the evolution of a weaker high-pressure phase concentration with growing rotation angle φ at fixed axial force for contact model for *k*=1, 5, and 10, and cohesion model. With the growth of the kinetic parameter *k*, the geometry of PT zone and rate of PT are quite different. For *k*=1, the rate of PT is much slower than the cases with *k*=5 and 10, and fully transformed (red) zone in Fig. 2(a) barely propagates towards contact surface in the center of a sample and slowly propagates towards periphery. Starting with $\varphi = 0.1$in Fig. 2(a), there is thin PT band which connects the center of sample (*r*= *z*=0) and contact surface, where plastic strain and PT are localized and strength in this region is lower than in the low pressure phase outside the band. With the growth of rotation angle, the torsion almost completely localizes inside this thin band and plastic strain almost does not spread outside of it (see Fig. 3(a)). Therefore, the region above this band twists almost like a rigid body together with an anvil, exhibiting a complete cohesion (Fig. 3(a)). Still, reduction in a sample thickness occurs by flow of material from this zone into shear band. It follows from Figs. 2(b) and (c) that geometry of PT zones for *k*=5 and 10 are mutually similar but differ from the cases for *k*=1, because the torsion does not spread within a thin PT and shear band only but through the whole sample, and plastic strain and the high pressure phase accumulate in the entire region from the symmetry plane to contact surface (Fig. 3).

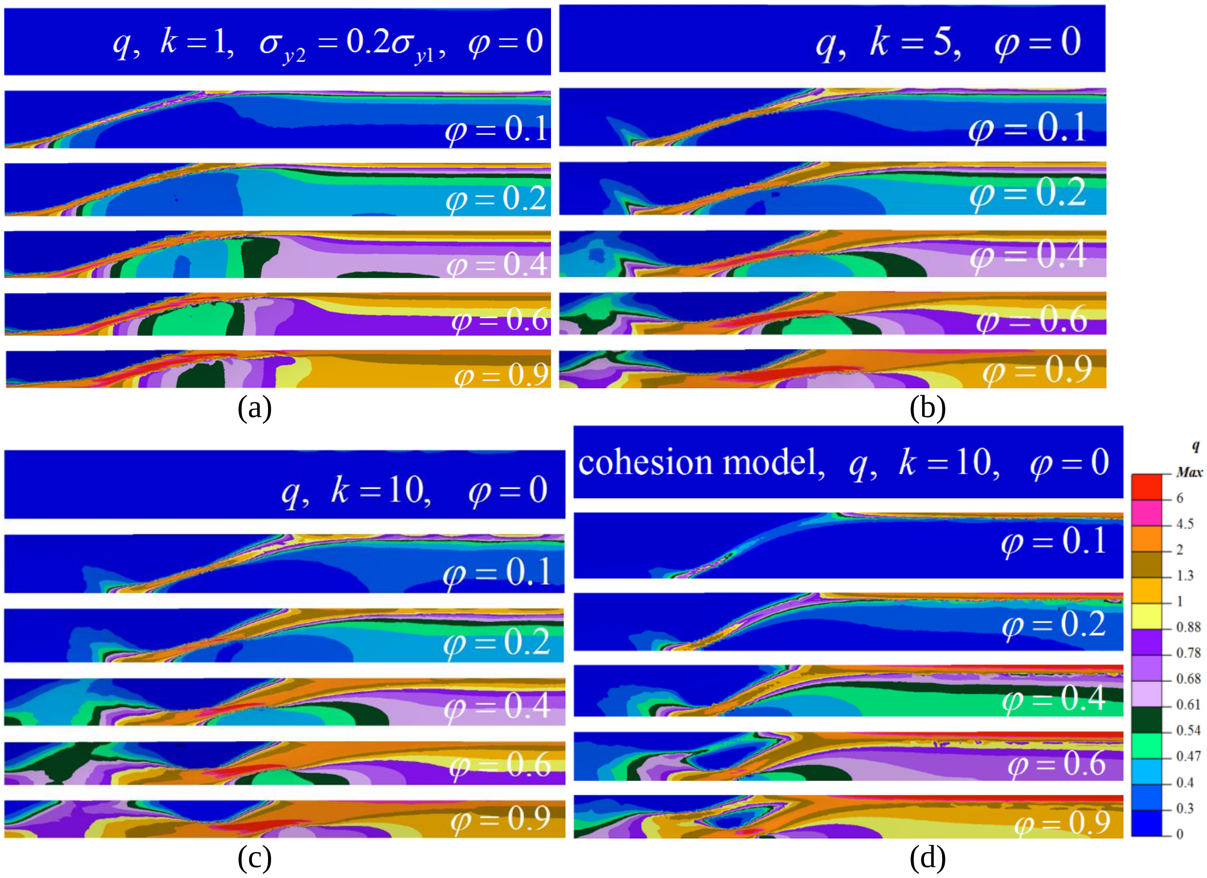

(a) (b)

(c) (d)

FIG. 3. Distribution of accumulated plastic strain *q* with rising rotation angle φ under a constant axial compressive force *F*=3.75, for $\sigma_{y2}=0.2\sigma_{y1}$, and $r/R=0.72$. (a) *k*=1, (b) *k*=5 and (c) *k*=10, all for the model with sliding and friction coefficient $\mu=0.3$; (d) *k*=10 for model with cohesion. Rotation angle is (1) 0, (2) 0.1, (3) 0.2, (4) 0.4, (5) 0.6, and (6) 0.9. The maximum *q* at $\varphi=0.9$ in the sample is 32.7, 50, 26.2, 30.1 for $k=$ 1, 5, 10 in contact models and $k=10$ in cohesion model respectively.

By comparing Figs. 2(c) and (d), it is evident that PT propagates faster when contact sliding is taken into consideration. This is true even without torsion ($\varphi=0$), which is consistent with results in Ref. 15. In all cases in this paper, torsion leads to the reduction in the sample thickness, as it was expected from simple analytical model[3]. However, thickness reduces more intensively with contact sliding, which leads to the increased "homogeneous" contribution to the plastic strain in the entire sample in comparison with the cohesion boundary condition. Indeed, accumulated plastic strain in the center of a sample, where PT occurs, grows faster for the contact model than for cohesion model (See in Fig. 3 (c) and (d)). There is a wider inclined yellow band with high accumulated plastic strain $\left(0.14 < r/R < 0.5\right)$ in Fig 3(c) than that in cohesion model, which connects symmetry plane and contact plane. This leads to intensification of the PT in the entire sample where $p > p_\varepsilon^d$. On the other side, for cohesion model plastic strain has stronger localization and accumulation near contact surface, but it mostly affects the region $r/R > 0.5$, where PT does not take place due to low pressure. Also, during torsion at a fixed axial force, due to condition of complete cohesion, accumulated plastic strain at the inclined surface $B'C'$ in Fig. 1(c) is artificially extremely large. However, when sliding is allowed, it occurs in this region due to small contact normal stress, and there is no plastic strain in the region close to the point C' at all.

Evolution of pressure p and high-pressure phase concentration c on the contact surface with the increasing rotation angle φ at fixed axial force is plotted in Fig. 4. One can note from Fig. 4(a) for k=1 that: 1) pressure grows from the periphery towards the center, which is followed by a drop of pressure due to volume reduction during the PT, and then it continues to rise again till the center of sample; 2) pressure at the center of a sample is higher than minimum pressure for direct PT p_ε^d but concentration is almost zero due to absence of plastic strain (see Fig. 3(a)), and 3) when rotation angle increases from 0.4 to 0.6, convective radial expansion (due to axial contraction) of PT zone without further PT is found because pressure is in the range $p_\varepsilon^r < p < p_\varepsilon^d$, where both direct and reverse PTs could not occur. Fig. 4(b) for *k*=10 shows that the pressure oscillations reduce due to more homogenous distribution of high-pressure phase and PT could not attain contact surface outside center of sample $\left(0.3 < r/R < 0.45\right)$ due to low pressure. Comparing solutions with and without contact sliding (Fig. 4 (b) and (c)), one can note that a higher pressure in the central zone for contact model (in addition to larger plastic strain) leads to a faster increase in *c* and broader completed high pressure phase region.

Note that oscillatory pressure distribution at the contact surface for weaker high-pressure phase was observed in experiments for CuI[23] and ZnSe[7]. Also, pressure increase at the center of a sample during rotation in Fig. 4, despite the volume reduction during PT, is consistent with experiments for ZnSe in Ref. 7.

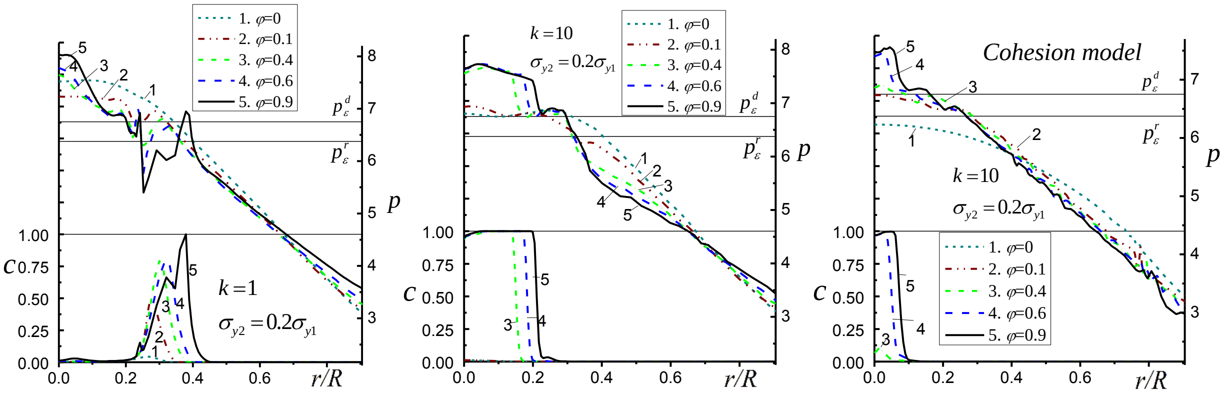

(a) (b) (c)

FIG. 4. Distributions of dimensionless pressure *p* and high-pressure phase concentration *c* at the contact surface during torsion under constant axial force *F*=3.75 for $\sigma_{y2} = 0.2\sigma_{y1}$. (a) *k*=1 and (b) *k*=10 (both for contact model), and (c) *k*=10 for cohesion model. Rotation angle is (1) 0, (2) 0.1, (3) 0.4, (4) 0.6, and (5) 0.9.

Equal strength phases

For strain-induced PTs for equal strength phases, results are completely different than in previous section, because of lack of phase softening, material instabilities, and strain and PT localization. The distribution of high-pressure phase in Fig. 5 is more regular; it is concentrated at the center of a sample, where pressure exceeds p_ε^d; and with the increase in parameter *k*, the rate of PT for contact model grows and width of two-phase region reduces. While for *k*=1 in Fig. 5(a) PT region is relatively small and PT is not completed in the major part of the region, for *k*=5 and 10 the entire central part of a sample is getting completely transformed. By comparing Figs. 5(b) with (d), the reduction in thickness is faster for the contact model than for case with cohesion, which is the primary source for larger accumulated plastic strain in the PT zone and intensification of PT when sliding is allowed.

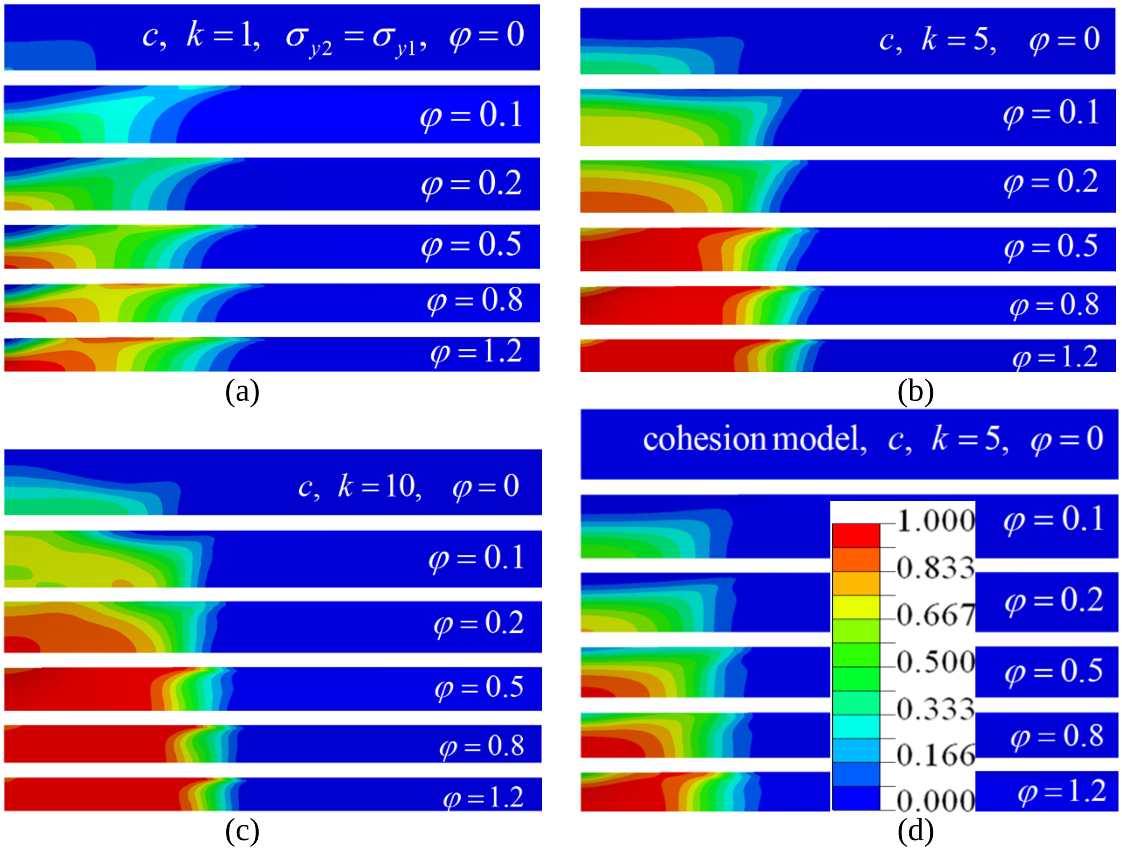

(a) (b) (c) (d)

FIG. 5. Evolution of distribution of high-pressure phase c with increasing rotation angle φ under a constant compressive axial force *F*=3.75, for *k*=1, 5, and 10, $\sigma_{y2}=\sigma_{y1}$, and $r/R \leq 0.72$. Rotation angle is (1) 0, (2) 0.1, (3) 0.2, (4) 0.5, (5) 0.8, (6) 1.2. (a) *k*=1, (b) *k*=5, and (c) *k*=10 for contact model, and (d) *k*=5 for cohesion model.

Distributions of pressure and concentration of high-pressure phase at the contact surface are presented in Fig. 6. For contact model in Fig. 6 (a) and (b), when φ changes from 0.1 to 0.5, PT propagates very fast at the contact surface and pressure increases at the center of sample and decreases at the periphery. However, further increase in rotation angle does not lead to essential PT progress and pressure does not change significantly as well. This is because region where pressure exceeds p_{ε}^{d} is almost completely transformed and expansion of the radius of high pressure phase occurs due to radial flow below p_{ε}^{d}. For cohesion model in Fig. 6 (c), pressure monotonously grows in PT region during torsion and PT is not completed. Comparison of Fig. 6(a) and Fig. 6(c) shows that allowing for contact sliding promotes PT both due to larger plastic strain and higher pressure in a broader region.

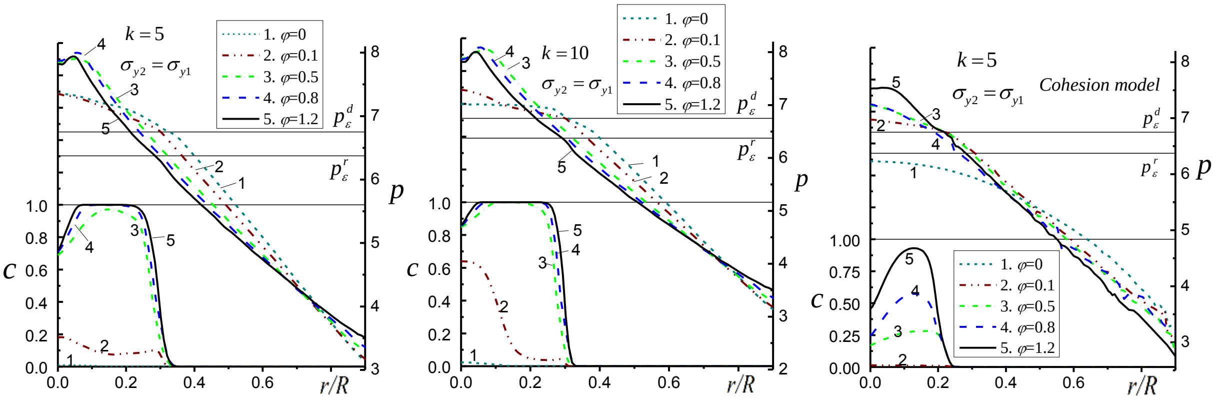

(a) (b) (c)

FIG. 6. Distributions of dimensionless pressure p and high-pressure phase concentration c at the contact surface under constant axial force F=3.75 with $\sigma_{y2}=\sigma_{y1}$ for contact model (a) with k=5 and (b) with k=10, and for cohesion model (c) with k=5. Rotation angle is (1) 0, (2) 0.1, (3) 0.5, (4) 0.8, (5) 1.2.

Distribution of the rotation angle β of the material points at the contact surface with respect to symmetry plane is shown in Fig. 7 for contact model for different rotations of an anvil $\varphi/2$ (which corresponds to β in the region with r very close to 0).

For cohesion model, $\beta = \varphi/2$ and all curves are horizontal. Horizontal parts in Fig. 7 for small r also mean that there is complete cohesion for these points. Sliding increases with increasing r. With the increasing rotation angle, slip occurs in a wider region and for $\varphi/2 = 0.6$, there is only very small region $(r/R < 0.08)$ without slipping. This is different from the case with a weaker high pressure phase, because during phase softening for $\sigma_{y2} = 0.2\sigma_{y1}$, the critical shear stress on contact surface could be much larger than the shear yield strength of high-pressure phase. That is why torsion of the contact surface transfers to the region with lower strength and leads to broader complete cohesion region at the sample center. One also can note that with the growth of kinetic parameter k, the slipping does not change significantly in Fig. 7. We would like to mention that the assumption in analytical model[3] that the rotation angle β is the same along the radius does not have support from the current results.

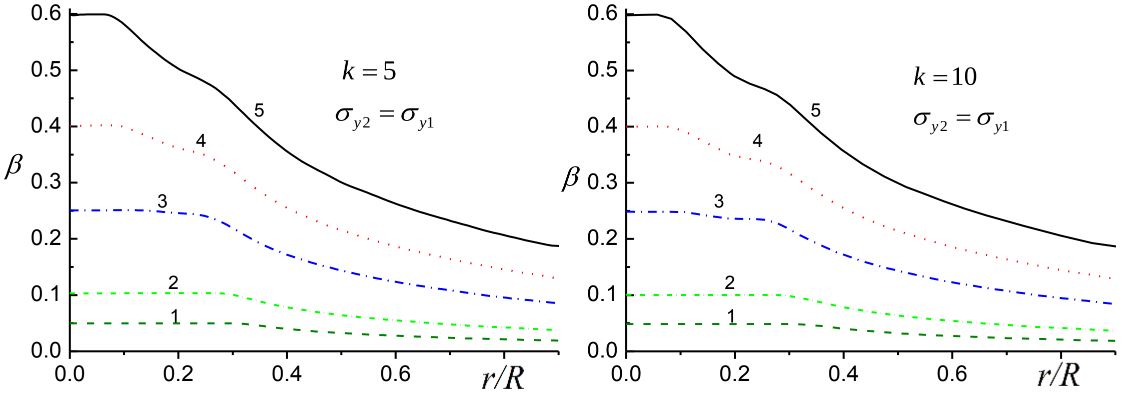

(a) (b)

FIG. 7. Distribution of the rotation angle β of the material points at the contact surface with respect to symmetry plane under constant axial force F=3.75 for (a) k=5 and (b) 10, $\sigma_{y2} = \sigma_{y1}$, and contact model for different angles of anvil rotation $\varphi/2$ which correspond to β for r close to 0.

Stronger high-pressure phase

We will discuss the simulation results for stronger high-pressure phase $\left(\sigma_{y2} = 5\sigma_{y1}\right)$, which are qualitatively similar to those for equal strengths of phases. Fig. 8 shows that PT starts at the center of sample and then propagates towards the contact surface and periphery. With the increase in rotation angle, the thickness of sample gradually reduces because of materials flow from the center to the periphery. With growth of kinetic parameter *k*, the rate of PTs increases and the width of two-phase region become thinner. It could be seen in Fig.8 (d) that at $\varphi = 1.1$, a quite sharp interface separates sample into complete high- and low-pressure phases. Comparing with cohesion model, the thickness of sample in contact model reduces much faster, which induces larger accumulated plastic strain and accelerates the PT.

Distribution of dimensionless pressure *p* and concentration *c* of high-pressure phase at the contact surface is presented in Fig. 9. In the PT zone, pressure increases significantly during PTs when rotation angle increases from 0.1 to 0.5, despite the volume reduction during the PT. This reproduces the pressure self-multiplication effect, which was experimentally observed in Refs. 2, 4, 9, 24. The reduction in sample thickness during torsion compensates the transformation-induced volume reduction; higher yield strength for high-pressure phase induces a rising friction stress (see Fig. 10(c)), and consequently leads to an increase in pressure. The pressure growth at the center of a sample during PT provides a positive feedback to accelerate PT kinetics, and also leads to pressure reduction at the periphery to keep a constant axial force. Small "steps" in the pressure distribution localized in the two-phase region become more obvious with growth of the kinetic parameter *k* in our simulations. Such steps have been observed in experiments for KCl and fullerene[2, 4, 9, 24]. Pressure at these steps is between p_ε^r and p_ε^d, which helps in determination of these parameters from experiments. Similar to the previous cases for weaker and equal-strength high pressure phases, larger growth of pressure and larger plastic strain in the center of a sample for contact model accelerates the PT kinetics in comparison with cohesion model in Fig. 9(d).

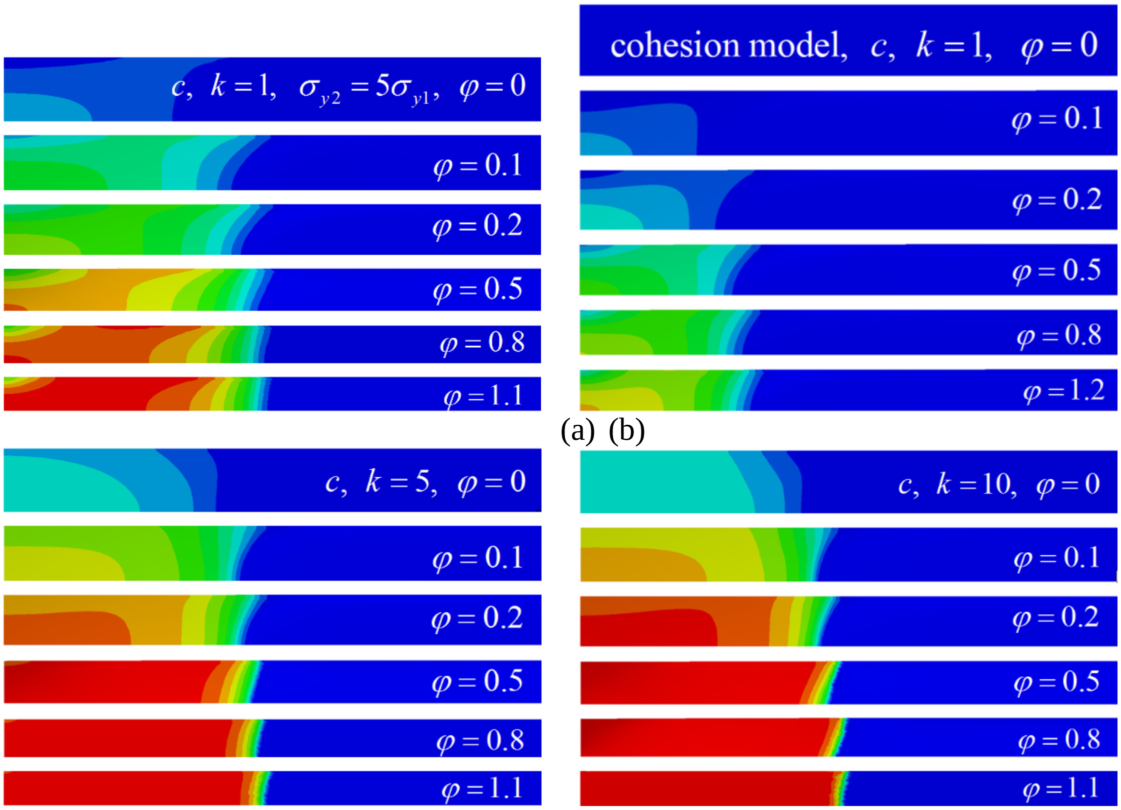

(c) (d)

FIG. 8. Distribution of concentration of high-pressure phase c with increasing rotation angle φ under a constant compressive axial force F=3.99 for k=1, 5, and 10; $\sigma_{y2}=\sigma_{y1}$, and $r/R \leq 0.72$. Rotation angle is (1) 0, (2) 0.1, (3) 0.2, (4) 0.5, (5) 0.8, (6) 1.1. (a) k=1, (c) k=5 and (d) k=10, all for the contact model, and (b) k=1 for cohesion model.

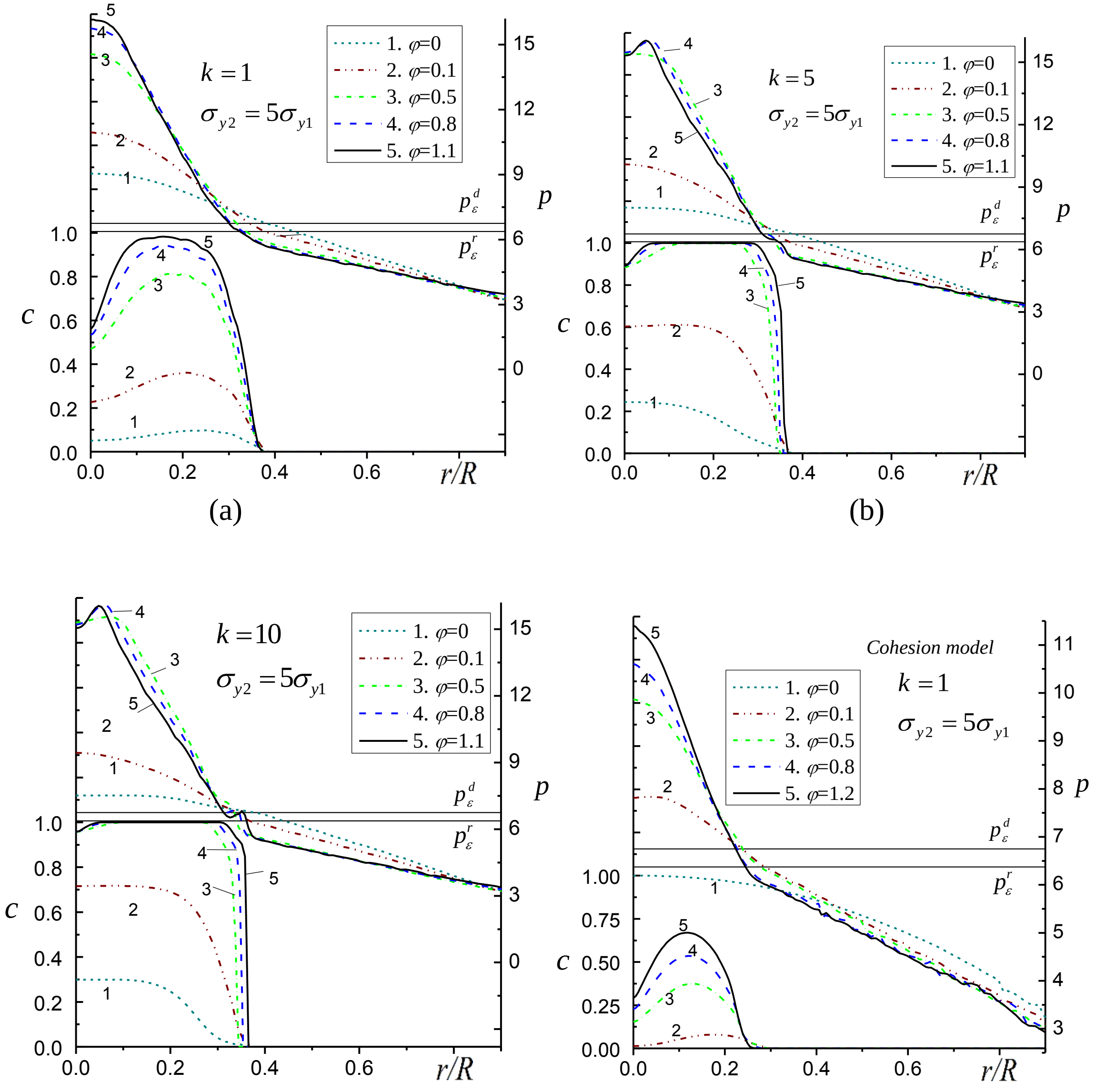

(a) (b)

(c) (d)

FIG. 9. Distributions of dimensionless pressure p and high-pressure phase concentration c at the contact surface under constant axial force F=3.99 for $\sigma_{y2} = 5\sigma_{y1}$. Rotation angle is (1) 0, (2) 0.1, (3) 0.5, (4) 0.8, (5) 1.1. (a) k=1, (b) k=5 and (c) k=10 for contact model and (d) k=1 for cohesion boundary conditions.

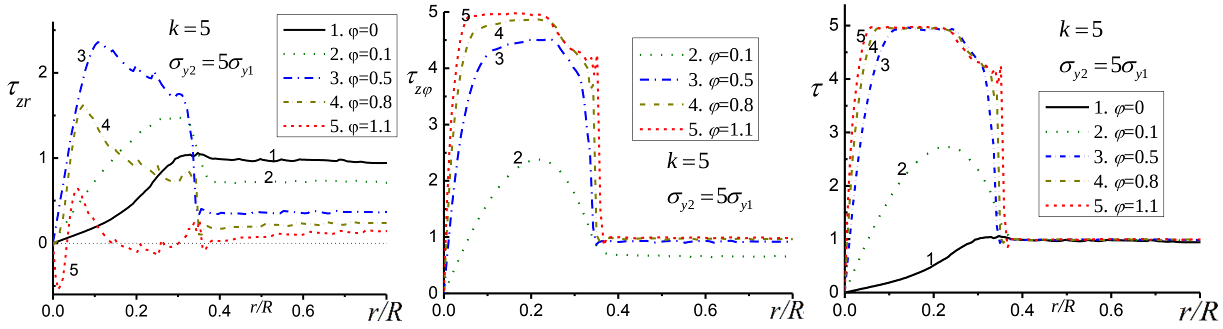

(a) (b) (c)

FIG. 10. Distribution of the dimensionless radial τ_{zr} (a), circumferential $\tau_{z\varphi}$ (b), and resultant friction stresses τ (c) at the contact surface normalized by τ_{y1}, for the contact model, under constant axial force F=3.99 for $k=5$ and $\sigma_{y2}=5\sigma_{y1}$. Rotation angle is (1) 0, (2) 0.1, (3) 0.5, (4) 0.8, (5) 1.1.

Fig. 10 shows the dimensionless radial τ_{zr}, circumferential $\tau_{z\varphi}$, and resultant friction stresses $\tau=\sqrt{\tau_{rz}^2+\tau_{z\varphi}^2}$ at the contact surface normalized by τ_{y1}. At $\varphi=0$, there is no circumferential component of friction stress and shear stress τ_{rz} at the periphery attains the shear strength limit τ_{y1} due to intense material flow towards periphery during compression. With the growth of rotation angle φ, both radial τ_{zr} and torsional $\tau_{z\varphi}$ shear stresses at the contact surface are almost homogenous in the low-pressure phase region; increase in $\tau_{z\varphi}$ is accompanied by a reduction in τ_{zr} to keep constant magnitude of the friction stress $\tau=\tau_{y1}$. At the initial stage of torsion, $\varphi<0.5$, both radial τ_{zr} and torsional $\tau_{z\varphi}$ shear stresses in the transforming region grow because of the increase of material strength during PT. At the later stage $\varphi>0.5$, when PT is almost completed in the region with $p>p_{\varepsilon}^{d}$ (see Fig. 9 (b)) and material strength does not change anymore, the increase of circumferential friction stress $\tau_{z\varphi}$ is accompanied by the reduction of radial component τ_{zr} to keep the magnitude of the friction stress $\tau = \tau_{y2}$. We should mention that the radial component τ_{zr} drops to a value slightly lower than zero in the region $r/R < 0.03$ because of a small volumetric reduction during PT there and a radial flow to the center; such a radial flow to the center is observed in experiments[7].

5.4 Effects of friction on phase transformation and plastic flow

In this section, the effects of friction coefficient μ on PT and plastic flow will be analyzed, and slipping and cohesion models will be further compared, considering examples for $\sigma_{y2} = \sigma_{y1}$ and *k*=5.

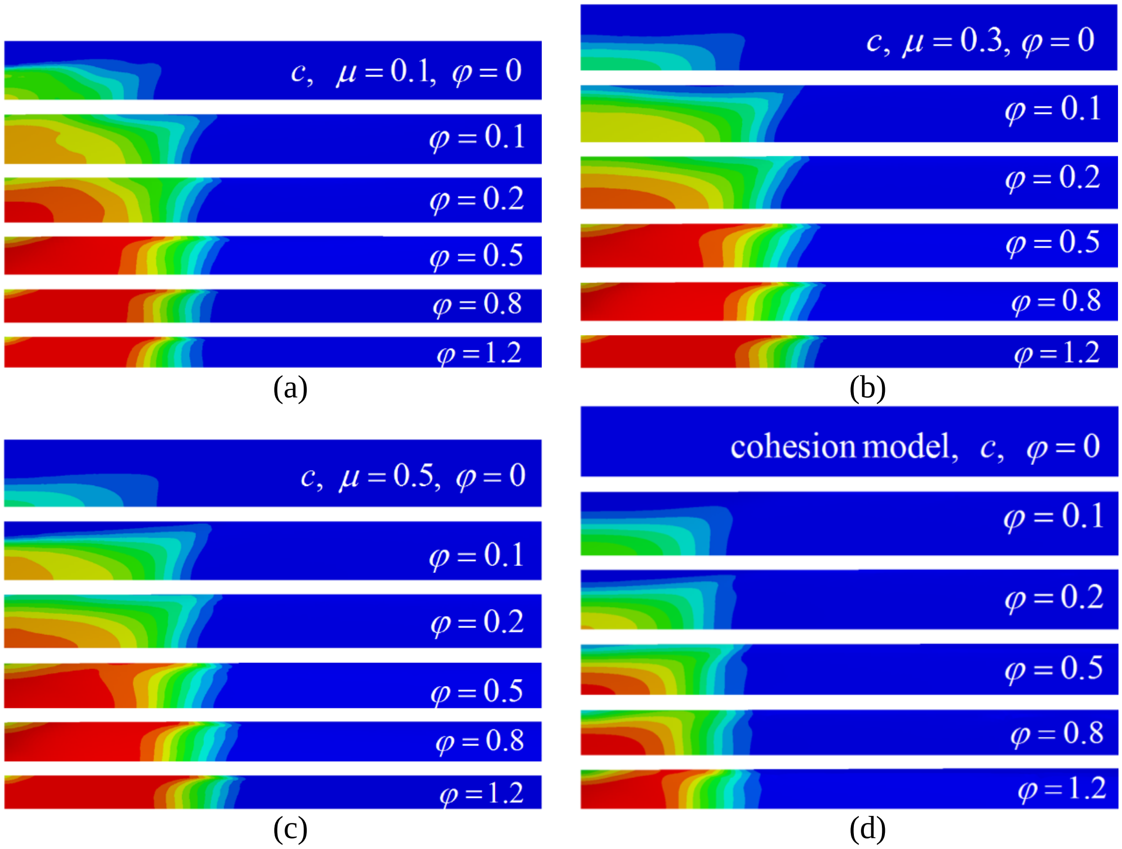

FIG. 11. Change in concentration of high-pressure phase *c* with growing rotation angle φ under a constant compressive axial force *F*=3.75, for *k*=5, $\sigma_{y2} = \sigma_{y1}$ and $r/R \leq 0.72$. Rotation angle is (1) 0, (2) 0.1, (3) 0.2, (4) 0.5, (5) 0.8, (6) 1.2. (a) , (b) and (c) are for the contact model with friction coefficients of 0.1, 0.3 and 0.5, respectively; (d) is for cohesion model.

Fig. 11 shows the evolution of high-pressure phase concentration for the contact model ($\mu = 0.1$, 0.3 and 0.5) and cohesion model. For compression, there is clear intensification of PT with transitions from cohesion to sliding and with reduction of the friction coefficient, which is consistent with our previous results[15]. For torsion, results are not so monotonous. It is clear that sliding promotes PT in comparison with cohesion conditions for any of friction coefficient and rotation angle. However, the effect of friction coefficient is more sophisticated. For $\varphi = 0.1$, when μ increases from 0.1 to 0.3, concentration c reduces at the center and contact surface. When μ increases from 0.3 to 0.5, concentration c increases at the center but reduces near contact surface. For $\varphi = 0.2$, when μ increases from 0.1 to 0.3, concentration c again reduces at the center and contact surface, but it changes slightly when μ increases from 0.3 to 0.5. For $\varphi = 0.5$, concentration of the high pressure phases is close for all of the friction coefficients under study. Finally, for $\varphi \geq 0.8$, concentration c μ=0.3 and 0.5 is close but radius of high pressure zone and fully transformed high pressure phase is larger for μ=0.3 and 0.5 than for 0.1. Such a nonmonotonous effect of the friction coefficient is caused by sophisticated, inhomogeneous, and nonlinear interaction between plastic strain and pressure fields (Figs. 12 and 13), torsion-induced reduction in sample thickness (Fig. 14), and radial and torsional friction stresses (Figs. 15 and 16) at the contact surface. Remarkably, for μ=0.1, slight reverse PT occurs for $\varphi > 0.5$ (Fig. 11(a)) because of local pressure reduction (Fig. 13(a)).

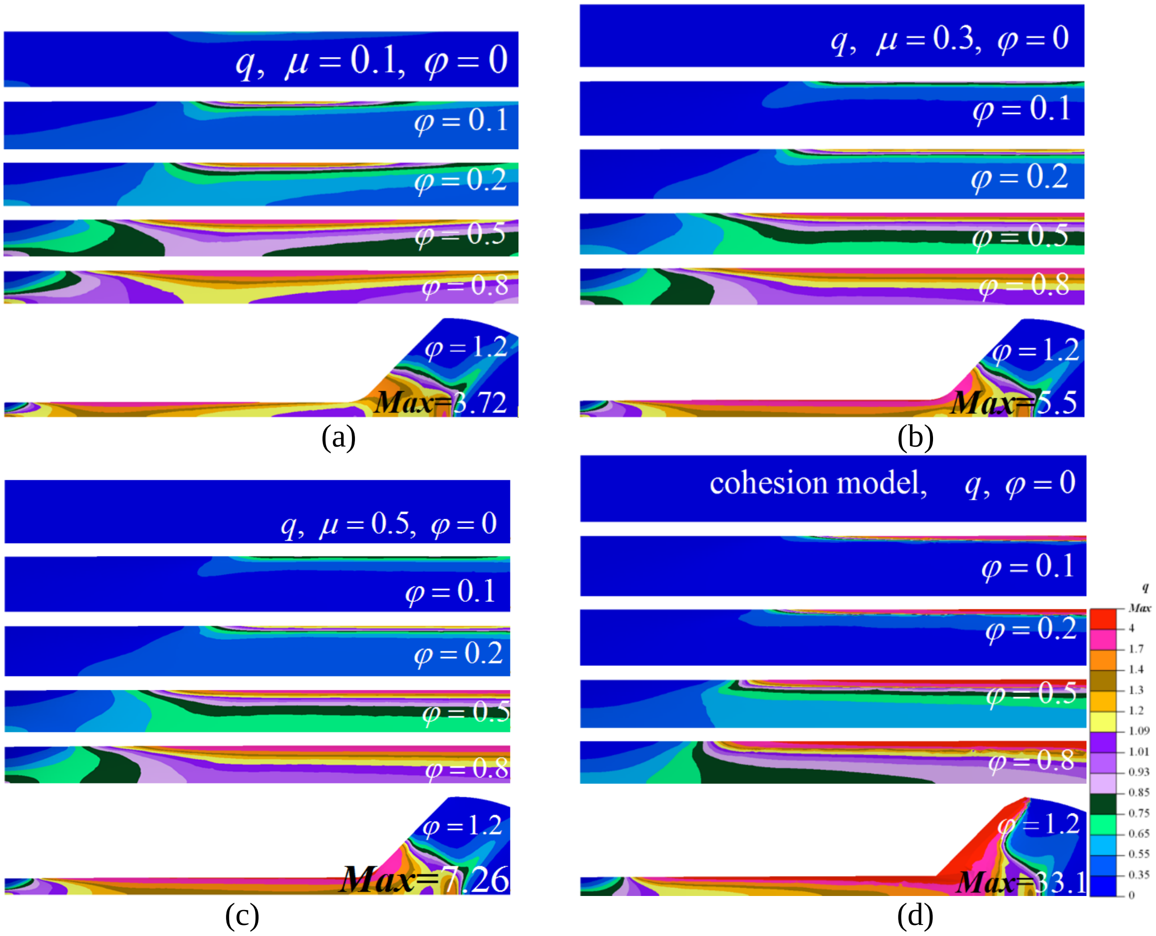

FIG. 12. Distribution of accumulated plastic strain q, for k=5, $\sigma_{y2} = \sigma_{y1}$, $r/R \leq 0.72$, friction coefficient (a) $\mu = 0.1$, (b) $\mu = 0.3$, and (c) $\mu = 0.5$; (d) is for cohesion model. Rotation angle is (1) 0, (2) 0.1, (3) 0.2, (4) 0.5, (5) 0.8, (6) 1.2.

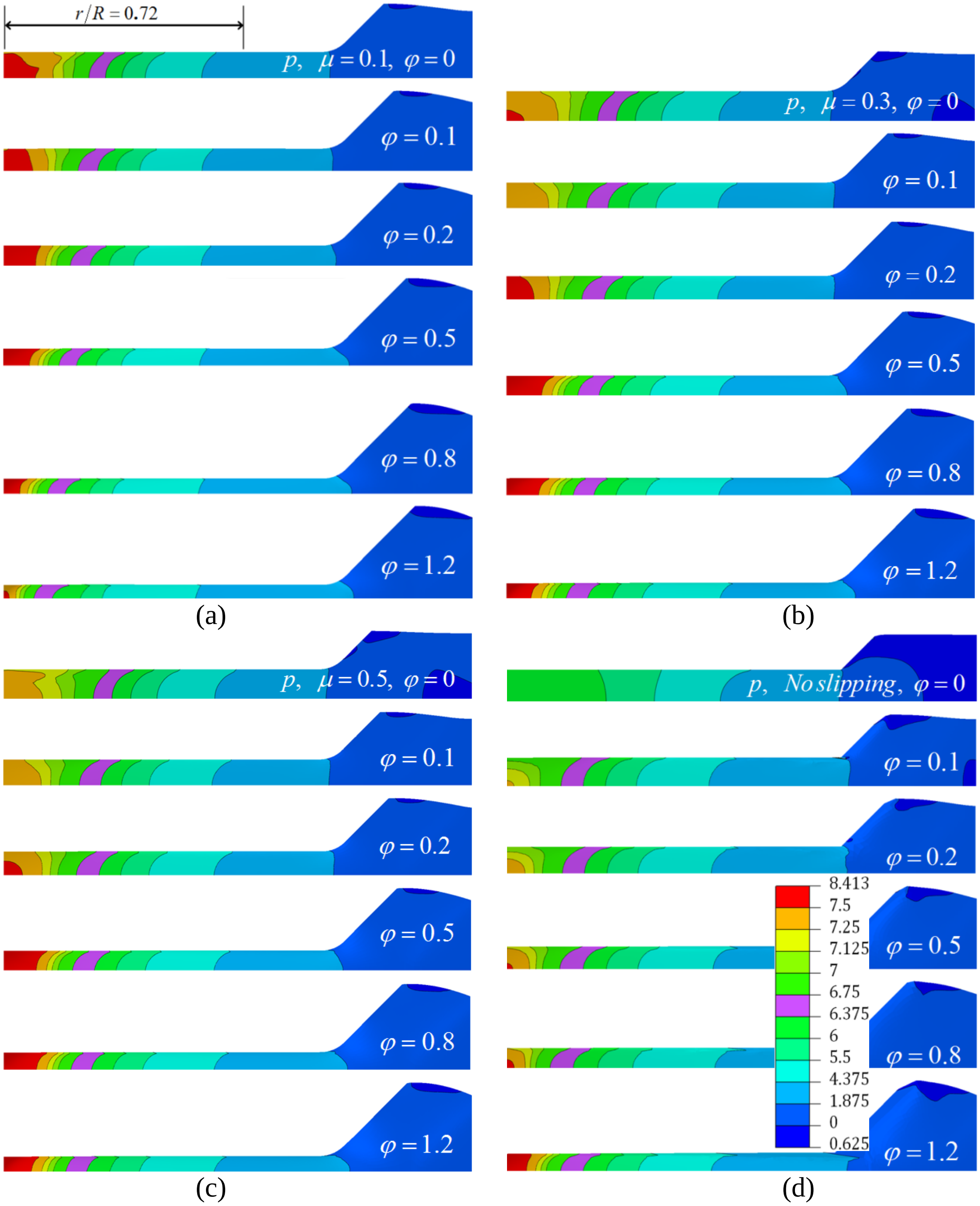

FIG. 13. Distribution of pressure for k=5, $\sigma_{y2} = \sigma_{y1}$, friction coefficient (a) $\mu = 0.1$, (b) $\mu = 0.3$, and (c) $\mu = 0.5$; (d) is for cohesion model. Rotation angle is (1) 0, (2) 0.1, (3) 0.2, (4) 0.5, (5) 0.8, (6) 1.2. Magenta region corresponds to $p_\varepsilon^r < p < p_\varepsilon^d$ and none of the PTs occurs in it.

With the growth of friction coefficient μ, accumulated plastic strain also does not change monotonously in PTs zone (Fig. 12). One of the contributions to plastic strain comes from the reduction in sample thickness during torsion (Fig. 14). The smallest reduction is for cohesion model; results for μ=0.5 and 0.3 are very close, and the largest reduction is for μ=0.1. Circumferential deformation produces large contribution to accumulated plastic strain, but it is localized close to the contact surface in the region $r/R > 0.5$, where the maximum accumulated plastic strain in the sample is located but PT does not occur due to low pressure. In particular, the maximum accumulated plastic strain at $\varphi = 1.2$ is equal to 3.72 ($\mu = 0.1$), 5.5 ($\mu = 0.3$), and 7.26 ($\mu = 0.5$) respectively. For cohesion model, a shear band is formed in the first layer of finite elements with the maximum plastic strain q=33.1 at $\varphi = 1.2$ (Fig. 12(d)). Thus, for a cohesion model solution is in principle mesh dependent, which is overcome in the contact model; in contact model, shear strain reduction from the contact surface to symmetry plane occurs gradually and for fine mesh is independent of the number of finite elements. In addition, sliding occurs in the inclined surface $B'C'$ (see Fig. 1(c)) in contact model, which avoids appearance of artificial large accumulated plastic strain in the region close to the point C' in cohesion model.

Pressure distributions are presented in Fig. 14. At the initial stage of torsion $\varphi < 0.5$, pressure in PT zone is higher for smaller friction coefficient, which promotes PT. At larger rotations, the area of the red zone with maximum pressure is the smallest one for $\mu = 0.1$. However, since the central region is completely transformed, this does not affect PT. What is important is the location of magenta region, in which $p_\varepsilon^r < p < p_\varepsilon^d$ and neither direct nor reverse PT occurs in it. High pressure phase is moved to this region by convective radial flow or this region moves toward high pressure phase. For $\mu = 0.1$, due to moving of magenta region toward the center, high pressure phase even reaches region with $p < p_\varepsilon^r$ and reverse strain-induced PT starts. For $\mu = 0.3$ and 0.5, magenta region also moves toward the center but the reverse PT does not start. For cohesion model, motion of "no-transformation" region is quite small. Since region with direct PT was smaller than for contact problems for any rotation angle, and reduction in thickness and convective flow of the high pressure phase was smaller as well, the final radial size of the transformed zone for cohesion is smaller than for contact problem for any μ.

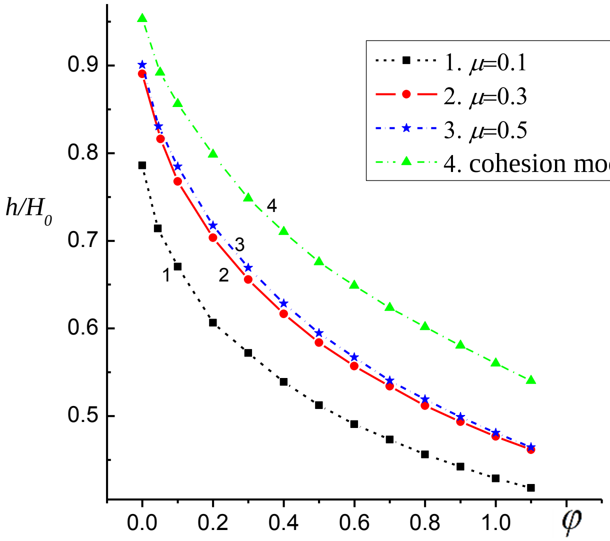

FIG. 14. Thickness of the sample h/H_0 in the deformed state normalized by initial thickness H_0 in the undeformed state versus rotation angle φ for $k = 5$, $\sigma_{y2} = \sigma_{y1}$, $\mu = 0.1$, 0.3 and 0.5, and cohesion model.

Note that radial flow of high pressure phase into low pressure region may lead to misinterpretation of experimental results. Indeed, experimentalists report PT pressure as the lowest pressure measured at the points where high pressure phase is detected. If high pressure phase flowed to the region in which $p_\varepsilon^r < p < p_\varepsilon^d$, it will not transformed back; if it flowed to the region in which $p < p_\varepsilon^r$, reverse PT may not complete. Thus, experimentalists may report PT pressure lower than the actual value. Allowing for contact sliding promotes radial flow and increases the probability and magnitude of misinterpretation.

Distribution of radial τ_{zr} and torsional $\tau_{z\varphi}$ friction stresses in Figs. 15 and 16 shed some light on the occurring processes. For $\mu = 0.1$ and $\varphi = 0$, friction stress could not reach the yield strength in shear because sliding starts when the critical shear stress $\mu\sigma_n$ is attained. Low friction caused large reduction in thickness during compression. Similar, during torsion the magnitude of the friction force τ did not reach τ_y and both radial and circumferential friction stresses reduce linearly for $r/R > 0.4$. However, the magnitude of the friction force τ reaches τ_y for $\mu = 0.3$ in quite large region, both for compression and torsion, which limits radial flow and thickness reduction. The same is true for $\mu = 0.5$, which explains small difference between these two cases.

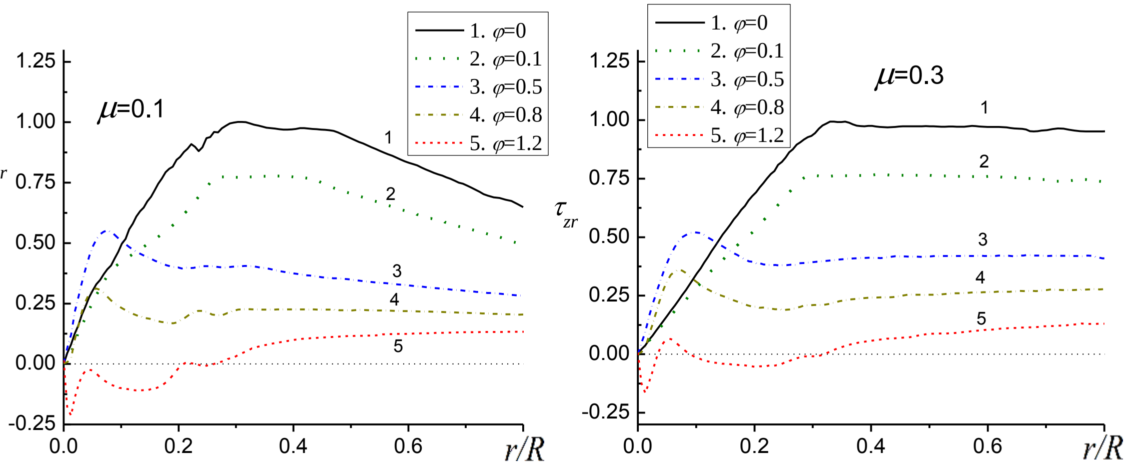

(a) (b)

FIG. 15. Distribution of dimensionless radial friction stresses τ_{zr} at the contact surface for k=5, $\sigma_{y2} = \sigma_{y1}$, (a) $\mu = 0.1$ and (b) $\mu = 0.3$.

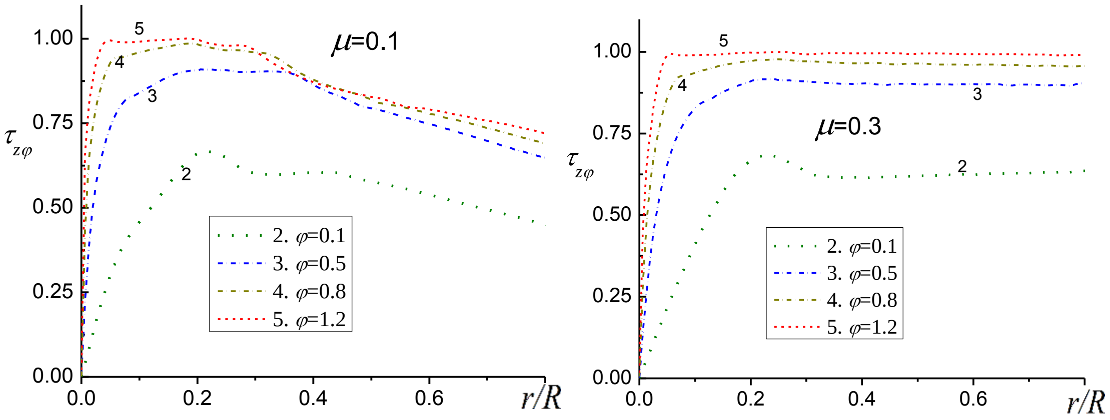

(a) (b)

FIG. 16. Distribution of dimensionless circumferential friction stresses $\tau_{z\varphi}$ at the contact surface for *k*=5 and $\sigma_{y2} = \sigma_{y1}$, (a) $\mu = 0.1$ and (b) $\mu = 0.3$.

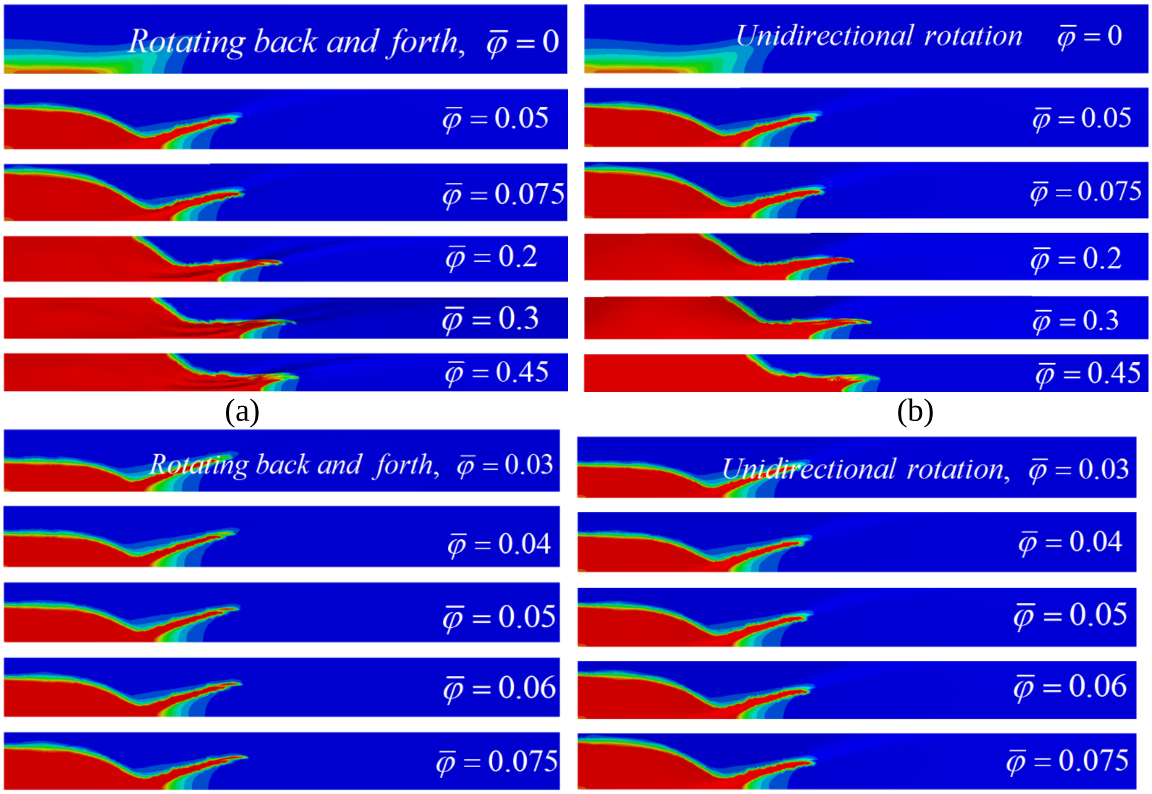

(a) (b)

(c) (d)

FIG. 17. Concentration c of a weaker $\left(\sigma_{y2} = 0.2\sigma_{y1}\right)$ high-pressure phase with rising accumulated rotation angle $\bar{\varphi}$ under constant compressive axial force *F*=3.75, for *k*=10, and $\mu = 0.3$. After first rotation with $\Delta\varphi_i = 0.05$ (a) and 0.002 (c), respectively, back and forth rotation with the increments $|\Delta\varphi_i| = 0.1$ (a) and 0.004 (c), is performed; (b) and (d): unidirectional rotation is applied.

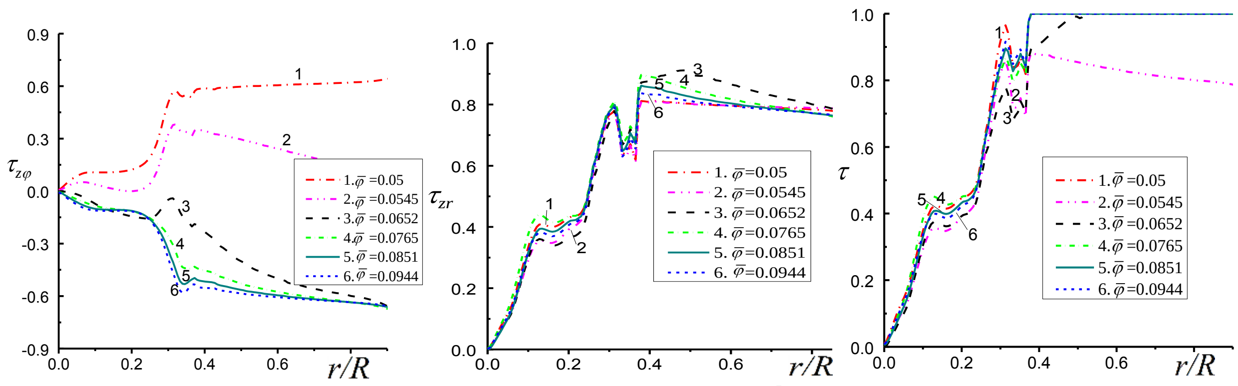

(a) (b) (c)

FIG. 18. Distribution of dimensionless circumferential $\tau_{z\varphi}$ (a), radial τ_{zr} (b), and resultant τ (c) friction stresses at the contact surface for the contact model, $k = 10$, and $\sigma_{y2} = 0.2\sigma_{y1}$, under constant axial force F=3.75. After first rotation with, back and forth rotation with the increments $|\Delta\varphi_i| = 0.1$ is applied.

5.5 Effects of change in rotation directions

In the previous sections, diamond anvil was rotated in one direction. In many experiments, back and forth rotations with different magnitude are utilized^{25}. One of the reasons for such a loading is that it leads to smaller radial shift of the center of one anvil with respect to another, reducing misalignment and probability of breaking anvils. Keeping geometry closer to axisymmetric also increases accuracy of pressure measurement. However, such a loading was never studied numerically to find out what are the differences in comparison with unidirectional rotation. This problem will be treated in this Section. We define the accumulative rotation angle between one anvil and symmetry plane, $\bar{\varphi} = \sum_i |\Delta\varphi_i|$, where $\Delta\varphi_i$ is the rotation increment relative to the symmetry plane for back (negative) or forth (positive) anvil rotation. In Fig. 17, after first rotation with $\Delta\varphi_i = 0.05$ and 0.002, respectively, back and forth rotation with the increments $|\Delta\varphi_i| = 0.1$ and 0.004, respectively, are compared with the unidirectional rotation with the same accumulated rotation in terms of concentration distribution. There is no obvious difference in high-pressure phase concentration c for $|\Delta\varphi_i|=0.1$ and there is slightly larger fully transformed zone for unidirectional rotation for $|\Delta\varphi_i|=0.004$. Fig. 18, which exhibits variation of the circumferential $\tau_{z\varphi}$, radial τ_{zr} , and resultant τ friction stresses after change in rotation direction allows one to better understand the reasons for the above results. The circumferential friction stress reduces its magnitude, changes direction, but then practically restores its magnitude at $\bar{\varphi}=0.0795$. The distribution of the radial friction stress slightly oscillates during this process but in the first approximation can be considered unchanged. The distribution of the resultant friction stress restores faster than the circumferential stress. While for $0.05<\bar{\varphi}<0.0652$ cohesion condition is satisfied at the periphery, for $\bar{\varphi}\geq 0.0652$ contact slip occurs again, making conditions close to those before change in rotation direction. Thus, there is a small difference between conditions for unidirectional and two directional rotations, which cause small differences in concentration distribution, but these changes accumulate with increasing number of cycles. Because total number of back and forth cycles is just 4 at $\bar{\varphi}=0.45$, there is no obvious change in concentration distribution in Figs. 17(a) and (b). However, when the number of cycles increases, e.g., to 19 in Fig. 17 (c), the obvious reduction in high-pressure phase concentration is found. This reduction is related to change in contact conditions at the periphery from slipping to cohesion for some rotation stage, which reduces radial flow and plastic strain, and further leads to slower PT kinetics.

5.6 Concluding remarks

In this paper, the effect of contact sliding and friction coefficient at the anvil-sample contact surface on the pressure distribution, plastic flow, and strain-induced PT is studied during torsion at the constant axial force in RDAC using FEM and code ABAQUS. User subroutines USDFLD and HETVAL are implemented to consider a stain-controlled kinetics for PT. Coulomb and plastic friction are combined, which are implemented with the help of user subroutine FRIC. Results are obtained for weaker, equal-strength, and stronger high pressure phases and for three values of the kinetic coefficient *k*. Cohesion model possessed three main drawbacks: (a) shear band was developed near the contact surface in the one finite element wide layer, i.e., solution was mesh-dependent; (b) cohesion at the conical surface where pressure is small and large sliding is expected is very artificial and leads to artificial large plastic deformation in that region; (c) increased resistance to the radial plastic flow suppresses it as well as reduction in thickness leading to unrealistic redistribution of plastic deformation and concentration of high pressure phase. All these drawbacks are overcome in the current contact formulation. Thus, contact sliding leads to gradual reduction in shear strain away from the contact surface and for fine mesh it is independent of the number of finite elements. Sliding at the conical surface eliminates plastic strain in the adjacent region. In comparison with complete cohesion model, sliding and reduction in friction coefficient intensify radial plastic flow, which leads to larger reduction in sample thickness and "homogeneous" contribution to the plastic strain. Larger plastic strain and increased pressure in the central region, as well as growth of the region where $p > p_{\varepsilon}^{d}$ lead to intensification of PT. Reduction in plastic strain in the shear band near contact surface does not affect PT essentially, because it occurs in the region $r/R > 0.5$, where PT does not take place due to low pressure. Sliding increases with increasing *r* and rotation angle and is weakly dependent on the kinetic coefficient *k*. Also, with the increasing rotation angle, slip occurs in a wider region closer to the center. However, for a weaker high pressure phase, shear localization occurs within a volume due to phase softening. Cohesion zones also do not change as fast as for equal and higher strength phases. The assumption in analytical model[3] that the rotation angle of the material points at the contact surface is the same along the radius does not correspond to the obtained results. For compression, there is a clear intensification of PT with reduction of the friction coefficient. For torsion, results are not monotonous. PT is promoted in one region but decelerated in another, depending on the friction coefficient and rotation angle. Such a nonmonotonous effect of the friction coefficient is caused by sophisticated, inhomogeneous, and nonlinear interaction between plastic strain and pressure fields, torsion-induced reduction in sample thickness, and radial and torsional friction stresses at the contact surface. Remarkably, for μ=0.1, slight reverse PT occurs for $\varphi > 0.5$ because of local pressure reduction. Convective radial flow of high pressure phase into low pressure region (where it cannot appear) may lead to misinterpretation of experimental results: experimentalists report PT pressure as the pressure measured at the points where high pressure phase is detected, i.e., they may report PT pressure lower than the actual value. Allowing for contact sliding promotes radial flow and increases the probability and magnitude of misinterpretation. It is found that back and forth rotation of an anvil slightly decelerates PT progress in comparison with unidirectional rotation and this can be visible after large number of cycles. Several experimental phenomena, including pressure self-multiplication effect at constant axial force (despite the volume reduction due to PT), small steps at pressure distribution, flow to the center of a sample, and oscillatory pressure distribution for weaker high-pressure phase, are reproduced and interpreted.

Developed approach allows us to address strain-induced PT in a two material system, i.e., sample within gasket, which is often used in experiments [6, 8, 9]. With cohesion condition, sample-gasket boundary would be artificially fixed at the diamond surface. Considering sample with gasket and providing quasi-homogeneous pressure distribution[9] will allow us to develop a method of determination of PT kinetic equation from experiments.

Acknowledgments

The support of Army Research Office (W911NF-12-1-0340) managed by Dr. David Stepp, Defense Advanced Research Projects Agency (W31P4Q-13-1-0010) managed by Dr. Judah Goldwasser, and Iowa State University is gratefully acknowledged.

References

[1] M. M. Alexandrova, V. D. Blank, and S. G. Buga, Solid State Phys. **35**, 1308 (1993).

[2] V. D. Blank, Y. Y. Boguslavsky, M. I. Eremets, E. S. Itskevich, Y. S. Konyaev, A. M. Shirokov, and E. I. Estrin, Zh. Eksp. Teor. Fiz. **87**, 922 (1984).

[3] V. I. Levitas, Phys. Rev. B **70**, 184118 (2004).

[4] N. V. Novikov, S. B. Polotnyak, L. K. Shvedov, and V. I. Levitas, J. of Superhard Mater. **3**, 39 (1999).

[5] V. D. Blank, Z. H. Malyushitska, and B. A. Kulnitskiy, High Press. Phys. Eng. **3**, 28 (1993).

[6] C. Ji, V. I. Levitas, H. Zhu, J. Chaudhuri, A. Marathe, and Y. Ma, P. Natl. Acad. Sci. USA **109**, 19108 (2012).

[7] V. D. Blank and S. G. Buga, Instrum. Exp. Tech. **36**, 149 (1993).

[8] V. I. Levitas, Y. Z. Ma, E. Selvi, J. Z. Wu, and J. A. Patten, Phys. Rev. B **85**, 054114 (2012).

[9] V. I. Levitas, Y. Z. Ma, J. Hashemi, M. Holtz, and N. Guven, J. Chem. Phys. **125** 044507 (2006).

[10] V. I. Levitas and O. M. Zarechnyy, J Phys. Chem. B **110**, 16035 (2006).

[11] V. D. Blank and G. A. Dubitsky, *High pressure science and technology*, Proc. Joint XV AIRAPT and XXXIII EHPRG International Conf. (Warsaw) ed W. A. Trzeciakowski (London: World Scientific Publishing) **pp** 325-7 (1995).

[12] V. I. Levitas and O. M. Zarechnyy, Phys. Rev. B **82**, 174123 (2010).

[13] V. I. Levitas and O. M. Zarechnyy, Phys. Rev. B **82**, 174124 (2010).

[14] V. I. Levitas and M. Javanbakht, Phys. Rev. B **86**, 140101(R) (2012).

[15] B. Feng, V. I. Levitas, and O. M. Zarechnyy, J. Appl. Phys. **114** (2013), http://dx.doi.org/10.1063/1.4816050 (In press).

[16] B. Feng, O. M. Zarechnyy, and V. I. Levitas, J. Appl. Phys. **113** 173514 (2013).

[17] V. I. Levitas, J. Mech. Phys. Solids **45**, 923 (1997).

[18] V. I. Levitas, J. Mech. Phys. Solids **45**, 1203 (1997).

[19] O. M. Zarechnyy, V. I. Levitas, and Y. Z. Ma, J. Appl. Phys. **111** 023518 (2012).

[20] V. I. Levitas, *Large Deformation of Materials with Complex Rheological Properties at Normal and High Pressure* (Nova Science, New York, 1996).

[21] V. I. Levitas, Int. J. Solids Struct. **35**, 889 (1998).

[22] Abaqus V6.11. Abaqus User Subroutines Reference Manual: HETVAL and USDFLD. Providence RI, USA: ABAQUS INC. (2011).

[23] S. S. Batsanov, N. R. Serebryanaya, V. D. Blank, and V. A. Ivdenko, *Crystallography Rep.* **40**, 650 (1995).

[24] V. D. Blank, S. G. Buga, M. Y. Popov, V. A. Davydov, and V. Agafonov, New J. Chem. **19**, 149 (1995).

[25] M. M. Aleksandrova, V. D. Blank, A. E. Golobokov, Yu. S. Konyaev and E. I. Estrin, *Solid State Phys* **29** 2573 (1987).

CHAPTER 6. STRAIN-INDUCED PHASE TRANSFORMATIONS UNDER COMPRESSION IN A DIAMOND ANVIL CELL: SIMULATIONS OF A SAMPLE AND GASKET

Modified from a paper published in Journal of Applied Physics

Biao Feng,[1] Valery I. Levitas,[2,*] and Yanzhang Ma[3]
1) Department of Aerospace Engineering, Iowa State University, Ames, Iowa 50011, USA

2) Departments of Aerospace Engineering, Mechanical Engineering, and Material Science and Engineering, Iowa State University, Ames, Iowa 50011, USA

3) Department of Mechanical Engineering, Texas Tech University, Lubbock, Texas 79409, USA

Abstract

Combined high pressure phase transformations (PTs) and plastic flow in a sample within a gasket compressed in diamond anvil cell (DAC) are studied for the first time using finite element method (FEM). The key point is that phase transformations are modelled as strain-induced, which involves a completely different kinetic description than for traditional pressure-induced PTs. The model takes into account contact sliding with Coulomb and plastic friction at the boundaries between the sample, gasket and anvil. A comprehensive computational study of the effects of the kinetic parameter, ratio of the yield strengths of high and low-pressure phases and the gasket, sample radius and initial thickness on the PTs and plastic flow is performed. A new sliding mechanism at the contact line between the sample, gasket, and anvil called extrusion-based pseudoslip is

---

* Corresponding author.
Email: vlevitas@iastate.edu

revealed, which plays an important part in producing high pressure. Strain-controlled kinetics explains why experimentally determined phase transformation pressure and kinetics (concentration of high pressure phase vs. pressure) differ for different geometries and properties of the gasket and the sample: they provide different plastic strain, which was not measured. Utilization of the gasket changes radial plastic flow toward the center of a sample, which leads to high quasi-homogeneous pressure for some geometries. For transformation to a stronger high pressure phase, plastic strain and concentration of a high-pressure phase are also quasi-homogeneous. This allowed us to suggest a method of determining strain-controlled kinetics from experimentation, which is not possible for weaker and equal-strength high-pressure phases and cases without a gasket. Some experimental phenomena are reproduced and interpreted. Developed methods and obtained results represent essential progress toward the understanding of PTs under compression in the DAC. This will allow one optimal design of experiments and conditions for synthesis of new high pressure phases.

6.1 Introduction

A DAC is a powerful and primary tool to generate high pressure and *in-situ* study the material physical behavior and PTs to high pressure phases, by using advanced diagnostics, such as Raman, x-ray, and optical techniques.[1-5] In some cases the material under study is compressed between two diamond anvils without any external support,[6-8] i.e., the external part of the sample serves as a gasket for the internal part, which is under high pressure. However, in most cases[9-14], the sample is placed inside of a deformable gasket made of a material with different strength. If achieving maximum possible pressure in a reasonably large volume is the goal, the gasket is made of the strongest possible materials, such as T301 stainless steel[13], rhenium[10, 15], and even diamond powder[16]. If the goal is just to avoid an intense flow of powder sample at the initial stage of compression, a weak gasket could be made of polymer, paper, or cardboard. Utilization of the gasket, in particular, allows one: 1) Performing experiments under hydrostatic conditions by filling gasket hole with fluid, in which sample is placed. 2) Performing experiments under reduced nonhydrostatic (deviatoric) stresses by filling the gasket hole with media with low yield strength (e.g., neon, argon, mixture of methanol and ethanol, cesium iodide[17], and sodium chloride[17, 18]), in which the sample is placed. 3) Reducing plastic flow in a sample from the center and causing flow to the center, thus increasing pressure level. 4) Reducing radial pressure gradients and even producing an almost homogeneous pressure distribution[19, 20]. This allows one to perform a quantitative study of phase transformations and achieve complete phase transformation in a sample. This also reduces the probability of fracture of an anvil, because without the gasket, pressure grows at the center above the level required for transformation, or grows at the center after completing phase transformation in the central region during transformation at the periphery. Detailed discussions of the effect of a gasket can also be found in Refs. 11, 21, 22.

Within a liquid the sample is subjected to hydrostatic loading and undergoes pressure-induced phase transformations. Without hydrostatic media, or above the solidification pressure for transmitting media, the sample is under nonhydrostatic stresses or stress tensor. Moreover, if there is an irreversible reduction in the sample thickness, significant plastic straining in the sample may drastically affect phase transformations through changing their mechanism, as it was recognized in Refs. 23, 24. For pressure-induced or stress-tensor-induced phase transformations below the yield strength of the material, a high pressure phase nucleates at pre-existing defects, e.g., dislocations, that represent pressure and stress concentrators. In contrast, plastic strain-induced PTs under high pressure occur by nucleation at new defects, which are continuously generated during plastic deformation[23, 24]. Thus, dislocations as the main kind of defects are generated and densely piled up against grain boundaries or other obstacles during plastic flow, which creates a strong concentrator of the stress tensor and may lead to an obvious reduction of threshold pressure for PTs. For example, the rhombohedral-to-cubic boron nitride (rBN-to-cBN) transformation under compression without hydrostatic media starts at 5.6 GPa[8], while it takes place at 55Gpa under hydrostatic conditions[9]. A corresponding analytical model[23] and much more detailed finite element simulations[25] are developed to elucidate strain-induced nucleation at dislocation pile ups. The best way to study strain-induced PTs and the effect of plastic strain on thermodynamics and kinetics of PTs is to utilize combined compression and torsion loading in a rotational diamond anvil cell[19, 20, 26-29]. However [23, 24], there is no fundamental difference between strain-induced PTs under plastic compression in traditional DAC and under pressure and shear in rotational DAC in terms of mechanism, thermodynamics, and kinetics. The only difference is in the pressure-plastic strain loading path: while in rotational DAC one can increase plastic strain at constant pressure, in traditional DAC both pressure and plastic strain grow during compression of a sample, and the effect of plastic strain on PT thermodynamics and kinetics is not easy to separate.

In experiments under nonhydrostatic conditions in DAC, PT is characterized by pressure for initiation of transformation (e.g., Refs. 8, 12, 18) and, in rear cases, for completing PT, and the pressure-concentration of high pressure phase curve[20]. Results for the same materials differ essentially in different papers[12, 17-20, 30]. In some cases the reason is specified, e.g., transmitting media with different yield strength (degree of nonhydrostaticity)[18]. In most cases without transmitting media, the reasons for discrepancy are not clear. However, if one would consider *PT as strain-induced rather than pressure-induced, the difference is caused by different plastic strain, which was not measured*. Different geometric parameters and elastoplastic properties of the gasket and sample lead to different plastic strains and, consequently, transformation pressure and pressure-concentration of high pressure phase curves. Thus, experimental results *do not characterize thermodynamic and kinetics of a sample material* but represent complex behavior of the sample-gasket (and, at very high pressure, anvil) system. This is also the reason that the threshold pressure for PTs under non-hydrostatic condition differs for different types of high-pressure apparatuses, due to distinct degrees of plastic flows. For example, when different gaskets and high-pressure apparatuses are utilized, PT of the highly ordered hexagonal BN to wBN are found at 9.6 GPa[19, 20], 10 Gpa[12] and 12.5 Gpa[30] respectively.

Thus, there is clear necessity to consider phase transformations under compression of a sample in a gasket as *strain-induced rather than pressure-induced*. Note that pressure-induced PTs in DAC have been modelled in Refs. 31, 32 using theory developed in Refs. 33, 34 and FEM algorithm in Refs. 35, 36, which are very much different from the current paper. Since plastic strain field in a sample is not measured directly, the only way to gain understanding and develop combined experimental and theoretical methods of characterization is to develop corresponding models and perform simulations. In comparison with pressure-induced PTs, strain-induced ones are not just terminologically different, but require completely different thermodynamic and kinetic descriptions, as well as experimental characterization. Nanoscale models and mechanisms of strain-induced PTs at dislocations generated during plastic flow are presented in Refs. 23, 25. Based on the understanding gained at the nanoscale, a microscale theory is developed[23, 37]. In this theory, strain-induced PTs are described (characterized) by a pressure-dependent, strain-controlled (instead of time-controlled) kinetic equation (see Eq. (8)), for concentration of the high-pressure phase *c*, which depends on four main parameters: (1) kinetic parameter *k*, which scales the rate of PTs, (2) the minimum pressure p_ε^d, below which direct strain-induced PT does not take place, (3) the maximum pressure p_ε^r, above which reverse strain-induced PT cannot occur, and (4) the ratio of yield strengths of low (σ_{y1}) and high-pressure (σ_{y2}) phases. This is an equation which ideally should be found from experiments. However, it was not done before because there is only one paper[20] where the distribution of concentration of high-pressure phase along the contact surface diamond-sample was measured and plastic strain distribution was not measured in literature at all. That is why the simulation of strain-induced PTs in DAC[38-41] and rotational DAC[42-44] have been performed for generic material and the effect of the four material parameters above have been elucidated. Simulations first have been performed with complete adhesion between sample and diamond[39-41, 43, 44] and then with allowing for contact sliding[38, 42], and it was demonstrated that contact sliding significantly affects all fields and should be included. However, all these papers are devoted to sample without gasket. It is known from experiments that pressure distribution, and character and intensity of plastic flow with and without the gasket are completely different. That is why in the current paper we will study for the first time strain-induced PTs in a sample within a gasket. This is computationally a more complex problem, because it contains one more contact surface between sample and gasket and, more importantly, contact line between sample, gasket and anvil. This introduces additional nonlinearities and often causes divergence of the iterative procedure.

In this paper, strain-induced PTs under compression of a sample in DAC including a gasket are modeled and simulated. A coupled problem is solved using FEM for PT and mechanics with large plastic flow and contact sliding at all three contact surfaces, which thus leads to high complexity in simulations. The combined effect of the following parameters on phase transformation kinetics and heterogeneity of the pressure, concentration of high pressure phase, and accumulated plastic strain fields in the sample has been studied: kinetic parameter *k*, which scales the rate of PTs; the ratio of yield strengths σ_{y2}/σ_{y1} of phases; ratio of the yield strength of gasket and sample σ_g/σ_{y1}; relative radius and height of a sample. A gasket with essentially higher strength than a sample could fundamentally change direction and heterogeneity of plastic flow and contact friction, causing a more homogeneous pressure field, which would change PT kinetics. It was demonstrated that any pressure p -concentration c of high pressure phase curve is not related directly to PT kinetics but represents the behavior of a sample-gasket system, which determines the pressure – plastic strain loading curve. That explains why gaskets with different strength and geometric parameters change pressure for initiation and completion of PT and the entire *p*-*c* curve. In particular, the growth of pressure required to continue and complete PT is not a necessity or a fundamental property of the

PT. It is just consequence that in DAC plastic straining creating nucleation sites cannot be produced without pressure increase. If such a straining would be produced at constant pressure, like in rotational DAC, PT could occur at much lower pressure (see Refs. 19, 20, 26-29).

Many of obtained results are essentially different from previous results[38-41] for DAC without a gasket or even have opposite trends. Utilization of a gasket changes radial plastic flow toward center of a sample, which leads for some geometries to high quasi-homogeneous pressure. For transformation to a stronger high-pressure phase, plastic strain and concentration of high pressure phase are also quasi-homogeneous. This allows us to suggest a method of determination of strain-controlled kinetics from experiments. This is not possible for a weaker or equal-strength high-pressure phase and case without a gasket, for which a completely transformed high pressure phase near the sample-anvil boundary is separated from almost an untransformed low pressure phase by a very sharp interface. A new sliding mechanism at the contact line between sample, gasket, and anvil called extrusion-based pseudoslip is revealed, which plays an important part in producing high pressure. Some experimental phenomena are reproduced and interpreted.

6.2. Problem formulation

A. Geometry and boundary conditions

A scheme of DAC subjected to an axial compressive force P is shown in Fig. 1 (a). Due to symmetries of the load and geometry, a quarter of DAC is taken into consideration. In Fig. 1(b), a quarter of an initial undeformed sample (the rectangle $oabe$) is encapsulated into the gasket's hole and they contact along the cylindrical surface be. The initial thickness of the sample and gasket inner side is H_0; the thickness of a gasket at the periphery is $H_1 + H_0 \left(H_1 = m \cdot H_0\right)$; sample radius ab is $R_s = n \cdot H_0$; and the radius of flat surface of a diamond anvil is $R = 5H_1 = 5m \cdot H_0$. Effects of gasket size on PT and plastic flow will be studied by changing parameters *n* and *m*. The contact algorithm in ABAQUS requires the smooth master surface in a contact pair (referring to the surfaces of a diamond anvil) to avoid penetration of slave surface (referring to a gasket surface) into it. Consequently, a small fillet radius $r_0 = H_1/2$ is utilized to substitute the sharp corners of the diamond anvil and gasket at point *c*. The geometry of the inclined contact surface *cd* is shown in detail in Fig.1 (c). The point *b* in Fig. 1 (b) is the intersection of three contacting bodies: sample, anvil, and gasket. Due to smooth contact for each contact pair, penetration of slave surface into master surface does not occur and a sharp 90^o angle is utilized at the corners of the sample and gasket at point *b* in the initial undeformed state in Fig.1 (b). Boundary conditions in Fig. 1(d) are accepted as follows:

(1) The contact sliding conditions (which will be characterized in Sec. II.C) are applied on all contact pairs between three different components, namely the diamond with the gasket and sample, and the gasket with the sample.

(2) At symmetry axis $r = 0$, shear stress τ_{rz} and radial displacement u_r are zero.

(3) Due to symmetry, the radial shear stress $\tau_{rz} = 0$ and the axial displacement $u_z = 0$ on the symmetry plane *z*=0.

(4) Surfaces of the gasket which are not in contact with the diamond anvil or sample are stress-free.

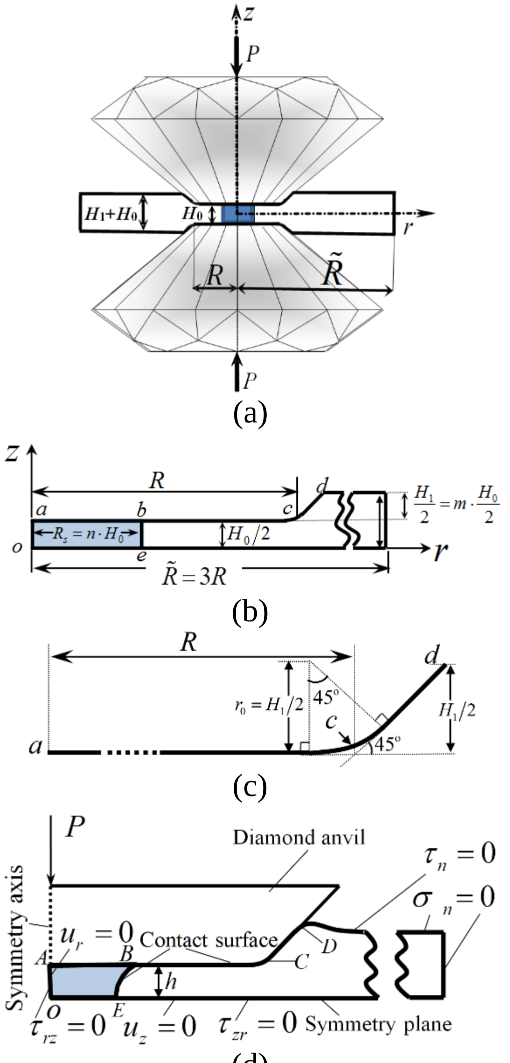

(a)

(b)

(c)

(d)

FIG. 1. (a) Diamond anvil cell scheme, (b) a quarter of the sample and gasket in the initial undeformed state, (c) geometry of the contact surface in the undeformed state, and (d) boundary conditions for sample and gasket in the deformed state.

B. Material model

Similar to Refs. 38-44, the simplest isotropic, perfectly plastic model for the sample and also for the gasket will be utilized to obtain the generic solutions. The deformation of a material is described by the position vector of the particle in the deformed state $\boldsymbol{r}=\boldsymbol{r}(\boldsymbol{r}_0,t)$, as a function of its position $\boldsymbol{r}_0$ in the initial (undeformed) configuration and time *t*. The multiplicative decomposition of the deformation gradient,

$\boldsymbol{F} = \partial \boldsymbol{r} / \partial \boldsymbol{r}_0 = \boldsymbol{V}_\mathrm{e} \cdot \boldsymbol{F}_\mathrm{t} \cdot \boldsymbol{F}_\mathrm{p}$, into symmetric elastic stretch tensor $\boldsymbol{V}_e$, transformational $\boldsymbol{F}_t$, and plastic $\boldsymbol{F}_p$ contributions is accepted. While elastic and transformational strains are assumed small (i.e., $\boldsymbol{\varepsilon}_e = \boldsymbol{V}_e - \boldsymbol{I}$ and $\boldsymbol{\varepsilon}_t = \boldsymbol{V}_t - \boldsymbol{I}$, where $\boldsymbol{I}$ is the second-rank unit tensor), plastic strains and material rotations are large. Since the gasket material does not undergo phase transformation, $\boldsymbol{F}_\mathrm{t} = \boldsymbol{I}$. The justification of the applicability of this perfectly plastic and isotropic model independent of the deformation history could be found in Ref. [45] for various materials (e.g. rocks, powder, metals) starting with accumulated plastic strain $q > 0.6 \div 1$, and under monotonous loading. In addition, for simplification, diamond anvils are assumed to be a rigid body in this paper, which is reasonable when small elastic strain assumption in the sample and gasket is made (but large plastic deformation and sliding are allowed). A total system of equations for the problem of coupled strain-induced PT and mechanics with plastic flow in a sample is utilized in the simulations as follows:

Decomposing the deformation rate $\boldsymbol{d} = \left(\dot{\boldsymbol{F}} \cdot \boldsymbol{F}^{-1} \right)_s$ into elastic (subscript *e*), transformation (subscript *t*), and plastic (subscript *p*) components:

$$\boldsymbol{d} = \overset{\nabla}{\boldsymbol{\varepsilon}}_e + \dot{\varepsilon}_t \boldsymbol{I} + \boldsymbol{d}_p . \tag{1}$$

Hooke's law for deviatoric and volumetric parts of the Cauchy stress $\boldsymbol{T}$

$$\boldsymbol{s} = 2G \, dev \boldsymbol{\varepsilon}_e ; \qquad p = -\frac{\sigma_{rr} + \sigma_{\phi\phi} + \sigma_{zz}}{3} = -K \varepsilon_{e0} . \tag{2}$$

Transformation volumetric strain:

$$\varepsilon_t = \bar{\varepsilon}_t c . \tag{3}$$

Von Mises yield condition for two-phase mixture

$$\sigma_i = \left(\frac{3}{2}\boldsymbol{s}:\boldsymbol{s}\right)^{0.5} \le \sigma_y; \qquad \sigma_y = \begin{cases} (1-c)\,\sigma_{y1} + c\sigma_{y2} & \text{for sample} \\ \sigma_{yg} & \text{for gasket} \end{cases} . \tag{4}$$

Plastic flow rule in the elastic region:

$$\sigma_i < \sigma_y \qquad \rightarrow \qquad \boldsymbol{d}_p = 0 . \tag{5}$$

in the plastic region:

$$\sigma_i = \sigma_y \qquad \rightarrow \qquad \boldsymbol{d}_p = \lambda \boldsymbol{s}\,; \quad \lambda \ge 0 . \tag{6}$$

Equilibrium equation:

$$\nabla \cdot \boldsymbol{T} = 0 . \tag{7}$$

Based on the microscale theories[23, 37], strain-induced PTs were characterized in terms of strain-controlled, pressure-dependent kinetic equation:

$$\frac{dc}{dq} = 10k\,\frac{(1-c)\bar{p}_d H(\bar{p}_d)\dfrac{\sigma_{y2}}{\sigma_{y1}} - c\bar{p}_r H(\bar{p}_r)}{c + (1-c)\sigma_{y2}/\sigma_{y1}} . \tag{8}$$

Here c is concentration of high-pressure phase; the accumulated plastic strain q is defined by $\dot{q} = (2/3\boldsymbol{d}_p : \boldsymbol{d}_p)^{1/2}$; $\bar{p}_d = \dfrac{p - p_\varepsilon^d}{p_h^d - p_\varepsilon^d}$ and $\bar{p}_r = \dfrac{p - p_\varepsilon^r}{p_h^r - p_\varepsilon^r}$ are dimensionless characteristic pressures, which are used for direct and reverse PTs; p_h^d and p_h^r are the pressures at which direct and reverse PTs occur under hydrostatic loading, respectively; H is the Heaviside step function; subscript s means the symmetric part of tensor; $\overset{\nabla}{\boldsymbol{\varepsilon}}_e$ and $\overset{\nabla}{\boldsymbol{s}}$ is the objective Jaumann time derivative of the elastic strain and deviatoric stress; ε_{e0} and $\bar{\varepsilon}_t$ are the elastic volumetric strain and transformation volumetric strain for complete PT;

K and G are the bulk and shear moduli, respectively; σ_i is the stress intensity or effective stress. Parameter λ is iteratively updated by satisfaction of the yield condition (4); and subscript y, $y1$, and $y2$ are for the yield strength for the sample with concentration $0 \le c \le 1$, $c = 0$, and $c = 1$, respectively.

For gasket material, which does not undergo phase transformations, Eqs. (3) and (8) are irrelevant; in Eq. (1) $\dot{\varepsilon}_t = 0$; in Eqs. (4)-(6) c is irrelevant and the yield strength σ_y is equal to the yield strength of a gasket σ_{yg}.

C. Friction model

This section focuses on the introduction of the friction model between sample and diamond or between sample and gasket. Due to axial symmetry, the direction of relative sliding is known (to within its sign): it is along the curve ABCD between diamond and sample and gasket, and along the curve BE between sample and gasket, without circumferential component. The contact behavior between diamond and gasket is similar and even simpler due to an absence of strength changes in materials. In standard Coulomb friction, the slippage on the contact surface initiates only when friction stress τ arrives at the critical friction stress $\tau_{crit} = \mu\sigma_n$ where σ_n is normal contact stress. While standard Coulomb friction is reasonable in the elastic state, once friction stress on the contact surface reaches the yield strength in shear $\tau_y = \sigma_y / \sqrt{3}$ (von Mises yield condition (4) is used here) in plastic state, slipping can occur even if $\tau < \mu\sigma_n$. As a consequence, the standard Coulomb friction could be modified by redefining the critical friction stress as $\tau_{crit} = \min(\mu\sigma_n, \tau_y)$, and conditions of sliding and cohesion are separated when friction stress τ reaches this value. In principle, the critical friction stress for the contact pair between sample and gasket should be defined as $\tau_{crit} = \min(\mu\sigma_n, \tau_y, \tau_{yg})$, where τ_{yg} is the yield strength in shear for gasket. The gasket with higher yield strength than sample is utilized in most cases to produce high pressure. Therefore, we accept $\tau_{crit} = \min(\mu\sigma_n, \tau_y)$. Theoretically, such a definition of the critical friction stress, along with sliding rule, is sufficient for a solution of the contact problem. However, in numerical simulations, the sudden change of contact conditions between cohesion and slip may result in divergence of results, especially for the large sliding problem with complex contact conditions (e.g. at point B in Fig. 1(d), where there are three different contact pairs). A penalty method is utilized to make the contact conditions continuous, in which cohesion condition will be substituted with a small elastic reversible slippage u^e. While penalty method is a mathematical regularization, this elastic slip could be also physically interpreted as elastic deformation of asperities of the thin contact layer. In addition, the elastic slip u^e should be constrained in the small range to obtain an accurate solution, for example, the specified maximum elastic relative slip u_{crit} equals 0.5% of average element length for fine-meshing models. Note that there are more than 25 finite elements in the current simulations within half of the thickness of a sample along the *z*-axis.

One could introduce the magnitude of elastic slip by the simplest linear relation with shear stress τ, $\tau = k_s u^e$, where k_s is elastic slip stiffness. The magnitude of k_s could be defined by the condition that sliding starts when elastic slip u^e reaches the prescribed critical value u_{crit}. Then one obtains $\tau_{crit} = k_s u_{crit}$ and $k_s = \tau_{crit} / u_{crit}$. Consequently, k_s linearly varies with the normal stress σ_n or the yield strength in shear

τ_y. Coupling between PTs and sliding occurs because τ_y for the sample is not a constant but depends on concentrations and yield strengths of phases by relation: $\tau_y = (1-c)\tau_{y1} + c\tau_{y2}$. The complete system of equations for contact pairs is summarized below, and to some extent it is similar to that for elastoplasticity theory.

Decomposing contact relative displacement u^c into elastic (reversible) and sliding (irreversible) parts:

$$u^c = u^e + u^s . \tag{9}$$

Yield strength in shear:

$$\tau_y = \begin{cases} (1-c)\tau_{y1} + c\tau_{y2} & \text{for sample} \\ \tau_{yg} & \text{for gasket} \end{cases} \cdot \tag{10}$$

Critical friction shear stress:

$$\tau_{crit} = \min(\tau_y,\ \mu\sigma_n) . \tag{11}$$

Rule for elastic contact displacement:

$$\begin{cases} u^e = \dfrac{\tau \cdot u_{crit}}{\tau_y} & if \quad \mu\sigma_n > \tau_y \\ u^e = \dfrac{\tau \cdot u_{crit}}{\mu\sigma_n} & if \quad \mu\sigma_n \le \tau_y \end{cases} \tag{12}$$

Sliding rule below critical shear stress:

$$|\tau| < \tau_{crit} \quad \rightarrow \quad \dot{u}^s = 0 . \tag{13}$$

Sliding rule at critical shear stress:

$$\begin{cases} \tau = \pm\ \mu\sigma_n & if \quad \mu\sigma_n \le \tau_y \\ \tau = \pm\tau_y & if \quad \mu\sigma_n > \tau_y \end{cases} \rightarrow \qquad Sign(\dot{u}^s) = Sign(\tau) \tag{14}$$

D. Numerical procedure

To solve pressure-dependent strain-controlled kinetic Eq. (8), ABAQUS user subroutines USDFLD and HETVAL are implemented, in which concentration c is modeled by temperature and transformation strain is treated as thermal strain. Further, the coupled mechanics and PT problem is simulated by a coupled thermo-plasticity problem.

For contact pairs between sample and gasket or between sample and diamond anvil, the critical friction stress is defined as $\tau_{crit} = \min(\mu\sigma_n, \tau_y(c))$ and yield strength in shear $\tau_y(c)$ is not constant but depends on concentration c and yield strengths of phases. That is the reason why the contact problem could not be solved by the standard procedure in ABAQUS and the user subroutine FRIC should be utilized to consider Eqs. (12)-(14). For a particular case, when high- and low-pressure phases have the same yield strengths $\left(\tau_{y1} = \tau_{y2}\right)$, yield strength in shear is independent of concentration and becomes a constant. In this case, the contact problem could be also solved by standard procedure without using the subroutine FRIC, which could be utilized to confirm the consistency of results obtained with FRIC and the standard procedure. For the contact pair between diamond anvil and gasket, standard procedure in ABAQUS can be utilized as well.

In the dimensionless form, except for friction shear stress normalized by the yield strength in shear τ_{y1}, all stress-related parameters (e.g., pressure p, parameter p_h^d, etc.) are normalized by σ_{y1}; the dimensionless compressive force F is the axial force P normalized by the product of σ_{y1} and the undeformed contact area (which is equal to the area of the surface of revolution produced by complete revolution of the curve $abcd$ in Fig. 1(b) about the z-axis). The related material parameters as follow: $p_h^d = 33.75$,

$p_h^r = -1$, $p_\varepsilon^d = 6.75$, $p_\varepsilon^r = 6.375$, Young modulus $E = 162.5$, Poisson's ratio $\nu = 0.3$, volumetric transformation strain for direct PT $\bar{\varepsilon}_t = -0.1$, and *k*=6 if there is no special note. In addition, the yield strength for the gasket $\sigma_{yg} = 3\sigma_{y1}$ is utilized in the major parts of this paper. A high value of p_h^d and a low value of p_h^r, which will not be reached in our simulations means that pressure-induced phase transformations are excluded.

6.3. Simulation results for coupled plastic flow and phase transformation

Strain-induced PT coupled with plastic flow under high pressure in a sample within a gasket will be discussed. As stated in Refs. 38-41, the strength of high-pressure phase strongly influences the kinetics of PT and plastic flow in a traditional diamond anvil cell. Similarly, in this section, the cases with equal-strength, weaker, and stronger high-pressure phases will be investigated by assuming $\sigma_{y2}/\sigma_{y1} = 1, 0.3, 3$ respectively. In addition, the kinetic parameter *k* in Eq. (8) determines the rate of PT and will also be studied. In Fig. 1(b) *m*=1, *n*=2 and the gasket yield strength $\sigma_{yg} = 3\sigma_{y1}$ are used throughout this entire section; the effects of gasket strength and sizes will be investigated in detail in the next section. To understand the effects of PT on the plastic flow and pressure, the model without PT will be utilized for comparison.

A. Equal-strength phases

For equal strengths between high- and low-pressure phases $\left(\sigma_{y2} = \sigma_{y1}\right)$, Fig. 2 (a) shows that the PT in the sample propagates from the contact surface to the symmetry plane, and from the periphery to the center, and that the fully-transformed sample is obtained without large reduction of sample thickness, which are completely different from the results[38-41] in DAC without the gasket. In the previous simulations[38-41], the PT progresses from the center to the periphery. Due to the absence of the gasket, there is a large pressure gradient and maximum pressure is located at the center of a sample, which intensifies the PT kinetics.

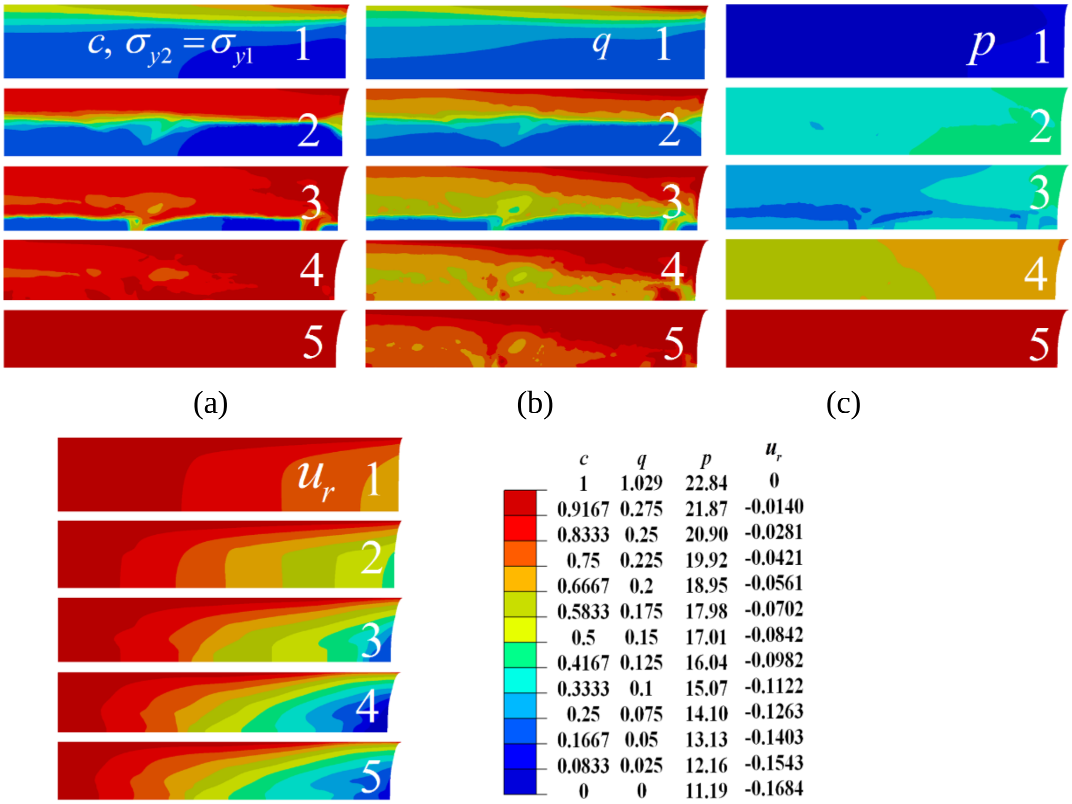

(a) (b) (c)

(d)

FIG. 2. Distributions of (a) concentration of high-pressure phase c, (b) accumulated plastic strain q, (c) pressure p, and (d) radial displacement u_r (normalized by a half thickness of undeformed sample $H_0/2$) in the sample for $\sigma_{y2}=\sigma_{y1}$. The increasing dimensionless axial compressive force F is (1) 9.22, (2) 10.85, (3) 11.13, (4) 12.43, (5) 13.29.

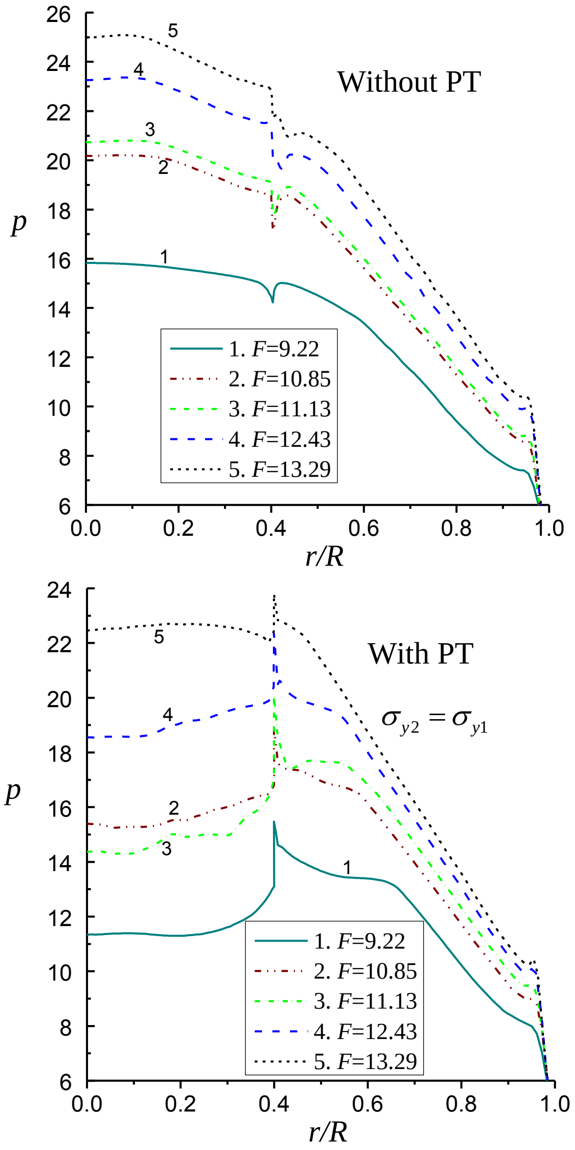

(a) (b)

FIG. 3. Distribution of pressure p at the contact surface for (a) the model without PTs and (b) with PT for $\sigma_{y2} = \sigma_{y1}$. The dimensionless axial force F is (1) 9.22, (2) 10.85, (3) 11.13, (4) 12.43, (5) 13.29.

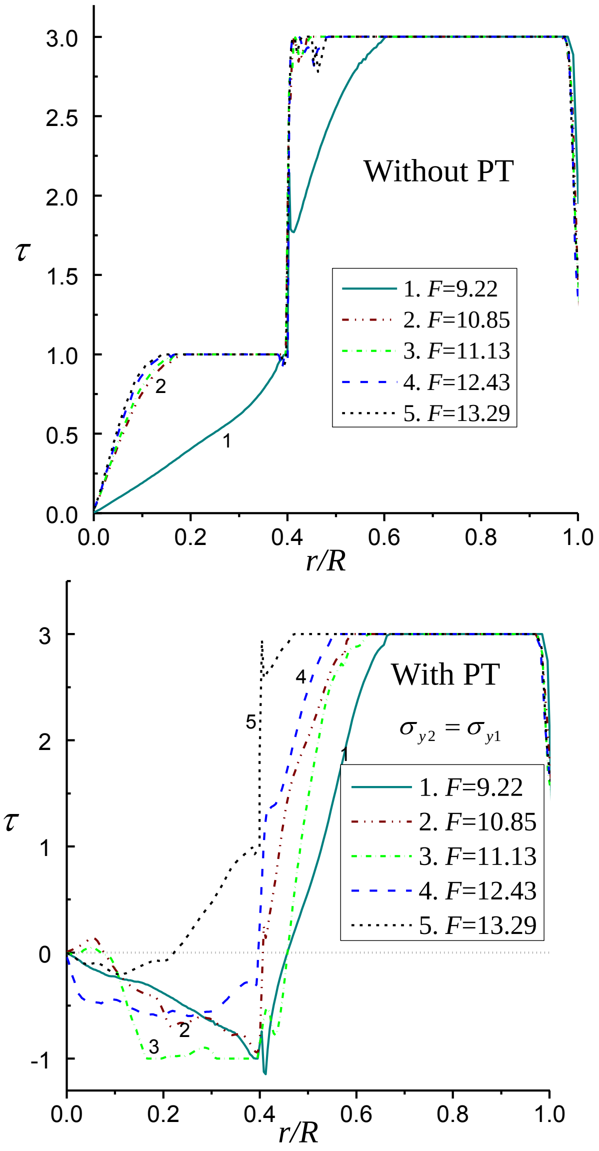

(a) (b)

FIG. 4. Distribution of the friction stress τ at the contact surface for the models (a) without PT and (b) with PT for $\sigma_{y2} = \sigma_{y1}$. The dimensionless axial force F is (1) 9.22, (2) 10.85, (3) 11.13, (4) 12.43, (5) 13.29.

Such a difference in the PT propagation directions in comparison with previous results[38-41] is caused by obvious distinctions in the distributions of accumulated plastic strain and pressure (see in the Figs. 2(b) and 2(c)), which determine PT kinetics. One can note that accumulated plastic strain is larger at the periphery and on the contact surface than the center and symmetry plane respectively. Larger accumulated plastic strain intensifies the PT kinetics. Before the pressure distribution in Fig. 2(c) is discussed, we first consider a simpler case without PT in the sample. Fig. 3(a) shows that the maximum pressure is located at the center and pressure gradually reduces from the center to the periphery. Friction shear stress in Fig. 4(a) at the contact surface of the gasket reaches the yield strength in shear, which is three times of the shear yield strength of a sample. The gasket with high yield strength greatly reduces radial flow in a sample, and pressure could reach a very high value in the sample before thickness significantly decreases. This is in fact one of the reasons for utilization of a gasket in order to produce very high pressure in relatively low strength materials. Friction stress in the entire sample and gasket in Fig. 4(a) does not change the direction because material flows from the center to the periphery under a rising loading. When PT is taken into account, in contrast to previous results[38-41] in the traditional DAC without a gasket, pressure is quite homogeneous and high in the entire sample (see Fig. 2(c) and Fig. 3(b)). Before PT, pressure monotonously reduces from the center to the periphery (Fig. 3(a)). With the increase in the applied force F from 9.22 to 13.29, PT occurs and the concentration of the high-pressure phase grows. Homogeneous and high pressure provides a large driving force for fast PT kinetics in the entire sample. Fast volume reduction due to PTs causes material flow from the periphery to the center. This is opposite to the case without PT and induces the change of shear stress direction. The decreasing pressure with increasing radius in Fig. 3(a) changes into an increasing one in the sample at $F \leq 12.43$ in Fig. 3(b). This is qualitatively consistent with the well-known from the metal forming simplified equilibrium equation $\frac{dp}{dr} = -\frac{2\tau_{zr}}{h}$ [23, 24, 40] .

Since radial flow is limited and radial and axial deformation is approximately homogeneous, shear deformation makes the main contribution to the heterogeneity of the accumulated plastic strain and concentration of the high-pressure phase. Shear stress at the center and on the symmetry plane is zero and increases to its maximum in value at the periphery and contact surface, which causes larger plastic shear strain at the periphery and contact surface (Figs. 2(b) and 4(b)). According to kinetic Eq. (8), high pressure (much above minimum pressure $p_{\varepsilon}^{d} = 6.75$) and moderate plastic strain intensify PT kinetics and further plastic flow to the center due to volume reduction during PT, which surpasses the flow to the periphery due to compression. Note that when F changes from 10.85 to 11.13, pressure in the sample even drops due to intense transformation and volume reduction. Without a gasket, the flow to the center could not be found in Ref. 40 at all and a very slight flow to the center in a small central region was found for faster kinetics in Refs. 38, 39, 41. High pressure in the entire sample and limited radial flow due to gasket make it possible to obtain a fully-transformed sample without a large reduction of sample thickness. This was not the case in a DAC without a gasket, where pressure in the periphery is too small to activate nucleation of a high-pressure phase and thickness always reduced significantly to cause large enough plastic straining. Due to a rather homogenous distribution of pressure in the sample, heterogeneous distribution of plastic strain becomes the only player to determine heterogeneity of high pressure phase concentration in the sample. Since at F=12.43 PT almost completes, at F=13.29 pressure at the center becomes slightly larger than at the periphery (Fig. 3(b)), because the flow from the center to the periphery starts. Indeed, shear stress in the major region of a sample becomes positive at F=13.29 (Fig. 4(b)). Still, the total radial displacement is negative (see Fig. 2(d)) because of previous larger flow to the center during PTs.

While there is a very sharp, approximately horizontal boundary between fully transformed and almost nontransformed regions, pressure at this interface is significantly higher than p_ε^d. This is in contrast to compression without a gasket when pressure is close to p_ε^d at the diffuse interface between fully transformed and nontransformed regions[38-41]. The reason of this difference is because of large plastic strains in Refs. 38-41, which initiates PT just above p_ε^d, and small and localized plastic straining here.

As it was suggested in Ref. 20, quasi-homogeneous pressure distribution simplifies the significantly quantitative study of the PT kinetics. It also eliminates the misinterpretation of minimum transformation pressure related to radial flow of the material transformed at high pressure but convectively moved to low pressure regions. Some simplified methods to choose parameters of a gasket to ensure quasi-homogeneous pressure and their experimental confirmation for PT from hexagonal to wurtzitic BN have been presented in Ref. 20. Current work suggests a much more precise tool for design of experiments with a quasi-homogeneous pressure distribution. Still, due to heterogeneity of plastic strain and concentration of high-pressure phase in the form of fully transformed and almost nontransformed regions divided by a relatively sharp interface, the extraction of material parameters in kinetic equation (8) is not easy. One needs to eliminate these heterogeneities as well, which is probably possible by computational design of an optimal sample-gasket system utilizing current model and numerical approach.

B. Weaker high-pressure phase

We will discuss PT and plastic flow in a sample with weaker high-pressure phase $\left(\sigma_{y2}=0.3\sigma_{y1}\right)$, under a rising compressive force *F*. Due to high-pressure phase with low strength, material softening during PT induces instabilities, which do not occur for equal-strength and stronger high-pressure phases.

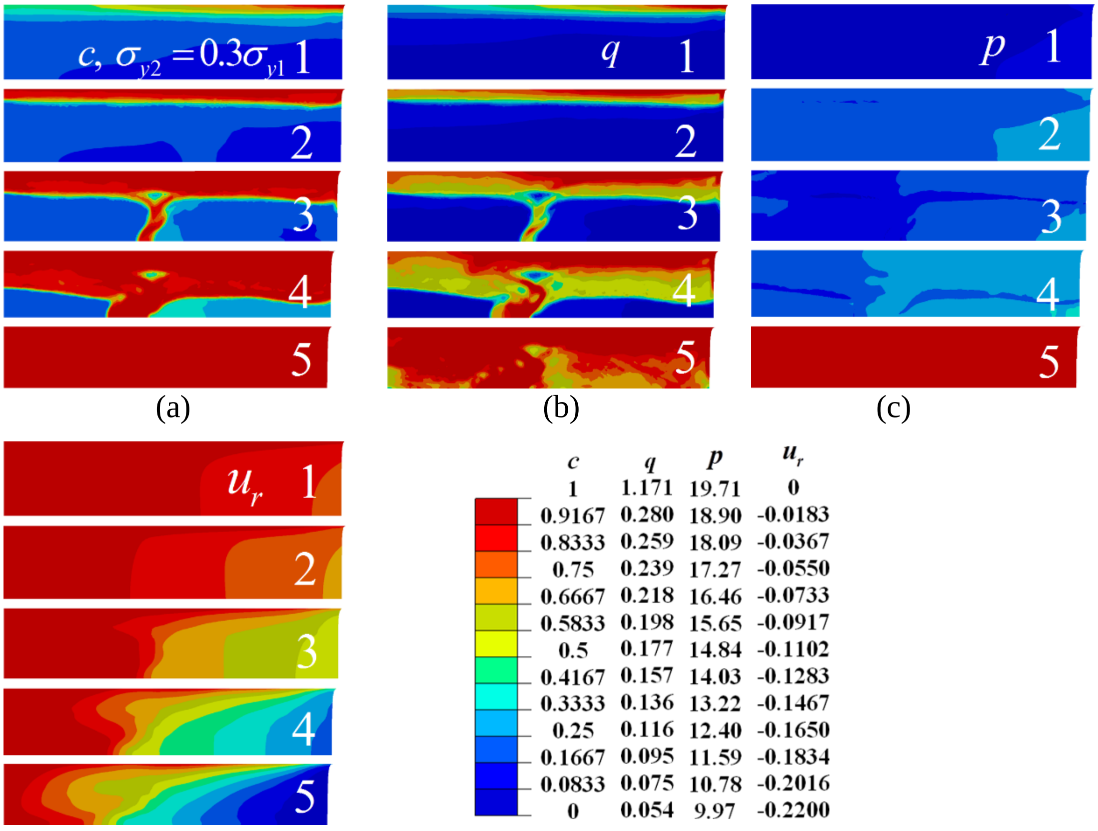

(a) (b) (c)

(d)

FIG. 5. Distributions of (a) concentration of high-pressure phase *c*, (b) accumulated plastic strain *q*, (c) pressure *p*, and (d) radial displacement u_r (normalized by a half thickness of original sample $H_0/2$) in the sample for $\sigma_{y2}=0.3\sigma_{y1}$. The dimensionless axial force *F* is (1) 8.59, (2) 9.33, (3) 9.69, (4) 10.3, (5) 12.21.

Fig. 5(a) shows the distribution on the concentration *c* of high-pressure phase in the sample during the growth of compressive force *F*. PT starts at the contact surface of the periphery and propagates towards the symmetry plane and the center of sample. When the axial compressive force reaches $F=9.33$, transformation is almost completed within a very thin contact layer, while it practically does not occur in the rest of the sample. This is consistent with experimental observation for the transformation from semiconducting Si I to weaker metallic II under compression in diamond anvils[46]. Such a correspondence with experiments also confirms that strain-induced rather than pressure or stress-induced PT occurs in Ref. 46, because pressure is practically homogeneous in the sample and shear stresses are very small in comparison with pressure. To some extent, this phenomenon was reproduced in our previous model[40] without the gasket. However, it was based on a cohesion model and caused artificial strain localization near the contact surface. In Refs. 38, 39, 41, PT always started in the center rather than at the contact surface. Plastic flow in the whole sample towards the central region of the sample due to compressive transformation volumetric strain (see Fig. 5) is more pronounced than for the cases with equal-strength and stronger high-pressure phase. Such a flow of material towards the center of the sample during PT was experimentally found for weaker high-pressure phase of ZnSe[28]. Generally, the plastic flow and PT behavior is quite similar for the cases of weaker and equal-strength high pressure phase. However, there are some differences. Thus, at $F = 9.69$ in Fig. 5, there is a curved band of localized plastic strain and completely transformed high-pressure phase connecting symmetry plane and high pressure phase near the contact surface PT. It is caused by material instability due to materials softening during phase transformation. However, the material instability is not as strong as the one in models without a gasket[38-41] because plastic flow in a sample is confined by a stronger gasket. There are no strong oscillations in pressure (Fig. 6) and shear stress (Fig. 7) at the contact surface like for the case without a gasket[38-41]. As it was mentioned in Refs. 38-41, strong strain and transformation localizations, and oscillation of stresses create significant problems in extracting kinetic equation (8) from results of experiments for weaker high-pressure phase. With a strong gasket, the extraction of kinetic information from experiments for a weaker high-pressure phase is not more complicated than for equal-strength high-pressure phase.

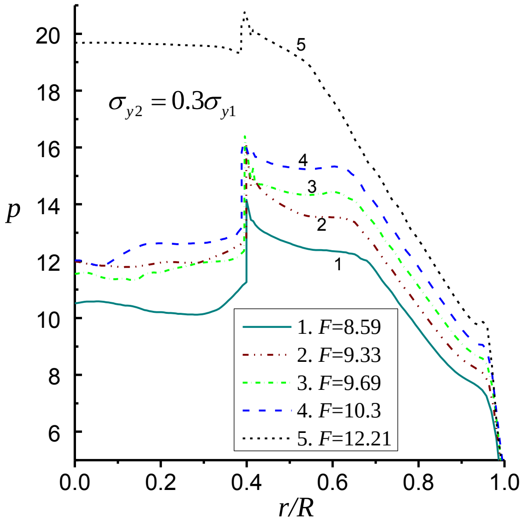

FIG. 6. Distribution of pressure p at the contact surface for $\sigma_{y2} = 0.3\sigma_{y1}$. The dimensionless axial force F is (1) 8.59, (2) 9.33, (3) 9.69, (4) 10.3, (5) 12.21.

An interesting mechanism, a sliding of a sample and gasket along the diamond, is revealed at point *b* (Fig. 1b), where all three materials are in contact. For the sample, contact shear stress reaches critical value τ_{y2} (after PT is completed at this point) and sliding toward the center is possible (see Fig. 5). However, friction stress at the inner side of the gasket does not reach the critical value $\tau_{yg} = 3\tau_{y1}$ and sliding of gasket is forbidden. Then the gasket material at the boundary between the gasket and sample slides up (with respect to sample), extrudes, and produces a new contact surface with an anvil (see Fig. 8). Such an extrusion allows the sample to slide toward the center while satisfying the cohesion condition at the preexisting and new surfaces between gasket and anvil. We called this sliding mechanism “extrusion-based pseudoslip”. The revealing of this mechanism also confirms the accuracy of the algorithm and the solution of the contact problem for contact of three materials.

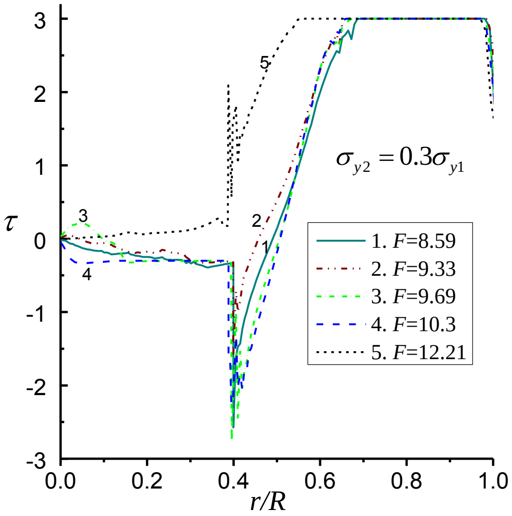

FIG. 7. Distribution of friction stress τ at the contact surface for $\sigma_{y2}=0.3\sigma_{y1}$. The dimensionless axial force F is (1) 8.59, (2) 9.33, (3) 9.69, (4) 10.3, (5) 12.21.

For stronger high-pressure phase $\left(\sigma_{y2}=3\sigma_{y1}\right)$, results in Figs. 9-11 are very different in comparison with the previous two cases with equal-strength and weaker high-pressure phases. Hardening due to phase transformation leads to reduced plastic flow with increasing concentration *c* and delocalization of phase transformation. That is why plastic deformation and transformation occur much more homogeneously within the sample without formation and propagation of a completely transformed region. Pressure during transformation is quasi-homogeneous as well. It grows faster in comparison with the previous two cases due to a larger yield strength, which is why plastic strain required for complete transformation is smaller. Since the strength of a gasket and transforming sample is becoming comparable, material flow to the center due to PT reduces in comparison with the previous two cases. Based on friction shear stress distribution (Fig. 11), the material at the exterior of the sample starts to flow to the periphery at *F*=13.17, when transformation is almost complete. Further compression is equivalent to the compression of a sample without a gasket (because the strength of the sample and gasket is almost the same and the volume reduction due to a small increment in *c* is small), which leads to a flow from the center, an increase in the shear friction stress and the pressure gradient, and consequently pressure heterogeneity and maximum pressure at the center.

FIG. 8. Extrusion-based pseudoslip as the mechanism of sliding at the contact line (line *GBL*) between sample (left to the curve *BE*), gasket (right to the curve *BE*), and anvil (line *GBL*) during compression. Initially, points B of the sample and K of the gasket coincide. The evolution of geometry of two layers of finite elements along the contact surface (*BE*) in Fig. 1(d) during compression. Point L of gasket does not slide along the anvil because the sliding condition for it is not met, while sliding condition for points of the sample is satisfied. Sample sliding with respect to the anvil is possible because of the sliding of the gasket material along the sample and its extrusion, which produces a new gasket-anvil contact surface (*BK*).

C. Stronger high-pressure phase

Due to quasi-homogeneous distributions of pressure, plastic strain, and concentration of high-pressure phase, this case is the easiest one from the point of view of the extraction of kinetic properties from experiments. Thus, averaged over sample (or central part of sample) pressure, plastic strain, and concentration of high pressure phase, determined both experimentally and in simulations, can be utilized for the determination of the kinetic equation of the type of Eq. (8). This will be discussed below. Since at the symmetry axis material undergoes uniaxial compression without shear and material rotation, all tensors in the multiplicative decomposition of the deformation gradient $\boldsymbol{F} = \boldsymbol{V}_{\mathrm{e}} \cdot \boldsymbol{F}_{\mathrm{t}} \cdot \boldsymbol{F}_{\mathrm{p}}$ are coaxial, i.e., have the same principal axes, one of which is the *z*-axis and the two others are in the plane orthogonal to the *z*-axis. Then, multiplicative decomposition transforms into an additive decomposition of the logarithmic strains:

$$\ln \boldsymbol{F} = \ln \boldsymbol{V}_{\mathrm{e}} + \ln \boldsymbol{F}_{\mathrm{t}} + \ln \boldsymbol{F}_{\mathrm{p}}. \qquad (15)$$

Because for uniaxial compression the integration of the equation $\dot{q} = (2/3 \boldsymbol{d}_p : \boldsymbol{d}_p)^{1/2}$ shows that *q* is equal to the negative logarithmic plastic strain along compression axes, along the *z*-axis, Eq. (15) simplifies to

$$\ln H / H_0 = \ln(1+\varepsilon_{\mathrm{ze}}) + \ln(1+1/3\,\varepsilon_t c) - q, \qquad (16)$$

where $\varepsilon_{\mathrm{ze}}$ is the elastic strain along *z* axis.

Pressure can be routinely measured using fluorescence of ruby particles. Concentration *c* is measured using relative intensities of *x*-ray diffraction peaks[19, 20]. Thickness of the sample *H* under load can be measured using a special pre-calibrated sensor[47].

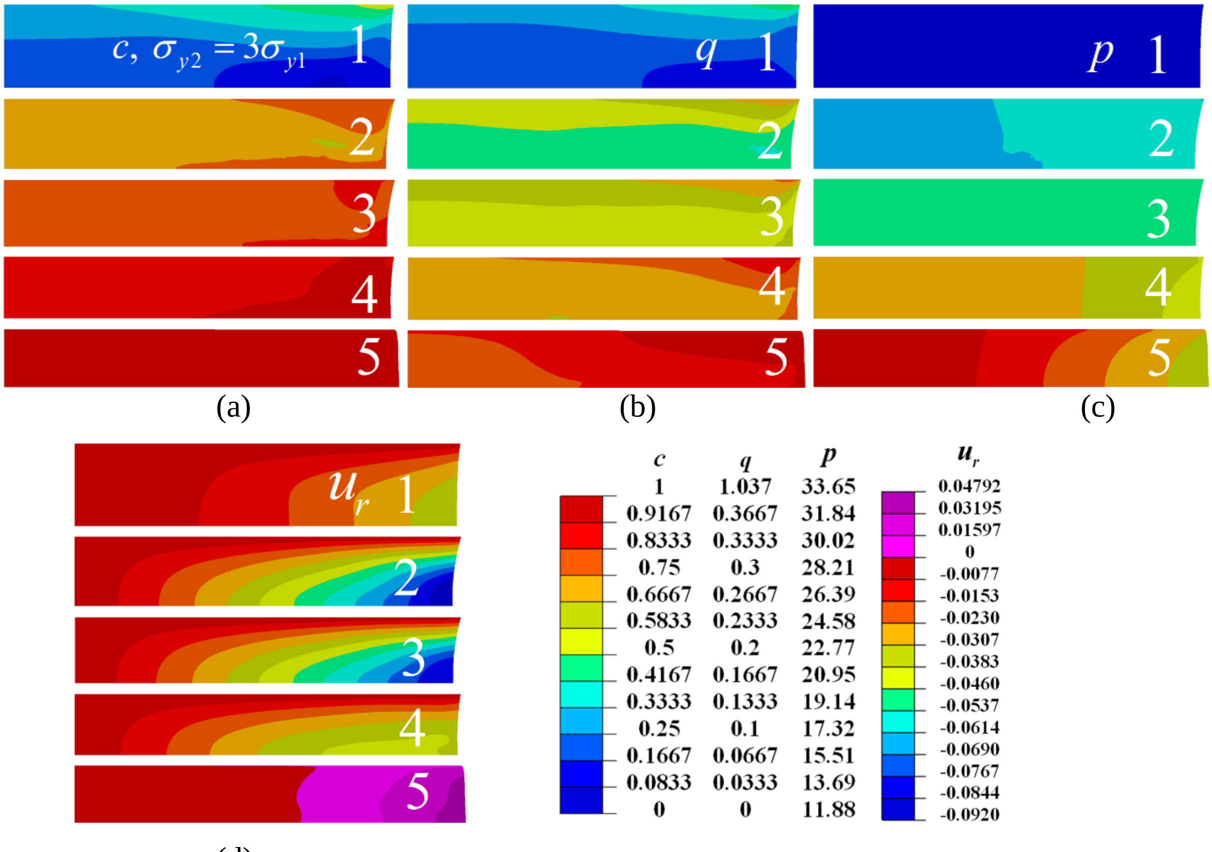

(a) (b) (c)

(d)

FIG. 9. Distributions of (a) concentration of high-pressure phase *c*, (b) accumulated plastic strain *q*, (c) pressure *p*, and (d) radial displacement u_r (normalized by a half thickness of original sample $H_0/2$) in the sample for $\sigma_{y2} = 3\sigma_{y1}$. The dimensionless axial force *F* is (1) 9.42, (2) 12.35, (3) 13.17, (4) 14.4, (5) 15.47.

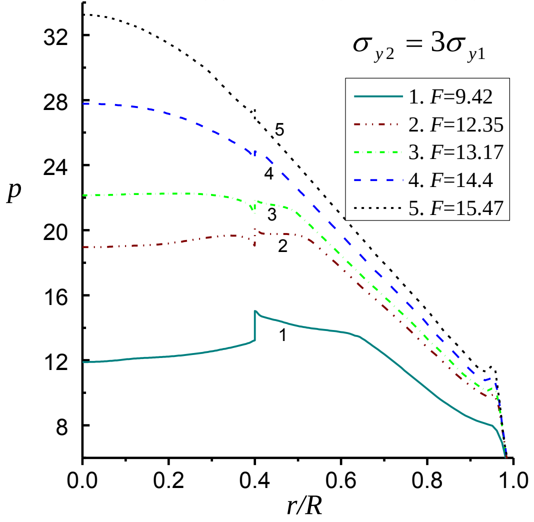

FIG. 10. Distribution of pressure *p* on the contact surface for $\sigma_{y2} = 3\sigma_{y1}$. The dimensionless axial force *F* is (1) 9.42, (2) 12.35, (3) 13.17, (4) 14.4, (5) 15.47.

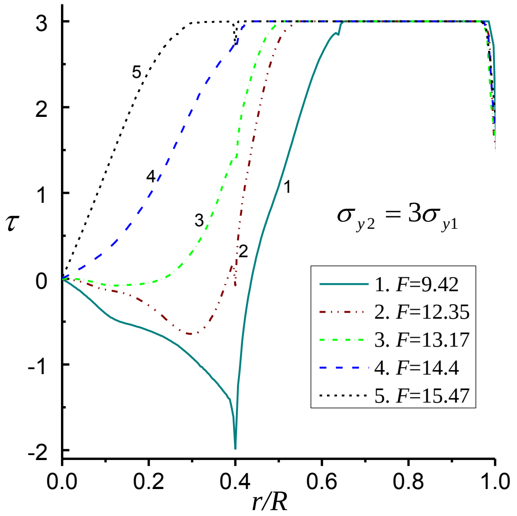

FIG. 11. Distribution of friction stress τ at the contact surface for $\sigma_{y2} = 3\sigma_{y1}$. The dimensionless axial force *F* is (1) 9.42, (2) 12.35, (3) 13.17, (4) 14.4, (5) 15.47.

D. Effects of kinetic parameter *k*

In addition to the ratio of the yield strength of phases in a sample, the kinetic parameter *k* in Eq. (8) also has strong effect on PT and plastic flows. In this section, the effects from *k* will be investigated by comparing results of *k*=6 and *k*=30 for equal yield strengths between phases. As shown in Fig. 12, with growth of *k* from 6 to 30, the rate of PT increases at the initial stage of loading $F < 11.3$. At initial loading, the sample volume reduces much faster during fast PT for *k*=30, which leads to lower pressure than that for *k*=6 and negative mechanochemical feedback. As a result, there are not essential differences in concentration of high pressure phase for *F*=12.43 and PT for both *k*=6 and 30 are completed at almost same load *F*. Initially, flow to the center is more pronounced for *k*=30 than *k*=6, which is determined by faster volume reduction during PT. In addition, faster kinetics leads to the formation of vertical strain and PT localization zones, like for *k*=6 and a smaller yield strength of the high-pressure phase. Pressure is quite homogeneous in the sample for both cases.

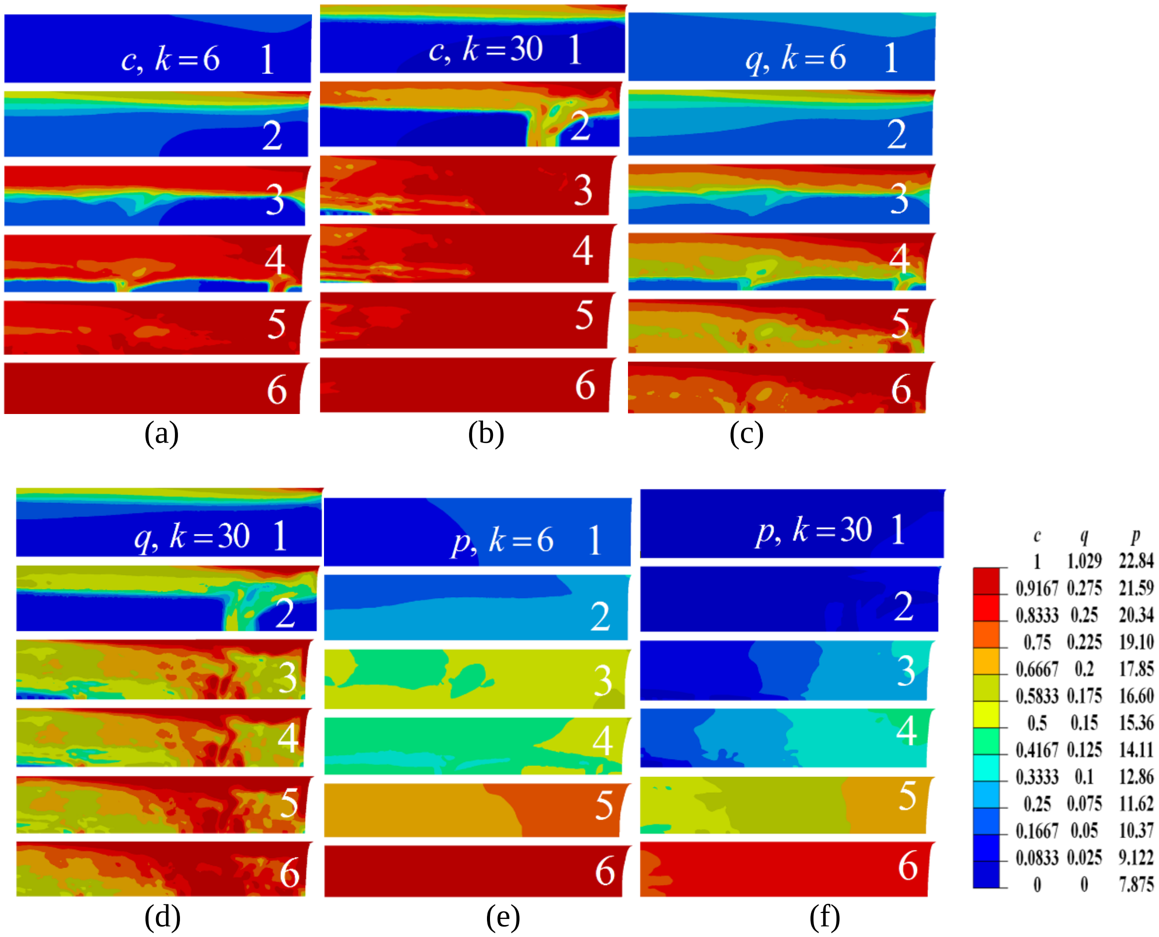

(a) (b) (c)

(d) (e) (f)

FIG. 12. Distributions of concentration of high-pressure phase *c*, accumulated plastic strain *q*, and pressure *p* in the sample for $\sigma_{y2} = \sigma_{y1}$, with *k*= 6 for (a), (c), and (e), and k=30 for (b), (d), and (f). The dimensionless axial force *F* is (1) 8.19, (2) 9.22, (3) 10.85, (4) 11.13, (5) 12.43, and (6)13.29. At k=30, extrusion-based pseudoslip is observed.

6.4. Effects of gasket/sample parameters

In Sec. III, we found that the strain-induced PT and plastic flow under compression of a sample with a gasket are much different from those in a DAC without gasket[38-41]. In this section, the effects of a gasket/sample will further be investigated in detail in three aspects: relative sample radius, gasket/sample thickness, and gasket strength. A sample with equal-strength phases $\left(\sigma_{y2} = \sigma_{y1}\right)$ will be analyzed.

A. Effects of relative sample radius

A gasket with higher yield strength (e.g., here $\sigma_{yg} = 3\sigma_{y1}$) could effectively impede the flow of the sample to the periphery and reduce heterogeneity of all parameters along the radial direction. This effect decreases with the increase of the relative sample radius $S = R_s / R$ and the reduction of the relative gasket length *G*=1-*S*, because the total friction force between anvil and gasket reduces with a decreasing contact area. Fig. 13 shows the distributions of the concentration of high-pressure phase *c* and pressure *p* in the sample for relative sample radii *S*=0.4 and *S*=0.7 under a rising axial force *F*. As it follows from Figs. 13 and 14, because of smaller yield strength, the thickness of a longer sample reduces much faster with increasing force than of a shorter sample. This induces larger plastic deformation (both due to axial strain and shear strain due to friction) and leads to faster PT kinetics for a longer sample. As can be seen in Fig. 13 (a) and (b), approximately 80% of the material completely transforms into high-pressure phase at *F* =9.22 in the sample with *S*=0.7, while PT just starts at the contact surface of the shorter sample with *S*=0.4.

Also, maximum pressure required for almost complete transformation in the entire sample is significantly larger for the shorter sample. For *S*=0.9, a completely transformed sample could not be obtained anymore, because the sample material flows outside of the flat anvil region, where the pressure is low. The developed simulation technique could be utilized for finding the optimal parameter *S* for different objectives. One can formulate the following possible objectives: (a) creating homogeneous pressure distribution to simplify extraction of kinetic material parameters from experiments; (b) to obtain a detectable amount of high-pressure phase at lowest pressure, which is important for the search for new phases while avoiding fracture of an anvil; (c) to obtain the maximum amount of high-pressure phase at the lowest maximum pressure, which is important for technological application, and others. The requirement of minimum pressure can be substituted with a stricter requirement of a lack of fracture of anvils based on strength criterion.[48, 49]

Fig. 15 shows variations of concentration of high-pressure phase c_0 and accumulated plastic strain q_0 averaged over a deformed sample thickness at the *z*-axis ($r = 0$) versus pressure *p* on the contact surface at the symmetry axis *z*. The reason for focusing on these parameters is that c_0 and *p* can be directly measured and plastic strain at the *z*-axis for relatively small *S* can be calculated based on a reduction in thickness (which can be measured) and measured c_0 and *p* (see Section 6). One could note that for the same pressure, the rate of PT with a longer sample is faster than for a shorter one due to larger plastic deformation during initially faster thickness reduction (Fig 15). For the shorter sample, when force exceeds 11 (Fig. 14), a very fast reduction in thickness occurs, which causes a sharp increase in plastic strain, concentrations, and corresponding pressure drop (Fig. 15) due to volume reduction. After this, the pressure grows up to 25 to complete PT for the shorter sample in comparison with 18 for the longer sample.

PT starts at different pressures for different *S*. Thus, if initiation of PT is accepted as a detection of $c_0 = 0.025$, then it starts at $p \approx 8.23$ for the longer sample and at $p \approx 8.89$ for the shorter sample. This is one possible explanation for different transformation pressure observed in experiments with different gaskets[12, 30].

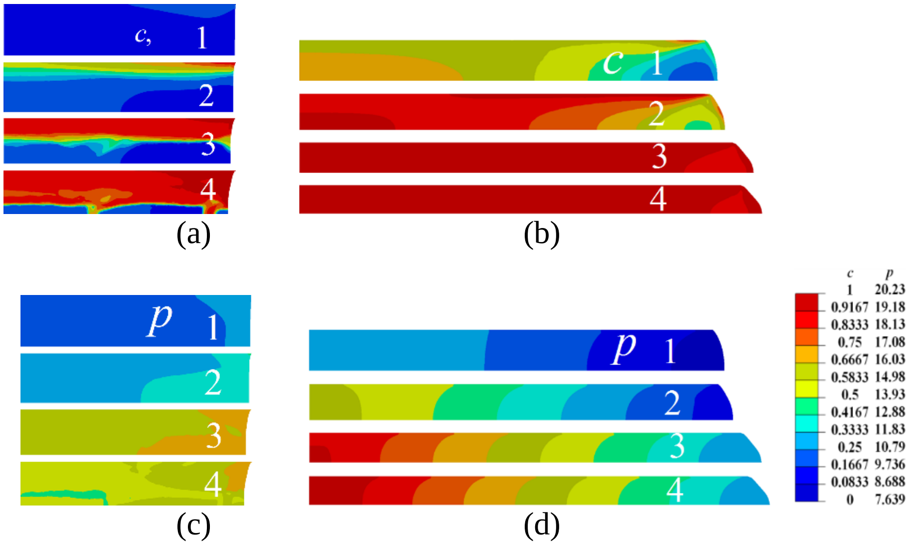

(a) (b)

(c) (d)

FIG. 13. Distributions of concentration of high-pressure phase *c*, and pressure *p* in the sample for $H_1 = H_0$ and $\sigma_{yg} = 3\sigma_{y1}$, for relative sample radii $S = 0.4$ ((a) and (c)) and $S = 0.7$ ((b) and (d)). The dimensionless axial force *F* is (1) 8.19, (2) 9.22, (3) 10.85, (4) 11.13.

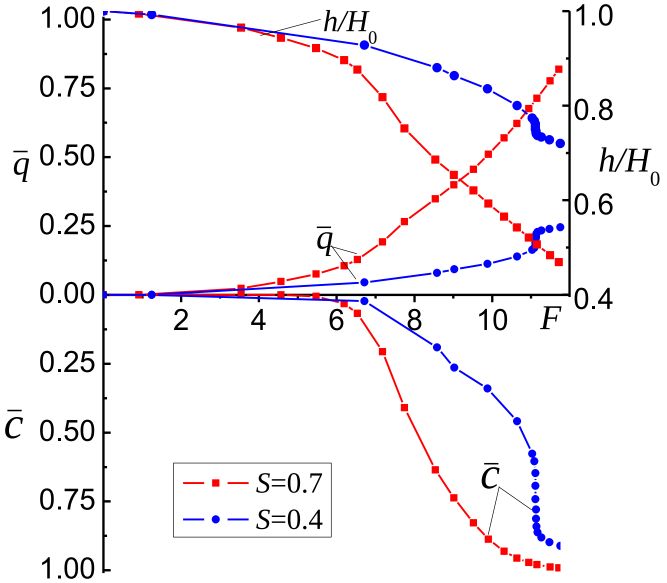

FIG. 14. Variations of concentration of high-pressure phase $\bar{c}$ and accumulated plastic strain $\bar{q}$ averaged over the entire sample, and current relative thickness of sample h/H_0 versus axial force *F* for $H_1 = H_0$, $\sigma_{yg} = 3\sigma_{y1}$, and different relative sample radii $S = 0.4$ and $S = 0.7$.

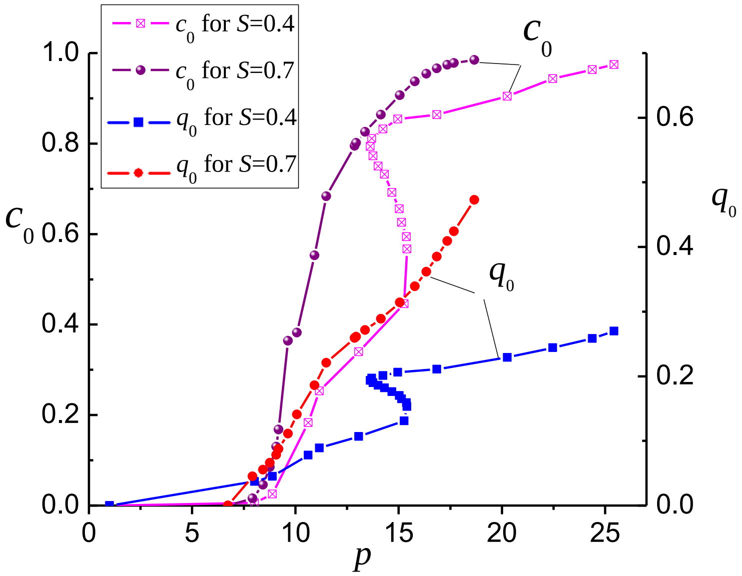

FIG. 15. Variations of concentration of high-pressure phase c_0 and accumulated plastic strain q_0 averaged over deformed sample thickness at $r=0$ versus pressure p at the contact surface at $r=0$, for $H_1 = H_0$, $\sigma_{yg} = 3\sigma_{y1}$ and different relative sample radii $S = 0.4$ and $S = 0.7$.

B. Effects of sample relative initial thickness

In this section we will discuss the effects of the sample initial thickness on the deformation and transformation processes. From Fig. 16, one can note that the geometry of the sample exterior in the deformed configuration is different for thin and thick samples. While for $H_0/R = 0.2$ sliding to the periphery at the contact surface of a sample is well visible, for $H_0/R = 0.3$ sliding at the contact surface of a sample is practically absent but radial flow intensifies away from the contact surface and is maximal at the symmetry plane. Figs. 16 (a) and (b) show that for the same axial force *F* the PT progress is slightly faster in a thinner sample (except at the periphery), which is caused by both higher pressure and larger accumulated plastic strain. However, the PT propagates much faster in the small periphery region of a thicker sample, because of higher pressure and larger plastic deformation (Fig. 16). Since the volume at the periphery is much larger than the volume at the center, the average concentrations $\bar{c}$ over the entire sample for both cases in Fig 17 are surprisingly very close. It could be seen in Fig. 16 that pressure is very heterogeneous for both cases, but for a larger thickness the pressure heterogeneity in the radial direction is obviously smaller. Fig. 17 presents that averaged over sample accumulated plastic strain is slightly larger for the thinner sample, which is caused by a slightly faster reduction in relative thickness. Note that the total axial displacement for the thicker sample is larger but h/H_0 is smaller. Although for the same axial force F an averaged PT kinetics is faster and accumulated plastic strain is larger in Fig. 16 at the center of a thinner sample, Fig. 18 shows that at the center, for the same pressure, concentration of the high-pressure phase and accumulated plastic strain are almost the same.

To summarize, for the same force and pressure, PT progress is practically independent of the thickness H_0/R of a sample. This means that the volume of transformed phase is larger for larger initial thickness. Pressure heterogeneity is smaller for larger thickness as well.

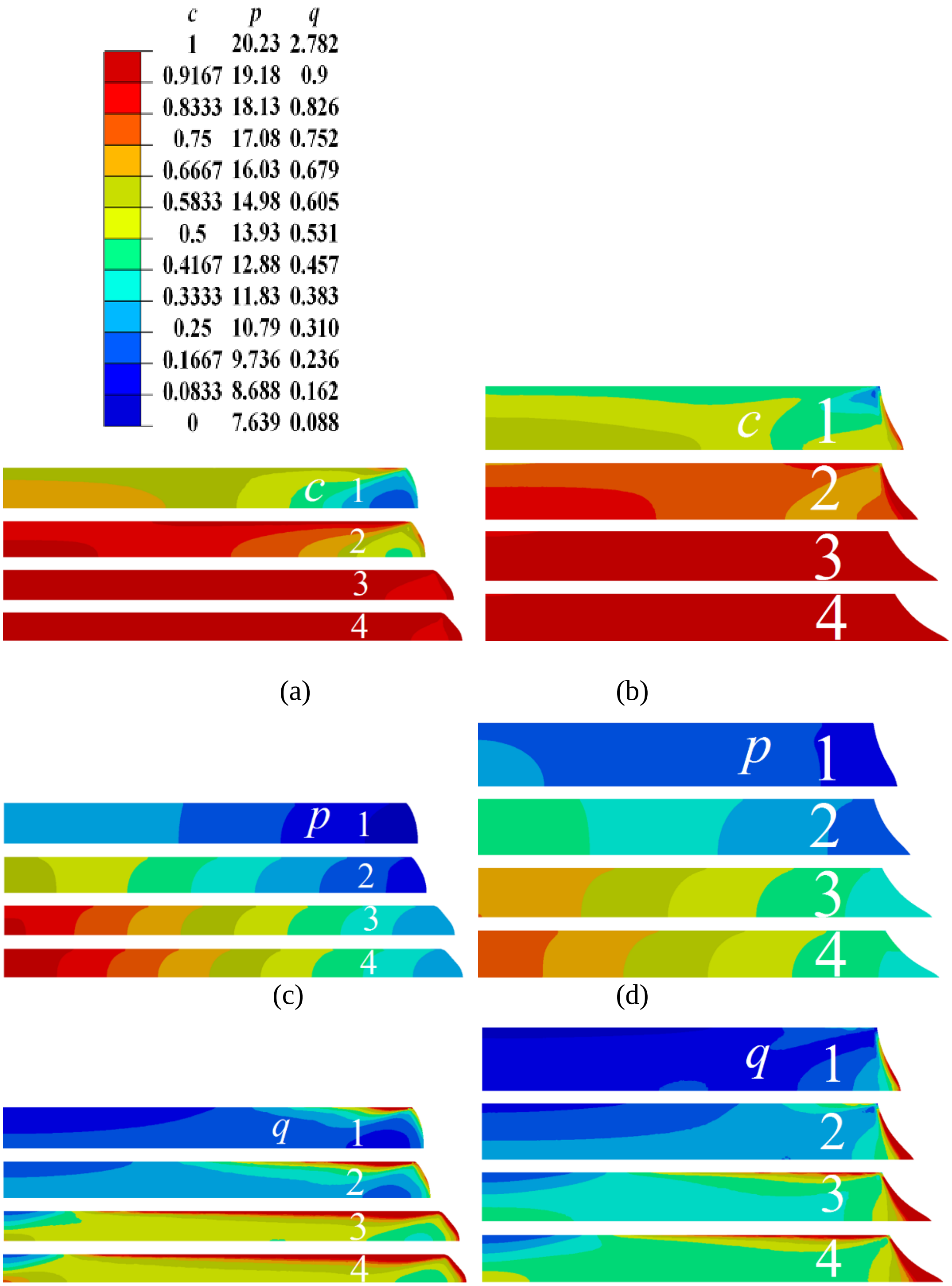

(a) (b)

(c) (d)

(e) (f)

FIG. 16. Distributions of concentration of high-pressure phase *c*, pressure *p*, and accumulated plastic strain *q* in the sample for $S = 0.7$ and $\sigma_{yg} = 3\sigma_{y1}$, for relative sample thickness $H_0/R = 0.2$ ((a), (c) and (e)) and $H_0/R = 0.3$ ((b), (d) and (f)). The dimensionless axial force *F* is (1) 8.19, (2) 9.22, (3) 10.85, (4) 11.13.

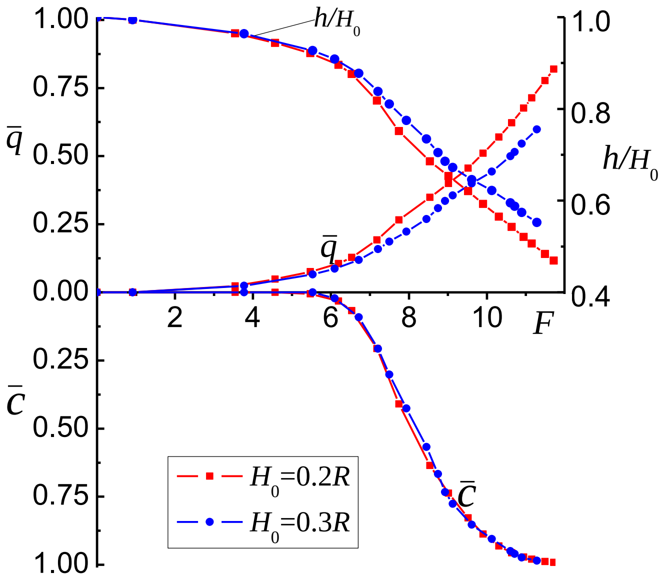

FIG. 17. Variations of concentration of high-pressure phase $\bar{c}$ and accumulated plastic strain $\bar{q}$ averaged over the entire sample and current relative thickness of sample h/H_0 versus axial force F for $R_s = 0.7R$, $\sigma_{yg} = 3\sigma_{y1}$, and two different sample thicknesses $H_0 = 0.2R$ and $H_0 = 0.3R$.

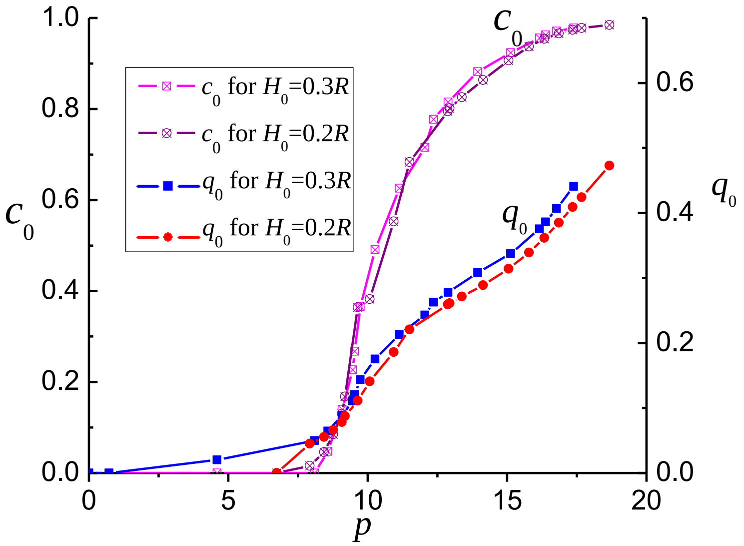

FIG. 18. Variations of concentration of high-pressure phase c_0 and accumulated plastic strain q_0 averaged over deformed sample thickness at $r = 0$ versus pressure p at the contact surface for $r = 0$, for $R_s = 0.7R$, $\sigma_{yg} = 3\sigma_{y1}$, and for different sample thicknesses $H_0 = 0.2R$ and $H_0 = 0.3R$.

C. Effects of gasket strength

The effects of gasket strength on PT and plastic flow will be studied by comparing results for gaskets with yield strengths $\sigma_{yg} = 3\sigma_{y1}$ and $\sigma_{yg} = 2\sigma_{y1}$. With the reduction of gasket strength, the reduction in sample thickness and radial material flows are intensified (Fig. 19). At F=11.09 in Fig.19 (b) and (d), the sample points reach the anvil radius *R*. This means that pressure at the periphery is low and the material does not transform completely. The sample with a weaker gasket has much larger accumulated plastic strain, which intensifies PT kinetics. At the initial loading, higher pressure close to the center is another reason for faster PT rate for the case with a weaker gasket. Therefore, some reduction of the yield strength of the gasket intensifies PT kinetics due to larger plastic deformation, but it increases the heterogeneity of pressure (Fig. 19). Fig. 20 presents that at the initial loading averaged over sample concentration of high pressure phase is larger for a weaker gasket, due to larger plastic strain during faster thickness reduction. At the late stage of loading, PT is uncompleted only at the periphery (Figs. 19 (a) and (b)), and averaged concentration over the sample increases more slowly for a weaker gasket (Fig. 20), due to lower pressure in the periphery. At the center of a sample, for the same pressure at the contact surface, Fig. 21 shows that PT progress is slightly more pronounced for the case with a weaker gasket, due to larger accumulated plastic strain during faster reduction of thickness.

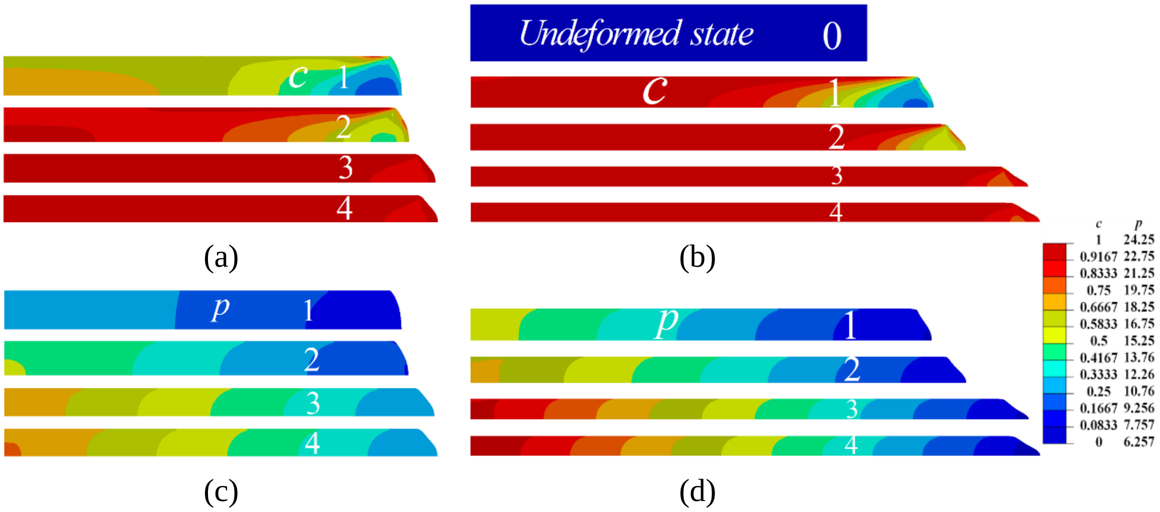

FIG. 19. Distributions of concentration of high-pressure phase c and pressure p in the sample for $R_s = 0.7R$ and $H_1 = H_0$, with gasket strength $\sigma_{yg} = 3\sigma_{y1}$ ((a) and (c)) and $\sigma_{yg} = 2\sigma_{y1}$ ((b) and (d)). The dimensionless axial force F is (1) 8.19, (2) 9.22, (3) 10.85, (4) 11.09.

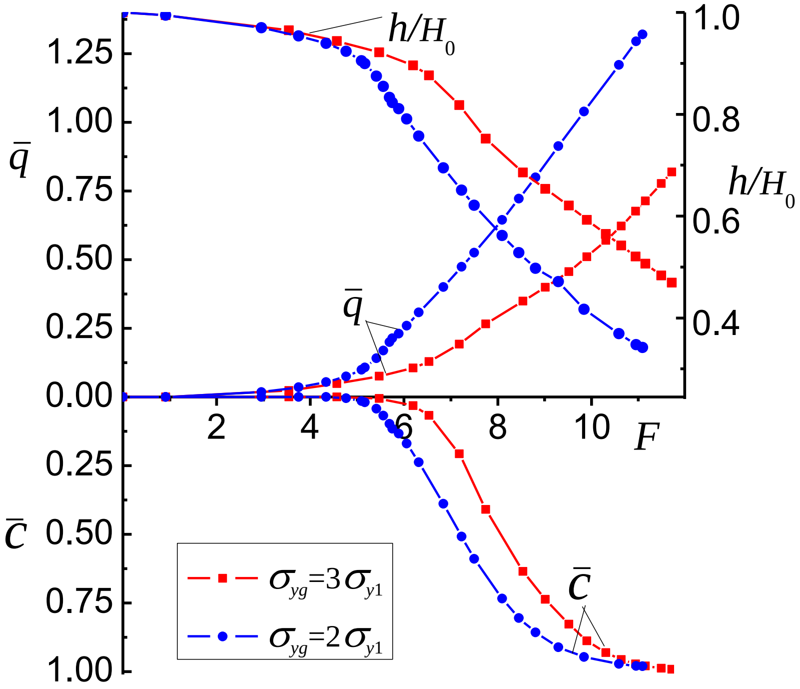

FIG. 20. Variations of averaged over the whole sample concentration of high-pressure phase $\bar{c}$ and accumulated plastic strain $\bar{q}$, and relative current thickness of sample h/H_0 as functions of axial force F for $R_s = 0.7R$ and $H_1 = H_0$, with different gasket strengths $\sigma_{yg} = 3\sigma_{y1}$ and $\sigma_{yg} = 2\sigma_{y1}$.

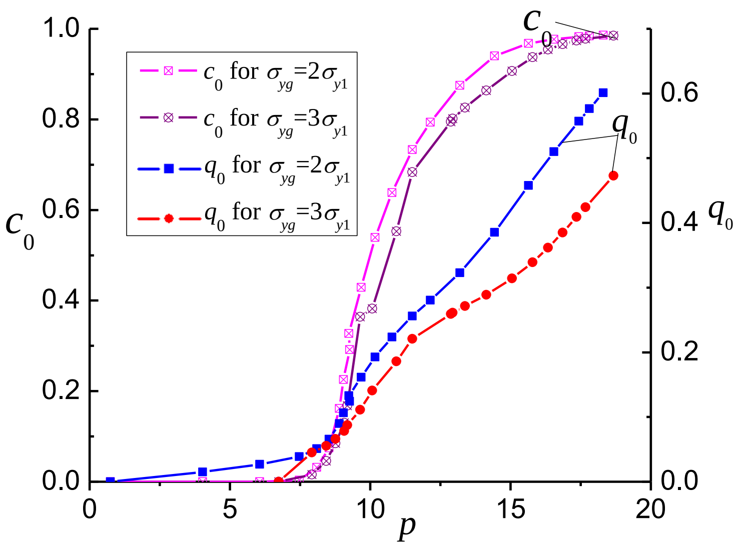

FIG. 21. Variations of concentration of high-pressure phase c_0 and accumulated plastic strain q_0 averaged over current sample thickness at $r = 0$ versus pressure p at the contact surface at $r = 0$, for $R_s = 0.7R$, $H_1 = H_0$, and different gasket strengths $\sigma_{yg} = 3\sigma_{y1}$ and $\sigma_{yg} = 2\sigma_{y1}$.

6.5 Possibility of experimental determination of kinetic equation for phase transformations to stronger high pressure phase

Here we will discuss how to apply obtained results for experimental determination of kinetic equation of the type of Eq. (8). As it was discussed in Section III, for the high pressure phase with lower and equal yield strengths than for low-pressure phase, we do not currently see a simple way to determine kinetic equation. This is because the solution for concentration has a form of localized high-pressure and low-pressure phases separated by a quite narrow interface, which makes it difficult to determine intermediate values of concentration c. However, for a stronger high-pressure phase, all fields (pressure, concentration, and plastic strains) are quasi-homogeneous at least near the center of a sample and can be determined without direct measurement of the plastic strain.

To simplify the procedure and eliminate strain hardening of phases (i.e., dependence of the yield strength on accumulated plastic strain q), the sample material should be initially strongly plastically deformed to q>1. This can be done by compression, extrusion, rolling, ball milling, and other methods of plastic deformation. Then constant or pressure-dependent yield strength of phases σ_{y1} and σ_{y2} can be determined by compression of a sample without a gasket (or with a gasket but $R_s \approx R$) by measuring pressure distribution and sample thickness H for single-phase samples, i.e., before and after complete phase transformation (see Ref. 45). There are some different methods, (see e.g., Ref. 50).

Since at the symmetry axis the material undergoes uniaxial compression without shear and material rotation, all tensors in the multiplicative decomposition of the deformation gradient $\boldsymbol{F} = \boldsymbol{V}_{\mathrm{e}} \cdot \boldsymbol{F}_{\mathrm{t}} \cdot \boldsymbol{F}_{\mathrm{p}}$ are coaxial, i.e., have the same principal axes, one of which is the z-axis and the two others are in the plane orthogonal to the z-axis. Then multiplicative decomposition transforms to an additive decomposition of the logarithmic strains:

$$\ln \boldsymbol{F} = \ln \boldsymbol{V}_{\mathrm{e}} + \ln \boldsymbol{F}_{\mathrm{t}} + \ln \boldsymbol{F}_{\mathrm{p}}. \tag{15}$$

Along the z-axis, Eq. (15) simplifies to

$$\ln H / H_0 = \ln(1+\varepsilon_{\mathrm{ze}}) + \ln(1+1/3\varepsilon_t c) - q, \tag{16}$$

because for uniaxial compression, the integration of the equation

$\dot{q} = (2/3\boldsymbol{d}_p : \boldsymbol{d}_p)^{1/2}$ shows that q is equal to the negative logarithmic plastic strain along the compression axis. Indeed, for constant principle axes of plastic deformation gradient $\boldsymbol{F}_{\mathrm{p}}$, $\boldsymbol{d}_p = \dot{\boldsymbol{F}}_p \cdot F_p^{-1} = \frac{d}{dt} \ln F_{\boldsymbol{p}}$. Plastic incompressibility condition $\ln F_{\boldsymbol{pz}} + 2 \ln F_{\boldsymbol{pr}} = 0$

results in $\mathrm{d}_{pr} = -1/2\,\mathrm{d}_{pz}$, and

$$\dot{q} = \left(\frac{2}{3}\left(\mathrm{d}_{pz}^{2} + 2\,\mathrm{d}_{pr}^{2}\right)\right)^{\frac{1}{2}} = \left|\mathrm{d}_{pz}\right| = \left|\frac{d}{dt}\ln F_{\boldsymbol{pz}}\right| = -\frac{d}{dt}\ln F_{\boldsymbol{pz}}$$, which leads to

$q = -\ln F_{\boldsymbol{pz}}$.

Pressure can be routinely measured using fluorescence of ruby particles. Concentration *c* is measured using relative intensities of *x* ray diffraction peaks[19, 20]. Thickness of the sample *H* under load can be measured using a special pre-calibrated sensor[47, 50]. Pressures at which direct p_h^d and reverse p_h^r PTs occur under hydrostatic loading can be determined using standard methods.

Stress state at the symmetry axis is characterized by three principle stresses σ_z, σ_r, σ_r, which gives mean stress $\sigma_0 = -p = (\sigma_z + 2\sigma_r)/3$ and deviatoric stresses $s_z = \sigma_z - \sigma_0 = 2(\sigma_z - \sigma_r)/3$ and $s_r = \sigma_r - \sigma_0 = (\sigma_r - \sigma_z)/3$. The stress intensity $\sigma_i = \sqrt{3/2(s_z^2 + 2s_r^2)^2} = \sigma_z - \sigma_r = \sigma_y$. Thus, knowledge of σ_y and pressure *p* allows one to define stresses σ_z and σ_r, and then with the help of elasticity rule Eq. (2) . Then all parameters for the determination of accumulated plastic strain in Eq. (16) are known. In such a way, for each loading step, one can determine *p*, *c*, and *q* and thus have all the parameters in the kinetic equation Eq. (8). By varying initial thickness and relative radius of the sample and gasket material, one can obtain various combinations of pressure and plastic strains and corresponding transformation kinetics. One can check correctness of Eq. (8) and if accuracy is not sufficient, determine more precise kinetic equation and find rationale for it.

6.6 Concluding remarks

In this paper, an advanced modeling approach for high-pressure phase transformations in a sample within a gasket compressed in the DAC is developed. The key point is that under such conditions phase transformations are treated as the plastic strain-induced ones rather than pressure-induced transformations. This is not just a terminological difference. Strain-induced PTs have completely different mechanisms and thermodynamic and kinetic description. In particular, a strain-controlled and pressure-dependent kinetic equation (8) is utilized in the model. Other points that ensure an adequate modeling are: a description of coupled PTs and plastic flow under large strains and allowing for contact sliding with combined Coulomb and plastic friction at the boundaries between sample, gasket and anvil. The latter allowed us to reveal new sliding mechanism at the contact line between sample, gasket, and anvil. When the sliding condition along the boundary with the diamond is met for the sample but not for gasket, the sample still can slide without producing a gap between the sample and gasket. Gasket material at the boundary with the sample slips along the sample and extrudes to the diamond-gasket boundary, producing a new surface area. This mechanism was called extrusion-based pseudoslip and it is very important for providing the possibility of sample flow toward the center and producing high quasi-homogeneous pressure. Obtained results demonstrate that experimentally obtained pressure for initiation and completion of PT and the entire *p*-*c* curve do not represent fundamental properties of phase transformation but rather deformation and transformation behavior of the sample/gasket system. That is why pressure for initiation and completion of PT and the entire *p*-*c* curve vary in different works that use different geometric parameters and gasket materials, as well as different high-pressure apparatuses. Consequently, plastic strain is a primary parameter, which should be measured, along with pressure and concentration of high-pressure phase. One of the most important results consists of the suggested method to extract full kinetic information (including plastic strain) from experiments for stronger high-pressure phase, which was not possible without the gasket. If realized in practice, it will completely change the characterization of high-pressure phase transformation and lead to the possibility of characterizing material transformation behavior rather than mechanical and transformational behavior of a sample/gasket/anvil system. It is still impossible for a material with weaker and equal-strength high-pressure phase. For such materials, completely transformed high-pressure phase appears at the diamond-sample boundary (which corresponds to experiment in Ref. 46) and propagates toward the symmetry axis without large regions with intermediate values of c. We hope that superposition of torsion will create a more homogeneous distribution of all parameters in the sample, which will allow us to formulate methods of experimental determination of the strain-controlled kinetic equation. This will be studied in future works. The obtained model and results are also beneficial to design high pressure experiments for different purposes, including producing the highest possible and quasi-homogeneous pressure without breaking the diamond.

Acknowledgment

The support of the Army Research Office (W911NF-12-1-0340) managed by Dr. David Stepp, Defense Advanced Research Projects Agency (W31P4Q-13-1-0010) managed by Dr. Judah Goldwasser, and Iowa State University is gratefully acknowledged.

References

[1] T. S. Duffy, G. Y. Shen, D. L. Heinz, J. F. Shu, Y. Z. Ma, H. K. Mao, R. J. Hemley, and A. K. Singh, Phys. Rev. B **60**, 15063 (1999).

[2] A. Lazicki, P. Loubeyre, F. Occelli, R. J. Hemley, and M. Mezouar, Phys. Rev. B **85**, 054103 (2012).

[3] C. Nisr, G. Ribarik, T. Ungar, G. B. M. Vaughan, P. Cordier, and S. Merkel, J. Geophys. Res. **117**, B03201 (2012).

[4] A. R. Oganov, et al., Nature **457**, 863 (2009).

[5] C. S. Zha, Z. X. Liu, and R. J. Hemley, Phys. Rev. Lett. **108**, 146402 (2012).

[6] D. M. Adams, S. J. Payne, and K. Martin, Appl. Spectrosc. **27**, 377 (1973).

[7] D. Greig, D. F. Shriver, and J. R. Ferraro, J. Chem. Phys. **66**, 5248 (1977).

[8] V. I. Levitas and L. K. Shvedov, Phys. Rev. B **65**, 104109 (2002).

[9] M. Ueno, K. Hasegawa, R. Oshima, A. Onodera, O. Shimomura, K. Takemura, H. Nakae, T. Matsuda, and T. Hirai, Phys. Rev. B **45**, 10226 (1992).

[10] R. J. Hemley, H. K. Mao, G. Y. Shen, J. Badro, P. Gillet, M. Hanfland, and D. Hausermann, Science **276**, 1242 (1997).

[11] H. K. Mao and P. M. Bell, Science **200**, 1145 (1978).

[12] T. Taniguchi, T. Sato, W. Utsumi, T. Kikegawa, and O. Shimomura, Appl. Phys. Lett. **70**, 2392 (1997).

[13] J. Zhao, R. J. Angel, and N. L. Ross, J. Phys.-Condens. Mat. **23**, 175901 (2011).

[14] J. P. Rueff, M. Krisch, Y. Q. Cai, A. Kaprolat, M. Hanfland, M. Lorenzen, C. Masciovecchio, R. Verbeni, and F. Sette, Phys. Rev. B **60**, 14510 (1999).

[15] K. Shimizu, K. Suhara, M. Ikumo, M. I. Eremets, and K. Amaya, Nature **393**, 767 (1998).

[16] G. T. Zou, Y. Z. Ma, H. K. Mao, R. J. Hemley, and S. A. Gramsch, Rev. Sci. Instrum. **72**, 1298 (2001).

[17] N. Bargen and R. Boehler, High Pressure Res. **6**, 133 (1990).

[18] D. Errandonea, Y. Meng, M. Somayazulu, and D. Hausermann, Physica B-Condensed Matter **355**, 116 (2005).

[19] V. I. Levitas, Y. Z. Ma, and J. Hashemi, Appl. Phys. Lett. **86**, 071912 (2005).

20 V. I. Levitas, Y. Z. Ma, J. Hashemi, M. Holtz, and N. Guven, J. Chem. Phys. **125**, 044507 (2006).

21 W. A. Bassett, High Pressure Res. **29**, 163 (2009).

22 A. Jayaraman, Rev. Mod. Phys. **55**, 65 (1983).

23 V. I. Levitas, Phys. Rev. B **70**, 184118 (2004).

24 V. Levitas, *Continuum mechanical fundamentals of mechanochemistry* edited by Y. Gogotsi, and V. Domnich in *High-pressure surface science and engineering* (Institute of Physics Publishing, London, 2004).

25 V. I. Levitas and M. Javanbakht, Nanoscale **6**, 162 (2014).

26 V. Blank, et al., Phys. Lett. A **188**, 281 (1994).

27 V. D. Blank, Y. Y. Boguslavsky, M. I. Eremets, E. S. Itskevich, Y. S. Konyaev, A. M. Shirokov, and E. I. Estrin, Zh. Eksp. Teor. Fiz. **87**, 922 (1984).

28 V. D. Blank and S. G. Buga, Instrum. Exp. Tech. **36**, 149 (1993).

29 C. Ji, V. I. Levitas, H. Y. Zhu, J. Chaudhuri, A. Marathe, and Y. Z. Ma, P. Natl. Acad. Sci. USA **109**, 19108 (2012).

30 F. P. Bundy and R. H. Wentorf, J. Chem. Phys. **38**, 1144 (1963).

31 S. B. Polotnyak, J. Superhard Mater. **30**, 163 (2008).

32 S. B. Polotnyak, J. Superhard Mater. **30**, 82 (2008).

33 V. I. Levitas, Int. J. Plasticity **16**, 805 (2000).

34 V. I. Levitas, Int. J. Plasticity **16**, 851 (2000).

35 A. V. Idesman, V. I. Levitas, and E. Stein, Int. J. Plasticity **16**, 893 (2000).

36 V. I. Levitas, A. V. Idesman, and E. Stein, Int. J. Solids Struct. **35**, 855 (1998).

37 V. I. Levitas and O. M. Zarechnyy, J. Phys. Chem. B **110**, 16035 (2006).

38 B. Feng, V. I. Levitas, and O. M. Zarechnyy, J. Appl. Phys. **114**, 043506 (2013).

39 B. Feng, O. M. Zarechnyy, and V. I. Levitas, J. Appl. Phys. **113**, 173514 (2013).

40 V. I. Levitas and O. M. Zarechnyy, Phys. Rev. B **82**, 174123 (2010).

41 O. M. Zarechnyy, V. I. Levitas, and Y. Z. Ma, J. Appl. Phys. **111**, 023518 (2012).

[42] B. Feng and V. I. Levitas, J. Appl. Phys. **114**, 213514 (2013).

[43] B. Feng, V. I. Levitas, and O. M. Zarechnyy, Comp. Mater. Sci. **84**, 404 (2014).

[44] V. I. Levitas and O. M. Zarechnyy, Phys. Rev. B **82**, 174124 (2010).

[45] V. I. Levitas, *Large deformation of materials with complex rheological properties at normal and high pressure* (Nova Science Publishers, Commack, N.Y., 1996).

[46] Y. Gogotsi and V. Domnich, *High-pressure surface science and engineering* (Institute of Physics Pub, Bristol ; Philadelphia, 2004).

[47] N. V. Novikov, S. B. Polotnyak, L. K. Shvedov, and V. I. Levitas, Superhard Mater. **3**, 39 (1999).

[48] N. V. Novikov, V. I. Levitas, S. B. Polotnyak, and M. M. Potyomkin, High Pressure Res. **8**, 507 (1992).

[49] N. V. Novikov, V. I. Levitas, S. B. Polotnyak, and M. M. Potyomkin, Strength Mater. **26**, 294 (1994).

[50] M. Li, et al., Rev. Sci. Instrum. **78**, 075106 (2007).

CHAPTER 7. GENERAL CONCLUSIONS

When hydrostatic media is used, PT is classified as pressure-induced one and it starts by nucleation at pre-existing defects (pressure and stress concentrators). In order to study the effect of plastic deformations on PTs, a RDAC and DAC without hydrostatic media were utilized, in which large plastic shear is superposed in the sample under high pressure. Such PTs are classified as strain-induced ones and they occur by nucleation at defects that continuously appear during the plastic deformation. Plastic strain-induced phase transformations (PTs) in a sample under compression in DAC, and compression and torsion in RDAC are investigated in detail, by applying finite element approach. A large-strain model for coupled PTs and plastic flow is developed, which includes micromechanically based strain-controlled kinetics.

First, detailed analyses of the coupled plastic flow and PTs in DAC and RDAC are studied during loading, unloading, and reloading for various ratios of the yield strengths of the low and high pressure phases, kinetic parameters, and friction parameters. In contrast to previous studies, the kinetic equation includes the pressure range, in which both direct and reverse PTs occur simultaneously. Results are compared to the case when “no transformation” region in the pressure range exists instead, for various values of the kinetic parameters and ratios of the yield strengths of low and high pressure phases. During unloading, unexpected intensive plastic flow and reverse PT are revealed, which change the interpretation of experimental results. After reloading, the reverse PT continues followed by intense direct PT and the effect of reloading paths on PTs is examined.

Second, an extended version of the Coulomb and plastic friction model for multiphase material with evolving concentration of phases is developed and implemented in ABAQUS to model contact interaction on the contact surface. All drawbacks typical of problem with cohesion are overcome, including eliminating mesh-dependent shear band and artificial plastic zones. A large contact sliding and the effect of self-locking of sliding are revealed in DAC. Also, cyclic back and forth torsion in RDAC is studied and compared to unidirectional torsion. Sliding and the reduction in friction coefficient intensify radial plastic flow in the entire sample (excluding a narrow region near the contact surface) and a reduction in thickness. Increases in both plastic strain and pressure lead to intensification of strain-induced PT. Thus, plastic flow and PT can be controlled by controlling friction.

Third, combined high pressure phase transformations (PTs) and plastic flow in a sample within a gasket compressed in diamond anvil cell (DAC) are studied for the first time using finite element method (FEM). The model takes into account contact sliding with Coulomb and plastic friction at the boundaries between the sample, gasket and anvil. A new sliding mechanism at the contact line between the sample, gasket, and anvil called extrusion-based pseudoslip is revealed, which plays an important part in producing high pressure. Strain-controlled kinetics explains why experimentally determined phase transformation pressure and kinetics (concentration of high pressure phase vs. pressure) differ for different geometries and properties of the gasket and the sample: they provide different plastic strain, which was not measured. Utilization of the gasket changes radial plastic flow toward the center of a sample, which leads to high quasi-homogeneous pressure for some geometries. For transformation to a stronger high pressure phase, plastic strain and concentration of a high-pressure phase are also quasi-homogeneous. This allowed us to suggest a method of determining strain-controlled kinetics from experimentation, which is not possible for weaker and equal-strength high-pressure phases and cases without a gasket.

Last, multiple experimental phenomena are reproduced and interpreted, including pressure self-multiplication/demultiplication effects, small 'steps' on pressure distribution in the two-phase region, simultaneous occurrences of direct and reverse PTs, oscillatory distribution of pressure for weaker high-pressure phase, and a thin layer of high-pressure phase on a contact surface. Two types of pressure variations are revealed in RDAC, which are qualitatively consistent within experimental observations for ZnSe and KCl. Reverse PT in high pressure phase that flowed to the low pressure region is revealed. Possible misinterpretation of experimental PT pressure is found. Obtained results lead to ways of controlling PTs by varying compression-torsion paths, by varying friction condition, and by varying the size and strength of sample/gasket. Similar numerical approaches can be also applied to study strain-induced PTs during ball milling, high pressure torsion, and other processes. The obtained models and results are beneficial to design high pressure experiments for different purposes, including the search of new high pressure phases and including producing the highest possible and quasi-homogeneous pressure without breaking the diamond.

In current models, we assume small elastic strains, which limits pressure to the value of 0.1 K (i.e., in the range of 10-20 GPa). However, for higher pressure, this small elastic assumption may not be suitable, and a new non-linear elasticity model will be utilized, in which the elastic moduli may be pressure-dependent. In addition, diamond anvil is assumed as rigid body and large deformation will appear after super high pressure is applied. Thus, a deformable anvils needs to take into account. Finally, perfectly plastic material is applied in sample for current models but yield strength may depend on pressure and accumulated plastic strain. In future, a large-deformation theory will be proposed, in which non-linear elasticity, dependence of yield strength on pressure and accumulated plastic strain, and deformable diamond anvil will be included.